2020

Determining ground-level composition and concentration of particulate matter across regional areas using the Himawari-8 satellite

Miles Sowden
Edith Cowan University

Edith Cowan University

Copyright Warning

Determining ground-level composition and concentration of particulate matter across regional areas using the Himawari-8 satellite

A thesis with publication submitted in fulfilment of
the requirement of the degree of
Doctor of Philosophy (PhD)

Miles Sowden

Supervisors: A/Prof Ute Mueller and Dr David Blake

School of Science
Edith Cowan University, Western Australia
2020

Abstract

Speciated ground-level aerosol concentrations are required to understand and mitigate health impacts from dust storms, wildfires and other aerosol emissions. Globally, surface monitoring is limited due to cost and infrastructure demands. While remote sensing can help estimate respirable (i.e. ground level) concentrations, current observations are restricted by inadequate spatiotemporal resolution, uncertainty in aerosol type, particle size, and vertical profile. One key issue with current remote sensing datasets is that they are derived from reflectances observed by polar orbiting imagers, which means that aerosol is only derived during the daytime, and only once or twice per day.

Sub-hourly, infrared (IR), geostationary data, such as the ten-minute data from Himawari-8, are required to monitor these events to ensure that sporadic dust events can be continually observed and quantified. Newer quantification methods using geostationary data have focussed on detecting the presence, or absence, of a dust event. However, limited attention has been paid to the determination of composition, and particle size, using IR wavelengths exclusively. More appropriate IR methods are required to quantify and classify aerosol composition in order to improve the understanding of source impacts.

The primary research objectives were investigated through a series of scientific papers centred on aspects deemed critical to successfully determining ground-level concentrations. A literature review of surface particulate monitoring of dust events using geostationary satellite remote sensing was undertaken to understand the theory and limitations in the current methodology. The review identified (amongst other findings) the reliance on visible wavelengths and the lack of temporal resolution in polar-orbiting satellite data. As a result of this, a dust-storm was investigated to determine how rapidly the storm passed and what temporal data resolution is required to monitor these and other similar events. Various IR dust indices were investigated to determine which are optimum for determining spectral change. These indices were then used to qualify and quantitate dust events, and the methodology was validated against three severe

air quality events of a dust storm; smoke from prescribed burns; and an ozone smog incident.

The study identified that continuous geostationary temporal resolution is critical in the determination of concentration. The Himawari-8 spatial resolution of 2 km is slightly coarse and further spatial aggregation or cloud masking would be detrimental to determining concentrations. Five dual-band BTD combinations, using all IR wavelengths, maximises the identification of compositional differences, atmospheric stability, and cloud cover and this improves the estimated accuracy. Preliminary validation suggests that atmospheric stability, cloud height, relative humidity, $PM_{2.5}$, PM_{10}, NO, NO_2, and O_3 appear to produce plausible plumes but that aerosol speciation (soil, sea-spray, fires, vehicles, and secondary sulfates) and SO_2 require further investigation.

The research described in the thesis details the processes adopted for the development and implementation of an integrated approach to using geostationary remote sensing data to quantify population exposure (*who*), qualify the concentration and composition (*what*), assess the temporal (*when*) and spatial (*where*) concentration distributions, to determine the source (*why*) of aerosols contribution to resulting ground-level concentrations.

Statement of original authorship and copyright

I certify that this thesis does not, to the best of my knowledge and belief:

i. incorporate without acknowledgement any material previously submitted for a degree or diploma in any institution of higher education;
ii. contain any material previously published or written by another person except where due reference is made in the text; or
iii. contain any defamatory material.
iv. I also grant permission for the Library at Edith Cowan University to make duplicate copies of my thesis as required.

I furthermore warrant that I have obtained, where necessary, permission from the copyright owners to use any third party copyright material reproduced in the thesis (e.g. artwork, e-mail), or to use any of my own published work (e.g. journal articles) in which the copyright is held by another party (e.g. publisher, co-author).

Signed: Miles Sowden  Date: **26 June 2020**

Linkage of scientific papers

Scientific papers have been renumbered and reformatted to match the style of the thesis. References have been moved to a consolidated set of references at the end of the thesis. Acknowledgements for the Australian Postgraduate Award (APA), Australian Bureau of Meteorology (BOM), Port Hedland Industrial Council (PHIC), National Computational Infrastructure (NCI), and Pawsey Supercomputing Centre have been moved into the main acknowledgement section to prevent duplication. Minor edits have been corrected based on examiners comments.

List of publications by candidate

Journal papers

1. **Sowden, M., U. Mueller, and D. Blake**. Review of surface particulate monitoring of dust events using geostationary satellite remote sensing. *Atmospheric Environment*, 2018 **183**, 154-164.

2. **Sowden, M., U. Mueller, and D. Blake**. What temporal resolution is required for remote sensing of regional aerosol concentrations using the Himawari-8 geostationary satellite?
   Atmospheric Environment, 2019, **216**, 116914.

3. **Sowden, M., D. Blake**. Which dual-band infrared indices are optimum in identifying aerosol compositional change using Himawari-8 data?
   Atmospheric Environment, 2020: 117620.

4. **Sowden, M., D. Blake, D.D. Cohen, A. Atanacio, and U. Mueller**. Development of an infrared pollution index to identify ground-level compositional, particle size, and humidity changes using Himawari-8.
   Atmospheric Environment, 2020, **229**, 117435.

5. **Sowden, M., U. Mueller, and D. Blake.** Determining ground-level composition and concentration of particulate matter across regional areas using the Himawari-8 satellite, ASAAQ15 *Special Issue, Air Quality, Atmosphere and Health*

6. **Sowden, M., Mueller, U., Blake, D.**
   Remote sensing of ground level particulate matter concentrations.
   (Positional paper at the request of the journal editor, not cited in the thesis)
   Air Quality and Climate Change 2018, **52**, 4, 13-17

International conferences

1. **M Sowden, U Mueller, D Blake, A Hinwood**. Remote sensing – how fast is fast enough? (peer reviewed extended abstract, won most innovative presentation) *23rd Clean Air Society of Australia and New Zealand (CASANZ) Conference, Brisbane*, 2017.

2. **M Sowden, U Mueller, D Blake**. Monitoring regional aerosol using Himawari geostationary data - a pilot study. (refereed abstract). *18th Annual Conference of the International Association for Mathematical Geosciences (IAMG), Perth*, 2017.

3. **Sowden, M., U. Mueller, and D. Blake.** Determining ground-level composition and concentration of particulate matter across regional areas using the Himawari-8 satellite. (refereed extended abstract and paper).*15th International Conference on Atmospheric Sciences and Applications to Air Quality (*ASAAQ15).

Local presentations

1. **M Sowden**. *Determining Ground Level Concentration of Particulate Matter across the Pilbara region using Himawari-8 Remote Sensing Data.* ECU Research week – Pawsey supercomputing 12 Oct 2017

2. **M Sowden**. *Using infrared light to detect pollution from space*. Sciteck After Dark light/optics science researchers from ECU 30 June 2018

3. **M Sowden**. *Satellite monitoring of regional aerosol concentration.* Three-minute thesis ECU, School of Science 2018 (Sep)

4. **M Sowden.** Determining GLCs of PM using Himawari-8. Western Australia CASANZ Branch Technical Event 3 October 2019

5. **M Sowden.** Determining GLCs of PM using Himawari-8. ECU, School of Science Postgraduate Seminar 5 Nov 2019

Acknowledgments

Completion of this Doctoral research would not have been possible without the support and assistance of numerous people throughout the research project. I want to express my appreciation to my principal supervisor, Associate Professor Ute Mueller, and associate supervisor Dr David Blake. Their support, guidance and professional advice provided to me throughout the research has been invaluable, and I am incredibly grateful for their assistance.

A special thanks to Dr Helen Renwick who helped change my consultant reporting style into academic prose during the dark "middle ages" of the thesis, restored my sanity during endless rounds of reviews, and told me not to use "scary quotes".

The Australian Postgraduate Award (APA) provided financial support for the PhD study by the principal author, and this funding allowed me to dedicate my time to the study, not financial worries.

Surface monitoring data was provided by the Port Hedland Industrial Council (PHIC), which was the basis of early validation and method development. A lack of speciated data necessitated that the study region be expanded and after discussions with a friend and former colleague, Dr Yvonne Scorgie, the study region was changed to New South Wales. The New South Wales Office of Environment and Heritage (OEH) has done an excellent service to the public and scientific community by providing free meteorological and ambient hourly data via their website. The OEH data was augmented by speciated particulate data from the Australian Nuclear Science and Technology Organisation (ANSTO).

Himawari-8 data was provided by the Australian Bureau of Meteorology (BOM) (from launch to current). Without this data, this study would not have been possible, and I am incredibly grateful to Dr Ian Grant, a satellite specialist at the Bureau of Meteorology, who examined my initial thesis proposal and provided constructive feedback, the contacts to the National Computational Infrastructure (NCI), and access to the data (via NCI).

This research was undertaken with the assistance of resources and services from the National Computational Infrastructure (NCI) (access to Himawari-8 data and

general processing) and the Pawsey Supercomputing Centre (visualisation of the data), both NCI and Pawsey are supported financially by the Australian Government.

Completing a PhD thesis in four years was a lot harder than I imagined. Fortunately, I was driven to solve a personal scientific challenge (the lack of background air concentrations), that affects my profession as an atmospheric modeller, or I may not have had the perseverance to persist in the isolation and self-doubt when progress seemed stuck in never-ending detours.

Completing this thesis would not have been possible without the support and encouragement from family and friends during my period of candidature: Firstly, to my former wife Leanne - for who the strain of the thesis was the final straw. Dr Peter Forster for his support and encouragement over the past four years. Dr Melissa Jennings, and the other members of the "Slim Picking's running group", for being great friends and reminding me that it is not all about work - but there is always time to run. My PhD candidate neighbour, Danica-Lea Larcombe (hopefully soon Dr) for prodding us both to finish in July (3 months late is not bad). Stewart and Jen Greensmith for their friendship and encouragement. Last, but not least, to the most enquiring non-scientist Brendon Smith for putting up with my rants about the thesis, and talking about the lack of progress, everything, and nothing on our Friday runs.

To all the above, and those not mentioned because of space constraints, a huge thank you to you all!

Abbreviations (excluding satellites and models):

ANSTO Australian Nuclear Science and Technology Organisation

AOD Aerosol optical depth

BOM Australian Bureau of Meteorology (also BOM airport monitoring site)

BT Brightness temperature

BTD Brightness temperature difference ($BT_{\lambda 1}$- $BT_{\lambda 2}$)

BTR Brightness temperature reduction, i.e. $BT_1 - BT_2$ where the suffix could be time or wavelength (Changed to BTD from Paper 2)

CDO Max-Planck's Climate Data Operators

GEO Geostationary earth-orbiting satellites

GLCs Ground level concentrations

IDDI Infrared Differential Dust Index, BTD but restricted to time-based differences

IR Infrared (2.5 μm to 25 μm)

LEO low earth orbit satellites

LOD Limit of detection (three times background)

LOQ Limit of quantification (ten times background)

MODIS MODerate-resolution Imaging Spectro-radiometer instrument

NDDI Normalised difference, dust indices ($BT_{\lambda 1}$ - $BT_{\lambda 2}$)/ ($BT_{\lambda 1}$ + $BT_{\lambda 2}$)

NIR Near infra-red (0.78 μm to 2.5 μm)

NSW New South Wales

OEH Office of Environment and Heritage

PCA Principal Component Analysis

PHIC Port Hedland Industrial Council

PM Particulate matter

RAT Ratio of BT across two wavelengths ($BT_{\lambda 1}$ / $BT_{\lambda 2}$)

TIR Thermal infra-red portion of the electromagnetic spectrum

UV Ultra-violet wavelengths of the electromagnetic spectrum

VIS Visible wavelengths of the electromagnetic spectrum

YUL Yule River PHIC monitoring site

Table of Contents

Abstract i

Statement of original authorship and copyright iii

Linkage of scientific papers iii

List of publications by candidate iv

Journal papers iv

International conferences v

Local presentations v

Acknowledgments vi

Abbreviations (excluding satellites and models): viii

List of Tables xiv

List of Figures xvi

List of Video URL's xxi

1. Introduction 22

1.1. Thesis structure and overview 22

1.2. The 5WH's of air quality 24

1.3. A tale of two cities 24

1.4. Monitoring of ground-level concentrations 26

1.5. Study areas 28

1.6. Dispersion modelling 30

1.7. Air quality remote-sensing fundamentals 32

1.7.1. Aerosol optical depth (AOD) 36

1.7.2. Dust indexes 38
1.7.3. Converting AOD to ground-level concentrations 38
1.8. Data gaps in monitoring regional air quality 39
1.9. Study aims and contribution 41

2. Thesis Overview 42

3. Literature Review 47
3.1. Abstract 47
3.2. Introduction 48
3.3. Challenges and Emerging Solutions 54
3.3.1. Spatial and Temporal Resolution 54
3.3.2. Background (i.e. zero) AOD 57
3.3.3. Aerosol Model Inversion Problem 59
3.3.4. Vertical Profiles 62
3.3.5. Validation/Accuracy 64
3.3.6. Emerging solutions 65
3.4. Conclusions 69

4. Temporal resolution 71
4.1. Abstract 71
4.2. Introduction 72
4.3. Methodology 76
4.3.1. Study design 76
4.3.2. Data 77
4.3.3. Determining the probability of a satellite overpass coinciding with a dust event 79
4.3.4. Scale factors for different time periods 79
4.3.5. Analysis of event duration using remote sensing data 80
4.4. Results 81
4.4.1. Probability of satellite overpass coinciding with a dust event 81

4.4.2. Scale factors of different time periods 83
4.4.3. Analysis of event duration using remote sensing data 84
4.5. Discussion 88
4.6. Conclusions 89

5. Indices **91**
5.1. Abstract 91
5.2. Introduction 92
5.3. Methodology 97
5.3.1. Study data 97
5.3.2. Statistical analysis 103
5.4. Results 105
5.4.1. Analysis of the three sample matrices (soil, plumes, monitoring) 105
5.5. Discussion 117
5.6. Conclusions 119
5.7. Appendix 121
5.7.1. CDO operations 122

6. Composition **124**
6.1. Abstract 124
6.2. Introduction 125
6.2.1. Surface monitoring requirements 125
6.2.2. Accuracy of estimations 126
6.2.3. Remote sensing of ground-level concentrations 127
6.2.4. Infrared indices 127
6.2.5. Aims of the study 128
6.3. Data and study area 128
6.3.1. NSW Office of Environment and Heritage 129
6.3.2. ANSTO data 130

6.3.3. Himawari-8 131
6.4. Methodology 132
6.4.1. Overview 132
6.4.2. Variations in the measured OEH and ANSTO data 132
6.4.3. Development of a pollution index 133
6.4.4. Calculating concentration from the pollution index 134
6.5. Results 135
6.5.1. Variations in the measured OEH and ANSTO data 135
6.5.2. Development of a pollution index 140
6.5.3. Determining concentration from the pollution index 144
6.6. Discussion 147
6.6.1. Variations in the measured OEH and ANSTO data 147
6.6.2. Pollution index 148
6.6.3. Calculating concentration from the pollution index 150
6.7. Conclusion 151
6.8. Appendix 153
6.8.1. SPSS OEH syntax code 153

7. Future Directions 160

7.1. Abstract 160
7.2. New GLCs product 160
7.3. Hybrid methods 161
7.4. Background subtraction 161
7.5. Rate of change 162
7.6. Atmospheric stability 163
7.7. Cloud height 164
7.8. Fires 165
7.9. Roll cloud dynamics 166
7.10. Validation 167
7.10.1. Methodology 167

7.10.2. Summer ozone episode (11 to 12 Feb 2017) 168
7.10.3. Smoke from prescribed burns (2 to 3 Sept 2017) 173
7.10.4. Dust episode from 22 to 24 Sept 2017 176
7.10.5. Discussion and conclusions 180

8. Summary 181

8.1. Abstract. 181
8.2. Introduction 182
8.3. Material and methods 183
8.3.1. Data sources 183
8.3.2. Methodology 184
8.4. Results and discussions 184
8.4.1. Literature Review 184
8.4.2. Temporal resolution requirements 184
8.4.3. Selection of dual-band indices 185
8.4.4. Calibrating aerosol change using the five BTD indices 185
8.4.5. Severe event case studies 185
8.5. Conclusions 186

9. Synthesis 188

10. References 192

Annexure A: Co-authorship statements for thesis with publication 229

List of Tables

Table 1-1: Himawari-8 bands and characteristic wavelengths and applications [58]. 34
Table 3-1: Current Earth Observational GEO satellites (excluding military, communications, and GPS satellites). Source: Union of Concerned Scientists Satellite Database https://www.ucsusa.org/nuclear-weapons/space-weapons/satellite-database. 51
Table 3-2: Recent literature describing GEO aerosol algorithms. 67
Table 4-1: Himawari-8 bands and characteristic wavelengths. 78
Table 5-1: USGS spectral absorbances averaged across each of the Himawari-8 seven infrared wavelength bands (mean ± standard deviation). 108
Table 5-2: Brightness temperature (relative to land/sea) of potential (as classified by the authors) cloud and aerosol plumes (mean ± standard deviation) in Kelvin for each of the ten Himawari-8 wavelength bands. 109
Table 5-3: Seven BTD indices which separated clouds and aerosols. All BT measurements are in Kelvin. 111
Table 5-4: Correlation (top right) and covariance (bottom left) of the seven BTD combinations which separated cloud and aerosol. 111
Table 5-5: Principal Component Score Coefficient Matrix and variance explained by the five BTD indices. 113
Table 5-6: Record numbers and soil descriptions from the United States Geological Survey (USGS) Spectral Library Version 7. 121
Table 5-5-7: Remainder of the BTD combinations correlation (top right) and covariance (bottom left). 123
Table 6-1: Average $PM_{2.5}$ concentration and aerosol percentages (by mass) PMF categories for each ANSTO site. 131
Table 6-2: Total data recovery rates (including parameters not monitored at sites) and concentration percentiles from a) the OEH dataset, and b) the ANSTO dataset. The number of valid

measurements per element is provided with the values in brackets representing the percentage of valid data recovered from total data records for each element. 136
Table 6-3: The most commonly occurring event types for a) the OEH API dataset and b) the ANSTO $PM_{2.5}$ dataset monitored over the three years (July 2015 to 2018) at the selected monitoring sites..... 139
Table 6-4: Weibull parameters per pollutant/aerosol factor sorted according to increasing shape parameter (β)..... 145

List of Figures

Figure 1-1: Schematic overview of the study design. 23
Figure 1-2: Dust storm, Sydney, 21-23 November 2018. Source: https://www.news.com.au/national/nsw-act/news/pub-manager-in-remote-nsw-captures-incredible-dust/news-story/99d33cb7bed0a4faf16c00f3afd080c5. 25
Figure 1-3: Dust storm, Onslow, 8 March 2017. Source: https://thewest.com.au/news/pilbara/huge-dust-cloud-captured-rolling-over-pilbara-ng-b88410059z. 25
Figure 1-4: NSW publicly available monitoring, data. Source https://www.environment.nsw.gov.au/aqms/search.htm. 27
Figure 1-5: Pilbara, red dots indicate sources in the National Pollution Inventory database and blue circles indicate BOM meteorological monitoring sites. 27
Figure 1-6: Port Hedland Industrial Council (PHIC) monitoring network. Source: http://www.phicmonitoring.com.au overlayed on Google Earth imagery. 29
Figure 1-7: Locations of monitoring sites in the greater Sydney region (South East Australia), UTM Zone 56S, NSW OEH sites as yellow triangles and joint OEH/ANSTO as blue squares. 29
Figure 1-8: HYSPLIT trajectory frequencies of the Onslow dust storm 8 March 2017..... 31
Figure 1-9: Sixteen wavelength bands (auto scaled) on Himawari-8, depicting the start of the Onslow dust storm. 33
Figure 1-10: MODIS datasets derived from remote sensing over the Himawari-8 observational area for the 8 March 2017. a) Natural colour, b) Cloud heights, c) fires, d) Combined 3 km AOD, e) 10 km DB AOD over land, and f) Ångström exponent (related to particle size) depicting latitudinal differences and data gaps due to non-overlapping swaths and cloud..... 35
Figure 1-11: MODIS visible (left) and Aerosol Optical Depth (right) data from 5th Jan 2014 over South Western Australia. The figure

shows fires in the south and smoke plume travelling westward and then recrossing the coast to the north over Perth. 37
Figure 1-12: Schematic overview of data gaps. 40
Figure 4-1: Frequency distribution of the ratios of maximum (ten-minute) and daily average PM10 concentrations at five monitoring sites near Port Hedland. 83
Figure 4-2: Cumulative frequency of the daily PM10 scale ratio (ten-minute/average) and during MODIS overpass times at two sites (BOM and YUL)..... 83
Figure 4-3: Exponent for converting between averaging time-periods. 83
Figure 4-4: a) Brightness temperature (band 7) vs. time and b) surface temperature at BOM on the 8th and 9th March 2017. 84
Figure 4-5: Taylor diagrams depicting variances of brightness temperatures across the study region using bands 7, 11 and 12 as reference. 85
Figure 4-6: Weight of the first principal component of six BTD combinations indicating changes to probable aerosol types. Frame 0 (UTC) represents 8 AM local time. (Legend depicts wavelength bands, not wavelengths). 87
Figure 4-7: BTD $_{(3.9 - 6.2\ \mu m)}$ depicting the development of the dust incident. 2 PM) wind reversal to offshore; 4 PM) start of dust storm; 6 PM) maritime air colliding with the wind blowing offshore; 9 PM) storm dissipated. 87
Figure 5-1: Potential plumes and points of interest identified from the daily standard deviation of band 7 (3. 9 μm) across the study domain. Scale is ln(standard deviation) in Kelvin. 101
Figure 5-2: Scatter plots of She's et al. (2018) BTD indices (in Kelvin) depicting the separation of cloud and aerosol plumes over arid and semiarid regions with threshold values given on the axis title. Aerosol plumes are not fully labelled to prevent overlapping. 107

Figure 5-3: Variance explained by the first principal component for three sample matrices for each wavelength. 110
Figure 5-4: Aerosol differences (standard deviation) against cloud separation (difference of means) using the three indices (a) BTD, b) NDDI, and c) RAT). 110
Figure 5-5: Separation of clouds (bottom left) and aerosols (top right) using $BTD_{3.9\ 6.2}$ µm and $BTD_{11\text{-}12}$ µm. Axis indicate approximate threshold values. 112
Figure 5-6: Separation of aerosols using $BTD_{9.6\text{-}13\ \mu m}$ and $BTD_{6.9\text{-}7.3\ \mu m}$. 112
Figure 5-7: Plot matrix depicting histograms and scatter diagrams between pairs of indices at 10 AM on the 8 March 2017 over the Western Pilbara region of Australia. 114
Figure 5-8: Histogram (standardised to max=100%) of $BTD_{\ 3.9\text{-}6.2\ \mu m}$ at midday, 4 PM and midnight (UTC+8) on 8 March 2017. 115
Figure 5-9: Fraction of pixels remaining and rate of change (first derivative) with different BTD thresholds at 10:30 AM (Terra) (UTC+8) on 8 March 2017. 115
Figure 5-10: Dust indices over the full Himawari monitoring hemisphere, with cloud masking, 10:30 AM (UTC+8) 8 Mar 2017. Captions based on band characteristics [58]. 116
Figure 6-1: Locations of monitoring sites in the greater Sydney region (South East Australia), UTM Zone 56S, NSW OEH sites as yellow triangles, and joint OEH/ANSTO as blue squares..... 129
Figure 6-2: Box and whisker plots by: a) OEH relative humidity; b) OEH percentage fines; c) ANSTO relative humidity, d) ANSTO percentage fines depicting API per pollutant (where a singular pollutant exceeded an API of unity for each monitoring site..... 138
Figure 6-3: Boxplots depicting BTD by event and severity (concentration). 141
Figure 6-4: Pollution index (PI) as a function of a) OEH events by relative humidity, b) OEH events by percentage fine aerosol, c) ANSTO events by relative humidity, and d) ANSTO events by percentage fine aerosol. 143

Figure 6-5: Average concentration and probability as a function of the pollution index. a) OEH relative humidity and particle size; b) probability below the mean or above the guideline (97.5%); c/d) OEH/ANSTO concentration; e/f) OEH/ANSTO probability; g/h) OEH/ANSTO probability as a Weibull function. 146
Figure 7-1: (a) Band 07, (b) Hourly change of band 07. 162
Figure 7-2: MSLP synoptic chart and atmospheric instability 5 PM AEDT 12 Feb 2017. 163
Figure 7-3: Cloud phase and temperature. 164
Figure 7-4: Estimate of cloud height 5 PM AEDT 12 Feb 2017. 164
Figure 7-5: $PM_{2.5}$ and PM_{10} emitted from a fire depicting size discrimination with downwind distance. 165
Figure 7-6: Hourly depiction of the roll cloud (demarcated) from the Onslow dust storm, depicted from the air towards the south-west using cooling of band seven to depict cloud height. 166
Figure 7-7: Maximum daily Ozone and temperature across all OEH monitoring sites for February 2017. 169
Figure 7-8: HYSPLIT backwards four-day trajectory analysis for the period 10 to 12 February 2017. 170
Figure 7-9: Terra Natural Colour 11 September 2017. 171
Figure 7-10: Potential ozone sources a) VOC's from fire and b) isoprene from vegetation. 172
Figure 7-11: Maximum daily PM_{10} and $PM_{2.5}$ concentrations across all OEH monitoring sites for September 2017. 174
Figure 7-12: HYSPLIT backwards four-day trajectory analysis for the period 2 to 4 September 2017. 174
Figure 7-13: Analysis of smoke event on 2 Sept 2017 showing a) stability; b) cloud height; c) NO_2, d) $PM_{2.5}$, e) PM_{10}, and O_3. 175
Figure 7-14: Maximum daily PM_{10} and $PM_{2.5}$ concentrations across all OEH monitoring sites for September 2017. 177
Figure 7-15: HYSPLIT backwards four-day trajectory analysis for the period 20 to 24 September 2017. 177

Figure 7-16: Dust source 20 Sept (a)natural colour, (b)AOD and (c)destination (23rdSept). 178
Figure 7-17: Analysis of dust event on 24 Sept 2017 showing a) stability; b) cloud height; c) NO_2, d) $PM_{2.5}$, e) PM_{10}, and O_3. 179

List of Video URL's

Video 3-1: 3D depiction of roll cloud	https://tinyurl.com/OnslowRollCloud
Video A-1: Cloud height	https://tinyurl.com/CloudHeight
Video A-2: Atmospheric stability	https://tinyurl.com/AtmosStability
Video A-3: Relative humidity	https://tinyurl.com/RelHumidity
Video A-4: $PM_{2.5}$ GLCs	https://tinyurl.com/FineParticles
Video A-5: PM_{10} GLCs	https://tinyurl.com/CoarseParticles
Video A-6: NO_2 GLCs	https://tinyurl.com/GLC-NO2
Video A-7: O_3 GLCs	https://tinyurl.com/GLC-O3
Video A-8: OEH 1-4 September 2017	https://tinyurl.com/SmokeEvent
Video A-9: OEH 19-24 September 2017	https://tinyurl.com/DustEvent

(tinyurl redirects to ECU box site)

1. Introduction

1.1. Thesis structure and overview

A recent review by Duncan et al. [1], listed numerous applications where remote sensing may be beneficial to atmospheric scientists and suggested that remote sensing should be more widely utilised. The review suggested that geostationary satellites, which remain over fixed locations and provide near-continuous data, could radically improve remote sensing monitoring. One of these geostationary satellites, Himawari-8, began supplying data (2 km spatial resolution and ten-minute temporal resolution) during July 2015 which covers East and South-East Asia, Australia, and New Zealand.

This thesis is therefore partially a response to Duncan's review – for the first time in two decades, there is potentially a credible method to monitor air pollution impacts from space and determine impacts across vast areas with moderate spatial and high temporal resolution. Much of the existing methodology assumes that a single daily snapshot can determine daily and annual average concentration levels [2-5]. The aims of this thesis are to expand upon the advantages of better time resolution and day/night coverage from the present generation of geostationary IR satellites and highlight new opportunities they offer compared to polar satellites. This is novel territory and therefore an experimental approach was taken to identify how spectral differences could be used to determine composition and concentration.

This thesis has used the "thesis with publication" methodology to present strategies to address deficiencies that have hindered the wider adoption of geostationary remote sensing to quantify ground-level concentrations (GLCs). This thesis is about air pollution, and specifically respirable particulate matter (PM) GLCs because of PM's ubiquitous presence in many areas across the world. It evaluates the use of geostationary satellite data to determine PM GLCs in remote and regional areas where there may be a lack of traditional monitoring data and suggests the use of infrared wavelength bands, rather than the more traditional, daytime only, visible bands, in order to provide near-continuous data.

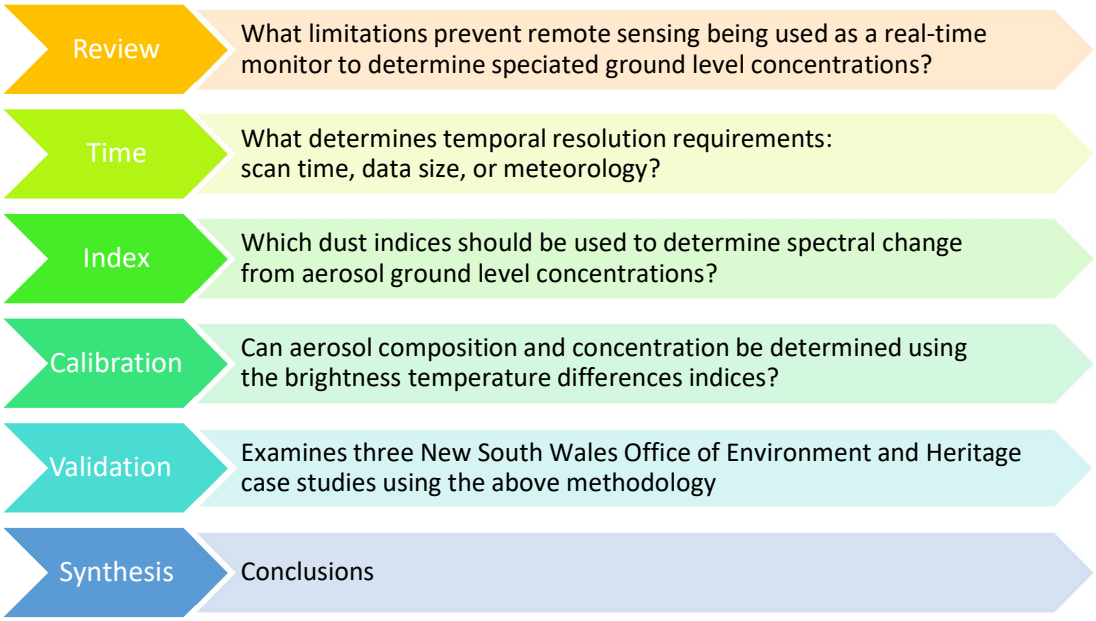

Figure 1-1: Schematic overview of the study design.

A schematic overview of the study design is presented in Figure 1-1. The introduction describes problems with determining GLCs and uses case studies to informally describe limitations in the existing methodology to reduce potentially of repetitive or disjointed statements in a "thesis with publication" leaving specific details to the subsequent publications. Chapter two is an overview of the thesis which brings together the publications in individual chapters, into a coherent narrative. Chapter three is the published literature review of geostationary remote sensing for atmospheric monitoring, which identifies gaps in the current body of knowledge [6]. Chapter four asserts that the temporal changes in a dust event require highly resolved temporal data, such as Himawari-8 data, to detect and map those temporal changes [7]. Chapter five argues that the requirement for near-continuous monitoring necessitates a shift in methodology from visible spectroscopy to infrared (IR), determines which IR wavelength bands are best able to detect changing aerosol composition, and recommends five dust indices [8]. Chapter six uses those dust indices to determine aerosol species compositional changes. Chapter seven describes potential further studies and presents preliminary validation of ground-level predictions over the greater Sydney region using three species-selective case studies [9]. Chapter eight is a mini summary of the research [10] and the concluding synthesis (chapter 9) describes how this thesis has advanced the field and discusses further research that is required.

1.2. The 5WH's of air quality

For in acts we must take note of who did it, by what aids or instruments he did it, what he did, where he did it, why he did it, how and when he did it - Aristotle

To understand air quality events, it is instructive to answer six interrogative word questions (who, what, when, where, why, how-to). There is thus the need to determine the affected parties (*who*), qualify the concentration and composition (*what*), assess the temporal (*when*) and spatial (*where*) concentration distributions, and determine the source (*why*) of emissions contribution to resulting ground-level concentrations with the long term goal of finding methods (*how-to)* to mitigate or minimise future events.

1.3. A tale of two cities

In many regions of the world, there is limited monitoring of air quality events, and social media and newspapers present the sole sources of information on these events. The lack of monitored surface atmospheric data (meteorological and concentration) in regional areas [11] is highlighted by comparing the information available regarding a dust storm in Sydney (November 2018) (Figure 1-2) that was monitored by the state environmental regulators and reported in numerous news reports, to a single news item for a dust storm in Onslow (March 2017) (Figure 1-3), which had no local surface monitoring with which to verify concentrations. Comparing the information between these two storms highlights the imbalance of scientific evidence of dust storms and smoke plumes between urban and regional communities.

While both events were dust storms, media reports indicated that the Sydney storm lasted two days while the Onslow storm lasted a few hours. Comparing the reduction in visibility across the two photographs suggests that much higher concentrations were experienced at Onslow than Sydney. However, there are insufficient data, from the photographs, to determine if the residents of Sydney, who breathed finer particles over two days (more time for erosion), were more or less exposed than the Onslow residents who received an acute dosage (see also roll cloud dynamics in Figure 7-6).

Figure 1-2: Dust storm, Sydney, 21-23 November 2018. Source: https://www.news.com.au/national/nsw-act/news/pub-manager-in-remote-nsw-captures-incredible-dust/news-story/99d33cb7bed0a4faf16c00f3afd080c5.

Figure 1-3: Dust storm, Onslow, 8 March 2017. Source: https://thewest.com.au/news/pilbara/huge-dust-cloud-captured-rolling-over-pilbara-ng-b88410059z.

1.4. Monitoring of ground-level concentrations

Various methods have been used to estimate, predict or measure airborne contaminant concentrations in order to quantify the population exposure [12]. Ambient monitoring using fixed locations provides reliable concentration data, often spanning decades. However, monitoring sites may be sparse in regional areas because of cost and infrastructure (power, cooling, and security) limitations [13, 14] and sited according to population, rather than areas of risk [15].

This sparsity in monitoring data is reflected in the publicly available data depicted in Figure 1-4 for New South Wales (NSW) across the greater Sydney area compared to confidential data for the Pilbara region in Western Australia. The Pilbara region is shown in Figure 1-5 and includes Onslow, which is a small town situated along the north-west Pilbara coast. The NSW website lists 45 air quality monitoring sites of which 17 have hourly long-term archived data that can be downloaded (as at July 2019). In contrast, in the Pilbara confidential monitoring is conducted in and around Port Hedland (http://www.phicmonitoring.com.au), Karratha (http://www.pilbarairon.com/dustmonitoring), and at mining sites according to licence conditions.

Three years (July 2015-2018) of surface concentration data (CO, NO, NO_2, $PM_{2.5}$, PM_{10}, SO_2, O_3) were obtained from the New South Wales (NSW) Office of Environment and Heritage (OEH) for the seventeen real-time monitoring sites across the greater Sydney region in eastern Australia. Data were also obtained from the Australian Nuclear Science and Technology Organisation (ANSTO), for five co-located sites over the same monitoring period as the OEH data. The ANSTO data were derived from positive matrix factorisation analysis, of $PM_{2.5}$ samples captured on filters over twenty-four hours twice weekly [16]. Port Hedland Industrial Council (PHIC) supplied three years of ambient air quality data for the study. These three concentration datasets were paired in time with ten-minute spectral data from the Himawari-8 geostationary satellite. No other monitoring data were available to the study.

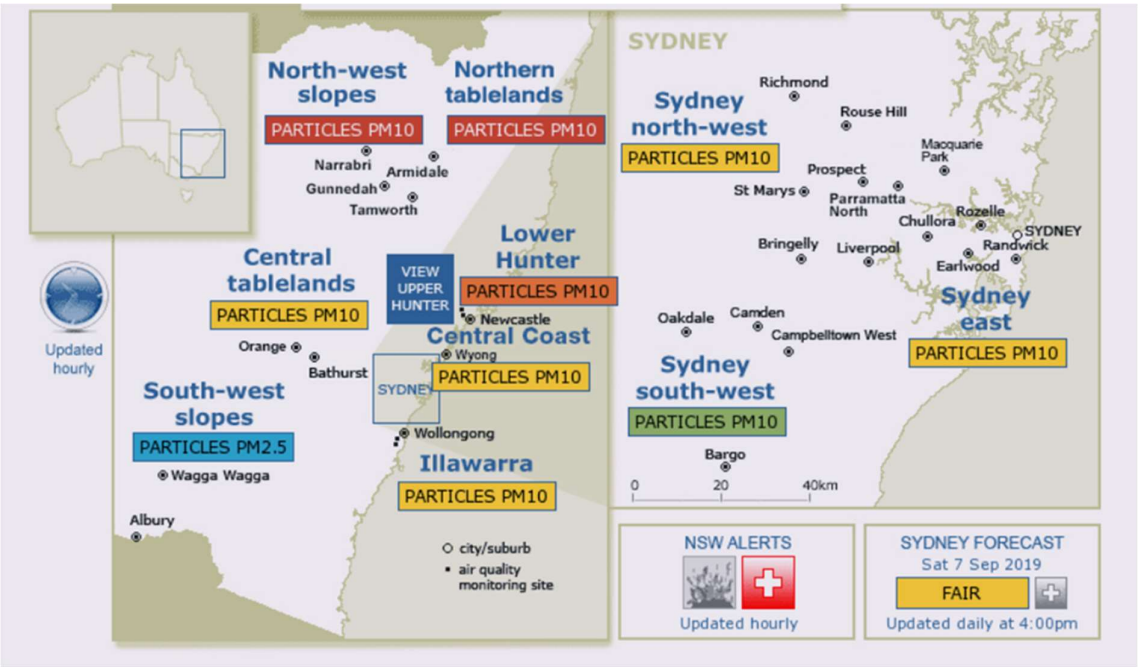

Figure 1-4: NSW publicly available monitoring, data.

Source https://www.environment.nsw.gov.au/aqms/search.htm.

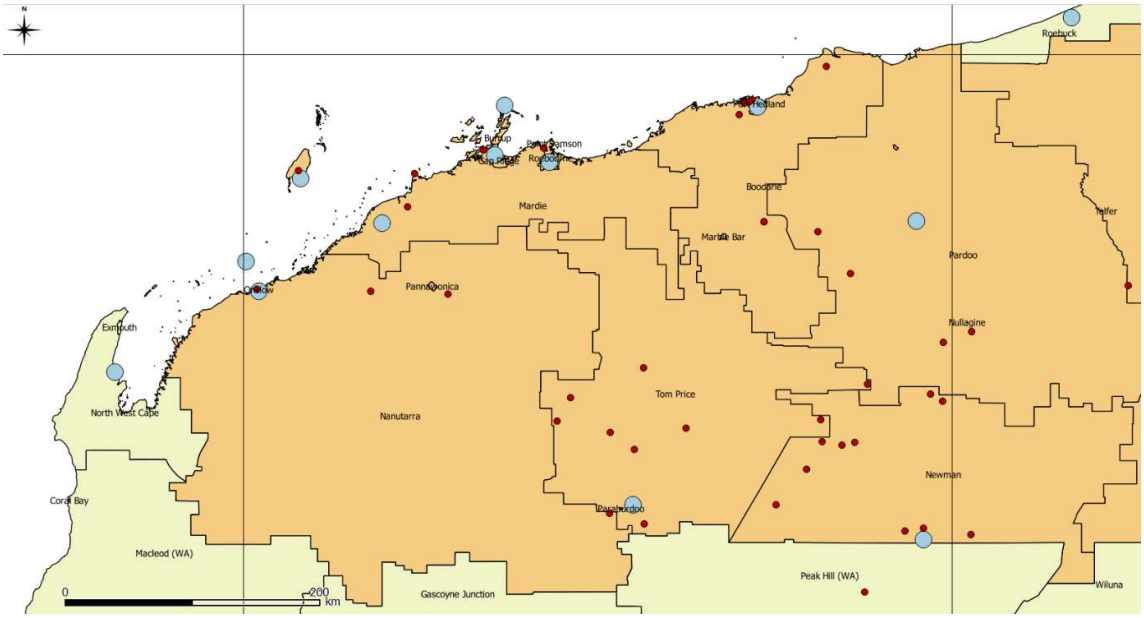

Figure 1-5: Pilbara, red dots indicate sources in the National Pollution Inventory database and blue circles indicate BOM meteorological monitoring sites.

1.5. Study areas

The Onslow dust storm (Figure 1-3), which occurred during the beginning of the thesis, was an ideal opportunity for method development. The Pilbara region (Figure 1-5) was initially selected as the study area as it is a dusty environment with comparatively low vehicle usage, is profoundly affected by local industry, and experiences widespread regional fires and dust storms [17-19]. It is a vast region of approximately 1,600 × 400 km^2 situated to the north of Western Australia and is known for its resource extraction (mining) and pastoral (rangeland) industries. Population congregates in the few mining towns of the region. Maximum daytime temperatures regularly exceed 50°C and the low rainfall (≤ 350 mm/year) contributes to the arid nature of the region [20]. The study area, therefore, provided a unique opportunity to study natural dust emissions and resultant concentrations in the absence of primary confounding urban sources.

Port Hedland is a major town along the northern Pilbara coast and is a distribution hub for enormous quantities (513 Mt in 2018) [21] of iron ore, and other commodities, which are shipped through its port. Port Hedland has an extensive long-term air quality monitoring network [22] that identifies frequent exceedances of PM national standards, which are often attributed to background events [23]. However, there is limited rural monitoring with only one site located outside Port Hedland at Yule River, about 20 km inland. This monitoring network is maintained by the Port Hedland Industrial Council (PHIC), in conjunction with local industry. It consists of eight sites (see Figure 1-6), which monitor at five-minute intervals for $PM_{2.5}$, PM_{10}, NO_2 and SO_2. PM_{10} is measured at all eight sites, $PM_{2.5}$ is only measured at five sites while NO_2 and SO_2 are measured at four sites.

The lack of widely dispersed sites (monitoring sites were collocated on the same Himawari-8 "pixel"), minimal $PM_{2.5}$ monitoring and the lack of ground-level speciated particulate matter concentration data for this area made it challenging to calibrate (i.e. determine ground level concentration and aerosol speciation from the satellite data) using this data. A second study area was therefore chosen, which had diverse sites, comprehensive monitoring and speciated aerosol data.

Figure 1-6: Port Hedland Industrial Council (PHIC) monitoring network. Source: http://www.phicmonitoring.com.au overlayed on Google Earth imagery.

Figure 1-7: Locations of monitoring sites in the greater Sydney region (South East Australia), UTM Zone 56S, NSW OEH sites as yellow triangles and joint OEH/ANSTO as blue squares.

The Greater Sydney region in New South Wales in Eastern Australia was selected as the additional study area (Figure 1-4 and Figure 1-7) since the state regulators provide hourly historical data of size apportioned particulate matter concentrations and meteorological parameters (via their web page) and the Australian Nuclear Science and Technology Organisation (ANSTO) provided daily speciated particulate data from windblown soil, sea-spray, smoke, secondary sulphates, and vehicles. The region is more vegetated than the Pilbara (i.e. less contribution from desert dust), has a higher population density (i.e. more contribution from urban sources), experiences more fires from prescribed burns, and more cloud cover as a consequence of the higher humidity [24].

1.6. Dispersion modelling

Dispersion modelling is used to estimate concentrations at unmonitored locations. Dispersion modelling was first proposed by Taylor [25] and has undergone numerous revisions to refine the underlying theories and improve predictions based on validation studies [26, 27]. The advantage of dispersion modelling is that it predicts concentrations at any point, time and from any source within the modelling domain, so that health impacts can be inferred at any location, from any source (size or composition) or projected forward/back in time [28]. Knowing the chemical composition at source, and computing chemical transformations during dispersion [29] allows the composition to be determined anywhere within the modelling domain [30].

Dispersion modelling takes the estimated emission from each source and disperses the pollutants according to parameterisations of the prevailing meteorology (wind-field) [31, 32]. The accuracy of the predicted concentrations and spatial distribution of the sources is dependent on correctly identifying and quantifying emission sources in a detailed emission inventory [33-36] and not ignoring or poorly quantifying, large area sources, such as sporadic fires [37]. Wind field errors arise from incorrect internal model parameterisations (e.g. stability class coefficients) and meteorological input approximations [36, 38]. Emission errors affect concentration (magnitude), while wind field errors predominantly affect the position and, to a lesser extent, concentration.

Although dispersion modelling can, and does, provide regional concentrations, it is severely limited by missing or incorrect input data. These errors are apparent in the HYSPLIT trajectory analysis (elementary dispersion model showing plume movement not concentration) [39] for the Onslow dust storm is depicted in Figure 1-8. It is apparent that the predominant wind direction, from the sea, collided with desert air. However, the specific source location, source parameters (particle size and source emission rate (g/s)) and timing are unknown and estimating those parameters negatively affects the accuracy and usefulness of a dispersion model. There is, therefore, a requirement for a monitoring method that can observe over a vast region, at a high spatial and temporal resolution, to quantify rapidly changing atmospheric events such as dust storms and smoke from fires.

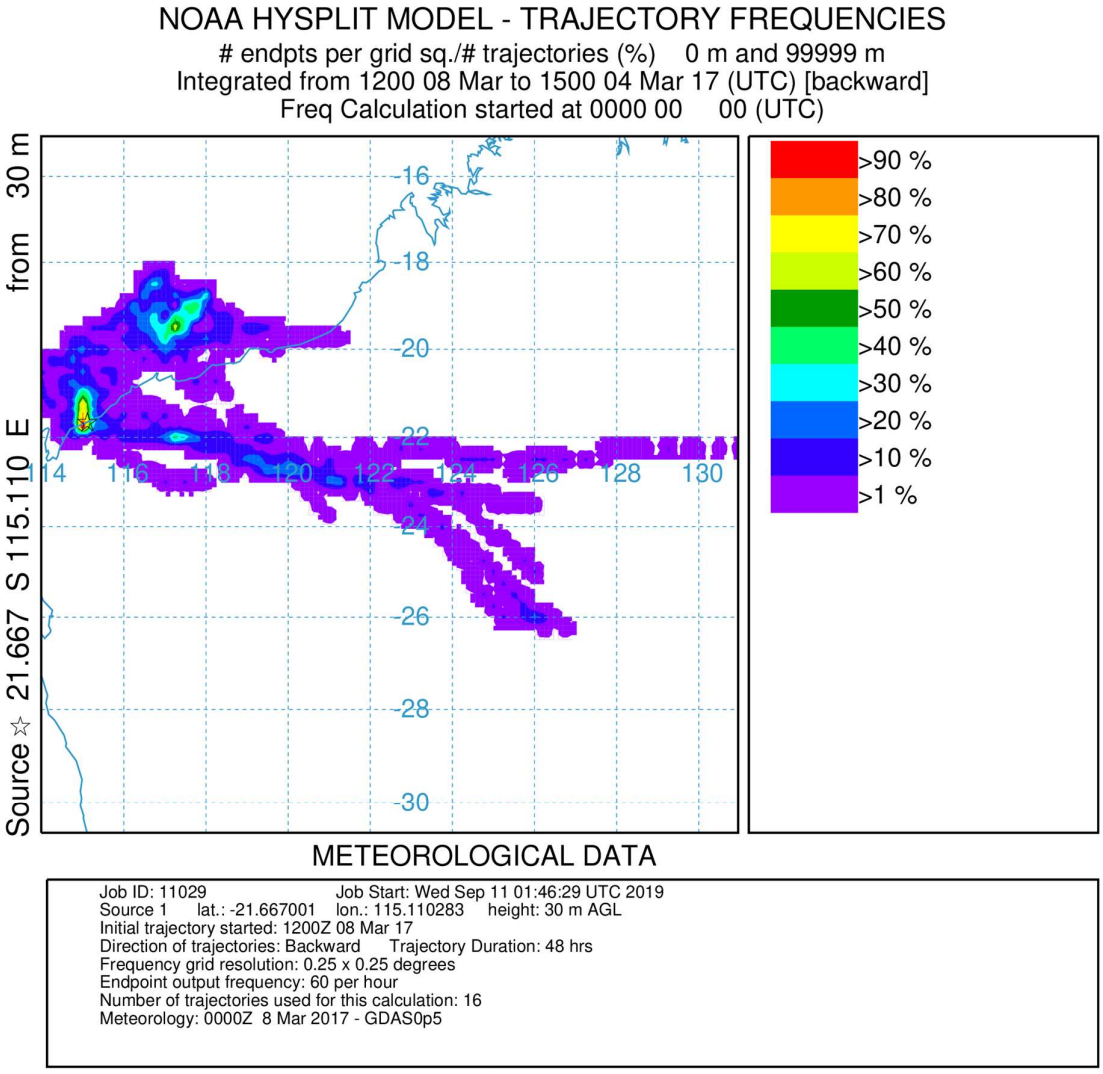

Figure 1-8: HYSPLIT trajectory frequencies of the Onslow dust storm 8 March 2017.

1.7. Air quality remote-sensing fundamentals

In contrast to dispersion modelling, remote sensing is seen as an increasingly valuable tool in determining concentrations over large areas, especially where a large sampling grid is impractical because of cost or infrastructure concerns [40, 41]. Over the past thirty years, there has been substantial growth in the number of satellites related to communications, navigation and scientific studies [1, 42-46]. The spatial resolution of the sensor is primarily linked to the orbit height of the satellite and the focal distance. The orbit height determines the size of the swath (and temporal resolution), but at the cost of resolution per pixel. For example, Landsat-8 has a swath of 185 km but a pixel resolution of 15 m (channel dependent) every two weeks [47] in contrast to MODIS with a swath of 2330 km and a pixel resolution (channel dependent) of 250 m (to 1 km) updated daily [48].

The orbit characteristics of the sensors determines the temporal resolution. Two common "flight paths" are used. Polar-orbiting satellites continually rotate around the poles, while the rotation of the earth provides much of the sideways "movement". They are usually set to return over a location once a day, e.g. the MODIS satellites [48]. In contrast, geostationary satellites attempt to stay over the same location and provide rapid updates, e.g. 10 min data from Himawari-8, but at the cost of only a portion of the earth being observed [49, 50].

A standard camera captures visible light by separating and storing the three primary components, or channels, of visible light, namely red, green, and blue. In contrast, remote sensing uses more channels to measure a broader portion of the electromagnetic spectrum [51]. The number of channels, the width, and the frequencies of each channel are determined during the design phase according to the scientific objectives of the satellite. Figure 1-9, depicts the extent of the sixteen wavelength bands on Himawari-8, at the start of the Onslow dust storm, and the similarities between bands are apparent. The first six bands are visible and near-infrared wavelengths compared to the ten infrared wavelengths (a different false-colour scheme was used to highlight the IR bands).

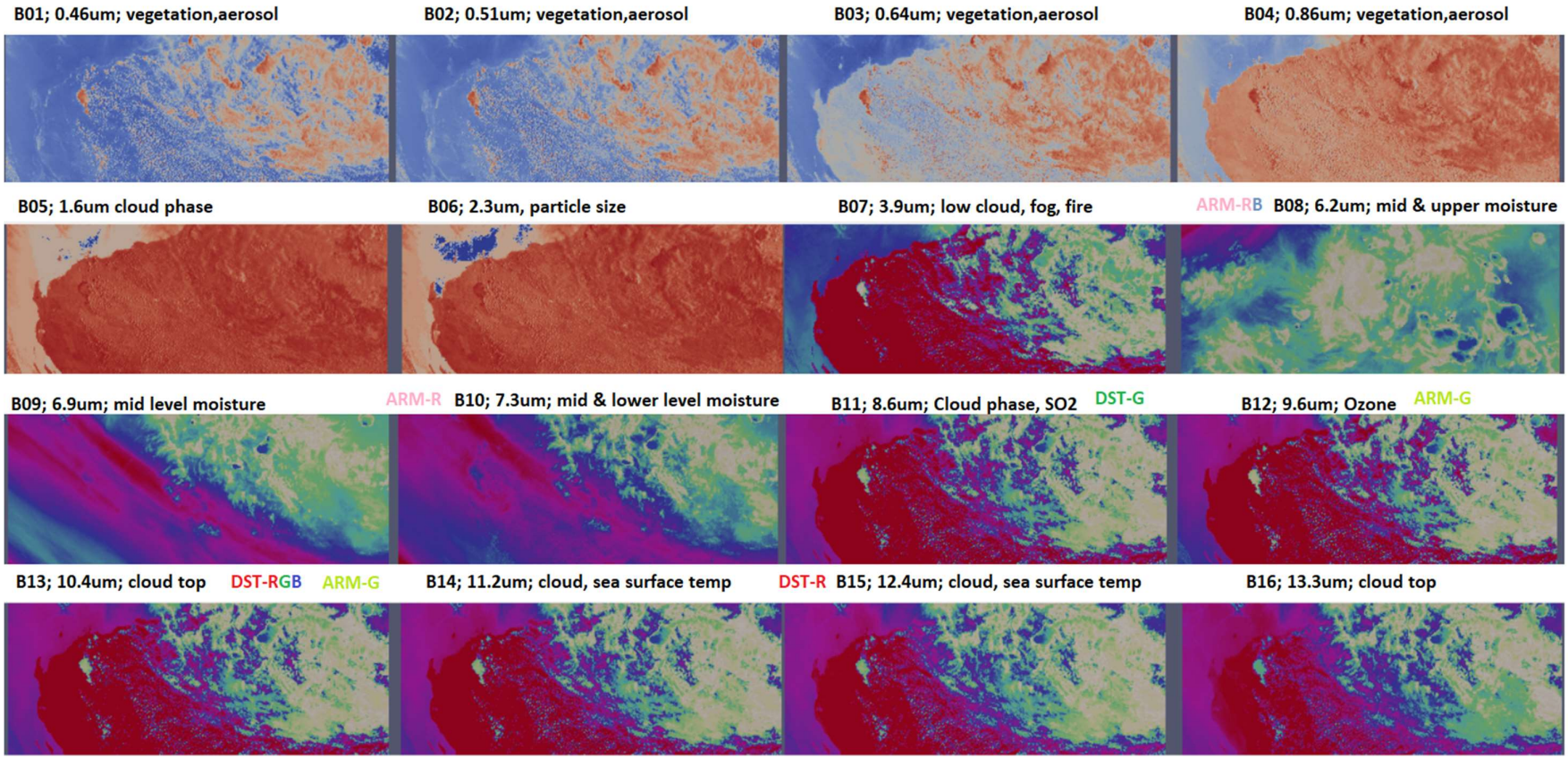

Figure 1-9: Sixteen wavelength bands (auto scaled) on Himawari-8, depicting the start of the Onslow dust storm.

Some satellites, such as SCIAMACHY [52, 53], use a hyperspectral sensor [54] for detecting pollution while others seek to record severe weather events using fewer channels [55]. Compounds exhibit different absorption and reflectance properties at different wavelengths [51, 56] and these characteristic spectra are available in databases such as JPL's Aster spectral library (http://speclib.jpl.nasa.gov) and wavelength tables produced by most satellite providers [57]. Table 1-1 details the sixteen Himawari bands and typical applications of those bands.

Table 1-1: Himawari-8 bands and characteristic wavelengths and applications [58].

Band	Wavelength (μm)			Applications
	Low	High	Central	
1	0.43	0.48	0.471	vegetation, aerosol
2	0.5	0.52	0.51	vegetation, aerosol
3	0.63	0.66	0.639	low cloud, fog
4	0.85	0.87	0.857	vegetation, aerosol
5	1.6	1.62	1.61	cloud phase
6	2.25	2.27	2.257	particle size
7	3.74	3.96	3.885	low cloud, fog, forest fire
8	6.06	6.43	6.243	mid and upper-level moisture
9	6.89	7.01	6.941	mid-level moisture
10	7.26	7.43	7.347	mid and low-level moisture
11	8.44	8.76	8.593	cloud phase, SO_2
12	9.54	9.72	9.637	ozone content
13	10.3	10.6	10.407	cloud top, "clean longwave window"
14	11.1	11.3	11.24	cloud, sea surface temperature
15	12.2	12.5	12.381	cloud, sea surface temperature, "dirty longwave window"
16	13.2	13.4	13.281	cloud top, CO_2

Satellite products use this information to determine various computed products from multiple channels and/or incorporate data from other sensors to perform their calculations [48]. MODIS products are possibly the best known because of their long history, as reflected in the recently revised collection six products, ease of access, algorithms peer-review process and extensive publication record [48]. Of interest to atmospheric scientists are products (as depicted in Figure 1-10) that provide information about fire, cloud, meteorological, soil, vegetation and pollutants such as ozone, SO_2 and aerosols products [1] as these products are relevant to determining ground-level concentrations. Figure 1-10 depicts latitudinal differences and data gaps due to non-overlapping swaths and cloud,

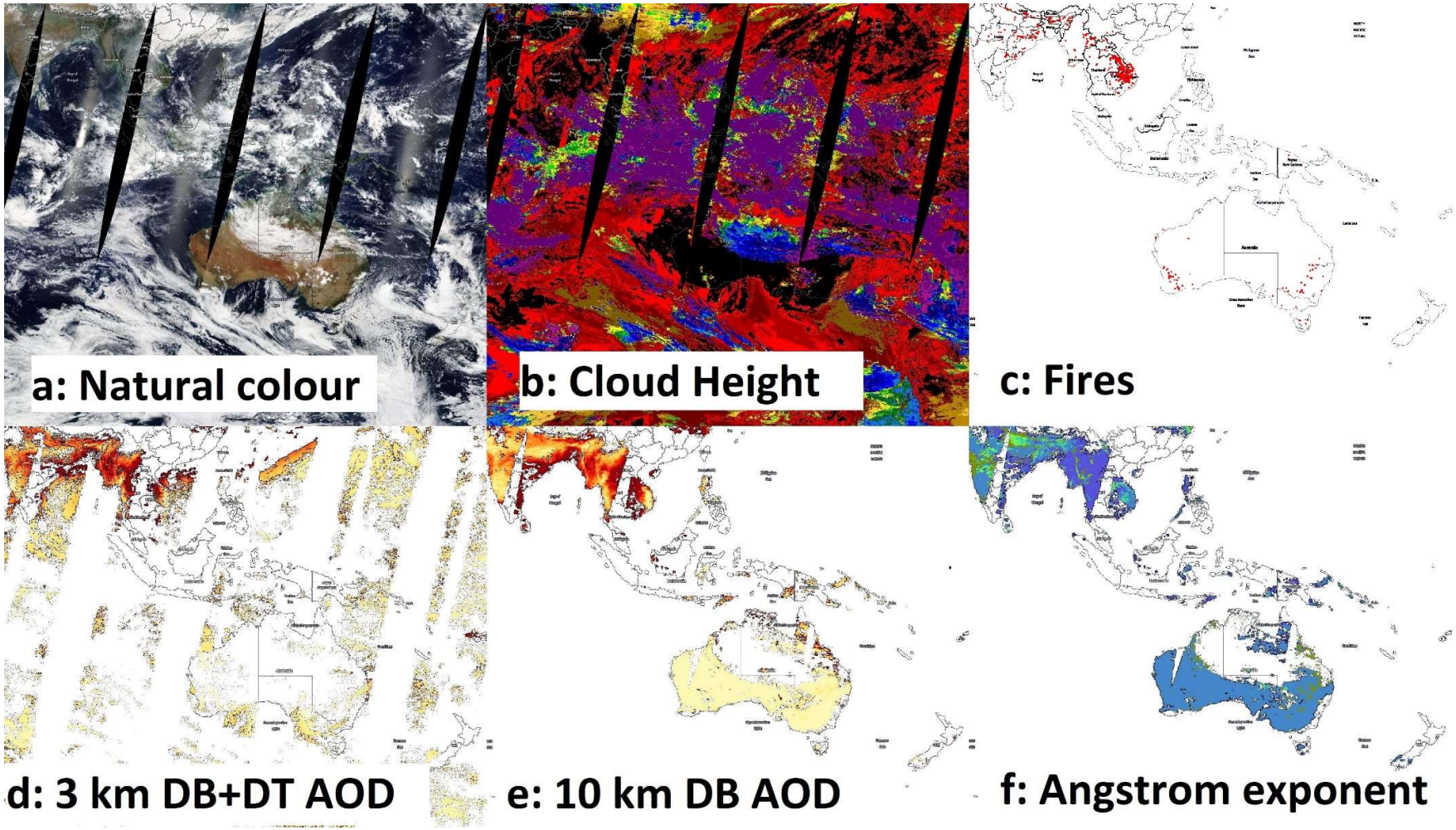

Figure 1-10: MODIS datasets derived from remote sensing over the Himawari-8 observational area for the 8 March 2017. a) Natural colour, b) Cloud heights, c) fires, d) Combined 3 km AOD, e) 10 km DB AOD over land, and f) Ångström exponent (related to particle size) depicting latitudinal differences and data gaps due to non-overlapping swaths and cloud.

1.7.1. Aerosol optical depth (AOD)

Remote sensing has been beneficial in understanding global aerosol movements of large-scale dust events [1] such as the Sydney storm during September 2009 [59]. Despite its potential benefits, the general scientific community has been reluctant to use remote sensing data to determine atmospheric compositions, citing difficulties in accessing, processing, and interpreting the data [1, 60, 61]. The potential benefit of remote sensing is demonstrated in Figure 1-11, which shows a major fire near Denmark, along the southern coastline of Western Australia which contributed to dense smoke being observed in Perth (~400 km to the north).

The locations of the fires were detected with a resolution of 1 km^2 in the MOD14 thermal anomalies product [46, 62]. However, neither the fire location, nor the visible image, nor indeed any other MODIS product directly supplies aerosol ground-level concentrations. Aerosol Optical Depth (AOD) MOD04 [48, 63-65] is a measure of the extinction of the solar beam by dust and haze which can block sunlight by absorbing or scattering light. AOD is a dimensionless number that is related to the total amount of aerosol in the vertical column of atmosphere over a location. The MODIS AOD product is spatially averaged, to remove cloud interferences, and is computed to 100 km^2 (collection 5) [63] or 9 km^2 (collection 6) [48] spatial resolution.

Figure 1-11 highlights several problems in comparing the true-colour against the AOD imagery from MODIS. The observational swath does not cover the globe instantaneously, and multiple observations need to be joined together. These joins created discontinuities and gaps along the boundaries due to differences in the timing of the observations. Cloud masking is especially noticeable over land, and the AOD 9 km^2 aggregation creates pixelation and a loss of detail in the smoke plumes. A lack of temporal resolution creates a disjoint between the smoke plume near the source of the fire, and the stagnant plume 500 km to the north, over the ocean. While it is probable that the high AOD over the sea arose from the smoke plume, there is no definitive smoke trail showing this. Lastly, while the AOD plume over the ocean is well defined, the AOD over land is pixelated and poorly defined as a plume.

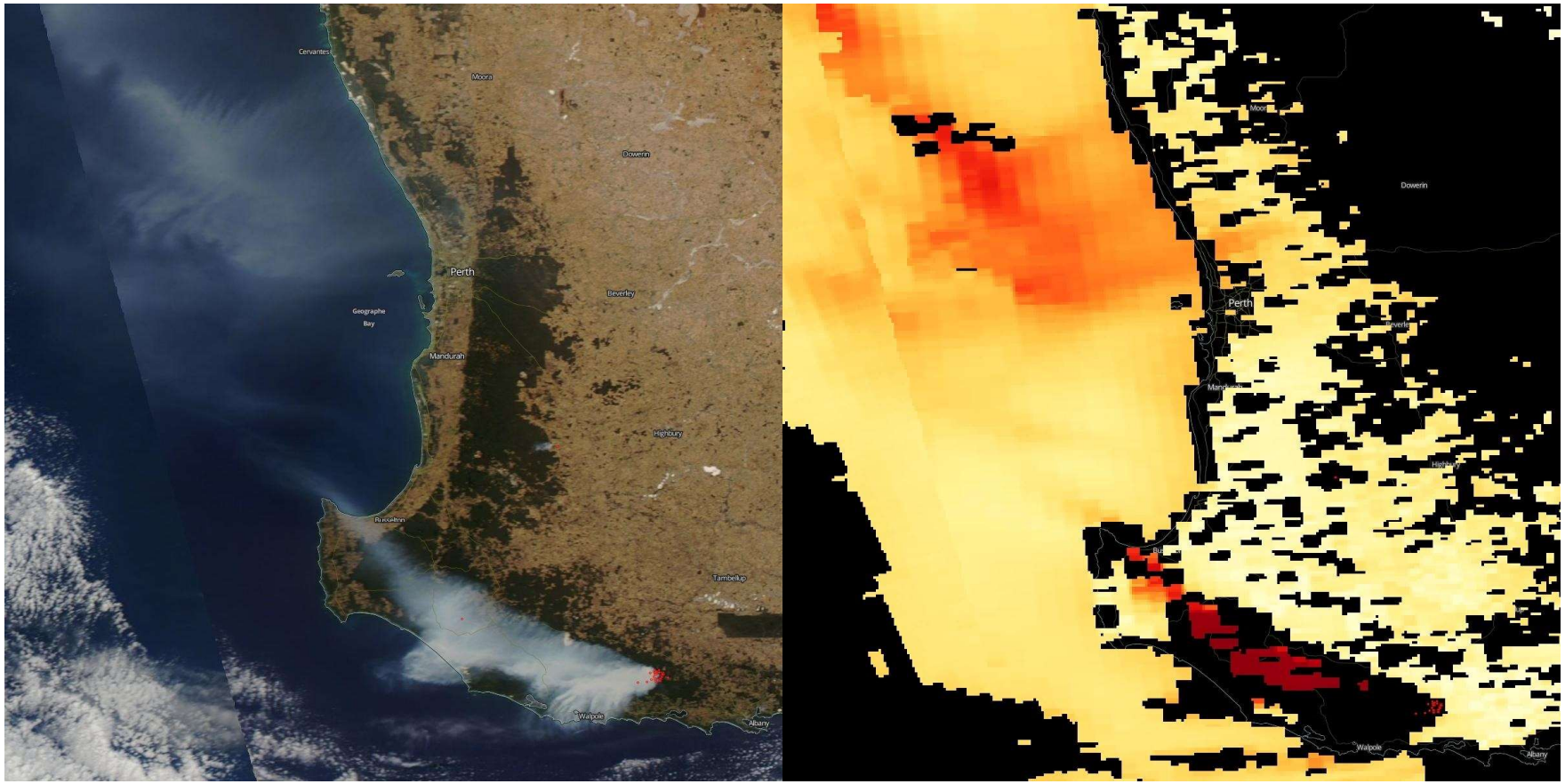

Figure 1-11: MODIS visible (left) and Aerosol Optical Depth (right) data from 5th Jan 2014 over South Western Australia. The figure shows fires in the south and smoke plume travelling westward and then recrossing the coast to the north over Perth.

1.7.2. Dust indexes

In contrast to AOD which can be used to quantify aerosol quantities, dust indexes are often used to determine plume locations. In part, this is due to the difficulties experienced with AOD to resolve aerosols from clouds and ground-based soils [66, 67]. As depicted in Figure 1-9, there are minimal spatial differences between the sixteen Himawari bands. The similarities are due to land, sea and clouds comprising most of the observation and trace constituents of air pollutants have a marginal impact on the overall spectral result. A high-pass filtering method is required to increase the spectral differences and decrease common factors to enable aerosols to be distinguished from clouds [51, 57, 68-70].

A tri-phase dust index uses the different spectral properties of compounds at different wavelengths [56, 71]. The EUMETSAT RGB dust product is a false colour product obtained by depicting the output from infrared channels in a standard RGB image from the 12.4, 10.4 and 8.6 μm infrared channel outputs. Differencing of channel outputs (i.e. subtract one channel from another) changes the focus from the magnitude of the signal and highlights the cause of the change. This method is known as the Infrared Split-Window technique or Brightness Temperature (BT) Difference (BTD) when it uses two channels or triple-band when it includes three channels [69, 72].

Dust index methods typically use a simplified Wen and Rose [73] AOD lookup diagram to infer plume mass and average particle size from the $BT_{10.8\ \mu m}$ (x-axis) and $BTD_{\ 10.8\text{-}12\ \mu m}$ (y-axis). However, Ackerman (1997) suggests [74] quantifying using raw spectra, after atmospheric correction, as the high-pass filtering results in insufficient sensitivity for calibration.

1.7.3. Converting AOD to ground-level concentrations

Although studies show a correlation between AOD and ground-level concentrations of $PM_{2.5}$ [69], these studies are complicated by comparing ground-level concentration with a total column dimensionless number under the incorrect assumption that the ground-level concentration is proportional to the total column

concentration. While there is some justification that wind-blown dust may be inversely proportional to plume height [75], this is only true under neutral meteorological conditions. If the plume was rapidly rising, e.g. a plume from a fire or on a hot day), or inversion conditions were present, then the assumption that concentration is proportional to the inverse of plume height is not valid, and the ground-level fraction of the total column should be determined under those meteorological conditions. This fraction is a function of dispersion properties namely the particle properties (mass and size), wind speed (horizontal and vertical) and the atmospheric turbulence of the plume and surrounding air mass (i.e. rising, falling, dispersing) [75]. This fraction is especially crucial in understanding ground-level $PM_{2.5}$ concentration from fires [76, 77] where the ratio is complicated by meteorology and emission factors [78]. Backscatter from ceilometers has been used to determine the vertical profile [79] as well as multi-angles satellites such as MISR [80-82].

Despite the requirement to determine the plume profile, the literature indicates that the majority of studies used linear regression to convert AOD to ground-level $PM_{2.5}$ concentration [3, 41, 83-89]. However, meteorological information may be used to refine the regression analysis [2, 90-93], such as the influence of relative humidity, which coagulates particles [94] and seasonal influences [95].

1.8. Data gaps in monitoring regional air quality

The preceding sections identified several gaps, from an air quality perspective, in the ability to determine regional ground-level speciated particulate matter concentrations. Closing these data gaps is vital as elevated concentrations of particulate matter (PM) from numerous sources and PM's prominence in airsheds have a detrimental impact on human health. These data gaps (summarised in Figure 1-12) are the following:

1. Limited speciated regional monitoring of ground-level PM concentrations from sporadic non-urban sources impacts the ability to determine health exposures, as neither magnitude nor composition of impacts is known;

2. The spatial extent, temporal duration, and emission parameters to quantitate sporadic sources are uncertain or unknown.
3. Until recently, suitable geostationary satellites were not available to provide the required temporal resolution for monitoring air quality and methods specific to these satellites should be developed to take advantage of the increased temporal resolution available.
4. The traditional AOD approach, which downscales to 9 km^2 pixel averaging, and has data gaps from clouds, is too coarse for air quality studies.
5. Current AOD algorithms using visible data spectra are unsuitable for detecting dust events at night or pre-dawn inversion conditions during which high concentrations could occur. Near-continuous wavelengths, such as infrared, should be used instead to provide these data.
6. Dust indices focus on detecting an event, not quantifying composition, and concentration. Methods should quantify PM concentrations, particle size and composition in order that these data can be used to evaluate health exposure risks.
7. Ground-level PM concentrations (GLC) may be unrelated to the total column aerosol optical depth (AOD) due to the air stability during air quality incidents.

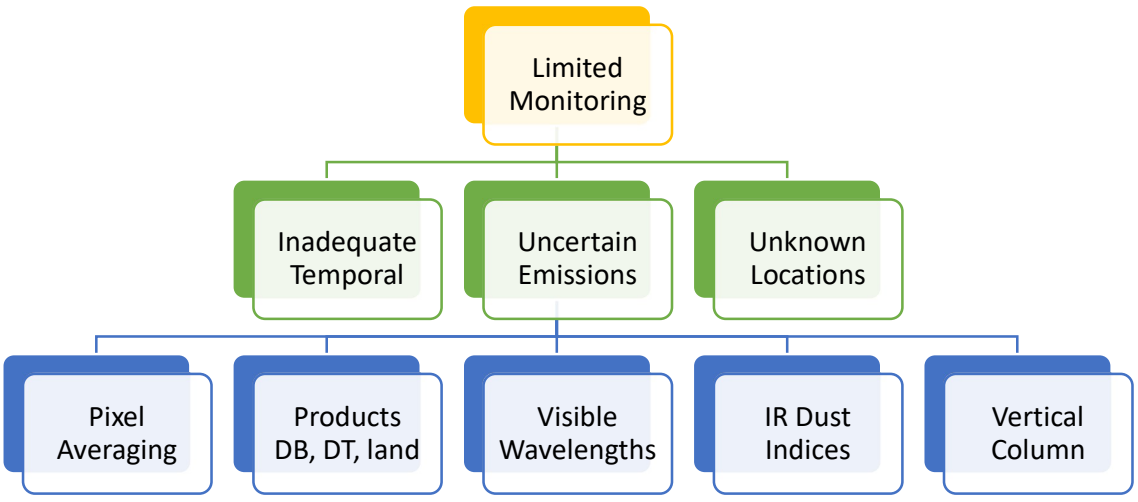

Figure 1-12: Schematic overview of data gaps.

1.9. Study aims and contribution

Air quality monitoring is required to inform on: population exposure (*who*); composition and concentration (*what*); temporal (*when*) and spatial (*where*) resolution; and identify the source of incidents (*why*), as an understanding of impacts are a prerequisite to mitigation (*how-to*). This information is lacking over vast regions across the globe which are currently unmonitored.

This study aimed to address that void by determining whether the availability and accuracy of regional ground-level concentrations of $PM_{2.5}$ and PM_{10} can be improved using ten-minute infrared spectral data from the Himawari satellite.

The review considered what limitations prevent remote sensing being used as a real-time monitor to determine speciated GLCs. The temporal resolution requirements were determined to be meteorological not scan time or data size. Five optimum dust indices were identified to determine spectral change from aerosol GLCs, and these five indices were used to determine aerosol composition and concentration and validated against three OEH case studies.

This work will have global impacts for air quality management in determining PM contributions from natural sources in regional areas. It will be useful for air quality modellers, who are currently severely limited by input data constraints and wind field errors, from accurately predicting PM concentrations in regional areas. It will improve the temporal resolution from the current daily (MODIS) and hourly (dispersion modelling) to ten minutes. While the newly launched Himawari satellite was used for the study, the techniques described could be used with any geostationary infrared sensor.

2. Thesis Overview

Climate change-induced drought, across large regions of Australia, has contributed to severe dust storms and the loss of soil and vegetation moisture. Recent extreme temperatures, combined with vegetation desiccation, has ignited wildfires across vast regions of eastern Australia, resulting in destruction of property and life. Secondary effects of smoke and dust inhalation, which has exacerbated health effects, are poorly measured because of cost and infrastructure demands - as monitoring sites are based on population, not geogenic risk areas.

Speciated ground-level aerosol concentrations are required to understand and mitigate health impacts from dust storms, wildfires and other aerosol emissions. While remote sensing can help estimate respirable (i.e. ground level) concentrations, current observations are restricted by inadequate spatiotemporal resolution, uncertainty in aerosol type, particle size, and vertical profile. One key issue with current remote sensing datasets is that they are derived from reflectances observed by polar orbiting imagers, which means that aerosol is only derived during the daytime, and only once or twice per day.

Remote sensing has the potential to monitor air quality over large domains, but the lack of temporal resolution from polar-orbiting satellites, the reliance on day-time only visible spectra, and coarse-grid spatial averaging methodology has resulted in remotely sensed datasets not being suitable to monitor ground-level (i.e. respirable) concentrations. However, with recent advances, including sub-hourly, infrared (IR) observations from geostationary orbit, there is great potential to improve ground-based aerosol estimates. In particular, the ten-minute infrared geostationary data from the Advanced Himawari Imager (AHI) on Himawari 8, may be used to continually observe and quantify dust and smoke events. This thesis, therefore, proposes that infrared geostationary data should be used to determine ground-level (i.e. respirable) speciated concentrations of air pollutants.

The format adopted for the manuscript was “thesis by publication”. Chapters three to six present published scientific papers, chapter seven presents preliminary potential future studies and includes a validation study of three significant aerosol events in New South Wales. Chapter eight presents an extended conference

abstract which also serves as a summary of the thesis. Finally, a synthesis is provided in chapter nine. The following paragraphs provide an overview of the content of the published work.

The thesis topic was inspired by two recent review articles in Atmospheric Environment on remote sensing by Duncan et al. [1] and Streets et al. [60]. Duncan et al. argued that remote sensing is a mature product and that atmospheric scientists should routinely use remote sensing while Streets et al. presented the status and limitations of remote sensing to determine aerosol optical depth and suggested that polar-orbiting satellites that are reaching the end of their service life will be replaced by geostationary satellites. Himawari-8 and GOES-16 (-R prelaunch) were launched, in 2015 and 2016 respectively after the review by Streets et al., and this presented an ideal opportunity to review the potential of geostationary satellites to determine ground-level aerosol concentrations.

My literature review therefore looked at the deficiencies of current techniques (e.g. using AOD, see Figure 1-11). In my review, it was clear that the current AOD product does not meet the needs of the air quality community. The temporal and spatial resolutions of polar-orbiting satellites are too coarse, the predicted AOD over land (especially bright surfaces) is dubious and misses plumes (see Figure 1-11), the remote-sensing aerosol 'type' does not represent aerosol composition, and the AOD is fundamentally the wrong metric (a dimensionless, full-column property) for describing GLCs needed for health studies.

My review found that new "second generation" geostationary satellites provide excellent temporal resolution (ten-minute) but coarse spatial resolution (2 km). A conclusion drawn from the review was that continuous infrared instead of visible bands are required to provide continuous monitoring.

My review further highlighted the following issues:

1. The lack of temporal resolution has historically constrained the wider adoption of remote sensing for atmospheric studies. Therefore, there is a need to understand if the temporal resolution requirements are driven by chemical transformations, health criteria, hardware (scan time), big-data (volume, network, processing) or meteorological (turbulence) drivers.

2. Continuous wavelengths (such as IR) are required to quantify sporadic dust events throughout the day. AOD methodology has focussed on the stronger visible spectra. Recently there has been renewed interest in using dust indices for the detection of aerosol events. These dust indices were developed previously but, presumably due to the predominance of visible AOD studies, limited attention has been paid to determining which IR indices are optimal for identifying spectral changes from aerosols, prompting an evaluation of BTD, NDDI and RAT. .
3. There is a need to change the AOD methodology to include infrared wavelengths to obtain temporal coverage and following on from the identification of suitable indices, a calibration of those indices against surface monitored compositional data.

These three aspects provided the focus for Chapters 4, 5 and 6 of the thesis.

In Chapter 4 the issue of temporal resolution was examined. Remote sensing of surface PM concentrations is, invaluable for regional areas which have limited ground-based monitoring. However, there is a lack of research that addresses the temporal resolution required for these satellite data. This is highlighted in studies which address daily averaged data, yet are unable to detect sporadic dust events, or in studies which exclusively use the visible wavelength spectrum, and hence are unable to detect events that occur in the evening. In contrast, merely increasing observation times leads to excessively large data files and processing.

In Chapter 4 infrared bands from Himawari-8 were used to determine the speed of compositional changes. It was found that compositional change is driven by atmospheric turbulence which suggests that five to ten minutes scan times are optimal for detecting sporadic effects.

Having identified suitable IR wavelengths in Chapter 4, the work in Chapter 5 focused on how these wavelengths can be combined, using different ratio methods to develop indices to determine specific air quality events. Specifically, in Chapter 5 three index types (subtraction, normalised differences, and ratio) were evaluated across three types of samples (spectral database of pure soils, potential aerosol plumes from a dust storm, and annual variance at a surface monitoring site). The

results showed that BTD was marginally better than NDDI at identifying aerosol changes and recommended that all ten of the Himawari-8 infrared bands should be used with five dual-band combinations to maximise the identification of compositional changes. Using the five dual-band indices enhances quantification across diverse regions and different aerosol species and was illustrated by comparing index differences across the entire Himawari-8 monitoring region. The results of this chapter, therefore, improve the ability to identify spectral changes from aerosols at a high temporal (ten minutes) and spatial (2 km) resolution.

In order to understand the efficacy of the indices examined in Chapter 5, they were tested against GLCs data. This was done in Chapter 6 where the indices were calibrated against surface monitored compositional data using seventeen ground-level monitoring sites in the greater Sydney region in New South Wales, Australia which measured NO, NO_2, SO_2, $PM_{2.5}$, PM_{10}, and O_3, and this data was augmented with positive matrix factorisation aerosol source apportionment data (soil, sea-spray, smoke, auto, and secondary sulfates) for five collocated sites.

While it was not the intention to consider gaseous species in this thesis, ground-level ozone had the highest compositional correlation whilst aerosol speciation correlation was weak. It has been suggested by Ackerman (1997) that the BTD differencing results in a lack of sensitivity and poor correlation to concentration. A pollution index was developed that predicts particle size, humidity and species probability and it is suggested that the predicted concentrations should be multiplied by the probability derived from the pollution index to reduce the high predictions at low probabilities.

Research is often an iterative process whereby topics arise that require further investigation or prompt a refinement of existing findings. In this regard interim results are presented in Chapter 7 with limited (or no) evidential data as a prompt for further development and potential future research.

Preliminary validation was conducted using three OEH selected case studies (section 7.10) and composite GLC's of these events are depicted in Figure 7-13, Figure 7-17 and the timeseries videos. In contrast, Figure 1-11 depicts the current

status of AOD prior to this study and the improvement in spatial resolution, treatment of cloud, and composition is apparent.

The validation studies reflect that water vapour is a strong absorber of infrared and consequently atmospheric stability (vertical movement of water vapour), cloud height (and phase), and relative humidity are determined with high confidence. However, the strong absorption of water vapour negatively impacts the calibration of GLCs and therefore it is suggested that the calibration process should be repeated according to atmospheric stability and cloud height categorisations. Secondly, the validation studies failed to detect plausible plumes from aerosol species (soil, sea-spray, smoke, auto, and secondary sulfates) and this was attributed to the daily filter analysis and cloud spectral interference.

The thesis concludes with summary and synthesis chapters. Chapter 8 (as presented at the 15th International Conference on Atmospheric Sciences and Applications to Air Quality in Kuala Lumpur in Malaysia at the end of October 2019) summarises the work accomplished during this thesis and highlights methods, results, and conclusions.

The concluding synthesis in Chapter 9 evaluates the study and considered the broader significance of the findings. The major finding of this thesis is that all ten IR bands should be used with the five BTD indices to optimise the identification and quantification of aerosol speciation, particle size, and GLCs. The first $BTD_{3.9\text{-}6.2\mu m}$ is a moisture parameter, the second $BTD_{11\text{-}12\mu m}$ is related to particle size and the third $BTD_{6.9\text{-}7.3\mu m}$ is related to atmospheric stability. The remaining two are potentially related to the oxidation state of the atmosphere ($BTD_{9.6\text{-}13\mu m}$) and sulphates ($BTD_{8.6\text{-}10\mu m}$). The atmospheric stability parameter is vital in calibrating the columnar estimate (AOD equivalent) to GLCs while the absorbed moisture and particle size is indicative of source type (chapter 6). This study has shown that the availability and accuracy of regional GLCs of $PM_{2.5}$ and PM_{10} can be improved using ten-minute infrared spectral data from geostationary satellites.

3. Literature Review

Sowden, M., U. Mueller, and D. Blake.
Review of surface particulate monitoring of dust events using geostationary satellite remote sensing.
Atmospheric Environment, 2018. **183**: p. 154-164.

3.1. Abstract

The accurate measurements of natural and anthropogenic aerosol particulate matter (PM) is important in managing both environmental and health risks; however, limited monitoring in regional areas hinders accurate quantification. This article provides an overview of the ability of recently launched geostationary earth orbit (GEO) satellites, such as GOES-R (North America) and HIMAWARI (Asia and Oceania), to provide near real-time ground-level PM concentrations (GLCs). The review examines the literature relating to the spatial and temporal resolution required by air quality studies, the removal of cloud and surface effects, the aerosol inversion problem, and the computation of ground-level concentrations rather than columnar aerosol optical depth (AOD).

Determining surface PM concentrations using remote sensing is complicated by differentiating intrinsic aerosol properties (size, shape, composition, and quantity) from extrinsic signal intensities, particularly as the number of unknown intrinsic parameters exceeds the number of known extrinsic measurements. The review confirms that development of GEO satellite products has led to improvements in the use of coupled products such as GEOS-CHEM, aerosol types have consolidated on model species rather than prior descriptive classifications, and forward radiative transfer models have led to a better understanding of predictive spectra interdependencies across different aerosol types, despite fewer wavelength bands. However, it is apparent that the aerosol inversion problem remains challenging because there are limited wavelength bands for characterising localised mineralogy.

The review finds that the frequency of GEO satellite data exceeds the temporal resolution required for air quality studies, but the spatial resolution is too coarse

for localised air quality studies. Continual monitoring necessitates using the less sensitive thermal infra-red bands, which also reduce surface absorption effects. However, given the challenges of the aerosol inversion problem and difficulties in converting columnar AOD to surface concentrations, the review identifies coupled GEO-neural networks as potentially the most viable option for improving quantification.

Keywords: Geostationary Earth Orbiting satellites; Aerosol Optical Depth; Particulate Matter; Thermal infra-red; spatiotemporal resolution.

3.2. Introduction

Elevated concentrations of airborne particulate matter (PM) are a cause of global concern given the associated environmental [96] and human health risks to both cardiovascular and respiratory systems [97, 98]. High concentrations can cause haze (or smog) to form, which may affect visibility, and soiling via deposition of fine material can lead to amenity degradation [99, 100]. Airborne PM concentrations are dependent on the magnitude of source emission rates [60, 101] whilst the type of emission affects the spatial concentration distribution as a large area source typically results in lower concentrations (mass/volume) but may impact a wider region (i.e. larger initial volume) that would be the case if it were a coherent plume from a point source. Similarly, sources such as industrial stacks or hot gas from fires can inject material at a high elevation but with minimal initial horizontal variance, and the plume may then be dispersed over large distances before being diluted [4, 102, 103]. During the plume dispersion, the compounds in the air may undergo chemical [104, 105] (such as photochemical reactions) and physical (such as deposition) transformations which alter the amount and composition carried in the plume [106-109].

Unlike industrial emissions from point sources, which are highly regulated and monitored with in-line stack analysers and/or fence-line monitoring, diffuse PM area sources present unique challenges in that fugitive emissions and events are usually unquantified. A large fire may be monitored due to its potential danger and damage to life and property, but the secondary effects of smoke from fires are seldom documented regarding magnitude, frequency, and spatial extent.

Similarly, significant fugitive emissions of PM arise from the movement of people [110], biomass burning [111-113], wind erosion [114-116], and volcanic events [101, 117]. Whilst modern technology and regulations can force reductions of industrial emissions; fugitive emissions are challenging to monitor and manage. As such, fugitive emissions require indirect mitigation strategies to reduce impacts such as the use of controlled burning to reduce fuel loads [118] and creating windbreaks to reduce wind speed dependent dust erosion [119].

Elevated concentrations coupled with the difficulty in managing these emissions have led to a need to understand the impacts and consequences of these emissions. PM health studies [97, 120] predominantly characterised health impacts in terms of particle size [111, 121-123], but more recent studies document the role of PM composition on health impacts [124, 125]. Contemporary research is unanimous that these health effects are critically dependent on both particle size and composition [98, 126, 127]. It is therefore imperative not only to determine total PM concentration or apportion to size fractions (i.e. PM_{10} and $PM_{2.5}$), but to quantify and fully classify the source by particle size, composition and/or source type (i.e. biomass burning, wind erosion, sea -salt, volcanic, urban etc.) [125] so that the full impact of elevated concentrations can be determined.

These impacts need to be quantified using monitoring, modelling and/or estimation techniques [2, 116]. Dedicated surface-based monitors are preferred for their accuracy and temporal resolution [128], but cost and infrastructure requirements limit the number and distribution of surface monitors. It is impractical and costly to continually monitor for all pollutants across large regions at the fine monitoring scale needed by air quality studies. Most monitoring is performed in populated urban areas as this maximises cover per capita and urban areas have the necessary infrastructure to support the monitoring. However, fugitive dust sources such as wildfires and dust storms regularly occur in regional areas as these areas have the necessary biomass or bare exposed soil to support emissions from large area sources and these sources, therefore, have the potential to influence air quality on local regional populations and impact regional air quality.

Quantification at a local level will minimise confounding chemical and physical plume dispersion effects in determining source emissions which make it challenging to quantify emissions further downwind from the sources. These dispersion effects arise from changes in wind direction and wind speed along the plume's path, which result in the monitored concentration depending on plume age and path. Regional-scale quantification considers the cumulative frequency and spatial extent of long-range transported events, particularly where this impacts populated urban areas [129], and global scale quantification determines the impact an event has on background concentration levels.

Where monitors are not available, mathematical tools such as dispersion modelling [100, 104, 130, 131], neural networks [50, 116, 132] and statistical procedures such as source apportionment [133] methods can model impacts. However, these calculation methods have higher uncertainties than direct monitoring due to approximations and input assumptions inherent to the chosen model [106]. Increasingly, remote sensing has been used as a surrogate method to determine aerosol concentrations [2, 4, 93, 134]. The advantages of remote sensing are that it can monitor a wide area simultaneously, does not require an emissions inventory [135], and does not need a dense monitoring network to determine concentrations. Indeed, in many areas of the world, including regional Australia, remote sensing offers the only potential alternative to understanding and estimating the surface concentration of $PM_{2.5}$ and PM_{10} where direct monitoring is not available [129, 131, 136]. Where direct monitoring or emission inventories are available, remote sensing using the latest geostationary satellites can augment these data, improving the temporal resolution to ten minutes, and emission factors can be constrained based on aerosol optical density [137]. This was demonstrated in an Italian study which used 686 surface PM_{10} monitors to refine the spatial concentration estimates [137].

Launching and placing heavy equipment in space is both difficult and costly. As a result, polar-orbiting, low earth orbit (LEO) satellites were initially favoured for remote sensing [45, 138, 139]. The MODerate-resolution Imaging Spectro-radiometer (MODIS) instrument is an example of a LEO satellite that has supplied daily data for two decades, utilising extensively peer-reviewed algorithms

[48]. Older LEO satellites [140] are now being decommissioned, whilst "second generation" new satellites at higher geostationary earth orbits (GEO) are being deployed in greater numbers. A list of currently orbiting GEO satellites is provided in Table 3-1.

Table 3-1: Current Earth Observational GEO satellites (excluding military, communications, and GPS satellites). Source: Union of Concerned Scientists Satellite Database https://www.ucsusa.org/nuclear-weapons/space-weapons/satellite-database.

Name of Satellite, Alternate Names	Longitude (degrees)	Launched (year)
GOCI/COMS-1 (Communication, Ocean, and Meteorological Satellite; Cheollian)	128	2010
Electro-L1 (GOMS 2 [Geostationary Operational Meteorological Satellite 2]	76	2011
Electro-L2	77.8	2015
Fengyun 2D (FY-2D)	86.51	2006
Fengyun 2E (FY-2E)	123.59	2008
Fengyun 2F (FY-2F)	105	2012
Fengyun 2G (FY 2G)	0	2014
Gaofen 4	105.5	2015
GOES 13 (Geostationary Operational Environmental Satellite, GOES-N)	-75	2006
GOES 14 (Geostationary Operational Environmental Satellite, GOES-O)	-104.41	2009
GOES 15 (Geostationary Operational Environmental Satellite, GOES-P)	-135	2010
GOES 16 (Geostationary Operational Environmental Satellite GOES-R)	-75	2016
Himawari 8	140	2014
Himawari 9	140	2016
INSAT 3A (Indian National Satellite)	93.53	2003
INSAT 3D (Indian National Satellite)	82	2013
INSAT 3DR (Indian National Satellite)	74	2016
Kalpana-1 (Metsat-1)	74.07	2002
SEVIRI/Meteosat 10 (MSGalaxy-3,MSG 3)	0	2012
SEVIRI/Meteosat 11 (MSG 4)	0	2015
SEVIRI/Meteosat 8 (MSGalaxy-1, MSG-1)	41.5	2002
SEVIRI/Meteosat 9 (MSGalaxy-2, MSG 2)	-0.02	2005
MTSAT-2 (Multi-Functional Transport Satellite)	145.06	2006

GEO satellites rotate at the speed of the earth and thereby generate a continuous view of one hemisphere of the earth [141-143], in contrast to LEO satellites which return overhead once per orbit cycle. Because these GEO satellites stay over a fixed point and the temporal resolution is dependent on sensor technology rather than orbit periodicity this results in continuous data acquisition rates for all

locations. However, the enhanced temporal resolution comes at the cost of reduced spatial resolution because of the higher orbit. Furthermore, the curvature of the earth restricts useful retrievals to a 120-degree arc, making GEO data unsuitable for polar and other high latitude studies. GEO satellites such as Himawari-8 (Asia and Oceania) [144-146] and GOES-R (North America) [147], typify the sub-hourly data with half the spatial resolution of MODIS.

Numerous research articles and reviews of aerosol remote sensing have considered history, platforms, orbits, the theory of scattering (Rayleigh and Mia) and adsorption (infra-red) in detail [60, 148, 149]. Considerable success of a qualitative nature (depicting the plume spatially and temporally) has been achieved to verify emissions inventory changes [150], study large-scale long-range transport events (LRT) [105, 115] and short-term exceptional events (i.e. fires and volcanoes) [145, 151]. Whilst fires are significant for the frequency of events, volcanoes are significant in terms of the size of emissions. Fire agencies routinely use fire detection methods to estimate resultant emissions [152] and track the movement of fire and smoke using remote sensing data [145]. Similarly, recent volcanic eruptions have resulted in a refinement of plume detection methodology and improved understanding of the vertical plume structure. Passive scattering, with the Multi-angle Imaging Spectro-radiometer (MISR) [115, 153], and active laser back-scattering using the Cloud-Aerosol Lidar and Infrared Pathfinder Satellite Observations (CALIPSO) [154] instruments have been used to determine the vertical profile. AERONET and other ground-based sun photometers have provided method validation over large regions [155, 156]. Aerosol Optical Depth (AOD) measurements have been integrated with Chemical Transport Models (CTM) [100, 104, 131], Bayesian analysis [120, 157] or neural networks [158] to improve the identification of background events and assist quantification.

Whilst remote sensing of particulate matter is a suitable tool for qualitative analysis (spatial and temporal) to identify dust events, there are significant problems that limit quantification [60, 148, 149]. These limitations arise from poor temporal resolution, inadequate background AOD determination, circular assumptions in the aerosol inversion model and vertical parameterisations of the dust plume. Of these limitations, the circular assumptions of the aerosol model

are the most significant. The aerosol inversion problems are a consequence of deriving solutions with more unknown intrinsic aerosol properties (size, shape, composition, refractive index) from known extrinsic scattering and absorption properties [45, 159, 160]. The inversion retrieval is constrained to aerosol types included in the lookup table, and the accuracy of the retrieval is dependent on the degree of independence in the spectral patterns (signatures), per aerosol type, which is further complicated by poorer spectral resolution on GEO satellites.

This literature review was undertaken to examine the limitations in remote sensing of ground-level particulate matter concentrations and the quantification challenges. The review sought to determine which of the methodology changes maximise the benefits from the enhanced temporal resolution of the GEO data. A "Web of Science" search for all review articles containing the topics aerosol and remote sensing shows that the number of review articles peaked in 2012/3 but that there has been a steady growth in the number of citations, indicative of a potentially greater acceptance of remote sensing.

The literature that was reviewed focussed on the derivation of surface concentrations of particulate matter using GEO data rather than the more commonly reported, aerosol optical depth remote sensing product, as it is the surface concentrations that directly affect health, not the total column parameter. The review has considered the large-scale movement of aerosols from fugitive dust sources (such as fires, dust storms, and volcanoes) rather than localised industrial sources which typically affect one or two neighbouring pixels. Fugitive sources are generated over large areas and are widely dispersed but less represented in sparse surface-based monitoring. The review has identified changes that occurred since Street's 2013 review (i.e. from 2014), during which both Himawari (July 2015) and GOES-R (Dec 2016) satellites were launched, in order to narrow down and identify progress and/or current trends in the methodology. The review ignores case-studies that simply use existing AOD product data without contributing additional information to the resolution of quantification challenges, nor does it replicate extensive historical theoretical frameworks which are discussed in other recent reviews [60, 148, 149].

3.3. Challenges and Emerging Solutions

3.3.1. Spatial and Temporal Resolution

One of the biggest criticisms of polar-orbiting satellites (such as MODIS), from an air quality perspective, is that they supply a single instantaneous measurement and not a period average [48]. Although numerous researchers have compared AOD to daily average concentrations [2], AOD reflects a short-term, temporal monitoring, gathered once a day, for the few seconds that the satellite was flying overhead. Apart from the temporal bias of comparing dissimilar timescales (seconds against hourly and daily monitoring), short-term events such as fires may be inactive during the satellite overpass, or clouds may obscure the scene, leading to the event being missed during the satellite overpass [104, 152, 161-163].

Whilst health and regulatory considerations include daily and annually-averaged concentrations of particulate matter [164], hourly (or sub-hourly) measurements are required to understand the transport and concentration of particulate matter from short-term significant events such as fires and dust storms. It has been shown experimentally [165], and proven theoretically [166], that turbulence drives air dispersion. Turbulence, therefore, determines the spatial and temporal scales required for monitoring and the spatial resolution and timing of samples should be dependent on average wind speeds to ensure that the plume movement between pixels can be detected in the monitored period. This supports the findings of health-related studies which suggest that a spatial resolution of about one kilometre and a temporal resolution of an hour are the minimum requirements for monitoring atmospheric events [167, 168]. Second generation GEO satellites such as SEVIRI (15 min, 3 km) [169], GOCI (hourly, 500 m (NIR)) [170], Himawari-8 (10 min, 2 km) [144] and GOES-R (15 min, 2 km) [171] meet the hourly and sub-hourly requirements overcoming the previous temporal resolution restriction of LEO satellites albeit with a reduction in spatial resolution.

Most case studies using GEO data take advantage of the enhanced temporal resolution, which implies a higher probability of cloud-free measurements and fewer missed events. These studies do not utilise the motion of the aerosols but

simply subtract a static background [172]. Aerosols, carried by turbulent air, implies motion as gravity will cause deposition of particulate matter under calm conditions [173, 174]. Therefore, motion detection methods including frame differences and tracking moving objects can be used to improve aerosol movement detection and quantification [175], and this has been demonstrated by some neural network solutions [116, 158]. Similarly, consistency tests can identify clouds and aerosols using the spatial differences in the homogeneity (i.e. standard deviation) across neighbouring pixels as clouds are patchier than an aerosol plume [176]. In the Infrared Differential Dust Index (IDDI) method the minimum reflectance over the chosen time period is subtracted from the current reflectance and so highlights areas of change (movement) [50]. As most pixels do not change between frames there is a significant reduction in the number of background pixels which are masked out if they have not changed between frames. The IDDI methodology has been used for time periods of three days [177], unspecified "days" [69], fortnights [50] and months [178]; however, there is no agreement on the choice of the correct timespan for the differentiation.

Whilst GEO satellites improve the temporal resolution, this is at a marginal cost to spatial resolution as evidenced by the latest GEO satellites such as Himawari-8 (10 min, 2 km) [144] and GOES-R (15 min, 2 km) [171]. To address what spatial resolution is required for GEO data the question is rephrased to consider how far a low wind speed would move an individual "puff" within a plume to be discernible either along the plume boundary (i.e. edge detection) or to a pixel with a different concentration within the plume (i.e. dispersion). For both cases, it is assumed that the concentration remains above detectable limits. A low wind speed of 1 m/s would disperse a plume/puff 600 m over ten minutes, and this is, therefore, the minimum spatial resolution required to detect a plume at this wind-speed. This is three times the spatial resolution of Himawari's infra-red spectral bands and double that of the visible and near infra-red bands. In an attempt to improve the spatial resolution of GEO data various mathematical treatments have been used. The greater spatial resolution of LEO (MODIS) satellites was used to refine GEO data in multi-satellite studies by determining a daily sub-grid calibration from the MODIS data and applying the sub-grid scale factors to the GEO data [138, 179].

This is not ideal as it assumes that the spatial calibration is not temporally dependent, which is not the case where an aerosol plume moves across an area. Other studies have demonstrated the ability to enhance the spatial scale of the infra-red channels by scaling the data using higher resolved visible and near infra-red (NIR) data during daylight hours [145, 180]. This can yield satisfactory results during daylight hours where there is a strong correlation between the higher resolved visible or near infra-red data and the infra-red data. This is similar to a method of detecting fire locations at sub-pixel resolution by applying a deconvolution filter that is reliant on the wavelength-dependent decrease in fire radiance power across neighbouring pixels [180].

Whilst there is potential to improve the spatial resolution using correlated channels of higher resolution, they cannot improve the spatial resolution during the night or across uncorrelated channels. Spatial averaging techniques such as Kriging may be able to double the perceived spatial resolution but do not yield further spatial improvements [181] as they cannot improve the detection of a plume which is unresolved in the original data.

Therefore, these studies show that the temporal resolution of GEO data is a substantial improvement over polar-orbiting satellites and is better than the hourly resolution from most dispersion models and is comparable to the temporal resolution of most on-line analytical instruments [168]. Unfortunately, this is at a marginal cost in spatial resolution, which is adequate for global and regional studies but too coarse for local studies. The ideal spatial resolution for local studies requires an order of magnitude improvement to be comparable to the resolution of dispersion model studies [106]. In contrast to the Meteosat, Himawari and GOES series of satellites, China's Gaofen-4 satellite claims an order of magnitude improvement in spatial (50m VIS and 400m IR) and temporal resolution (1 minute) [182]. The spatial and temporal resolution required for air quality studies is a fundamental aspect of remote sensing that has not received sufficient attention in the literature.

3.3.2. Background (i.e. zero) AOD

Determining Aerosol Optical Depth (AOD) from scattered reflectance and absorption temperatures uses Beer's law to integrate the extinction coefficients across the vertical column [149]. The determination of the integral from the surface to the top of the plume requires the surface extinction coefficients (i.e. background AOD) to be known or determined. Determining background AOD from scattering of electromagnetic energy in the visible part of the spectrum is complicated by reflective backgrounds such as roofs, bright reflective mineral sands in deserts and even the presence or absence of vegetation cover. Different algorithms are used to account for these reflective backgrounds. They depend on the nature of the surface background such as dark target (DT) algorithm [183] over the ocean, dark target algorithm over vegetation and deep blue (DB) algorithm [65] over bright land surfaces such as deserts [48]. In addition to MODIS, there are multiple sensors and satellites, each with slight differences in how AOD is calculated [61]. The retrieval of aerosol properties from these systems is impacted by cloud, surface, and molecular effects. These impacts must be accounted for before the aerosol properties can be determined.

To account for the variances in reflective backgrounds across an area, the surface reflectance has traditionally been averaged spatially when determining background AOD, for example, the MODIS algorithms average across 10x10 km^2 (at nadir) (collection 5) or 3x3 km^2 (at nadir) (collection 6) [48]. However, both these spatial resolutions are inadequate for monitoring air quality events which require approximately a 0.6x0.6 km^2 resolution, based on the time for a 1 m/s wind speed event to cross a pixel. The spatial resolution of the MODIS AOD product has been improved using the MAIAC algorithm which uses temporal changes to improve the spatial resolution [184] and the SARA algorithm which uses the resolution of the raw reflectances (500 m) and data from the AERONET surface-based AOD monitoring to refine the spatial resolution.

In addition to difficulties in determining background AOD from the surface variability, clouds may obscure the surface reflectance. This severely constrains the usefulness of AOD scattering methods to determine aerosol movement on a

global basis – especially in cloudy, tropical regions – as it leads to masked (i.e. unmeasurable) pixels where significant clouds are present, or the surface is not sufficiently homogeneous [136]. The high temporal volume of GEO data can reduce cloud masking by using the minimum temporal reflectance across longer time frames with the IDDI method. IDDI only requires a single cloud-free period (per pixel) during the longer timeframe and does not average across pixels, thus preserving the full pixel resolution with fewer masked events [185, 186]. An implicit assumption in the IDDI approach is that the period compared should have minimal surface reflectance changes (i.e. exclude seasonal effects) and it is thus suited for comparison across days rather than weeks or months.

The radiation energy received by a satellite sensor is inversely related to the wavelength and therefore scattering in the visible spectrum is more sensitive to changes in particle composition and size than absorption at thermal infrared wavelengths [56, 151]. Similarly, scattering effects from different surface backgrounds are more problematic than absorption in determining background AOD. Despite these problems, using the enhanced sensitivity of scattered reflectance is preferred to absorption when determining AOD. However, with the rapid temporal updates, there is a requirement to use wavelengths that are continually available (such as infra-red absorption) and not restricted to daylight hours. Therefore, GEO methods may need to use a combination of daytime scattering and infra-red absorption at night to maximise both signal strength and data availability. The NASA/NOAA products favour scattering using visible wavelengths to derive AOD estimates as used by MODIS [48, 65, 183], newer sensors such as VIIRS [187], GOES-R GEO satellites [188] and future missions using TEMPO [189]. In contrast, the EUMETSAT methods [50, 68, 143, 180] used by Meteosat and Himawari use thermal infrared bands to identify aerosol plumes and a lookup table to convert AOD to plume mass and average particle size [73].

The high temporal volume of data from GEO satellites allows a cloud-free background to be determined, which enables the determination of AOD from remote sensing data. The relative signal intensities at different wavelengths allow the aerosol type to be determined.

3.3.3. Aerosol Model Inversion Problem

The main limitation of using current AOD calculations to determine surface particulate matter concentrations is not the lack of temporal resolution, which is overcome using GEO data, nor the determination of background AOD but the choice of the aerosol model [141]. Atmospheric concentrations and the spatial distribution of particulate matter depend on the emission of new particles, the dispersion, chemical transformation, and physical removal of those particles [60]. Knowing the intrinsic properties of aerosols (size, shape, composition, and refractive indices) allows determination of the extrinsic spectral properties (radiance and brightness temperature) with a radiative transfer model [56, 190]. The cumulative effect of the substrate (e.g. soil type, vegetation type, barren rock, urban), moisture (e.g. sea, snow, ice, cloud, liquid, vapour) gaseous and particulate matter determine the total spectral property which can be calculated at each wavelength [191, 192].

Whilst the theoretical framework for calculating extrinsic optical properties from intrinsic source specific properties is well understood, it is not always possible to calculate the reverse [54]. Remote sensing methods use inversion techniques to solve the inverse of the radiative transfer equations in determining aerosol optical depth, particle composition, size, and number. These inversion equations cannot be solved explicitly as there are more unknown intrinsic aerosol properties than known extrinsic measurable parameters. This is worsened by GEO satellites with limited spectral resolution (for instance MODIS has 36 spectral bands compared to the Spinning Enhanced Visible and Infrared Imager (SEVIRI) with 12 bands) [143, 180]. An aerosol model assumes a fixed set of intrinsic aerosol properties (size, composition, humidity) and extrinsic radiances/absorption are calculated for each wavelength band. These extrinsic and intrinsic properties are used to populate a lookup table of aerosol properties [193, 194]. The most probable aerosol type, AOD and particle size (intrinsic) are determined using the best match spectral approximations (extrinsic) from the lookup table, and particle number (or concentration) is calculated based on signal intensity [195]. However, the inversion method introduces circular assumptions as the accuracy of the solution

is dependent on correctly including localised aerosol types and particle sizes [196] in global datasets.

The most significant recent contribution to knowledge in the field has been refinements to the aerosol model's lookup tables in preparation for the launch of new GEO satellites by pseudo-AOD datasets generation [99]. Radiative transfer (RT) model outputs were compared as part of the Modern Era Retrospective-analysis for Research and Applications Aerosol Reanalysis (MERRAero) which compared 16 RT models [102] against each other. Results suggest that assimilation of AOD data tends to improve the $PM_{2.5}$ temporal variability (i.e. temporal correlation) but cannot correct systematic errors in surface concentrations (i.e. spatial correlation or over/under predicting). The authors note that systemic errors were due to inadequate aerosol optical properties, missing species, and/or deficiencies in aerosol vertical structure [197]. Closure studies compared four aerosol models (NASA Global Modelling Initiative, GEOS-Chem v9, baseline GEOS-Chem with radiative transfer calculations (GC-RT), and the Optical Properties of Aerosol and Clouds (OPAC) package [190] with data gathered during the 2008 Arctic Research of the Composition of the Troposphere from Aircraft and Satellites (ARCTAS) campaign. These studies found significant differences (10-23%) between the four models, which were attributed to assumptions concerning fixed size distributions, external mixture assumptions and refractive indices used in the models [198].

Improvements to the RT models have encouraged aerosol classification changes from the vague "strongly absorbing" [48] and "non-spherical" [177] to more meaningful GEOS-CHEM species of dust, namely black carbon, other carbon, sea salt, sulphate and urban [135, 179]. These classification changes considered the natural abundance of particulate species [199]. Whilst the GEOS-CHEM (and similar) model species do not by themselves result in detailed chemical compound classifications, the refined species definition is a better source classification scheme [200] and by including local speciation effects (different mineral compositions for instance) [123] could allow the generation of more regionally specific, compound and size, lookup tables.

Comparative radiative transfer studies have highlighted that it is important to understand and optimise the inversion process and in this regard, a Jacobian error matrix approach (i.e. optimising a matrix of first-order derivatives instead of signal intensity against explicit aerosol parameters) that supplies a measure of uncertainty and quantification of the inversion process has been proposed [171]. The authors suggest that their study "should be viewed as the starting point for the development of a framework for objective assessment of aerosol information content for any real or synthetic measurements and that further development of particle scattering codes for non-spherical particles is essential, especially for large particles that are difficult to handle with current implementations of [radiative transfer] theory."

In tandem with, or possibly as a result of the errors in the uncertainty model approach, research has focussed on a dust index approach [73] using generic aerosol model lookup tables. This has used single spectra (0.550 μm or 11 μm) [201], double band brightness temperature reduction (BTR) (3.7 μm -11μm) [151, 177], triple band BTR (12 μm -11 μm, 4 μm -11 μm or 9 μm -11 μm) [116, 202], four BTR bands (10.3 μm –11.3 μm, 11.5 μm –12.5 μm, 6.5 μm –7.0 μm, 3.5 μm –4.0 μm) [201], ratio of NIR/Red [145] and IDDI methodologies [177] using simple cloud masking ratios. These dust index methodologies could be described as a rudimentary supervised classification scheme, based on expert knowledge of predominant spectral characteristics [203].

However, these dust index products are dependent on the intensity of an event, so the identification of a minor dust storm which relies on the temperature differences between the land surface and the cooler aerosols may be missed (i.e. BTR < detection threshold) [114, 161]. Dust storms can influence ambient surface temperatures by shielding the sun's energy from reaching the surface, thereby influencing the AOD/BTR relationship [123], and moisture effects need to be properly accounted for in the lookup table [151] to correct the non-linearity in the AOT/BTR relationship for cooler BTR thresholds.

Given the uncertainty of the inverse aerosol model retrievals and influences of external parameters such as humidity, temperature, topography, cloud cover,

cloud optical depth, local mineralogy and size parameters on the AOD/GLCs relationship, several studies have suggested using neural networks [105, 116, 158] or Bayesian studies [120] to improve the inverse aerosol retrievals. These multivariate, non-linear, and non-parametric approaches have been used in data assimilation of incompatible timescales (daily and hourly) or different satellite products of varying spatial resolution. However, whilst these methods can identify hidden nodes or relationships in the data, they are computationally expensive for large, near-real-time rapidly updating datasets unless the classification steps are predetermined during the initial training phase for the region [204].

Quantifying AOD and determining aerosol type remains an ongoing challenge in determining GLCs. However, despite the ongoing uncertainties related to quantifying AOD, the spatiotemporal qualitative aspects are one of the successes of remote sensing. Relative increases and/or decreases in AOD indicate sources and sinks of particulate matter [193, 205], verify emission rate changes [206], justify control strategies [207] and help understand the diurnal and annual transportation of aerosols both from local sources and long-range transport [179, 208]. Whilst knowing the columnar AOD is important, ground-level pollution is an important parameter from a human health and management perspective.

3.3.4. Vertical Profiles

Surface visibility has been used as a proxy for GLCs of particulate matter [99, 177], but where neither visibility nor concentration is measured, there is a need to extrapolate AOD to GLCs using mathematical methods. The methods may include simple linear approximation or multiple regression taking into consideration secondary effects such as hygroscopic and meteorological parameters [80, 209]. However, these approaches assume a well-mixed, steady-state plume which results in a predictable smooth Gaussian-plume vertical relationship where the concentration at different altitudes is correlated to ground level PM concentration [80]. Dispersion modelling studies show that a well-mixed neutral state (i.e. plume buoyance determined by adiabatic lapse rate) occurs half of the time where there is a moderate to high amount of cloud cover and wind speeds greater than 3 m/s at night or 5 m/s during the day) [210]. If the plume is

rising rapidly (e.g. near source, or from fires or volcanoes), or if temperature inversion conditions are present, then the assumption of well-mixed neutral plumes is invalid. Temperature inversions and increased wind speeds, leading to heightened dust-lift-off, are an indication of non-neutral weather conditions that commonly occur during dust storms [114]. Where plume stratification occurs from high wind-speeds trapping the plume in layers, or inversion conditions trap a plume below the mixing layer, or if the plume rises rapidly, the vertical distribution of the plume may be significantly non-Gaussian, and AOD may be uncorrelated to GLCs as detailed in some LRT dust studies [105].

Various methods exist for determining the vertical profile of the plume. Dispersion modelling can produce satisfactory results, but the accuracy of the vertical concentration profile depends on determining the correct meteorological profile for the model, which may lead to high uncertainties. Several studies have considered using Lidar backscattering from the CALIPSO satellite or forward multi-angular remote sensing methods such as from the MISR satellite [84, 106, 114]. However, both CALIPSO and MISR have reduced temporal and spatial resolution, and a hybrid approach is therefore common, where the dispersion model's vertical profile is constrained using limited satellite-derived approximations.

Hybrid methodologies have been noted as an emerging technology in the recent literature. Initially, a dispersion model such as CMAQ [205] or CAMx [163] was coupled to an independent meteorological model such as WRF [147] and AOD input data was used to constrain the dispersion model. However, with the advent of the GEOS-CHEM and HYSPLIT [179] models, meteorological fields are now obtained and processed directly from NCAR reanalysis files by the dispersion model, eliminating the separate pre-processing step [211, 212]. In a typical coupled modelling scenario, an emissions inventory is estimated and constrained by AOD data, in order to generate consistent surface concentrations taking into consideration the modelled mixing height and concentration at multiple internal heights. This is done by using the magnitude and spatial distribution of the AOD as initial emission input to a dispersion model and then rescaling the emissions to ensure a best match of the predicted AOD from the coupled model against the satellite-derived AOD data [137]. Studies have demonstrated that best results are

obtained by matching the model's grid resolution and internal time-steps to the underlying AOD spatiotemporal resolution and the need to understand the overall accuracy of the coupled methods [104].

3.3.5. Validation/Accuracy

It is vital that improvements to the methodology are developed to enhance accuracy. The current accuracy of the regression method (AOD to GLCs) is estimated to be twenty percent and the uncertainty of the aerosol model (wavelength signal intensity to AOD) is estimated to be thirty percent [108, 114]. However, researchers caution that the regression coefficients are not transferable to other regions and the true uncertainty could be an order of magnitude higher if assumptions in the aerosol model are not taken into consideration [108, 114]. This has been clearly demonstrated in validation studies that have compared multiple satellite products across an area and significant disagreements between them were ascribed to uncertainties in the aerosol retrieval properties of mass, size, and composition [148].

The Jacobian error matrix approach discussed earlier allows the uncertainty of the aerosol's model output to be directly quantified, which can aid in optimizing the matrix solution by testing alternative aerosol types and/or wavelengths. The uncertainty associated with converting aerosol radiation to ground level concentrations is reduced by the matrix optimised solution which requires using a chemical transport model (CTM), driven by assimilated meteorology and verified against observations to simulate radiative impacts and surface concentrations. It is critical for an accurate evaluation of aerosol concentrations and impacts that the matching of observations and simulations accounts for the timeframe differences between instantaneous satellite measurements and hourly dispersion predictions or daily measured concentrations in the comparisons between measured and predicted concentrations [213].

Most validation studies have used descriptive statistics to compare AOD-derived GLCs to ground-based measurements. Common statistical tools used to assess the accuracy of the method include Pearson's correlation coefficient I and the Root Mean Squared Error (RMSE) [5, 93]. However, this approach neglects the

statistical assessment of spatial (between pixels) and temporal (within time) accuracy [171], i.e., it does not clarify whether the variability in space and time is included in the descriptive statistics for each field or parameter being compared. This issue is evident in a recent study which compared surface $PM_{2.5}$ and PM_{10} concentrations and particle size ratios from four different countries (Israel, Italy, France, and the United States (California and NE-USA)), against collocated sun-photometer AERONET measurements and AOD products derived from MODIS Dark Target Collection 06 algorithm and the MultiAngle Implementation of Atmospheric Correction (MAIAC) algorithm [214]. Sorek-Hamer et al. (2016) concluded that there was a poor correlation between predicted and measured concentrations and apart from a slight seasonal bias were unable to account for the poor correlation. Despite having data from many sites, they restricted their spatial analysis to amalgamating across the five regions. Taylor diagrams have compared measured concentrations (or AOD) with monitored data and correlations across multiple sites have been evaluated to determine if algorithm improvements have led to improved correlations [201] in describing temporal variability at monitoring sites. Similarly, Maximum Covariance Analysis has been used to compare monthly spatial variances between different satellite products and ground-based measurements and these variances were depicted graphically [4]. What is lacking are statistical tools that combine the spatial, temporal, and field (or parameter) variability in one diagram.

Whilst AERONET sites are well distributed about the globe, there remain many locations without monitored data where it is impossible to determine if the aerosol retrieval has made reasonable choices, either for pixel selection, cloud screening, aerosol model type or surface reflectance assumptions [215]. If the spatiotemporal variability at monitoring sites is poorly defined, this is amplified when aerosol model uncertainty must be included in the assessment of the overall accuracy of the predicted GLCs.

3.3.6. Emerging solutions

One of the perceived problems with working with remote sensing is the difficulty of finding suitable products, downloading large files, and converting those files

into meaningful data in a suitable format [1]. Web-based graphical interface tools (such as those presented in Table 1 of Mhawish et al.) are gaining popularity as a means of rapidly screening and acquiring data [61].

Whilst these tools are excellent for routine screening, more intensive investigations may require the use of raw data files. Increasing standardisation on the netCDF (ver. 4) standard has seen the proliferation of simple command-line tools such as the University of California's netCDF Operators (NCO) and the Max-Planck's Climate Data Operators (CDO) [216]. Both tools allow easy data manipulation. A secondary benefit of the standardisation is the development of improved visualisation software, such as Paraview [217], which use the netCDF data standard and are preconfigured to take advantage of supercomputers.

However, the biggest change, in computing AOD, has come about with the development of the Meteosat/SEVIRI AOD algorithms. The Meteosat series of satellites has led the development of GEO satellites methodologies as reflected in Table 3-1 and Table 3-2. Table 3-2 describes recent literature which specifically considered the derivation of AOD and GLCs, rather than simple lookup of products. These studies show that the NASA/NOAA products predominantly determine AOD using scattering of visible wavelengths as demonstrated across a range of current and future satellite platforms including MODIS [48, 65, 183], VIIRS [187], GOES-R [188] and future planned satellites such at TEMPO [189]. In contrast to NASA, EUMETSAT methods favour using thermal infrared bands to identify and quantify aerosol plumes using thermal infra-red to determine a dust index [50, 68, 143, 180].

Table 3-2: Recent literature describing GEO aerosol algorithms.

Satellite/Sensor (Reference, Year)	Title	Source types	Algorithm/comments
GOES-R [171]	A numerical testbed for remote sensing of aerosols, and its demonstration for evaluating retrieval synergy from a geostationary satellite constellation of GEO-CAPE and GOES-R	Unspecified lookup table	Scattering
SEVIRI [218]	Retrieval of Aerosol Optical Depth from Optimal Interpolation Approach Applied to SEVIRI Data	Mineral dust, sea salt, particulate sulphates (SO_4) and smoke	AOD from 0.6 μm & 1.6 μm. Uses scattering Describes algorithms Compare to AERONET
SEVIRI [143]	The identification and tracking of volcanic ash using the Meteosat Second Generation (MSG) Spinning Enhanced Visible and Infrared Imager (SEVIRI)	Volcanic ash	RGB dust index using Red (12-10.8 μm), Green (10.8-8.7 μm), and Blue (10.8 μm)
SEVIRI [169]	Comparisons of aerosol optical depth provided by SEVIRI satellite observations and CAMx air quality modelling	CAMx aerosol model species	AOD (0.6 μm) Top of Atmosphere reflectance, corrections. Compare to AERONET
SEVIRI [205]	LSA SAF Meteosat FRP products - Part 2: Evaluation and demonstration for use in the Copernicus Atmosphere Monitoring Service (CAMS)	Wildfires	Heat of combustion proportional to amount being burnt not vegetation type. Uses MIR, NIR, burnt areas
SEVIRI [151]	Improved space borne detection of volcanic ash for real-time monitoring using 3-Band method	Volcanic ash	RGB dust index Displays thermal BTR spectra for common aerosols Compare to Mie theory
Himawari-8 [145]	Development of a Multi-Spatial Resolution Approach to the Surveillance of Active Fire Lines Using Himawari-8	Wildfires	Multispectral, Red, MIR & TIR

Himawari-8 [146]	Data Assimilation of Himawari-8 Aerosol Observations: Asian Dust Forecast in June 2015	Asian Dust	AOD from 470, 510 and 640 μm
Himawari-8 [144]	Aerosol data assimilation using data from Himawari-8, a next-generation geostationary meteorological satellite	Not stated, total AOD	Used AOD from visible (0.47, 0.51, and 0.64 μm) and near-infrared (0.86 μm)
INSAT [177]	Dust Aerosol Optical Depth Retrieval and Dust Storm Detection for Xinjiang Region Using Indian National Satellite Observations	Dust storm	Suggests not spectral but dust index (BTD & IDDI) to identify aerosol Included spectral graphs BTD detects event (by threshold exceedance) but not related to intensity. Compared to AERONET AOD from 1.6 μm
Himawari-8 [219]	Deriving Hourly $PM_{2.5}$ Concentrations from Himawari-8 AODs over Beijing-Tianjin-Hebei in China	Urban regions	AOD (500 nm) & AE from Himawari-8 compared to AERONET sites. Use statistical model with inputs of relative humidity, boundary height, NDVI (surface categories) and topography (DEM)
SEVIRI [220]	North Africa and Saudi Arabia Day/Night Sandstorm Survey (NASCube)	Sandstorms	NASCube compared to DB + AERONET pseudo-true colour day and night 10-day minimum Wide spectral range 0.6, 0.8, 1.6, 3.9, 8.7, 9.7, 10.8, and 12.0 μm RGB (12-10.8. 10.8-8.7, 10.8) AOD (12-10.8)
TEMPO [189]	Tropospheric emissions: Monitoring of pollution (TEMPO)	Wide range of pollutants	Vis & UV wavelengths

3.4. Conclusions

This review has highlighted the challenges faced with determining GLCs from remote sensing data. Because of these challenges, atmospheric scientists have in the past not fully utilised remote sensing to routinely determine GLCs [1]. GEO is a significant step forward in supplying highly resolved data that satisfy the temporal requirements for sub-hourly data. It goes beyond the hourly resolution of most dispersion models supplying sub-hourly data that allow aerosol and cloud dynamics to be investigated with almost near-real-time capabilities for the first time. Spatially the infra-red resolution is slightly coarse (Himawari 2 km) for localised studies, but adequate for regional and global studies. Kriging algorithms could potentially refine the continuous representation of the discrete observations in the spatial scale to be similar to local dispersion model studies, but this only produces a smoothed estimate and does not improve the underlying spatial resolution.

Currently, AOD methods utilise the enhanced temporal resolution of GEO data to obtain a cloud-free measurement and increase the analysis frequency. Methods that use the additional information supplied by the rate of change are notably absent and should be developed. The aerosol model supplies the concentration vector; the rate of change of this vector presumably determines the rate at which material is added, removed, or chemically transformed in the plume, and the second derivative determines if the plume is in an equilibrium state (i.e. stable constant emission) or an active source/sink. Analysis of these rate of change variables should allow for a better understanding of emissions and resulting chemical and physical transformations even if the underlying aerosol inversion model contains assumptions. However, the extent to which particle emission changes are reflected in satellite data is severely constrained by the resolution of the data [61]. The spatial resolution determines if the plume is discernible against background concentrations and if the plume spans multiple pixels or is fully contained within one pixel. The temporal resolution determines if the underlying chemical and physical changes can be discernible with the data frequency, for example, rapid photochemical reactions may be faster than the rate of data

updates. The data resolution (or sensitivity) determines the concentration changes that are detectable; for instance, Himawari-8 has a brightness temperature resolution of 1/16 Kelvin or 1/1024 of scaled radiance (based on personal inspection of the data). The spectral sensitivity is impacted by the width and number of bands: this determines what species can be identified. For instance, a hyperspectral instrument can determine targeted organic compounds while the broad bands of GEO satellites are limited to compound classes such as black carbon [221].

Understanding the error matrix of aerosol models is vital, and this should become routine instead of the lookup table of current methods. At a minimum, this will encourage the use of more than merely two or three-band methodologies in the development of dust indices and instead utilise all wavelength bands measured by the satellite to better determine the aerosol type. Given the rapid near real-time availability of the data, processing should at most take half the data rate, allowing the balance of time for slower data transfers. This implies that processing of all data products has at most five minutes to complete and this may involve approximations rather than exact solutions.

It is unlikely that GEO aerosol remote sensing will provide a complete standalone solution and in this, we agree with Hoff and Christopher: so long as the number of intrinsic properties to solve is greater than the number of reactive wavelengths, the circular assumptions of an aerosol model imply that quantification remains an approximation. It is highly probable that hybrid methods of neural networks, Bayesian probabilities and coupled CTM models such as GEOS-CHEM will continue to be developed and improved. However, the time constraints of near real-time modelling make a fully coupled CTM unlikely and favour the pre-processing of existing data from statistical neural network models into enhanced dust index products that take into consideration local mineralogy and particle size distributions, resolve the vertical profile and account for moisture and other external effects.

4. Temporal resolution

Sowden, M., U. Mueller, and D. Blake.

What temporal resolution is required for remote sensing of regional aerosol concentrations using the Himawari-8 geostationary satellite.

Atmospheric Environment, 2019: **216**: p. 116914

4.1. Abstract

Few studies have directly addressed the question of what temporal resolution is required for air quality studies using geostationary remote sensing data. If timescales are too large, there is a risk that events affecting air quality may be missed; and if too small, there is a possibility that large data files may be processed frequently, at significant computing cost and potentially without concomitant improvements in the monitoring of air quality. The problem is particularly significant in sparsely populated regional areas such as the Pilbara in Western Australia, where air quality issues arising from a range of events, dispersed over a vast area, increase the risk of environmental health and ecosystems impacts and where the use of conventional monitoring is impractical.

This study aimed to establish an optimum temporal sampling interval for air quality studies using geostationary data and determine the impact of different timescales on ground level concentrations. The study was based on an analysis of Himawari-8 satellite data relating to a dust storm within a roll cloud which occurred near Onslow in Western Australia on 8 March 2017. Data from the Himawari-8 satellite were obtained from the Australian Bureau of Meteorology relating to the event and were used to: (1) assess the probability of a satellite overpass coinciding with the event; (2) determine scale factors of different time periods during the event; and (3) undertake an analysis of event duration using remote sensing data.

The analysis identified numerous sub-phases of the dust event, each lasting between 30 and 50 minutes. Data analysis considered all thermal infrared bands and Taylor plot analysis reduced the ten wavelength bands to six independent bands. Principal component analysis of brightness temperature difference between

these six bands identified the rate of aerosol compositional change and established that an optimal geostationary sampling frequency of five to ten minutes would be required to quantify these temporal changes effectively.

Keywords: temporal resolution, geostationary, particulate matter, brightness temperature difference, Himawari-8.

4.2. Introduction

Remote sensing is appealing as a method to estimate concentrations over a vast region due to its spatial coverage, but it has been limited in the past by the single daily snapshot from polar-orbiting satellites which can miss events and not be representative of daily average concentrations [222]. Remote sensing satellites supply data used for air quality metrics at various spatial and temporal scales. Polar-orbiting satellites provide periodic measurements (e.g. MODIS once per day [48]) while second-generation geostationary earth orbiting (GEO) satellites such as SEVIRI [169], GOCI [170], Himawari-8 [144] and GOES-R [171] supply hourly and sub-hourly data. Aerosol Optical Depth (AOD) [48, 63-65] is one such air quality metric and is a measure of the extinction of electromagnetic radiation by dust and haze which can absorb or scatter light [223]. AOD is dimensionless and is related to the total amount of aerosol in the vertical column of atmosphere over a location. AOD measurements have been extrapolated to surface concentrations [3, 41, 84-87, 89] and compared with daily surface measured average concentrations [2]. Apart from the temporal bias of comparing different timescales (seconds against hourly and daily monitoring), short-term events such as fires and inversion weather conditions may be inactive during infrequent satellite observations, or clouds may obscure the scene, leading to the event being missed [104, 152, 161-163]. Low-cost monitors have been used to assess the spatiotemporal variability of aerosols in cities [224, 225]. These inter-day $PM_{2.5}$ spatiotemporal variations in concentrations have been confirmed in monitored data from 31 Chinese cities [226] and regional hourly AOD measurements using Himawari-8 [227]. These rapid fluctuations in air pollution concentration levels have been ascribed to changing meteorological conditions which affect all emission sources [228].

The temporal resolution of GEO satellites is a substantial improvement over polar-orbiting satellites and the hourly resolution of most dispersion models [28]. The temporal resolution of GEO satellites is comparable to most real-time land-based monitoring instruments [168] and has improved over time, as evidenced by the progression of GEO satellites from GOCI (hourly) [170], SEVIRI (15 min) [169], GEOS-R [58] ,and Himawari-8 (10 min) [144]. Himawari can supply finer resolution temporal data with 2.5-minute updates during severe weather events over a smaller targeted region [229], while China's Gaofen-4 satellite has a temporal resolution of one minute [182] over the entire domain.

Despite the improvement in the temporal resolution of GEO satellites, few studies have directly addressed the question of what temporal resolution is optimal for air quality studies using geostationary remote sensing data. If the time intervals are too large an event may be missed. Conversely, if they are too short, they may affect computing resources, such as larger files and central processing utilisation. Similarly, studies that only consider daytime impacts, using visible spectra [227], will miss dust events that occur at night and early morning inversion conditions. Addressing the timescale requirements of remote sensing for air quality estimates of aerosol species and concentration requires an understanding of both the fundamental drivers of air quality change and an estimation of how aerosol change drives, remotely-sensed, spectral changes [222, 230].

Particulate Matter Air Quality

PM composition is dependent on the source; for example, desert dust is principally crustal but may include biological material [231] while smoke from wildfires [232] is chiefly organic (combustion by-products) but may include inorganic compounds in the fly-ash. The composition of PM at any moment may be influenced by multiple source emissions (e.g. sea-spray, wind erosion, industry) resulting in a complex mix of compounds, and these compositional changes must, therefore, be analysed separately.

In regional areas, the contribution made by sources such as fires and dust storms is uncertain. The number of sources (e.g. fires) and the scale over which emissions occur may result in substantial PM emissions which may be transported vast

distances and affect air quality in areas far removed from the source [233]. Hourly (or sub-hourly) measurements are required to understand the transport, dispersion and resulting PM concentrations from significant short-term events where the exposure (concentration) is sporadic but severe in magnitude. For example, a dust storm usually lasts less than a day while a fire may change its path in minutes yet have a total duration of days to weeks.

The concentration differences between short and long-term timescales are primarily related to the changes in wind speed, direction, and emission strength. Decomposing the wind spectrum into frequencies determined that the primary factors driving wind change are short-term wind-gusts (lasting between one second and five minutes), the diurnal cycle (24-hours) and the passage of fronts (about four days) [165]. Wind gusts cause air turbulence, and this turbulence drives air quality events [32, 166]. In contrast, laminar wind flow occurs at longer wind frequencies (hourly to daily) and these wind frequencies have low variability [165].

The optimum monitoring interval is therefore expected to be on the cusp of the turbulent zone, i.e. five to ten minutes, for air quality events to achieve reproducible results and yet also be fast enough to detect those events. Despite this known variability of the daily diurnal cycle, the accredited PM sampling method [167, 168] draws a predetermined volume of air through a filter using a size-selective inlet and captures the total mass on the filter throughout a day (i.e. a 24-hour average). In contrast, electronic monitors, such as Beta attenuation monitors, usually record hourly or sub-hourly data. Given the temporal nature of dust events, it is vital that monitoring timescales be taken into consideration when comparing monitoring results. Health-related studies suggest that the minimum requirements for monitoring atmospheric events are a spatial resolution one kilometre and a temporal resolution of an hour [167, 168].

Remote sensing of PM

The limitation of a single daily snapshot from polar-orbiting satellites has been overcome by the rapid data updates from geostationary satellites [227, 234]. The primary function of these geostationary satellites is to supply weather-related

data, but as the weather is a strong driver of concentration [166], geostationary satellites may also be ideal for determining GLCs [234].

Remote sensing has been used to monitor GLCs using both visible wavelengths (detecting scattering) and infrared wavelengths (detecting thermal radiation) [234]. Clouds impact the aerosol analysis (Levy et al., 2013) using reflectance methods, and the strong water-vapour absorption affects the thermal infrared portion of the electromagnetic spectrum (Schmidt et al., 2016; She et al., 2018). Methods to monitor GLCs based on visible wavelengths yield stronger responses as reflected energy is greater than thermal vibrational energy. Scattering is inversely proportional to the incident wavelength raised to a power (dependent on particle size), and there is, therefore, minimal scattering observed at thermal infrared wavelengths [61, 235]. However, thermal infrared allows for continuous monitoring (i.e. 24 hours a day) while scattering by visible light requires direct light from the sun [234] (i.e. daytime only). In addition, using thermal infrared increases the number of potential wavelength bands from six to ten, which may improve the ability to determine composition from satellite data. Thermal infrared absorption is computed as the brightness temperature (BT) by the satellite sensor [229, 236].

Traditional AOD methods rely on spectral signatures to determine speciation [234]. However, the spectral properties of stationary surface soil and aerosol from wind-blown eroded soils are similar, as they have similar mineralogy. The lower mass density of the aerosol means that lateral heat loss is not compensated for by heating from other nearby particles, and this results in slight thermal differences between aerosol particles and surface soil [237-239] which can be used to quantify aerosol plume concentrations.

Most of the BT measurements relate to land and sea surfaces, which predominate (across the study region), rather than clouds and aerosols which are of short duration and limited in spatial extent. A method is required that highlights the aerosol rather than the land/sea BT change. Brightness temperature difference (BTD) between two thermal infrared wavelengths (λ) (i.e. $BT_{\lambda 1}$ - $BT_{\lambda 2}$) [6, 234] is a simple high-pass filtering method that enhances the differences between two

similar wavelength bands while minimising commonality between two wavelengths. For a satellite with N bands, there are N!/2!(N-2)! or N(N-1)/2 potential dual-band BTD combinations. Himawari-8 has ten infrared bands, and therefore there are 45 possible BTD combinations. Temporal implications must be considered in efforts to better understand air quality events, by using a wider spectrum of wavelengths, and obtaining continual coverage - rather than a single daily measurement.

4.3. Methodology

4.3.1. Study design

This study set out to investigate the optimum temporal sampling interval using GEO data from Himawari-8 and surface PM concentration data from the Port Hedland region in Western Australia. A rare meteorological event of a dust storm within a roll cloud was used as a case study. The incident included an onshore wind (diurnal event) - which brought in maritime air, and a subsequent wind reversal (diurnal event) - which generated crustal aerosols. The air mass containing crustal aerosols, blowing offshore, then collided with fresh maritime air which led to the dust storm and roll cloud (rare event) and subsequent rainstorm (regular event). This storm was, therefore, a composite event and, although rare in its severity and formation of the roll cloud, was an outcome of regular, daily, air mass movements.

The first phase of the study considered the probability of a polar-orbiting satellite overpass coinciding with dust events, i.e. how well does the instantaneous measurement reflect the daily concentration variability? The second phase investigated if monitoring for one time period can be used to predict for a different period, i.e. is it feasible to extrapolate an instantaneous measurement to a daily average? Lastly, the duration of each sub-phase of the dust storm was determined to identify the rate of compositional change using geostationary remote sensing data.

4.3.2. Data

Surface PM_{10} concentration data

The effect timescales have on concentration was investigated using ten-minute surface PM_{10} monitoring data from July 2016 to July 2017 for six sites in and near Port Hedland in the Pilbara region in the north-west of Australia. The Pilbara is a large arid regional area spanning approximately 1,600 × 400 km^2, known for its resource extraction (mining) and pastoral (rangeland) industries. The Pilbara was selected as a case study as the environment is dusty with comparatively low vehicle usage and is profoundly affected by local industry and experiences widespread regional fires and dust storms [17-19]. In addition to the storm that occurred during the case study, Port Hedland experiences on average 54 cloudy days per annum (http://www.bom.gov.au/climate/averages/tables/cw_004032.shtml).

Data for these six surface monitoring sites were obtained from the Port Hedland Industrial Council (PHIC), and the location of these monitoring sites are depicted on the PHIC website (http://www.phicmonitoring.com.au/). Of the six PM_{10} monitoring sites, Yule River (YUL) is the most remote. The airport site managed by the Bureau of Meteorology (BOM) is located some distance away from port operations while the other four sites are affected by port operations. Preference was given to analysing the monitored PM concentrations from remote sites, as previous studies have demonstrated that local sources would dominate concentrations from monitoring sites located within Port Hedland [18, 19, 23, 240].

Himawari-8 data

Raw data files of all ten thermal infrared bands from the Himawari-8 satellite were obtained from the Australian Bureau of Meteorology (BOM) for the period from July 2016 to July 2017. These data files were cropped to the study domain and analysed using the climate data operators (CDO) [216]. Table 4-1 lists the wavelength bounds for each band [57, 229, 236], the central wavelength for each band (from the metadata), and typical applications for each band [57, 58, 145, 234, 241]. Specifically, the literature indicates that bands 8 (6.2 µm), 9 (6.9 µm), and 10 (7.3 µm) are characteristic of strong water vapour bands [57, 58, 241]. This water vapour may be in the form of clouds or may be an indication of the water content

of an aerosol plume. Bands 13 (10.4 μm), 14 (11.2 μm), and 15 (12.4 μm) have been associated with aerosol plumes [234, 242]. The remaining bands may indicate chemical composition as band 7 (3.9 μm) has been associated with fires (potentially CO_2) [152, 243], band 11 (8.6 μm) with SO_2 [67, 244], band 12 (9.6 μm) with O_3 [58, 245] and band 16 (13.3 μm) with sea surface temperature, clouds (potentially water) [57, 241] and CO_2 [58].

Table 4-1: Himawari-8 bands and characteristic wavelengths.

Band	Wavelength (μm) Low	High	Central	Applications
1	0.43	0.48	0.471	vegetation, aerosol
2	0.50	0.52	0.510	vegetation, aerosol
3	0.63	0.66	0.639	low cloud, fog
4	0.85	0.87	0.857	vegetation, aerosol
5	1.60	1.62	1.610	cloud phase
6	2.25	2.27	2.257	particle size
7	3.74	3.96	3.885	low cloud, fog, forest fire
8	6.06	6.43	6.243	mid and upper-level moisture
9	6.89	7.01	6.941	mid-level moisture
10	7.26	7.43	7.347	mid and low-level moisture
11	8.44	8.76	8.593	cloud phase, SO_2
12	9.54	9.72	9.637	ozone content
13	10.30	10.60	10.407	cloud top, “clean longwave window”
14	11.10	11.30	11.240	cloud, sea surface temperature
15	12.20	12.50	12.381	cloud, sea surface temperature, “dirty longwave window”
16	13.20	13.40	13.281	cloud top, CO_2

4.3.3. Determining the probability of a satellite overpass coinciding with a dust event

The ratio of the maximum and daily ten-minute concentrations of the PHIC surface data was calculated, and the frequency distribution of the resulting ratios was determined. A concentration ratio was calculated to preserve confidentiality by depicting relative, not absolute concentrations. This ratio provides a means for identifying if a dust event occurred during the day, as a dust event would have higher concentrations than background levels (i.e. scale ratio greater than one). For this study, it was assumed that a dust event day had a ratio greater than two (based on the mean of the analysis).

The cumulative frequency distribution of the ratios was calculated for the BOM and Yule River sites a) using all the data and b) by restricting the analysis to match Terra and Aqua's (MODIS) overpass times of approximately 10:30 and 13:30 respectively. The difference between these six curves (2 sites x 3 overpasses (all, 10:30, 13:30)) indicated low or high measurements at the time of the overpass in relation to the daily average. The difference in the cumulative frequency between the three curves (per site) reflects the temporal bias of over/underdetermination and indicates the proportion of dust events detected at the fixed satellite overpass times. Ignoring issues of sensitivity, the probability of a satellite detecting an event (i.e. the probability of a satellite being overhead at the time of a dust event) is related to the number of measurements and the duration of an event.

4.3.4. Scale factors for different time periods

Scale factors are needed where monitoring data are reported for a period (e.g. instantaneous MODIS overpass), and an estimate is required for another period (e.g. daily). Similarly, there is a need to extrapolate hourly dispersion modelling to estimate short term (3-10 minute) odour estimates [246, 247]. Variability in emission source strength and changing meteorological dispersion parameters imply that measurements from a rapidly varying dust event monitored and recorded for ten-minute, hourly, or daily values will be different to measurements

recorded as an instantaneous snapshot and these differences may not be directly related to the duration of measurements.

Scale factors for varying time periods were calculated using the formula from dispersion modelling guidelines of $C_i/C_0 = (t_0/t_i)^{0.2}$ for scaling between different time periods (where C is concentration, t is time, and the subscript 0 and i are the two time-periods of interest) [246, 247]. Centred moving averages were calculated instead of period averages, to keep the number of data points constant between the different statistics (i.e. 24 x hourly, 1 x daily or a constant 144 moving ten-minute averages irrespective of the period). To investigate if the conversion is universally applicable, exponents were calculated for time ratios to scale from ten-minute data to 20 minutes, 30 minutes, an hour, and a day.

4.3.5. Analysis of event duration using remote sensing data

The brightness temperature (BT) changes across the region were used to determine the duration of a dust event which impacted Onslow in Western Australia on 8 March 2017 [248]. Given the sparseness and limited monitoring of the region, there are few records of such storms, and social media photographs and secondary sources such as newspapers are currently the most widely available sources of information. Brightness temperature histograms across the region were calculated using band seven (3.9 μm) of the Himawari-8 satellite for each observation period across the day of the incident and the following day (for comparison). Band seven was used as it had the greatest range (i.e. sensitivity) to BT changes across the day and region [58]. A temperature-time distribution was calculated from the histograms where the counts of temperature (y-axis) for each time interval (x-axis) was displayed as a colour-coded distribution.

Intensity changes across multiple wavelength bands, rather than just a single wavelength band, were used to identify compositional changes during the event as different compounds exhibit different spectral properties. Taylor diagrams [249] were used to identify where a change in one band correlated with a change in another band, i.e. indicative of the same compound (correlated) or different

compounds (weaker correlation). Identifying compositional change (changing spectral responses) thereby enables event duration to be determined rather than concentration change (changing intensity).

Taylor diagrams are radial plots and depict standard deviation, correlation, and root mean square error (RMSE) on one diagram. Taylor diagrams allow easy visual comparisons from the clustering based on the commonality of standard deviation, correlation, and RMSE. Taylor diagrams were constructed relative to each of the ten infrared bands to check the existence of any clusters and to identify redundant wavelengths. The data were further analysed via high-pass filtering and PCA.

Most of the BT measurements relate to sea and land surface temperatures as they predominate across the region with clouds and aerosols being outliers in the temperature-time distribution plot calculated earlier in this section (Figure 4-4). High-pass filtering using brightness temperature difference (BTD) between bands 11 (8.6 μm) and 7 (3.9 μm), i.e. $BTD_{(8.6\text{-}3.9\mu m)}$, was applied across the region over the two days to highlight aerosols and minimise commonality (i.e. sea and land) between the two wavelengths.

BTD wavelength combinations chosen from the Taylor analysis were analysed via PCA. The data were standardised by subtracting the mean and dividing by the standard deviation before undertaking the PCA analysis to give equal weight to the six BTD combinations. Paraview virtualisation software [217] was used to normalise the data, determine the weightings of the first principal component and visualise the results. For each satellite observation, the principal component weighting was determined.

4.4. Results

4.4.1. Probability of satellite overpass coinciding with a dust event

A histogram of the ratio of the daily maximum to the daily average was plotted for all six air monitoring locations across the year and is shown in Figure 4-1. The most rural location (YUL) had less of a discrepancy in PM_{10} concentrations

between the maximum and average than the other five sites. The mean ratio across all six sites was 2.69.

The cumulative frequency distribution of the scale ratio (Figure 4-2) shows that for a sizable portion of the data (~15 %) the ratio was greater than four. Figure 4-2 also demonstrates that at YUL 95 % of the instantaneous concentrations at the time of the MODIS overpasses, were lower than the daily average concentrations (i.e. scale ratio of one) compared to 70 % at BOM. This can be ascribed to the influence of wind speed on the concentrations. Night-time temperature gradients were weaker than daytime temperature gradients, and as a result, higher wind speeds were more probable in the daytime, leading to more favourable dispersion conditions and lower concentrations during the day at the time of the overpasses (10:30 and 13:30).

A dust event was deemed to have occurred if concentrations exceeded twice the background (i.e. a scale ratio of 2) – a conservative assumption given the "limit of detection" as three times background. This classification ascribed the probability, expressed as a percentage, of a dust event occurring sometime during the day as 80 % (100-20 %), at the BOM site (from Figure 4-2). In contrast, the probability of detecting a dust event at 10:30 or 13:30 was less than four percent (100-97 %) (conservatively rounded up). Therefore, it can be concluded that MODIS (using both Terra and Aqua sensors) will detect a sporadic event such as a fire or wind-blown dust from eroded areas in less than eight percent of cases. Furthermore, an average event duration can be crudely estimated as the probability of the ten-minute data (80 %) divided by the probability of the 10:30 (or 13:30) data (4 %) (i.e. the number of "events" a day) multiplied by the monitoring period (ten minutes). Therefore, this method estimates that elevated concentrations from a dust event are recorded for about three hours (80 %/4 % x 10 minutes) at a surface monitor before the wind changes direction, or the event ends. Given this short temporal span, the probability of MODIS detecting an event is unlikely as it is estimated at only four percent per overpass.

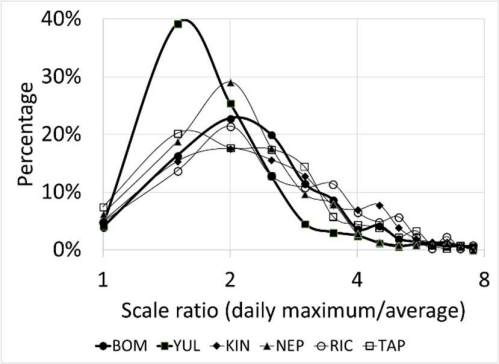

Figure 4-1: Frequency distribution of the ratios of maximum (ten-minute) and daily average PM10 concentrations at five monitoring sites near Port Hedland.

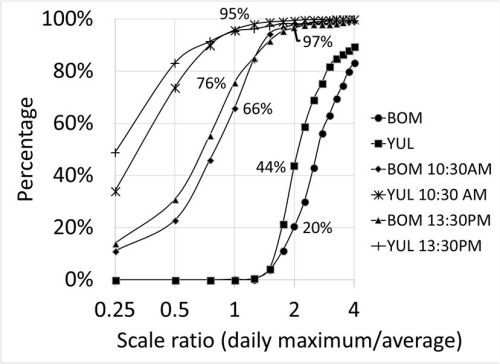

Figure 4-2: Cumulative frequency of the daily PM10 scale ratio (ten-minute/average) and during MODIS overpass times at two sites (BOM and YUL).

4.4.2. Scale factors of different time periods

The natural logarithm of the average concentration ratios divided by the time ratio was plotted against the time ratio (plotted on a log scale), and the results are displayed in Figure 4-3 for four time-ratios (2, 3, 6 and 24). The results show that at longer time ratios the factor is site-specific, but averages to 0.2. In contrast, there is less site-specific variability at shorter time ratios but for a much smaller exponent of about 0.05. Thus, the equation does not hold, and the results imply that instantaneous concentrations from dust events cannot be used to predict average concentrations over longer periods (and vice-versa) with a constant exponent.

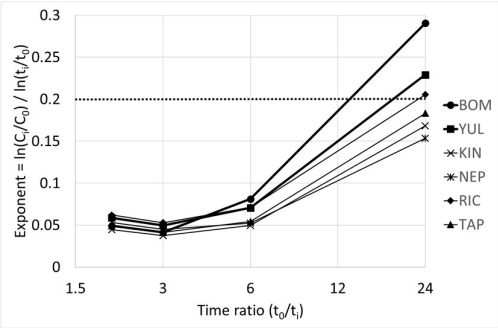

Figure 4-3: Exponent for converting between averaging time-periods.

4.4.3. Analysis of event duration using remote sensing data

The temperature-time distribution of the BT measurements for band seven (3.9 μm) was calculated for the two days and is displayed in Figure 4-4a. For comparison, the surface monitored temperature at the BOM site is given in Figure 4-4b. The frequency distribution of the BT (y-axis) for each time-interval (x-axis) is presented as a colour-coded frequency (depicted as counts) for all points across the region. The graph shows that most of the observed temperatures were from the diurnally fluctuating surface temperature (mostly depicted as orange and red) and the stable sea temperature (mostly depicted as magenta), which together (i.e. greater than 560 counts) account for 83 % of the measured data. The result was as expected as the region had few clouds (as verified by MODIS cloud imagery) and isolated aerosol plumes during the two days despite the severe but localised dust event. Therefore, the background or "noise" in the temperature-time distribution graph depicts typical diurnal sea and land temperature changes (83 %) and the small variances from the background (17 %) were due to localised temperature effects such as clouds, tidal sea-level changes, active fire hot spots, and aerosol plumes.

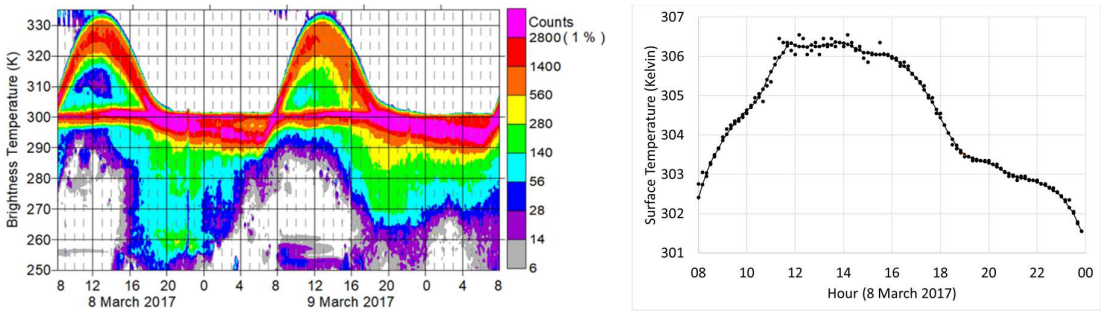

Figure 4-4: a) Brightness temperature (band 7) vs. time and b) surface temperature at BOM on the 8th and 9th March 2017.

These "outliers" (17%) in the BT data, therefore, reflect the radiometric signal of interest. Rapid cooling was observed during the day of the incident, starting late in the afternoon and extending over a series of five disjointed temperature changes, each lasting approximately two hours. From analysing the spectral time-series, it is postulated that these jumps reflected afternoon diurnal cooling (2-4

PM), clouds forming (4-6 PM), strong winds created from updrafts leading to the dust storm (6-8 PM), rain washout occurring (8-10 PM), and finally the dry remnants of the dust storm (10 PM-12 AM). Some of these changes are reflected in surface meteorological data and the afternoon MODIS overpass at specific sites, but the sparseness of surface monitoring precludes a definitive analysis.

Taylor plots were used to identify correlations between satellite bands as this could indicate redundant information if the bands were strongly correlated, i.e. compositional changes yielded similar spectral changes across multiple bands. Taylor plots are depicted in Figure 4-5(a-c) where bands 7 (3.9 μm), 11 (8.6 μm), and 12 (9.6 μm) were used as the reference. Three common clusters, or groups, were noted in each of the plots. The water vapour bands 8 (6.2 μm), 9 (6.9 μm), and 10 (7.3 μm) have less correlation to the other bands; the aerosol bands 13 (10.4 μm), 14 (11.2 μm), and 15 (12.4 μm) have high correlation and minimal variance; and the remaining "chemical" bands 7 (CO_2) (3.9 μm), 11 (SO_2) (8.6 μm), 12 (O_3) (9.6 μm), and 16 (sea surface temperature and H_2O) (13.3 μm) . These clustering patterns reflect the similarities between the bands for the event studied and the grouping could be different for a different event such as a volcanic plume or fire. The selection of the three reference bands in the Taylor plots was to avoid producing ten plots depicting similar information, and three of the "chemical" bands were chosen as the reference as the "chemical" clustering had the most differences.

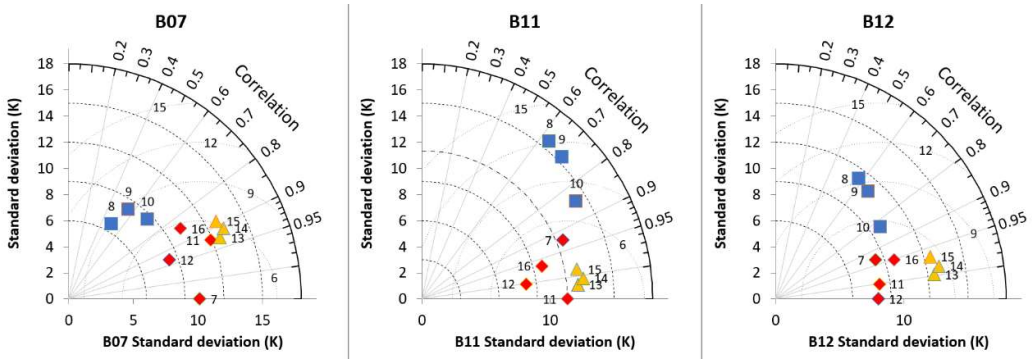

Figure 4-5: Taylor diagrams depicting variances of brightness temperatures across the study region using bands 7, 11 and 12 as reference.

The Taylor plots indicated that there was potentially redundant information in the three aerosol bands (13, 14, and 15). Furthermore, the three water vapour bands (8, 9, and 10) indicate cloud, not aerosol, movements [58]. Therefore, most of the BTD differences, which may be indicative of aerosol plumes, were expected to be contained in the bands 7, 11, 12, 16 and any one of the aerosol bands (15 was chosen). This reduced the 45 BTD combinations to 10, which was further reduced to six combinations (11-7; 12-7; 12-11; 15-12; 16-11; 16-12) based on the Taylor analysis and visually inspecting the satellite images and (1) ignoring those BTD combinations that resulted in minor changes between spectra, and (2) ensuring that the resulting images were consistent with plume behaviour (i.e. growth/dissipation of plumes) during the event.

PCA of the six BTD combinations demonstrated the changing spectral response during the event. The PCA weightings are depicted in Figure 4-6 for the six BTD combinations indicating how the weightings of the first principal component change over time across the day of the incident. (The first principal component accounted for approximately two-thirds of the variability in the data.) From the graph, it was apparent that dramatic shifts in the PCA weightings occurred over a period of about half an hour followed by stable periods (of about two hours). It was postulated, based on the air movement evident in the video in the supplementary material, and as highlighted in Figure 4-7 which depicts $BTD_{(8.6-3.9\ \mu m)}$ at various times during the day, that the four aerosol phases represented in Figure 4-6 were due to sea-spray (frames 0–13), wind-blown dust (frames 18-47), initial dust storm (wind-blown aerosol colliding with incoming maritime air creating a roll cloud) (frames 52-57), rain washout (frames 64-70) and the dry residual dust storm (frame 75 onwards).

Each phase of the event was defined by the rate of change of the primary principal component and the direction of the plume movement (on/offshore). Aerosol-type for each phase was postulated based on this primary PCA rate of change and plume movement. The results show that the timing of each stage matched the description and details given in the news report. Figure 4-7 demonstrates the progression of the storm as the aerosol plume was forced up and over itself by the incoming maritime air, which created the roll cloud. This level of temporal

resolution and spatial understanding of a dust storm with an associated roll cloud is unique in the literature and only possible with the availability of GEO data such as that from Himawari-8.

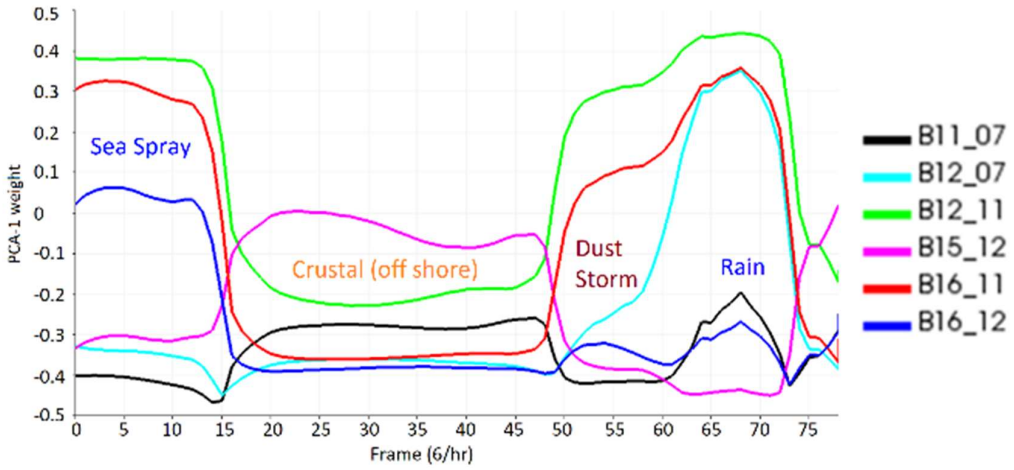

Figure 4-6: Weight of the first principal component of six BTD combinations indicating changes to probable aerosol types. Frame 0 (UTC) represents 8 AM local time. (Legend depicts wavelength bands, not wavelengths).

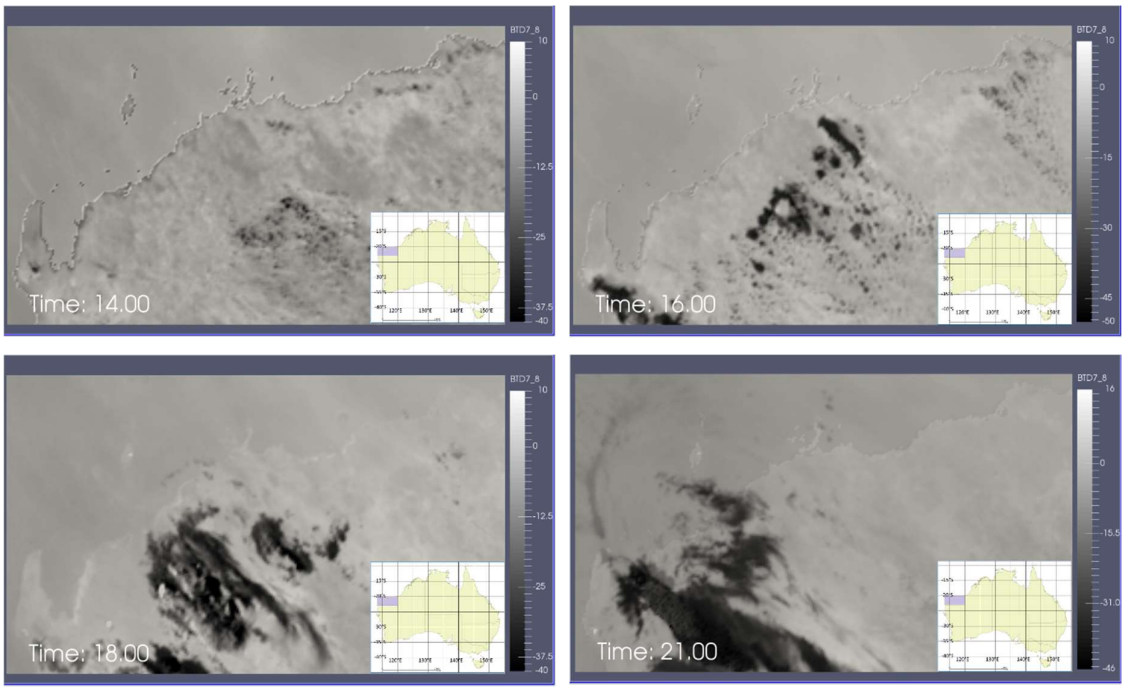

Figure 4-7: BTD $_{(3.9-6.2\ \mu m)}$ depicting the development of the dust incident. 2 PM) wind reversal to offshore; 4 PM) start of dust storm; 6 PM) maritime air colliding with the wind blowing offshore; 9 PM) storm dissipated.

4.5. Discussion

This study has investigated the optimum temporal sampling interval for determining GLCs from rapidly changing dust events in the Pilbara region of WA. The analysis of the temporal resolution of the Himawari-8 geostationary earth orbiting (GEO) satellite's data has contributed to a better understanding of the formation and dissipation of a rare meteorological and dust event of a dust storm being formed as part of a roll cloud. While a rare event, the causes were ascribed to regular daily air mass movements. In contrast to previous studies, no assumptions were made about the relevance of individual bands for determining composition. Instead, spectral differences were used to infer the duration of compositional changes. Similarly, the stronger signals from scattering in the visible portion of the electromagnetic spectrum were rejected in favour of the weaker thermal infrared absorbance bands, because of their continual radiation in contrast to the daytime only scattering of light.

Taylor plots identified four independent bands which were used by BTD as a high-pass filter to improve the spatial resolution, and PCA identified the first principal component for each time interval. The rate of change of the weight of the first principal component identified each phase of the event and allowed the aerosol type to be postulated based on video inspection of the plume direction (on/offshore). The timing of each stage matched the description and details given in the news report. It was not within the scope of this study to elucidate composition but merely to reflect on what observation periods are required for geostationary data to monitor plume movements accurately. The PCA analysis may exhibit entirely different factors for other compositions, mineralogy, or smoke.

The inflection points in Figure 4-6 showed that these compositional changes occurred over three to five frames of ten minutes, i.e. 30 to 50 minutes, while the dust storm (frames 52 to 57) lasted 50 minutes before the rain, which lasted 60 minutes (frames 64 to 70). Monitoring methods define a limit of detection (LOD) as three times the background variance and the limit of quantification (LOQ) as ten times the variance. Using these definitions against the 50-minute dry dust

storm phase implies that a fifteen-minute frame rate for LOD (50/3) is required, compared to a 5-minute frame rate for LOQ (50/10).

Himawari's ten-minute data resolution was adequate to detect rapidly changing air quality events. Some benefit may be achieved by halving the scan time to five minutes, but this will simultaneously double the already large data files and processing time. As shown by Hoven (1957), there is no benefit in reducing the scan time even further as the scan time will have to be faster than seven seconds to achieve the same variability as ten-minute data and this is not practical. Therefore, the five to ten-minute data rate represents an ideal balance as it is on the cusp of the turbulent range, which enables the rapid detection of changes, and the spectral gap region, which yields lower variability. Hourly averaging will reduce the variability, but the reduction in variability will come at the cost of early quantification, and rapidly changing aerosol plumes may be missed.

4.6. Conclusions

There are three timescales relevant to air quality: (1) the instantaneous [daily] snapshot from a polar-orbiting satellite [48]; (2) the minimum requirement of hourly monitoring [168]; and (3) the five-minute turbulent drivers of atmospheric change [165, 166]. This study has shown that air quality studies require a sufficiently fine temporal resolution to quantify sporadic dust events and that this high temporal resolution is lacking in data from polar-orbiting satellites (such as MODIS). It has demonstrated, based on a case study of a short set of measurements made of an opportunistic single dust storm event, that turbulent drivers of air quality are evident in geostationary data of high temporal resolution and emphasises that these drivers must be accounted for by remote sensing methods.

The analysis reiterated that MODIS is unsuitable for monitoring sporadic dust events - as less than four percent of events coincided with the satellite overpass. Using the infrared sensors on these satellites could potentially double the number of events detected - but would still miss ninety percent of short-term dust events because of the available temporal resolution. Remote sensing is therefore critically reliant on geostationary satellites such as Himawari to provide the required

temporal resolution for air quality analysis using the infrared bands and not be limited by the daytime-only restriction of visible wavelengths.

PCA analysis of six BTD ratios identified each phase of the event and allowed the aerosol type to be postulated based on video inspection of the plume direction (on/offshore). Using the LOQ definition on the duration of compositional changes indicated that an optimum temporal resolution of five-minute is required. This is faster than the current ten-minute Himawari-8 data rate, which may constrain the quantification of aerosol types during rapid aerosol compositional changes. However, given that these "rates of change" were calculated as the average across the domain, it is expected that the ten-minute data would be more than adequate when the location is taken into consideration.

It is vital that the frequency of severe events be better understood and that long-term data records be established to estimate health risks of sporadic air quality events on resident populations. The spatiotemporal information provided by GEO data unambiguously resolves the critical *where* and *when* for atmospheric scientists. However, the subsequent *what* (composition) and *how much* (concentration) is mostly unresolved, especially in the light of historical reliance on visible spectra. Work is currently being undertaken to determine composition using thermal infrared methods.

5. Indices

Sowden, M., and D. Blake.

Which dual-band infrared indices are optimum for identifying aerosol compositional change using Himawari-8 data?

Atmospheric Environment, 2020, 117620

5.1. Abstract

Aerosol optical depth algorithms predominantly use the visible portion of the electromagnetic spectrum. However, quantifying sporadic dust events throughout the full 24-hour period requires using continuous wavelengths such as infrared (IR). Identifying aerosols, using IR from geostationary data, has relied on subtraction indices rather than normalised differences. Limited attention has been given to determining which IR indices could be suitable for identifying aerosol compositional change. Suitable IR indices could potentially result in multi-spectral data from geostationary satellites, such as Himawari, being used to separate dust from other types of aerosols.

This study evaluated three index types: subtraction (brightness temperature difference (BTD)), normalised differences, and division (i.e. quotient). The effectiveness of these three indices were assessed against three sample matrix types: (i) pure soil spectra from the USGS Spectral Library Version 7 database; (ii) potential aerosol plumes, estimated from data relating to the formation and dissipation of a dust storm; and (iii) annual variance, at a surface monitoring site. Absorbance values from the USGS spectral database were aggregated into the spectrally broad Himawari-8 infrared bands. Potential plumes (i.e. transient over a small area) were identified from daily variances in the Himawari-8 satellite data. Principal component analysis was used to determine the variance explained by the first principal component for each of the sample and index types and to evaluate the effectiveness of the indices for detecting dust events.

Simple subtraction indices explained more of the variance than normalised differences or division for all sample types. Of the 45 BTD indices analysed, only seven resolved the cloud and aerosol plumes into separate groups. Of these seven

indices, $BTD_{3.9\text{-}6.2\,\mu m}$ and $BTD_{11\text{-}12\,\mu m}$ had the least correlation with the other indices and were chosen as the best indices to identify aerosol compositional change. A further three indices $BTD_{9.6\text{-}13\,\mu m}$, $BTD_{8.6\text{-}10\,\mu m}$, and $BTD_{6.9\text{-}7.3\,\mu m}$ were selected based on low correlations between other indices and ensuring that all ten IR wavelengths were utilised. This study indicates that the combination of these five indices, rather than a single index, may optimise the identification of aerosol compositional change.

Keywords: dust indices, aerosol, infrared absorption, Himawari-8.

5.2. Introduction

Regional air quality is often poorly measured due to cost and infrastructure demands. While remote sensing has the potential to monitor air quality, it faces numerous challenges – partly as a result of traditional computational practices. These challenges include (i) the lack of temporal resolution in data from polar-orbiting satellites such as MODIS, which make polar-orbiting satellites unsuitable for monitoring short-duration sporadic air quality events; (ii) the use of visible spectra is inadequate as it provides daytime only data; (iii) the use of infrared absorption wavelengths to identify but not quantify air quality events at a temporal resolution comparable to ground-based monitoring sites; and (iv) the cyclical assumptions in the use of the lookup tables limits identification of aerosol types only to those that are already matched with the database [6].

Traditional aerosol optical depth (AOD) methods rely on spectral signatures to determine speciation [234]. The width and number of spectral bands on a sensor determine the spectral resolution, which influences what species can be identified. For instance, a hyperspectral instrument can determine targeted organic compounds, while the broad bands of multispectral satellites are limited to the detection of generic classes [221]. While geostationary satellites have improved the spatiotemporal estimates of AOD [227], the methods used remain limited to day-time only estimates [250] and new methods must be developed that include dawn and night-time surface concentration estimates when high concentrations can occur from low wind-speeds and temperature inversion events [251].

Sub-hourly, infrared, geostationary data, such as the ten-minute data from Himawari-8, are required to monitor atmospheric changes to ensure that sporadic dust events can be continually observed and quantified. Newer methods of detecting these incidents using geostationary data have focussed on detecting the presence or absence of a dust event using infrared adsorption. However, there has been limited attention given to the determination of composition, or particle size, using only infrared frequencies, and this is compounded by a paucity of spectral libraries at those wavelengths [252].

Infrared spectral characteristics are required to classify aerosol composition (such as sulphates, black carbon, organic matter, sea salt, and mineral dust) [56, 253] to improve the understanding of source impacts. However, particularly in regional areas, it is often difficult to distinguish between the spectral properties of surface soils and wind-blown aerosols from these soils as they have similar mineralogy. The lower mass density of the aerosol implies that lateral heat loss is not compensated by heating from other nearby particles, and this results in slight differences between aerosol particles and surface soil [237-239]. Spectral differences have been used to determine soil composition using near-infrared (NIR) (i.e. wavelengths to 2.5 μm) techniques [254]. As soil composition takes time (years) to change, NIR can be used for soil quantification. In contrast, aerosol composition changes rapidly, and impacts may occur at night [22]. Consequently, infrared (i.e. wavelengths greater than 2.5 μm) are required to detect the night-time changes in composition [234]. She et al. (2018) is in contrast to other studies which used visible and infrared bands [255] and supports the ability to detect composition at night using infrared which is critical to determining continuous aerosol type and concentration.

Infrared brightness temperature (BT) is internally calibrated from spectral absorbance during the pre-processing of the satellite data [57, 68, 229]. Most of the BT measurements across the region relate to land and sea surface temperatures (which predominate background readings) rather than aerosols and to a lesser extent clouds, which are of short duration and limited spatial extent [7]. It is advantageous to remove regions of clouds from the data because water vapour absorption obscures aerosol absorbances [48]. However, this results in

undesirable gaps in the aerosol plume estimates [48]. Clouds are more opaque at higher wavelengths, and by retaining, rather than masking cloud regions, the data could potentially allow both aerosol and clouds to be partially detected provided the moisture signal does not saturate the BT measurement. A method is therefore required that amplifies the BT differences from clouds and aerosol plumes, rather than returning the bulk properties of land and sea surfaces.

Brightness temperature difference (BTD) between two infrared wavelengths (λ) (i.e. $BT_{\lambda_1} - BT_{\lambda_2}$) [74, 234, 256] is a simple high-pass filtering method that enhances the differences between two similar wavelength bands while minimising commonality between two wavelengths. BTD is reliant on the differences between absorbances at two wavelengths and is compound specific. Water (in all three phases) shows negative differences at higher wavelengths, in contrast to aerosols from wind-blown dust, which typically show positive differences [66, 67]. These differences have been used by BTD to distinguish clouds from aerosols [51, 57, 68-70]. For a satellite with N bands, there are N(N-1)/2 potential dual-band BTD combinations. Himawari-8 has ten infrared bands, and therefore, there are 45 possible BTD combinations. The literature indicates that bands 8 (6.2 μm), 9 (6.9 μm), and 10 (7.3 μm) are characteristic of strong water vapour bands [57, 241] and eliminating these three bands could potentially reduce this to 21 aerosol combinations.

Remote sensing, and consequently, the nomenclature, is evolving. For example, BTD has been referred to as brightness temperature difference (BTD) [234], Infrared Split-Window [67], and simple subtraction indices (SSI) [257]. Stagakis et al. (2010) investigated multiple vegetation indices that were grouped into BTD (referred to as SSIs in the reference), normalised differences (NDVI), $(BT_{\lambda_1} - BT_{\lambda_2})/(BT_{\lambda_1} + BT_{\lambda_2})$, and simple division (RAT), $(BT_{\lambda_1} / BT_{\lambda_2})$, [257].

Normalised difference, dust indices (NDDI) have been used to study dust storms [71, 258, 259]. However, She et al. (2018) suggest that NDDI is unable to distinguish aerosol over reflective desert regions. More recent studies favour BTD indices [57, 67, 68, 154, 177, 179, 201, 205, 229, 234]. These studies used dual-

band combinations of 11, 12, 8.6, 3.9, and 10 μm to detect dust events, of which the most commonly used BTD indices were $BTD_{8.6\text{-}11\ \mu m}$, $BTD_{11\text{-}12\ \mu m}$, $BTD_{3.9\text{-}11\ \mu m}$.

The research notes that the BTD thresholds are dynamic and may vary according to the mineralogy, region, and observed temperature [234, 242]. In assessing air quality data, it is apparent that significant air quality events (defined in this study as exceeding the Australian daily $PM_{2.5}$ and PM_{10} air quality criteria for an hour) only occur for approximately two percent of the time [7, 9]. Furthermore, the bulk of the measured satellite data is expected to be from surface soil, sea and clouds rather than from background concentration levels, while the "outliers" represent the air quality events, which are predominantly particulate matter in arid, sparsely populated regions such as this study. Fixed thresholds represent a crude approach to separating the data into cloud or aerosol, as thresholds are both regionally specific (composition and particle size) and moisture (cloud) dependent.

In an earlier study [7] on the rate of compositional changes, Taylor plots were used to identify correlations and clustering between dual-band wavelength combinations. We found clustering according to the water vapour bands (6.2, 6.9, and 7.3 μm), aerosols (10, 11, and 12 μm), and a third group which we attributed to "chemicals" (H_2O, SO_2, O_3) (3.9, 8.6, 9.6, 13 μm). We found that combining the 9.6 μm and 13 μm bands with the aerosol bands identified compositional changes despite these bands not being used in the existing studies identified above.

In addition to aerosol indices, other atmospheric-related remote sensing products exist that could assist in describing aerosol compositional change. Some of these products are described and are obtainable from https://worldview.earthdata.nasa.gov. These products present an overview of the atmospheric changes occurring across the hemisphere. Natural colour highlights the cloud cover over much of the globe, particularly in equatorial regions (where remote sensing analysis is severely restricted by cloud cover), and there are typically differences visible between Australia (more arid and less cloud) than northern Asia (more cloud). Dispersion conditions (and concentrations) are strongly dependent on the amount of cloud cover and cloud height - as this affects temperature inversions and atmospheric stability (i.e. the volume that a plume

may disperse into) and therefore, cloud height, i.e. the geopotential height of the highest cloud and cloud phase (quantified by the index $BTD_{8.6\text{-}11}$) may be essential parameters in estimating pollutant concentrations. Fires are detectable by the large radiation emitted in the near-infrared and thermal wavelengths, and fire detection is vital for identifying smoke from wildfires.

The 3 km MODIS AOD product typically shows gaps due to cloud masking and between the satellite tracks with high AOD concentrations over eastern Europe but not over Australia. Expanding the analysis to the 10 km Deep Blue AOD product over land reduces the cloud masking, as scattered clouds generally do not extend over the entire larger area, but do not alter the north/south concentration differential. There is typically a difference in the Ångström exponent (related to particle size) between the north (China) and south (Australia) land-masses observed in the Himawari-8 dataset, and these differences may reflect compositional and particle size differences due to urbanisation and industrialisation between the regions. The remote sensing products such as cloud cover, cloud height, moisture, and particle size are, therefore, important in understanding the formation and transport of aerosols, their source compositions, and may directly influence any aerosol index.

Some potential dust indices have been used in previous studies indices [7, 57, 67, 68, 154, 177, 179, 201, 205, 229, 234]. The differences between these dust indices are related to the characteristic wavelength bands used for each index, and it is vital to understand what each index depicts [58].

IR is required to obtain continual estimates of aerosol composition and concentration from geostationary satellite data. While there is merit in utilising visible reflectances during the day and infrared at night, this was beyond the scope of this study which focussed exclusively on the infrared absorption. It is expected that these enhancements will eventually augment not replace the AOD estimates, predominantly at night when visible reflectances are not available. Dual-wavelength indices are required to filter aerosol incidents from background surface BT data and ultimately determine the composition, particle size, and concentration. The focus of the present study aimed to investigate which of the

three index types (BTD, NDDI, and RAT) are best at resolving aerosol type and then determine if there is an optimum set of dual wavelengths IR combinations that account for most of the aerosol compositional changes and are potentially universally applicable.

5.3. Methodology

5.3.1. Study data

Overview

The hemisphere viewed by Himawari-8 every ten minutes is centred at the equator and 140°East. The curvature of the globe reduces potential uses of Himawari-8 at the extremes of the viewing angle. MODIS products are given for a snapshot in time at the local time of about 10:30 AM for Terra and 1:30 PM for Aqua. The MODIS data highlights the difference in cloud cover across the hemisphere. Australia generally has lower cloud cover than Asia, which in turn has less cloud cover than the equatorial regions. The amount of cloud cover impacts on the ability to distinguish aerosols, as moisture has high absorption properties and therefore may invalidate estimates during high cloud cover. This discrepancy has potentially impacted the historical development of dust indices across different regions due to the different moisture levels in the atmosphere.

Three different sample types were used to compare the performance of three index types (BTD, NDDI, and RAT) of: a) 23 infrared spectra from a soil spectra library (i.e. the spectra that would be expected if these soils were blown into the air (and ignoring heating/cooling effects); b) 26 infrared band data associated with localised aerosol and cloud plumes obtained from a dust incident day (8 March 2017); and c) ten-minute infrared differences at a surface monitoring site in Port Hedland during the Australian financial year (July 2016 to June 2017).

The study area is a vast arid region spanning approximately 1,600 × 400 km^2 and encompassing the western half of the Pilbara region in Western Australia (see highlighted region in Figure 5-1). The Pilbara region is known for its resource extraction (mining) and pastoral (rangeland) industries. The environment is generally cloud-free but dusty. It has comparatively low vehicle usage but is

profoundly affected by local industry and experiences widespread regional fires and dust storms [17-19]. Despite high concentrations recorded by local monitoring, MODIS's remote sensing does not depict this as a region of high aerosol optical depth (AOD). The low AOD estimates could be due to difficulties in determining AOD over the highly reflecting desert surfaces [149] compounded by a potential misclassification of the land cover as shrubland instead of desert [260]. However, the aim of the study was not to determine the cause of the low AOD estimates over Australia, but to develop a method that could potentially augment the AOD estimates (predominantly at night when visible reflectances are not available), and to understand which infrared indices are best able to detect changing spectral differences - be that from particle size changes, moisture absorption, or compositional changes (marine, crustal etc.). There are no AERONET sites across the region, and only limited ambient monitoring is conducted in the region at mine sites and port operations (http://www.phicmonitoring.com.au/ and http://www.pilbarairon.com/dustmonitoring). Specifically, for this study over the Pilbara region, there was no speciated particulate matter data available to quantify and calibrate the dust indices.

USGS Soil Spectra Library

The first sample set was laboratory soil spectra from a spectral database. These samples were included as these spectra would be expected if the soils were blown into the air by the wind (ignoring heating and cooling effects). This phase of the study aimed to determine which index type could best resolve soil types using theoretical published data. It was not intended to demonstrate if the spectra could be used to distinguish soils of the region. Limited aerosol infrared spectral databases (or libraries) exist, with the majority of published spectra having an upper wavelength limit of 2.5 µm [252, 261]. The publicly available USGS soil database was used instead of the more regionally specific Australian NatSoils database, as the Australian database is not publicly available and it has limited IR soil data with an upper wavelength limit of 2.5 µm . Of the 2468 spectra of specific minerals, plants, chemical compounds, and artificial materials in the USGS Spectral Library Version 7, only 647 (26%) include the infrared range from 2.5 µm to 25 µm [252]. These 647 spectra of infrared wavelengths include 23

spectra from soils, and these soil spectra were selected and used for the analysis to evaluate infrared indices of pure soil types. USGS record numbers and soil descriptions from the USGS spectral database are supplied in Table 5-6. Although record numbers and descriptions were retained in the analysis, the spectral database was viewed as 23 independent soil samples, and no attempt was made to explain the results based on similarities across the soil types or to comment on the regions where those soil samples were obtained. An average absorbance was calculated across each of the wavelengths of the Himawari-8 infrared bands ($\Delta\lambda$ ~0.2 μm) from the narrow wavelength bands ($\Delta\lambda$ ~0. 005 μm) in the spectral library. The water vapour bands 8, 9, and 10 were explicitly excluded from the analysis as it was expected that the soils would have been pre-dried in the laboratory before analysis. Therefore, these three moisture bands would not be indicative of actual wind-blown sample spectra.

Potential aerosol plumes

The second sample set identified twenty-six points of interest within potential aerosol plumes using data from 8 March 2017 over the Pilbara region in Western Australia during which a significant dust storm occurred as a result of two air masses which collided and formed a roll cloud [248]. Using visual assessment of the satellite data, monitored meteorology, and the news report it appears that the case study data depicted coastal fog along the coastline in the morning which developed into crustal plumes blown inland, during the mid-morning. A wind reversal in the late afternoon (caused by the land-sea temperature imbalance) led to the near-surface movement of crustal material being blown towards the coast. This crustal material then collided with incoming, upper level, maritime air which generated a roll cloud at the front of the two air masses. The updrafts lifted soil into the cloud forming a dust storm [7, 248]. In addition to the storm, a large fire (verified by MODIS imagery) in the south-west of the region contributed smoke plumes into the airshed.

While temporal AOD changes (calculated using Himawari data) could potentially identify aerosol plumes during the day, this study sought to enhance the AOD determination by utilising infrared channels to allow the methodology to be extended to include air quality events that occur at night or early morning when

visible reflectance methods cannot be used. Band 7 (3.9 μm) was chosen to track potential plume changes as it has the most sensitive response to changes, due to its lower wavelength and is thus sensitive to both reflected and emitted spectral components. The subtraction of the spatial mean for each timestep minimised the reflected differences as only the heating/cooling difference is used not the absolute values. The enhanced sensitivity of band seven has been used to determine land and sea surface temperatures, detect fog, and fire events [58]. The movement of a plume creates a temporal variation in the BT data, which enables the path of the plume to be identified from the changes. These locations of change were identified by calculating the daily standard deviation of band 7 (3.9 μm) across the study domain. The natural log of the standard deviation was determined to minimise the changes caused by clouds (which cause significant cooling) and enhance areas of aerosol movement. The location of changes across the day of the incident is depicted in Figure 5-1 based on the natural log of the daily standard deviation.

Figure 5-1 illustrates some plume cone-like shapes, and these "cones" were used to select the locations of the twenty-six points. If these were traditional dispersion plumes of aerosols, higher concentrations would be expected at the narrow base of the cone, i.e. before dispersion diluted and mixed the aerosol into the surrounding background air. Therefore, a point at the base of the cone should provide a purer aerosol spectrum for analysis than one in the tail of the plume. Twenty-six points of interest (i.e. keeping a similar number of samples for both soil and plumes) were chosen from this diagram. These twenty-six points of interest were selected to identify homogenous regions of change (in time and space) and minimise background interferences and thus represent spectral properties of potentially different aerosol composition.

Transient brightness temperature changes at each of these twenty-six locations enabled a smaller time window to be identified where the plume's composition change was evident by changes to the BT. Plumes were identified where the BT changed to a temporal minimum over approximately an hour and exhibited localised plume dispersion properties consistent with changing wind direction rather than regional diurnal temperature changes. The motion of wind data (obtained from PHIC) [22] and successive data frames across the study domain

indicated the direction of movement (on/offshore). The direction of plume movement and initial plume location allowed possible aerosol source types (coastal or terrestrial) to be inferred. The labels in Table 5-2 are a guesstimate of the plume composition and not a categorical assertion and were used to identify spectral differences and classify the twenty-six plumes as potentially cloud or aerosol. Unlike the spectral database of soil types, these potential plumes are not pure compounds, and the spectra reflect multi-species components – moisture (i.e. clouds), aerosols (i.e. salt, crustal, smoke), and background soil-temperature changes. The smoke plume, for example, was identified by the rapidly moving plume (using 3.9 μm) of air that was hotter than the surroundings in the vicinity of the fire.

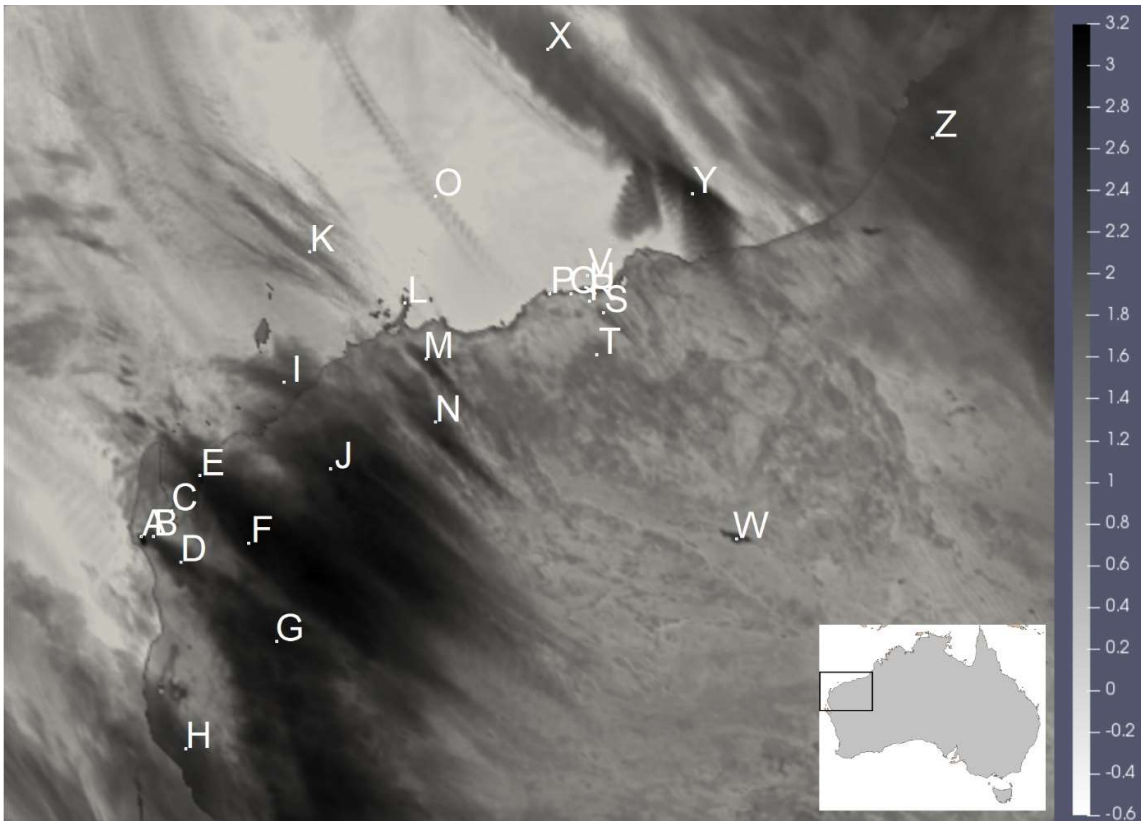

Figure 5-1: Potential plumes and points of interest identified from the daily standard deviation of band 7 (3. 9 μm) across the study domain. Scale is ln(standard deviation) in Kelvin.

Satellite data from these plumes allowed the different indices to be investigated under non-idealised conditions of multiple source types. The spatial mean land/sea temperature was subtracted from the BT for each time step in the data to reduce diurnal reflectance surface and sea temperature changes. While the initial analysis used band 7 (3.9 μm) to identify the plume location, all indices (i.e. all wavelengths) were investigated for each point in space and time then averaged, over the identified plume timespan, to reduce rounding-off errors.

Surface-monitored ground-level concentration data (site data)

In addition to the pure soil spectra and potential plumes, the study also considered air quality incidents (i.e. enhanced PM_{10} concentrations) and correlated these incidents with spectral changes in the remote sensing data during air quality incidents - as the purpose of this study was to investigate significant events, not background quantification of air quality. Ten-minute spectral data from the Himawari-8 satellite was matched in time with surface-monitored PM_{10} concentrations recorded at Port Hedland in Western Australia for the period 1 July 2016 to 31 June 2017. Only the highest thousand surface-monitored PM_{10} concentrations were retained to eliminate potential sensitivity to low concentrations from affecting the results (i.e. aerosol incidents were retained, not background averages). The paired satellite-site monitored data were used to determine how each of the three indices types (BTD, NDDI, RAT) compared in their ability to distinguish aerosols.

The spatial mean (30x30km^2) land/sea temperature was subtracted from the BT at the monitoring site for each time step in the data to reduce diurnal reflectance surface and sea temperature changes. The spectral data were then subsequently scaled by dividing by the monitored PM_{10} concentrations to account for differences in aerosol concentrations.

5.3.2. Statistical analysis

Variability assessment of principal components

Principal component analysis (PCA) [4, 262] was used to investigate each of the three index types (BTD, NDDI, RAT) and determine which index best resolves aerosol types. The "IBM Statistical Package for the Social Sciences" (SSPS) software package Version 25 was used for the PCA analysis. The three indices were standardised (to give equal weight to each index) by subtracting the mean and dividing by the standard deviation. Each satellite band (e.g. band 7) was analysed separately against the other bands (i.e. all bands less band 7). This resulted in ninety PCA analyses (3 sample types x 3 index types x 10 bands) dual-wavelength band combinations (n=9 per PCA analysis). The percentage variability accounted for was determined for each of the ninety analyses and used to compare the ability to resolve composition between the sample and index types. PCA was used to reduce the dimensionality of the spectral indices into fewer components and in so doing, enable an evaluation of the three indices' ability to differentiate between the different soil spectra and plume types. However, for both the soil and plumes matrices, the statistical analysis is ill-fitted with double the number of variables (3 indices types x 45 dual-bands) than cases. Therefore, an alternative method to PCA was investigated to determine the best dual-wavelength band combinations for separating cloud and aerosol plumes and ultimately determine aerosol composition.

Separating cloud and aerosol

In a separate analysis, the potential plumes were further categorised into cloud and aerosol-based on dual-band BT threshold differences over deserts and bright surfaces [234] and BT of band 7 (3.9 μm), which indicated significant (>20 K) cooling from clouds. The spatial mean was subtracted from the data for each time-period to minimise reflective components (i.e. average = zero for all time steps) in the spectral data and enhance the spatial adsorption differences. She et al., 2018 was used as a comparison base as it was a recent study using the same Himawari data but for a different location (China not Australia). This study does not compare their methodology to other literature but was used to illustrate how localised

effects can impact the applicability of indices between regions. The standard deviation and mean were calculated for the cloud and aerosol types individually for the potential plumes to indicate both separation (difference of means) and variability (standard deviation of aerosol types) for each of the 45 indices across the three indices types (BTD, NDDI, and RAT). This was undertaken to determine which of the three indices types best separated the different aerosol and cloud types.

This difference of means between the cloud and aerosol clusters and variability within the aerosol cluster was then refined to each of the 45 BTD indices individually to determine the threshold (i.e. the midpoint between the cloud and aerosol clusters), resolution (the distance from the midpoint to the first/last aerosol/cloud type), and correlation of the indices and determine the ability of each index to separate clouds and aerosol plumes. The two least correlated of the non-overlapping cloud and aerosol clusters were chosen as the best BTD indices, following which the next three least correlated of all remaining indices (excluding indices that used the preceding four wavelengths) were selected to return a total of five optimum dust indices.

Evaluating selected indices

Lastly, these five "optimum" dust indices were plotted for the entire Himawari monitoring area. Differences across these indices were examined in the context of the characteristic wavelengths used by each index. Scatter plots were used to identify relationships and outliers across multiple parameters, (matching Terra's overpass on 8 March 2017), across the study region, to determine if the indices correlated between each other - which could indicate a gradual temporal transition from one aerosol type to another, or if the scatter plots were widely dispersed - indicating multi-component influences from aerosol composition, particle size and water adsorption.

It is suggested that a time-varying threshold might be better at identifying aerosol plumes than fixed threshold limits. For the Pilbara region, these fixed thresholds appear to be based on the mean less one standard deviation. Histograms of the indices were prepared to determine the spread of the data and relationships

between the indices. The temporal histogram variation was studied for the first index (potentially moisture index) to determine if inflection points in the distributions may indicate threshold levels instead of using a location-specific threshold.

5.4. Results

5.4.1. Analysis of the three sample matrices (soil, plumes, monitoring)

The average absorbance for each of the Himawari-8 infrared bands (excluding the water vapour bands 8, 9, and 10) is given in Table 5-1 for each soil type described in the USGS Spectral Library Version 7 and Table 5-2 for potential cloud and aerosol plumes. Table 5-1, therefore, depicts data which was averaged across narrow wavelength bands from pure spectrum soil type components in the spectral database, in contrast to Table 5-2 which represents information that was averaged in space and time from the measured satellite wavelength bands of potential plumes.

Figure 5-2 reflects the ability of dual-band differences to distinguish aerosol plumes from clouds, based on indices (X and Y chart labels) described in She et al. (2018). Only $BTD_{11\text{-}12\,\mu m}$ (y-axis in both graphs) correctly ascribes the aerosol and clouds into the correct categories. Neither clouds nor aerosols are separated (x-axis) using the $BTD_{3.9\text{-}11\,\mu m}$ or $BTD_{11\text{-}8.6\,\mu m}$ indices, and this indicates that compositional differences (potentially moisture or particle size fraction) are potentially responsible for the difference indices between She et al.'s study region (China) compared to this study region (north-western Australia) and are not necessarily directly applicable between regions unless the compositional differences are also taken into account. Moisture in the clouds exhibited large negative brightness temperatures (BT) relative to average land BT (i.e. < -20 K for band 7, 3.9 µm) and this independently confirmed the aerosol plumes to be distinct from clouds. The fire is discernible by the sizeable thermal radiation emitted from the fire in band 7 (3.9 µm) which is greater than 20 K hotter than the surrounding land surface brightness temperature.

From the preliminary categorisation of the plumes (based on the large negative BT in band 7), it is apparent that aerosol plumes and clouds in Figure 5-2 form two separate categories. Clouds are dispersed across the two graphs (across both the X and Y axis) while aerosol plumes have low variability and are an indication that the composition of aerosol plumes are similar in this study (predominantly wind-blown dust). Some potential aerosol plumes could be clouds (e.g. crustal and offshore in Figure 5-2b). This is an expected normal result as clouds may consist of pure water, but aerosols are unlikely to be dry (i.e. zero moisture) [58].

Variability assessment of principal component

The percentage variance explained by the first principal component for each sample type (soil, plume, site) and index types (NDDI, BTD, RAT) using each band against all the other bands is given in Figure 5-3. The plume and site samples showed a slight increase in explained variance for the water bands (which were excluded in the soil analysis). Similar results (percentage variance) for all index types were apparent in the soil samples. NDDI and BTD yielded comparable results for the aerosol bands (but NDDI explained less of the variance for the water bands) in the plume samples. In contrast, only BTD explained at least fifty percent of the variance at the sampling site across all bands. Therefore, considering all three sample types, BTD performs slightly better than the other two indices.

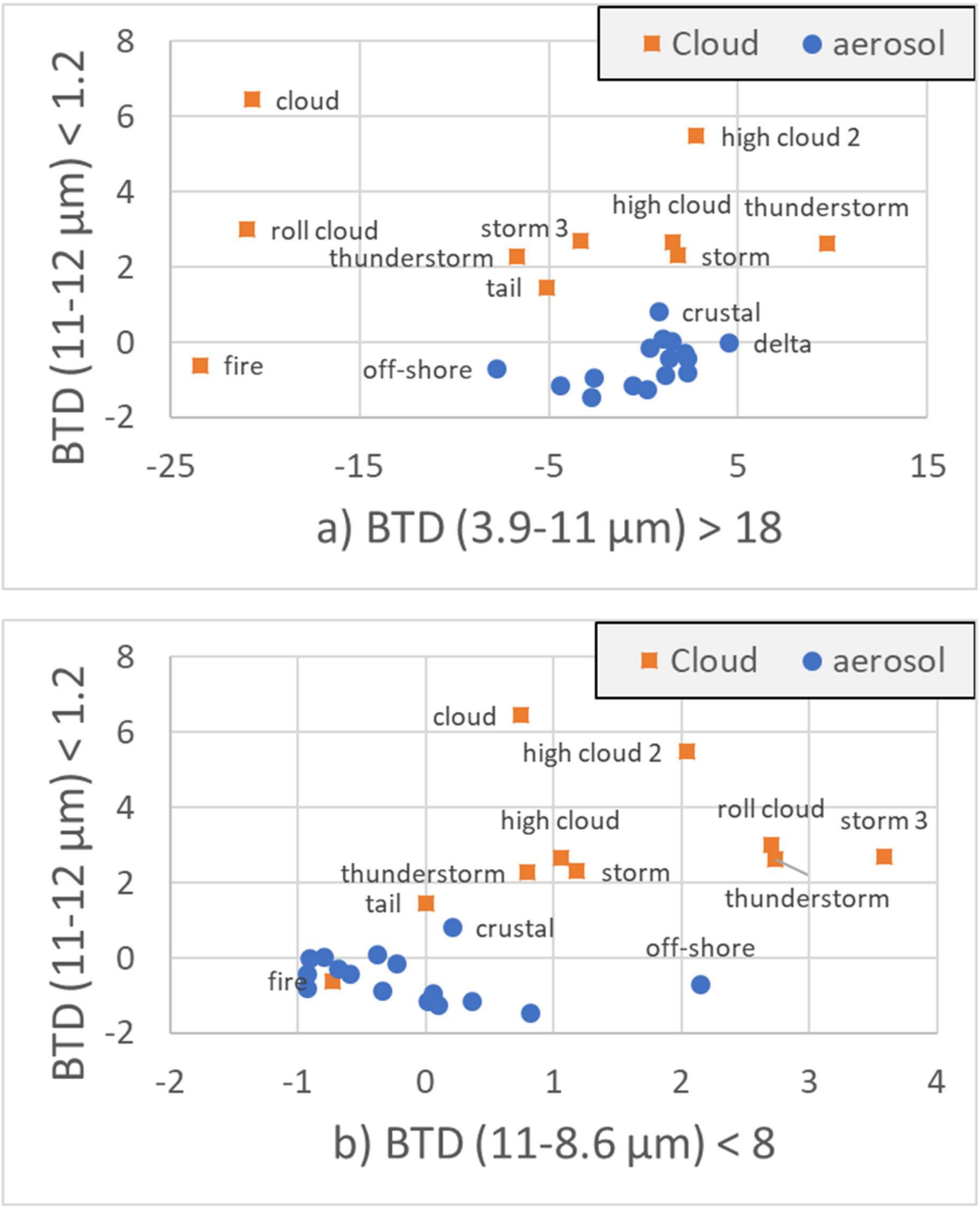

Figure 5-2: Scatter plots of She's et al. (2018) BTD indices (in Kelvin) depicting the separation of cloud and aerosol plumes over arid and semiarid regions with threshold values given on the axis title. Aerosol plumes are not fully labelled to prevent overlapping.

Table 5-1: USGS spectral absorbances averaged across each of the Himawari-8 seven infrared wavelength bands (mean ± standard deviation).

Central λ (μm)		3.885	8.593	9.637	10.407	11.24	12.381	13.281
USGS number	Band	7	11	12	13	14	15	16
11751		0.274 ±0.0029	0.076 ±0.0254	0.11 ±0.0127	0.025 ±0.0029	0.034 ±0.0013	0.014 ±0.002	0.012 ±0.0011
11831		0.404 ±0.0052	0.067 ±0.0154	0.064 ±0.0022	0.104 ±0.0015	0.082 ±0.0016	0.035 ±0.0036	0.012 ±0.0005
11869		0.173 ±0.0042	0.032 ±0.0052	0.055 ±0.0037	0.022 ±0.0022	0.024 ±0.0002	0.019 ±0.0003	0.015 ±0.0002
12101		0.099 ±0.0038	0.017 ±0.0035	0.092 ±0.001	0.07 ±0.0058	0.048 ±0.0009	0.026 ±0.0017	0.015 ±0.0006
12240		0.638 ±0.0046	0.131 ±0.0169	0.104 ±0.0212	0.2 ±0.0121	0.151 ±0.0039	0.093 ±0.0048	0.076 ±0.003
12291		0.205 ±0.0017	0.125 ±0.0096	0.121 ±0.0017	0.107 ±0.0066	0.065 ±0.0048	0.032 ±0.0055	0.041 ±0.0007
12330		0.064 ±0.0007	0.062 ±0.0001	0.064 ±0.0005	0.075 ±0.0011	0.08 ±0.0002	0.078 ±0.0001	0.08 ±0.0001
12415		0.281 ±0.0085	0.021 ±0.0003	0.043 ±0.0015	0.038 ±0.002	0.043 ±0.0005	0.019 ±0.0036	0.014 ±0.0002
12435		0.352 ±0.0036	0.025 ±0.0003	0.05 ±0.0016	0.067 ±0.0044	0.073 ±0.0018	0.02 ±0.0045	0.016 ±0.0005
12520		0.231 ±0.0026	0.009 ±0.0047	0.026 ±0.0019	0.007 ±0.0017	0.014 ±0.0012	0.007 ±0.0018	0.004 ±0.0003
12676		0.321 ±0.0491	0.062 ±0.0042	0.048 ±0.0024	0.035 ±0.0005	0.042 ±0.0012	0.026 ±0.0013	0.037 ±0.0004
12696		0.328 ±0.0054	0.046 ±0.0032	0.046 ±0.0031	0.028 ±0.0018	0.031 ±0.0006	0.015 ±0.0016	0.02 ±0.0002
12723		0.451 ±0.0062	0.04 ±0.0022	0.039 ±0.0025	0.032 ±0.0037	0.04 ±0.0031	0.016 ±0.0027	0.025 ±0.0003
12743		0.277 ±0.0091	0.034 ±0.0043	0.051 ±0.0051	0.021 ±0.0017	0.025 ±0.0004	0.011 ±0.0012	0.012 ±0.0001
12803		0.136 ±0.0411	0.071 ±0.0036	0.035 ±0.0017	0.044 ±0.0057	0.043 ±0.0104	0.049 ±0.0037	0.014 ±0.0033
12836		0.155 ±0.0114	0.014 ±0.0104	0.066 ±0.0068	0.037 ±0.004	0.053 ±0.0003	0.036 ±0.0033	0.021 ±0.0014
12857		0.481 ±0.0057	0.138 ±0.0085	0.156 ±0.0065	0.071 ±0.0061	0.046 ±0.001	0.027 ±0.0026	0.028 ±0.0017
12901		0.401 ±0.0095	0.022 ±0.0015	0.036 ±0.0005	0.056 ±0.0052	0.07 ±0.0011	0.021 ±0.002	0.017 ±0.0004
13054		0.233 ±0.0029	0.052 ±0.0158	0.132 ±0.0117	0.086 ±0.0089	0.062 ±0.0035	0.04 ±0.0023	0.029 ±0.0004
13285		0.681 ±0.0043	0.12 ±0.0141	0.127 ±0.0053	0.094 ±0.0055	0.126 ±0.0005	0.035 ±0.0005	0.036 ±0.0008
13321		0.381 ±0.0047	0.068 ±0.014	0.157 ±0.0084	0.071 ±0.0054	0.037 ±0.001	0.019 ±0.0005	0.025 ±0.0013
13341		0.042 ±0.0007	0.021 ±0.0002	0.022 ±0.0006	0.034 ±0.0003	0.022 ±0.0004	0.024 ±0.0003	0.022 ±0.0002
13399		0.252 ±0.0038	0.065 ±0.001	0.041 ±0.0013	0.03 ±0.0005	0.028 ±0.0006	0.019 ±0.0008	0.011 ±0.0006

Table 5-2: Brightness temperature (relative to land/sea) of potential (as classified by the authors) cloud and aerosol plumes (mean ± standard deviation) in Kelvin for each of the ten Himawari-8 wavelength bands.

Label	Probable source	Band 7 3.9 μm	Band 8 6.2 μm	Band 9 6.9 μm	Band 10 7.3 μm	Band 11 8.6 μm	Band 12 9.6 μm	Band 13 10.4 μm	Band 14 11.2 μm	Band 15 12.4 μm	Band 16 13.3 μm	Data (x,y,t_0,t_1,time)[1]
Possibly aerosol												
B	smoke	5.4±0.31	3.5±0.22	3±0.22	2±0.21	6.9±0.45	3.9±0.32	7.2±0.56	7.6±0.6	7.3±0.59	5.1±0.51	(64,228,66,72,20)
C	thin plume	7.6±0.48	4±0.54	4±0.6	3.5±0.7	9±0.44	5.7±0.23	9.5±0.48	9.9±0.57	9.1±0.7	6.2±0.67	(72,217,57,74,20)
D	tail smoke	4.8±0.45	3.6±0.41	3.1±0.42	1.7±0.44	6.5±0.53	3.5±0.32	6.6±0.58	7.1±0.69	6.7±0.76	4.9±0.59	(76,239,62,78,21)
G	condense	2.9±0.33	0.9±0.47	-0.2±0.33	-1.7±0.21	3.3±0.4	1.8±0.28	3.9±0.53	4.3±0.56	3.8±0.59	2.3±0.53	(117,273,94,104,1)
I	off-shore	-9±4.59	3.9±0.17	1.7±0.35	-2.9±1.1	-15±6.79	-11±4.78	-15±6.84	-17±7	-18±6.44	-13±4.01	(120,162,103,110,2)
K	maritime	2±0.1	2.2±0.26	2.3±0.24	1.7±0.39	2.1±0.14	1.2±0.08	2.2±0.13	2.3±0.22	2.2±0.32	1.4±0.31	(131,106,72,81,21)
L	Karratha	10±0.38	2.6±0.27	3.9±0.22	4.6±0.47	9.7±0.42	6.5±0.29	9.5±0.44	9.4±0.49	8.2±0.58	5.8±0.51	(172,128,65,79,21)
M	storm 2	9.1±0.67	3.3±0.84	4.1±0.6	3.8±0.37	9.4±0.63	6.2±0.42	9.3±0.59	9.3±0.69	8±0.74	5.6±0.49	(181,152,71,83,21)
O	maritime2	2.3±0.1	1.5±0.17	2.6±0.15	3.1±0.16	2.9±0.12	2.2±0.08	3±0.14	3.3±0.17	3.4±0.19	2.8±0.25	(185,82,103,117,3)
P	delta	1.3±0.41	-0.9±0.31	0.2±0.42	1.7±0.31	4.9±0.34	3.8±0.22	5.3±0.35	5.8±0.4	5.8±0.38	4.3±0.26	(234,124,0,10,9)
Q	sea spray	10±0.92	1.5±0.12	2.6±0.21	3.9±0.26	7.7±0.57	5.8±0.43	7.9±0.51	7.6±0.49	6.7±0.49	4.1±0.46	(243,124,30,37,14)
R	squall	8.5±0.23	1.5±0.1	3.1±0.15	4.7±0.15	9.3±0.26	7±0.18	9.5±0.35	9.6±0.39	8.8±0.34	6.5±0.24	(251,127,66,74,20)
S	crustal 2	3.7±0.4	-2.5±0.57	-1.3±0.35	-0.8±0.19	1.7±0.21	2.2±0.19	1.8±0.21	0.9±0.13	-0.6±0.09	-0.8±0.22	(257,132,6,14,10)
T	crustal	-6.2±0.21	-0.7±0.14	-0.2±0.13	0±0.15	-5.2±0.32	-3.4±0.2	-5.6±0.31	-5.4±0.35	-4.6±0.36	-2±0.21	(254,150,15,25,12)
U	Port Hedland	13±0.85	0.9±0.16	2.2±0.13	3.3±0.19	8.8±0.43	6.7±0.49	9.2±0.53	8.8±0.53	7.6±0.49	4.7±0.39	(251,122,20,30,13)
V	off-shore 2	4.3±0.21	1.4±0.3	2.7±0.34	3.7±0.35	5±0.32	3.6±0.23	5.2±0.36	5.8±0.41	5.8±0.44	4.3±0.39	(250,116,118,130,5)
Possibly fire and clouds -separated according to She et al. (2018) and Band 7 (3.9 μm)												
A	Fire[(2)]	31±18	1±0.49	1.6±0.4	1.2±0.37	7.3±1.27	4.5±1.03	7.7±1.21	8±1	7.4±0.67	4.9±0.45	(59,228,86,91,23)
E	residual storm	-20±2.74	2.4±0.24	0.4±0.28	-4.3±0.42	-24±1.53	-17±1.14	-24±1.59	-26±1.23	-24±0.84	-16±0.44	(84,202,109,114,3)
F	storm	-30±3.49	1.1±0.26	-1.1±0.21	-6.1±0.43	-27±1.93	-19±1.37	-28±2.12	-28±1.87	-26±1.53	-18±1.03	(105,231,93,115,3)
H	cloud	-31±2.62	0.2±0.37	-3.5±0.39	-11±0.6	-49±1.94	-36±1.35	-53±2.02	-52±1.69	-45±1.24	-29±0.92	(78,319,17,34,13)
J	roll cloud	-55±16	-28±4.4	-37±4.93	-44±4.77	-73±5.76	-48±3.45	-75±5.68	-76±5.84	-73±5.7	-58±5.15	(140,199,57,64,18)
N	storm 3	-33±13	-4.9±6.05	-7.7±8.09	-13±9.29	-34±13	-24±9.04	-36±14	-37±14	-34±13	-24±11	(185,179,56,69,19)
W	thunderstorm	-20±0.26	-2.3±0.34	-2.2±0.2	-0.7±0.14	-8.9±0.35	-6.9±0.36	-11±0.47	-9.9±0.46	-7.3±0.37	-3±0.22	(314,229,15,25,12)
X	high cloud	-24±1.26	-2.9±0.62	-3±0.78	-3.3±0.86	-21±1.35	-15±0.91	-22±1.46	-22±1.54	-19±1.56	-12±1.42	(233,19,128,136,6)
Y	thunderstorm	-38±21	-12±3.66	-17±6.2	-22±9.25	-43±18	-29±12	-44±17	-45±17	-42±15	-32±12	(295,81,115,120,4)
Z	high cloud 2	-30±0.51	-4.8±0.26	-4.4±0.13	-1.6±0.11	-25±0.45	-18±0.36	-28±0.58	-27±0.57	-21±0.45	-9.3±0.21	(398,57,29,37,14)

Note [(1)] represents the block of data, (index location x=0-450,y=0-350, t_0=start frame, t_1 end frame, and time is local time) Fire[(2)] is not treated as a potential plume and was excluded from further analysis.

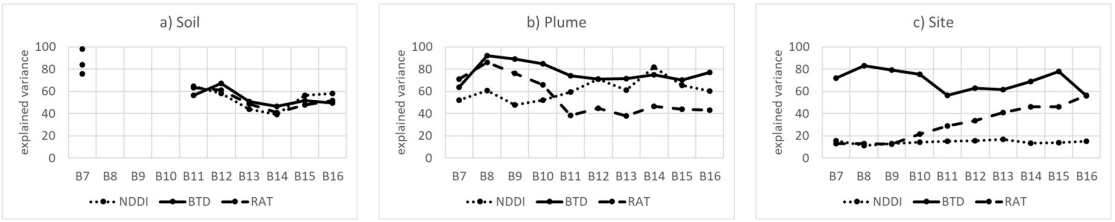

Figure 5-3: Variance explained by the first principal component for three sample matrices for each wavelength.

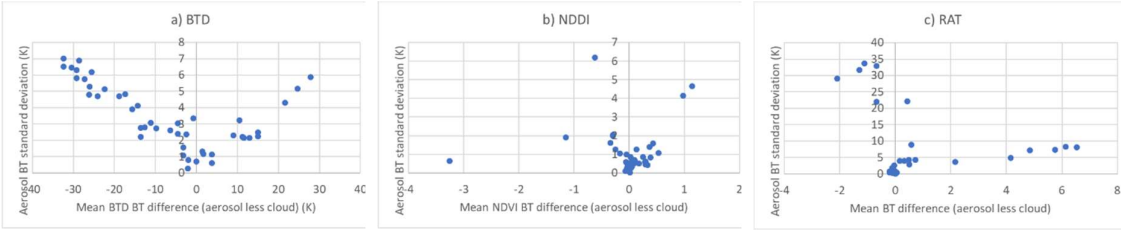

Figure 5-4: Aerosol differences (standard deviation) against cloud separation (difference of means) using the three indices (a) BTD, b) NDDI, and c) RAT).

Separation of cloud and aerosol

Table 5-3 depicts the separation between the 26 aerosol and cloud types which compares the aerosol spread (y-axis: standard deviation) against separation distance (x-axis: the difference of cloud and aerosol means) for each of the 45 indices (separate point) across each of the three index types (BTD, NDDI, RAT) (separate graph). Both NDDI and RAT showed a centralised cluster where there were minimal differences between the 45 wavelength indices. In contrast, the BTD analysis was more dispersed and had more variability between the 45 indices.

Table 5-3 expands the analysis, to consider only the BTD index type, and depicts the threshold (i.e. the midpoint between the cloud and aerosol clusters) and the resolution (the distance from the midpoint to the first/last aerosol/cloud type) of the aerosol and cloud clusters. Of the 45 BTD indices, only seven had non-overlapping aerosol and cloud clusters, and these seven BTD indices are presented in Table 5-3, with the columns sorted by descending resolution.

The correlation and covariance of these seven non-overlapping indices (Table 5-4) indicated that $BTD_{3.9\text{-}6.2\,\mu m}$ and $BTD_{11\text{-}12\,\mu m}$ had the least correlation (between the other six indices) and therefore potentially more independence. A subsequent plot

(Figure 5-7), depicts the relationship of the indices. These two indices ($BTD_{3.9\text{-}6.2\ \mu m}$ and $BTD_{11\text{-}12\ \mu m}$) are thus best able to describe changes in aerosol type. Figure 5-5 depicts the separation of cloud and aerosol for the 26 cloud and aerosol types and reflects an improvement (aerosol/cloud in the correct quadrant) over the separation obtained by She's et al. (2018) indices (Figure 5-2).

The correlation and covariance of the remaining indices (excluding the wavelengths used in the first two indices) are presented in the appendix (Table 5-5-7), again sorted in ascending correlation order. The first three indices were chosen, in addition to the previous two, and the aerosol separation based on the third and fourth indices is depicted in Figure 5-6.

Table 5-3: Seven BTD indices which separated clouds and aerosols. All BT measurements are in Kelvin.

	Statistic	$BTD_{3.9\text{-}6.9\ \mu m}$	$BTD_{3.9\text{-}7.3\ \mu m}$	$BTD_{3.9\text{-}6.2\ \mu m}$	$BTD_{10\text{-}13\ \mu m}$	$BTD_{8.6\text{-}13\ \mu m}$	$BTD_{11\text{-}13\ \mu m}$	$BTD_{11\text{-}12\ \mu m}$
Aerosol	mean	2.26	2.36	2.72	1.69	1.52	1.65	0.54
(n=16)	std	5.16	4.30	5.87	2.24	2.15	2.49	0.61
	min	-10.74	-6.26	-12.88	-3.60	-3.18	-4.75	-0.81
	max	11.02	9.87	12.25	4.52	4.09	4.08	1.47
Cloud	mean	-22.47	-19.21	-25.17	-13.33	-11.48	-13.35	-3.21
(n=9)	std	3.92	4.76	4.62	5.33	4.38	5.07	1.64
	min	-28.44	-27.44	-30.82	-24.15	-20.50	-23.20	-6.46
	max	-17.41	-10.98	-17.30	-7.79	-5.91	-6.96	-1.46
Analysis	difference	24.73	21.57	27.89	15.02	12.99	15.00	3.75
	threshold	-14.08	-8.62	-15.09	-5.69	-4.54	-5.86	-1.14
	resolution	3.33	2.36	2.21	2.09	1.36	1.11	0.32

Table 5-4: Correlation (top right) and covariance (bottom left) of the seven BTD combinations which separated cloud and aerosol.

	$BTD_{3.9\text{-}6.9\ \mu m}$	$BTD_{3.9\text{-}7.3\ \mu m}$	$BTD_{3.9\text{-}6.2\ \mu m}$	$BTD_{10\text{-}13\ \mu m}$	$BTD_{8.6\text{-}13\ \mu m}$	$BTD_{11\text{-}13\ \mu m}$	$BTD_{11\text{-}12\ \mu m}$
$BTD_{3.9\text{-}6.9\ \mu m}$		*0.96*	*0.99*	0.94	0.94	0.94	*0.60*
$BTD_{3.9\text{-}7.3\ \mu m}$	20		0.91	0.96	0.95	0.93	*0.71*
$BTD_{3.9\text{-}6.2\ \mu m}$	28	22		*0.91*	*0.91*	*0.92*	***0.55***
$BTD_{10\text{-}13\ \mu m}$	10	8.7	11		0.99	0.96	*0.75*
$BTD_{8.6\text{-}13\ \mu m}$	10	8.3	11	4.5		0.95	*0.76*
$BTD_{11\text{-}13\ \mu m}$	11	9.3	13	5.0	4.8		*0.55*
$BTD_{11\text{-}12\ \mu m}$	1.8	1.7	1.8	1.0	0.9	0.8	

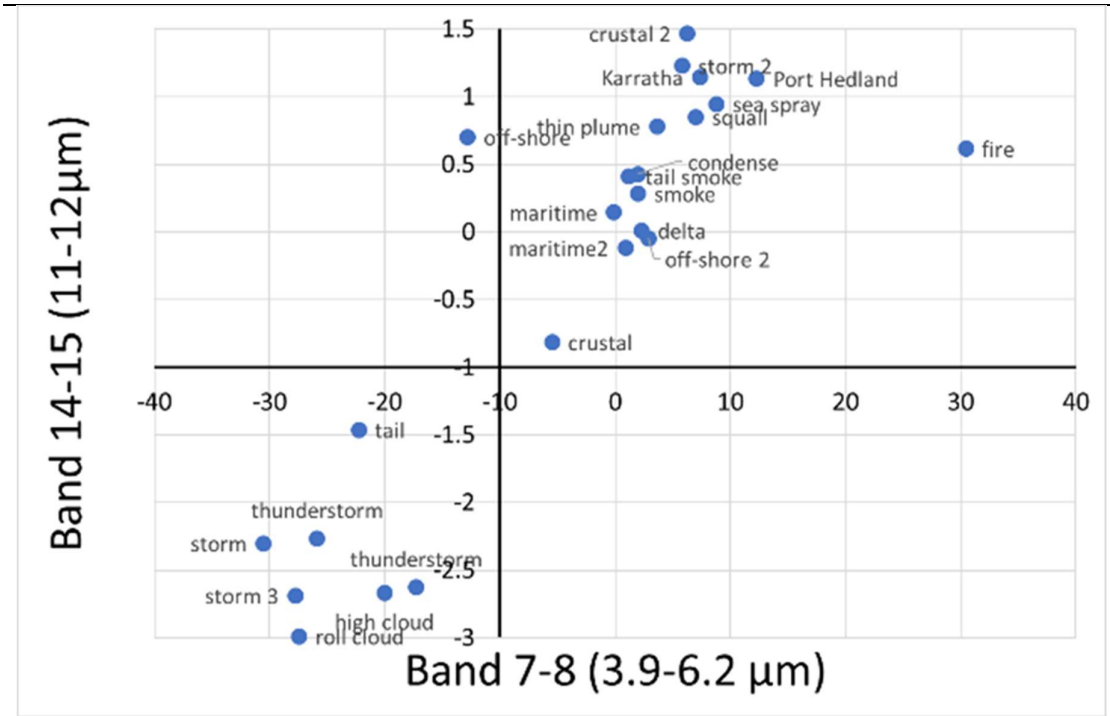

Figure 5-5: Separation of clouds (bottom left) and aerosols (top right) using $BTD_{3.9\ 6.2\ \mu m}$ and $BTD_{11\text{-}12\ \mu m}$. Axis indicate approximate threshold values.

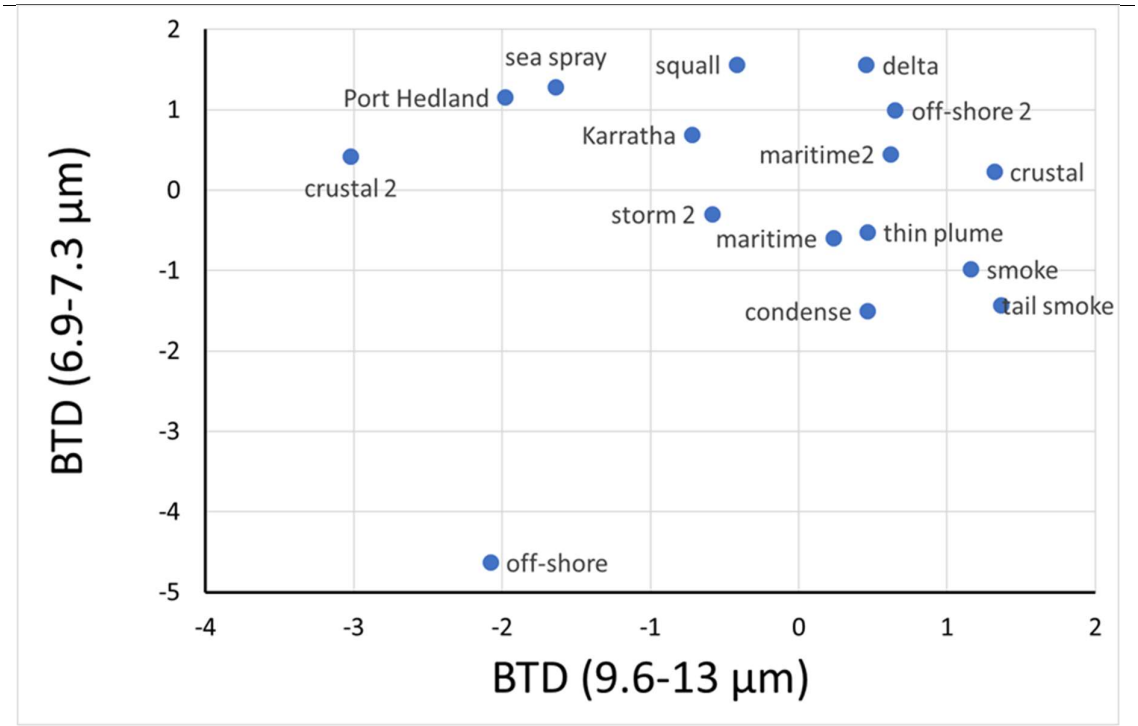

Figure 5-6: Separation of aerosols using $BTD_{9.6\text{-}13\ \mu m}$ and $BTD_{6.9\text{-}7.3\ \mu m}$.

These five indices selected were examined using principal component analysis, and the results of the analysis are depicted in Table 5-5. $BTD_{3.9\text{-}6.2\ \mu m}$, $BTD_{11\text{-}12\ \mu m}$ and $BTD_{8.6\text{-}10\ \mu m}$ are strongly represented in the first PCA component while $BTD_{6.9\text{-}7.3\ \mu m}$ and $BTD_{9.6\text{-}13\ \mu m}$ are strongly represented in the second component.

Table 5-5: Principal Component Score Coefficient Matrix and variance explained by the five BTD indices.

BTD index	**PCA 1**	**PCA 2**	**PCA 3**	**PCA 4**	**PCA 5**
$BTD_{3.9\text{-}6.2\ \mu m}$	***0.30***	-0.13	0.14	***2.06***	-0.72
$BTD_{6.9\text{-}7.3\ \mu m}$	-0.19	***0.53***	***-0.98***	***1.03***	0.46
$BTD_{8.6\text{-}10\ \mu m}$	***-0.30***	-0.10	***0.89***	***0.91***	***2.70***
$BTD_{11\text{-}12\ \mu m}$	***0.31***	0.13	-0.24	-0.41	***3.87***
$BTD_{9.6\text{-}13\ \mu m}$	0.11	***0.65***	***1.02***	-0.19	-0.89
% of variance	62.1	26.9	7.0	3.2	0.8
Cumulative %	62	89	96	99	100

Evaluation of selected indices

Differences between the five indices were attributed to the different IR spectral responses to aerosol particle size, water absorption, and aerosol composition. Figure 5-7 depicts the distribution (top plots) and scatter between the five indices. The multi-component nature of the sources is evident as distinct groups (or clusters) in the plots rather than smooth curves. The histograms indicate that most of the points are clustered at the mean rather than evenly distributed in contrast to the scatter plots where ignoring the central portion (mean) does not detract from the relationships.

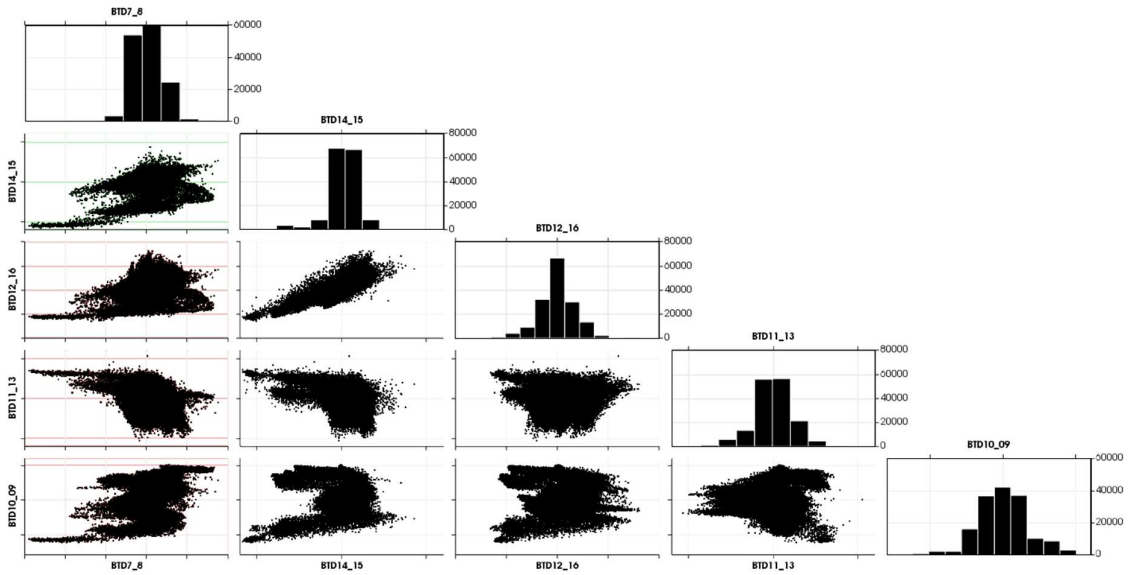

Figure 5-7: Plot matrix depicting histograms and scatter diagrams between pairs of indices at 10 AM on the 8 March 2017 over the Western Pilbara region of Australia.

The influence of the threshold to determine clouds was investigated by applying the indices to the entire Himawari hemisphere. In contrast to the first part of this study, the hemispherical analysis did not subtract the land/sea average temperatures in determining BTD indices because of the wide BT range expected across the domain. BTD $_{3.9\text{-}6.2\ \mu m}$ was used to assess the effect of the threshold limit on cloud cover. The histogram of the fraction of cloud cover for every ten minutes was studied, and it varied within an envelope defined by midday and midnight (UTC+8) as depicted in Figure 5-8. The inflection points, at about 20, 30 and 40 K, are potentially related to water phase changes, while the last inflection may indicate water/aerosol compositional changes. Figure 5-9 depicts the effect of applying a varying threshold (to the 10:30 AM data) and calculating the fraction of pixels remaining that were greater than that threshold. The first derivative of this fraction had a minimum at 62 K, which is the mean plus *half* the standard deviation. This 62 K threshold (i.e. Figure 5-10b) was used to remove cloud cover in Figure 5-10, which depicts the five dust indices coinciding with Terra's 10:30 AM overpass time.

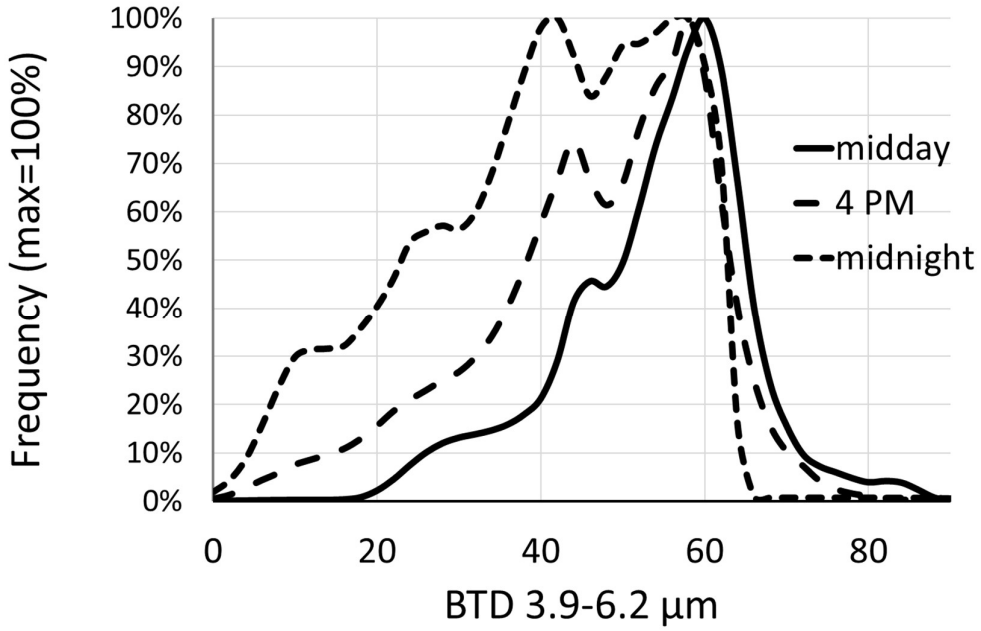

Figure 5-8: Histogram (standardised to max=100%) of BTD $_{3.9\text{-}6.2\ \mu m}$ at midday, 4 PM and midnight (UTC+8) on 8 March 2017.

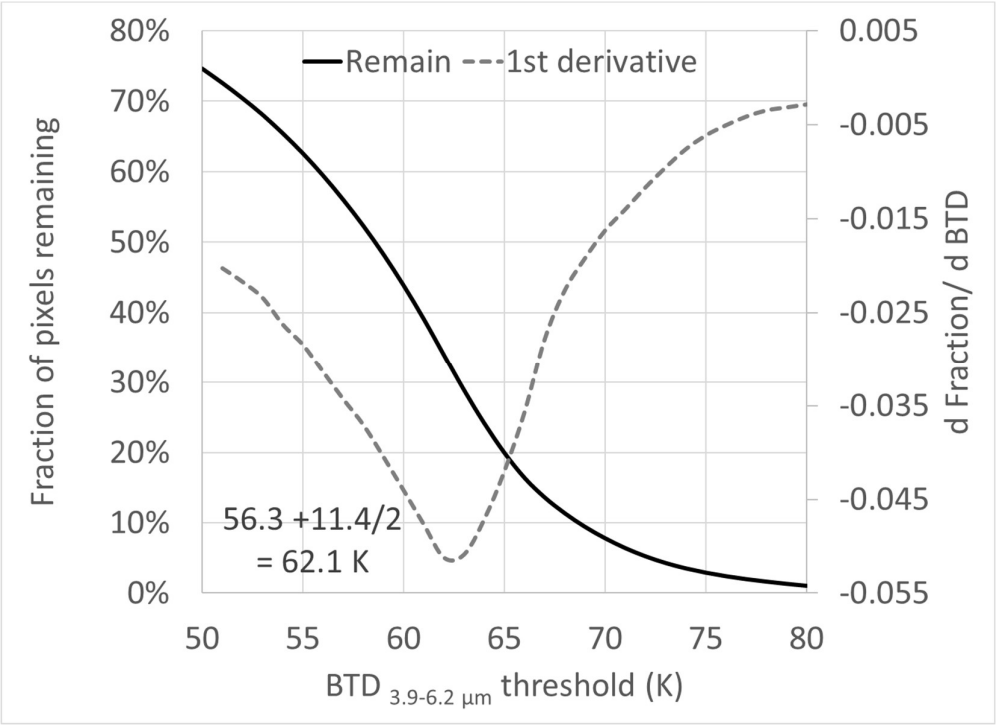

Figure 5-9: Fraction of pixels remaining and rate of change (first derivative) with different BTD thresholds at 10:30 AM (Terra) (UTC+8) on 8 March 2017.

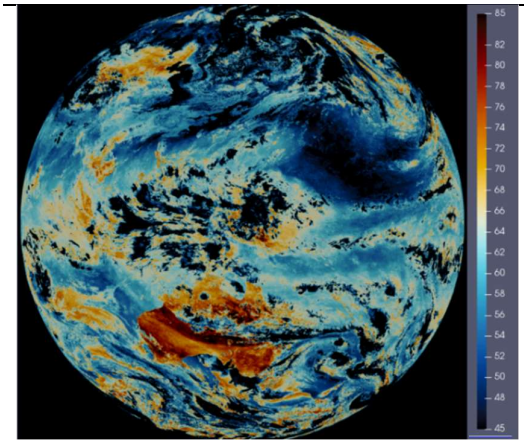

a) BTD 3.9-6.2 μm

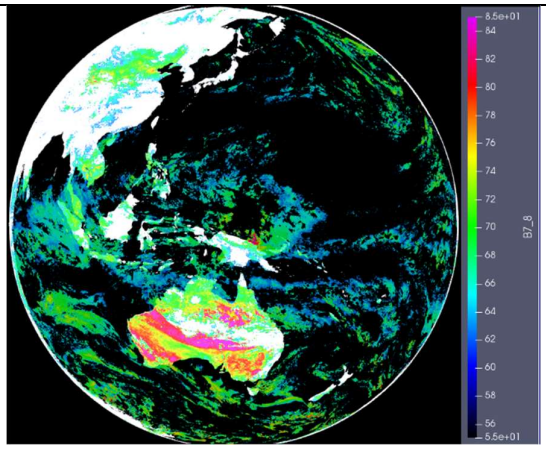

b) BTD 3.9-6.2 μm**,**
62 K threshold aerosol/moisture

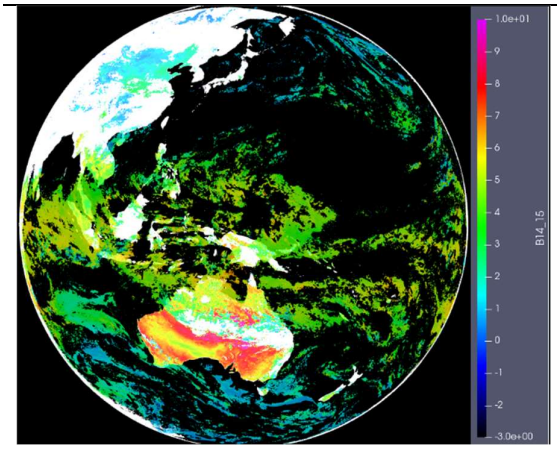

c) BTD 11-12 μm
particle size index

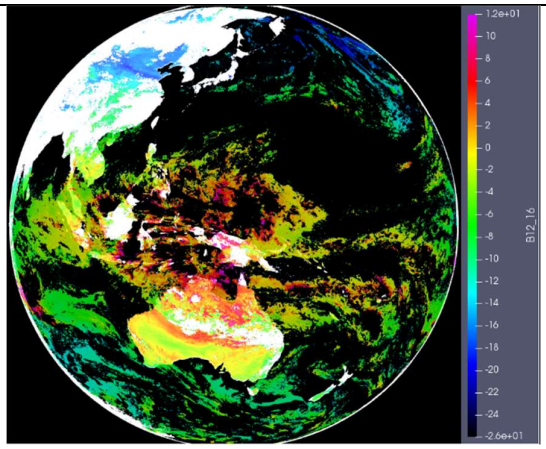

d) BTD 9.6-13 μm
O_3-CO_2 photochemical/oxidation

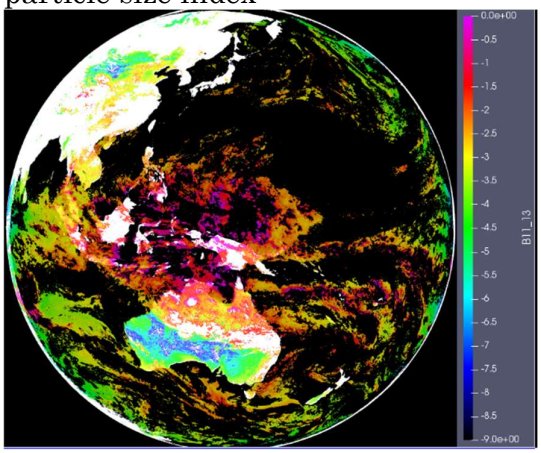

e) BTD 8.6-10 μm
sulphate – crustal index (& H_20)

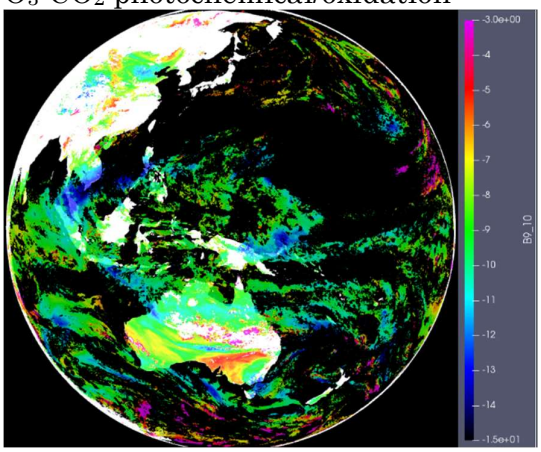

f) BTD 6.9-7.3 μm
atmospheric (in)stability

Figure 5-10: Dust indices over the full Himawari monitoring hemisphere, with cloud masking, 10:30 AM (UTC+8) 8 Mar 2017. Captions based on band characteristics [58].

5.5. Discussion

Analysis of study data

Few studies explain in detail why BTD is used for aerosol analysis in preference to NDDI, or other remote sensing indices, or the determination of threshold levels. In this regard, the results presented in Table 5-1 and Table 5-2 provide valuable background information on the infrared spectra of pure soils and potential plumes, respectively. Of the three thresholds described by She et al. (2018) to separate plumes into clouds and aerosols, only one satisfactorily classified all the 26 points of interest as clouds or aerosols. The inability of She's et al. (2018) indices to separate plumes into clouds and aerosols was possibly due to the similarities of the infrared (IR) spectra of the aerosol species of the region, and the known difficulties of indices, and thresholds, not being globally applicable. Evaluating the dust indices in a global context (Figure 5-10), highlights the different physical properties occurring between China (She et al. (2018)'s study area) and the Pilbara (this study area). As discussed by Schmit et al. (2018), it is vital that each characteristic wavelength used in the index be understood in determining the differences and thresholds of each index for different regions.

Variability assessment of principal component

The similarities of the USGS soil IR spectra resulted in the first principal component explaining a similar level of variability for all indices (NDDI, BTD, RAT) (Figure 5-3). The percentage variance explained by the first principal component for each index type of the potential plumes showed differences between the index types and according to the base component. NDDI was similar (60-80%) to BTD across the aerosol bands but explained less of the variability (~40%) for the water bands. RAT was comparable (60-80%) to BTD for bands seven and eight but worse (~40%) for all the others. Across all bands, BTD explained more of the variability for the potential plumes than other index types. The differences at the monitoring site can be ascribed to a combination of larger sample size (1000 points) and background thermal effects. Therefore, for all sample matrices (soil, plume, and site), the first principal component for BTD explains more of the variability than the other two index types. These differences were slight and reflected the

difficulties in determining the best index type using a limited IR database, categorising aerosol types on guestimates, and the unavailability of speciated surface monitored data.

Separation of cloud and aerosol

Seven indices of the total 45 BTD indices (see Table 5-3) were able to resolve clouds and aerosols into non-overlapping clusters. Two of these seven, BTD $_{3.9\text{-}6.2\,\mu m}$ and BTD $_{11\text{-}12\,\mu m}$ (one of She et al. (2018)'s indices), were selected as they had the lowest correlation of those seven indices and were expected to be more independent. The best of these indices at resolving the 26 plumes into clouds and aerosols, namely BTD $_{3.9\text{-}6.2\,\mu m}$, is not routinely used to distinguish between clouds and aerosols despite the recognised ability of $BT_{6.2\,\mu m}$ to detect upper atmospheric moisture. It is postulated that the low correlation between these two indices arises because BTD $_{11\text{-}12\,\mu m}$ is a known dust index while $BT_{6.2\,\mu m}$ may reflect the water content of the aerosol or cloud. Therefore, combining a dust index with a measure of water content may result in a better description of aerosol types than two dust indices.

The analysis of the cloud cover across the hemisphere showed that the threshold for cloud cover is better described by a temporary varying threshold of using half the BTD $_{3.9\text{-}6.2\,\mu m}$ standard deviation, as this removes thick cloud layers but retains more of the moisture effects in the indices. The importance of minimising the cloud "data gaps" is highlighted in that the conservative method, of subtracting half the standard deviation, still attributes ¾ rs of the data (across the hemisphere) to cloud.

Evaluation of selected indices

Spatially mapping the five indices demonstrated that each index behaved differently – as certain wavelength combinations may be more sensitive to the presence of water, particle size, or chemical composition. These differences were noted across both the Pilbara (initial study area depicted in Figure 5-1) and the hemisphere (Figure 5-10). The first index, BTD $_{3.9\text{-}6.2\,\mu m}$, uses the 3.9 µm band which is sensitive to most changes (fire, smoke, temperature) and subtracts the upper moisture band (6.2 µm) which is predominantly an indication of moisture, geopotential height, and cloud phase. The second index uses two aerosol bands (11

and 12 μm), and this minimises the similar moisture spectral response. The second index is therefore probably related to the Ångström exponent (i.e. particle sizes) or aerosol composition. The third index (BTD $_{9.6\text{-}13\ \mu m}$) is the difference between the ozone and CO_2 band and will indicate the photochemical and oxidative state of the atmosphere. The fourth index (BTD $_{8.6\text{-}10\ \mu m}$) uses the SO_2 band and a "clean aerosol band". Lastly, the fifth index (BTD $_{6.9\text{-}7.3\ \mu m}$) indicates lower atmospheric turbulence (and moisture) as it uses the lower and middle atmospheric water bands.

Using five indices may allow components that are not visible in one index to be observable in the other indices. While not typically used to detect smoke plumes due to the wavelength and non-detectable particle size of smoke, this study demonstrates that IR wavelengths may be able to be used to detect smoke plumes as these indices are not detecting aerosol types but the resultant spectral differences. A hot rising plume of smoke could initially have low moisture, due to the temperature of the fire, but these particles could absorb moisture from the atmosphere and be identified by the spectral response to BTD $_{3.9\text{-}6.2\ \mu m}$. Furthermore, the rising air could affect the vertical air movement, identified by BTD $_{6.9\text{-}7.3\ \mu m}$, despite potentially being transparent at BTD $_{11\text{-}12\ \mu m}$. Rising ash (large particle size) may indicate the initial spatial distribution of the smoke surrounding a fire as the larger ash particles would dissipate near to the fire.

Significant differences were noted for the dust indices across the globe (Figure 5-10). These changes reflect compositional differences and highlight the different physical properties that may occur between China and Australia and within smaller sub-regions. Neither a single index nor a global threshold can accurately determine aerosols because of the different aerosol composition, particle size and water adsorption properties which impact the spectral analysis.

5.6. Conclusions

The results of this study indicated that the arithmetically simpler BTD index is marginally better than both the NDDI and RAT indices at resolving both pure soil types and complex air plumes based on spectral differences. It was further confirmed, by analysing the resolution of the 45 dual-wavelength indices for each

of the three indices (BTD, NDDI, and RAT), that BTD is better than NDDI and RAT at resolving clouds and aerosols. However, the lack of speciated ground-level data precludes a definitive assertment that BTD is the best index type for determining aerosol compositional changes.

Analysis of each of the 45 BTD wavelength indices identified that only seven had non-overlapping cloud and aerosol clusters. Of these seven indices, $BTD_{6.2\ \mu m-3.9\ \mu m}$ and $BTD_{12.4\ \mu m-11.2\ \mu m}$ were selected as having the best ability to resolve cloud and aerosol types based on the least correlation, and therefore the most independence, between the two indices. The independence is a consequence of the first index being related to the water content of the aerosol while the second is a traditional dust index.

This study identified five indices that were based on minimising the correlation between selected indices. These five indices used different wavelength combinations and did not repeat or skip any of the ten available IR wavelengths available. Using each wavelength once, with five indices, maximises the probability of detecting aerosol compositional change, as every wavelength band is used, and minimises the number of potential indices (five vs 45). This study identified that moisture and composition influence all dust indices and that a generic singular index (and threshold) is regionally specific and that a combined set of indices that are globally applicable should rather be used. It suggests that a dynamic threshold based on half the standard deviation of the $BTD_{6.2\ \mu m-3.9\ \mu m}$ index may minimise cloud gaps and allow aerosol estimations during partly cloudy conditions.

It is therefore suggested that to determine aerosol composition requires using all of the IR wavelengths in the five indices proposed and understanding the impacts on each index due to chemical compositional changes. A follow-up study used these five BTD indices from the Himawari data to elucidate humidity, particle size, chemical composition and concentration using a pollution index [9].

5.7. Appendix

Table 5-6: Record numbers and soil descriptions from the United States Geological Survey (USGS) Spectral Library Version 7.

USGS record number	USGS soil description
11751	Alunite0.5+Kaol_Kga-1 AMX3
11831	Alunite_NH4+Jaro NMNH145596A
11869	Beidellite+Montmor GDS123
12101	Chabazite+Thom+Wair HS193.3B
12240	ClinozoisiteEpidote HS299.2B
12291	Cordierite-QtzMus HS346.3B
12330	Covellite-Pyrite HS477.2B
12415	Erionite+Merlinoite GDS144
12435	Erionite+Offretite GDS72
12520	Halloysite+Kaolinite CM29
12676	Kaolin/Smect KLF511 .12Kaol
12696	Kaolin_Smect H89-FR-2 .5Kao
12723	Kaolin_Smect KLF506 .95kaol
12743	Kaolin_Smect KLF508 .85Kaol
12803	Magnesite+Hydromag HS47.3B
12836	Mesolite+Hydroxyapop GDS6
12857	Microcline+others HS107.3B
12901	Mordenite+Clinopt. GDS151 u
13054	Natrolite+Zeolite HS168.3B
13285	Sanidine+albite NMNH103200
13321	Talc+Clinochlore HS327.3B
13341	Teepleite+Trona NMNH102798
13399	Zincite+Franklin HS147.3B

5.7.1. CDO operations

Linux command line, Climate Data Operators [216], were used extensively to extract and process the satellite data. Essential commands used for this paper are included below.

Land-sea masking

A land-sea mask was created by averaging the daytime reflectances over a year using band 4 (0.86 μm) and ignoring high cloud reflectances. This enabled a high-resolution mask, (i.e. 0 or 1) to be created over the area.

```
Cdo -s -gec,-0.04 -timmean -setmisstoc,0.5 -setvrange,-1,0.5 -sub year.nc -enlarge,year.nc -fldmean year.nc land.nc
```

A sea mask was created from the inverse of the land mask.

```
Cdo lec,0 land.nc sea.nc
```

To enable statistics (mean etc.) to be performed on the masked data, the zeros have to be first converted to missing values. However, when merging land and sea data together, the missing data must first be changed back to zero. This may be done either by a series of chained operations or by creating two new masked files for the missing data.

```
Cdo timmean -mul OBS.nc -setctomiss,0 sea.nc obs_sea.nc              #sea mask
cdo timmean -mul OBS.nc -setctomiss,0 land.nc obs_land.nc            #land mask
cdo add -setmisstoc,0 obs_land.nc -setmisstoc,0 obs_sea.nc obs_both.nc
#or create a new mask once, then use it
cdo setctomiss,0 sea.nc sea_miss.nc                  #sea missing mask
cdo setctomiss,0 land.nc land_miss.nc      #land missing mask
cdo timmean -mul OBS.nc sea_miss.nc obs_sea.nc                  #use sea missing mask
cdo timmean -mul OBS.nc land_miss.nc obs_land.nc                #use land missing mask
cdo add -setmisstoc,0 obs_land.nc -setmisstoc,0 obs_sea.nc obs_both.nc
```

Selecting a subset (time and/or space) of the data

```
cdo -seltimestep,0,25 -selindexbox,249,264,127,143 in.nc out.nc
```

Creating an index from primary channels and keeping existing channels

```
cdo -f nc -expr,"BTD7_8=B07-B08;BTD14_15=B14-B15;BTD10_09=B10-B09;BTD11_13=B11-B13;BTD12_16=B12-B16" in.nc tmp1.nc
cdo setrtoc,-1e99,-1,0 -setrtoc,-1,1,1 -setrtoc,2,1e99,2 -div -sub BTD.nc -enlarge,BTD.nc -fldmean BTD.nc -enlarge,BTD.nc -fldstd tmp1.nc tmp2.nc #set range based on mean and std
cdo -f nc -expr,"Atype=81*BTD7_8+27*BTD14_15+3*BTD11_13+9*BTD12_16" tmp2.nc out.nc
rm tmp?.nc
```

Table 5-5-7: Remainder of the BTD combinations correlation (top right) and covariance (bottom left).

	$BTD_{9.6-13}$	$BTD_{8.6-10}$	$BTD_{6.9-7.3}$	BTD_{10-13}	$BTD_{8.6-13}$	$BTD_{8.6-9.6}$	$BTD_{9.6-10}$	$BTD_{6.9-9.6}$	$BTD_{6.9-13}$	$BTD_{7.3-9.6}$	$BTD_{7.3-13}$	$BTD_{6.9-8.6}$	$BTD_{6.9-10}$	$BTD_{7.3-8.6}$	$BTD_{7.3-10}$	$BTD_{6.9-11}$
$BTD_{9.6-13}$		-0.01	0.01	0.31	0.32	-0.30	0.29	-0.02	-0.01	0.41	0.12	0.12	0.31	0.10	0.10	0.18
$BTD_{8.6-10}$	0.0		0.00	-0.36	-0.24	-0.24	0.35	0.40	0.28	0.36	0.39	0.34	0.26	0.28	0.32	0.31
$BTD_{6.9-7.3}$	0.0	0.0		-0.46	-0.48	-0.49	0.47	0.57	0.81	0.52	0.55	0.56	0.77	0.73	0.72	0.72
BTD_{10-13}	0.9	-0.2	-1.5		0.99	0.81	-0.82	-0.85	-0.79	-0.64	-0.87	-0.87	-0.65	-0.84	-0.84	-0.80
$BTD_{8.6-13}$	0.9	-0.1	-1.5	4.5		0.81	-0.81	-0.83	-0.79	-0.62	-0.86	-0.86	-0.64	-0.84	-0.84	-0.79
$BTD_{8.6-9.6}$	-0.8	-0.1	-1.5	3.6	3.5		-0.99	-0.83	-0.79	-0.88	-0.94	-0.94	-0.85	-0.91	-0.91	-0.91
$BTD_{9.6-10}$	0.8	0.2	1.5	-3.8	-3.6	-4.4		0.85	0.79	0.89	0.95	0.95	0.85	0.91	0.91	0.92
$BTD_{6.9-9.6}$	-0.1	0.3	2.3	-5.0	-4.7	-4.6	4.9		0.94	0.90	0.97	0.97	0.89	0.95	0.95	0.94
$BTD_{6.9-13}$	-0.1	0.3	4.6	-6.5	-6.2	-6.2	6.4	9.6		0.85	0.91	0.92	0.95	0.97	0.97	0.96
$BTD_{7.3-9.6}$	1.6	0.3	2.4	-4.1	-3.8	-5.4	5.7	7.2	10		0.93	0.93	0.95	0.91	0.91	0.94
$BTD_{7.3-13}$	0.7	0.5	3.9	-8.8	-8.3	-9.0	9.5	12	16	13		1.00	0.91	0.97	0.97	0.97
$BTD_{6.9-8.6}$	0.7	0.4	3.9	-8.6	-8.2	-8.9	9.3	12	16	13	21		0.91	0.97	0.98	0.97
$BTD_{6.9-10}$	1.6	0.3	4.7	-5.6	-5.3	-7.0	7.2	10	14	11	17	17		0.96	0.96	0.97
$BTD_{7.3-8.6}$	0.7	0.4	6.2	-10	-9.7	-10	11	14	20	15	25	25	21		1.00	1.00
$BTD_{7.3-10}$	0.7	0.5	6.2	-10	-9.8	-11	11	15	21	15	26	25	21	31		1.00
$BTD_{6.9-11}$	1.4	0.5	6.7	-11	-10	-12	12	16	22	17	28	27	24	34	34.3	

6. Composition

Sowden, M., D. Blake, D.D. Cohen, A. Atanacio and U. Mueller.
2020. Development of an infrared pollution index to identify ground-level compositional, particle size, and humidity changes using Himawari-8. Atmospheric Environment, 2020 117435.

6.1. Abstract

Speciated air quality data informs health studies and quantitates impacts. However, monitoring is concentrated around populated regions whilst, large remote and rural regions remain unmonitored despite risks of dust-storms or wild-fires. Sub-hourly, infrared, geostationary data, such as the ten-minute data from Himawari 8, could potentially be used to quantify regional air quality continually. Monitoring of Aerosol Optical Depth (AOD) is restricted to visible spectra (i.e. daytime only), while newer quantification methods using geostationary infrared (IR) data have focused on detecting the presence, or absence, of an event. Limited attention has been given to the determination of particle size and aerosol composition (such as sulfates, black carbon, sea-salt, and mineral dust), using IR exclusively, and more appropriate methods are required to improve the understanding of source impacts.

Hourly data were collected for a three-year study period (July 2015 to July 2018) across the greater Sydney region in Eastern Australia from seventeen ground-based sites that measured meteorological data and quantified ambient concentrations of NO, NO_2, SO_2, $PM_{2.5}$, PM_{10}, and O_3. This data was combined with source-apportioned categories (soil, sea-spray, smoke, secondary sulfates, and vehicles) from positive matrix factorization (PMF) of elemental aerosol collected on daily filters at five monitoring sites across the region. Regression analysis of five brightness temperature difference (BTD) infrared indices were used to determine a pollution index.

The pollution index was shown to be related to humidity, particle size, and compositional changes. Unlike fixed thresholds, the continual index function can be aggregated spatially and temporarily. Good resolution is obtained between $PM_{2.5}$

and O_3. BTD appears insensitive to concentration, and the pollution index was used to detect and identify composition prior to determining concentration.

Keywords: aerosol; Himawari-8; infrared; ground-level-concentration.

6.2. Introduction

The World Health Organization (WHO) estimates that globally 12.6 million deaths each year are attributable to unhealthy environments. Air pollution, both indoor (4.26 million deaths) and outdoor (3.73 million deaths) is a significant environmental factor in these deaths [263, 264]. The National Environment Protection Measure for Ambient Air (Air NEPM) sets national standards for six criteria air pollutants to which most Australians are exposed: carbon monoxide, ozone, sulfur dioxide, nitrogen dioxide, lead, and particulates [265].

Particulate matter is a significant criteria pollutant as it is ubiquitous and occurs at high concentration levels [266]. Particulate matter (PM) health effects include respiratory, lung cancer, and adverse cardiovascular effects [232, 267-271]. There is some debate about the significance of size fractions of PM and whether specific sources (i.e. composition) of air pollution are more important than others [231, 272, 273]. Urbanization, coupled with increased affluence, leads to an increase in vehicles and industrial activities with concurrent increases in ambient particulate levels [274, 275]. Additionally, geogenic emissions from fires [276] and wind-blown events [277] contribute to the ubiquity of PM events in populated, arid, and forested regions. The composition (and indirectly health impacts) of air pollution are dependent on the source, e.g. desert dust is principally crustal but may include biological material [231] while smoke from wildfires is chiefly organic, but may include inorganic compounds [232].

6.2.1. Surface monitoring requirements

Various methods have been used to estimate, predict, or measure airborne contaminant concentrations in order to quantify the population exposure [12]. Ambient monitoring using fixed locations provides reliable concentration data, often spanning decades. However, monitoring sites may be sparsely distributed in regional areas because of cost and infrastructure (power, cooling, and security)

limitations [13, 14] and situated according to population, rather than areas of risk [15].

Methods to determine concentration must have sufficient spatial and temporal resolution to accurately represent an event (typically minutes to hours or days) [278, 279]. The optimum monitoring interval is on the cusp of the turbulent zone, i.e. five to ten minutes, for air quality events, to achieve reproducible results and simultaneously be fast enough to detect those events [7]. Despite this temporal requirement, the accredited PM sampling method [167, 168] draws a predetermined volume of air over a daily period through a size-selective inlet and captures the total mass on a filter, which reduces short-term incident information to a smoothed daily average.

In contrast, electronic monitors, such as Beta attenuation monitors, record hourly or sub-hourly data [280]. Health-related studies suggest that the minimum requirements for monitoring atmospheric events are a spatial resolution of one kilometer and a temporal resolution of an hour [167, 168]. However, airborne concentrations may be below detection limits, even using twenty-four-hour filter samples [23]. Sophisticated analysis techniques such as accelerator-based ion beam analysis techniques [281] may be required to detect pollutants at those low concentration levels on small microgram samples.

6.2.2. Accuracy of estimations

In areas without dedicated monitoring, it may be possible to estimate concentrations using dispersion modelling [282] or remote sensing [11] and infer compositions based on the source [28, 84, 283]. Dispersion modelling takes the estimated emission from each source and disperses the pollutants according to parameterizations of the prevailing meteorology [31, 32].

For a simple source in flat terrain, dispersion modelling is very accurate. The US-EPA indicates the error margin to be a factor of two using period summations (maximum hourly daily and annual averages) and quantile plots [26]. Validation studies have identified where models successfully replicated annual averages and maxima but failed on paired hourly studies [284]. Most of the predicted

inaccuracies lie with the input data assumptions [285]. When including a large domain, with multiple natural sources and summating small wind field errors over hundreds of kilometres, the errors rapidly increase and make dispersion modelling unsuitable over large regions [286].

6.2.3. Remote sensing of ground-level concentrations

Remote sensing has been used to determine aerosol concentrations [2, 4, 93, 134], where direct monitoring is unavailable [129, 131, 136]. Aerosol Optical Depth (AOD) [48, 65] is a measure of the extinction of electromagnetic radiation by dust and haze, which can absorb or scatter light [223]. AOD is dimensionless and is related to the total amount of aerosol in the vertical column of the atmosphere over a location. AOD measurements have been extrapolated to surface concentrations [3, 41, 83, 85-89].

Short-term events such as fires, inversion weather conditions, and clouds should be taken into consideration as these events may be missed during infrequent satellite overpasses [104, 152, 161-163]. Similarly, there is a need to extrapolate the total AOD column amount into respirable ground level concentrations (GLCs) to ensure comparative measurements [80, 209]. While reviews [61] and studies [211] both indicate high correlations (~ 0.8) for long term studies between AOD and ground-based measurements, paired daily studies report lower correlations which were attributed to the inter-day fluctuations of particle size [287] .

6.2.4. Infrared indices

Remote sensing using both visible (scattering) and infrared (IR) wavelengths (detecting radiation) [234] has been used to monitor GLCs. Clouds impact reflectance [48] and the infrared portion of the electromagnetic spectrum [58, 234]. While traditional methods for quantifying aerosol relies on using the daytime-only visible portion of the electromagnetic spectrum [48], more recent studies, favour revising and utilizing older infrared dust detection methodologies [74, 256] to provide continuous monitoring (i.e. 24 hours a day) [234].

Satellite algorithms supply the cumulative infrared absorption (from land, sea, water vapor (clouds), and trace atmospheric gases) as a brightness temperature (BT) measurement. Brightness temperature difference (BTD) between two infrared wavelengths (λ) (i.e. $BTD_{\lambda 1-\lambda 2\ \mu m} = BT_{\lambda 1} - BT_{\lambda 2}$) [6, 95, 234] is a simple high-pass filtering method that enhances the differences (trace gases) between two similar wavelength bands while minimizing commonality (land/sea and cloud) between the two wavelengths. Following the methodology of our earlier work [8], we utilized five brightness temperature difference (BTD) indices ($BTD_{3.9-6.2\ \mu m}$, $BTD_{11-12\ \mu m}$, $BTD_{9.6-13\ \mu m}$, $BTD_{8.6-10\ \mu m}$, and $BTD_{6.9-7.3\ \mu m}$). These band combinations were chosen based on reducing correlations between indices and utilizing all ten IR wavelengths.

6.2.5. Aims of the study

This study seeks to understand if air quality events could be *detected* against background levels, *identify* which pollutants and source types contributed to the enhanced concentrations, and *quantitate* the concentrations of the events using the five, previously selected, BTD indices.

6.3. Data and study area

Three years (July 2015-2018) of surface concentration data were obtained from the New South Wales (NSW) Office of Environment and Heritage (OEH) for seventeen real-time monitoring sites across the greater Sydney region in eastern Australia. Figure 6-1 depicts the locations of these monitoring sites. Data from the Australian Nuclear Science and Technology Organization (ANSTO), for five co-located sites (blue squares in Figure 6-1) over the same monitoring period as the OEH data, were obtained. The ANSTO data were derived from sample analysis, which captured airborne $PM_{2.5}$ on filters over twenty-four hours twice weekly. These two concentration datasets were paired in time with ten-minute spectral data from the Himawari-8 geostationary satellite.

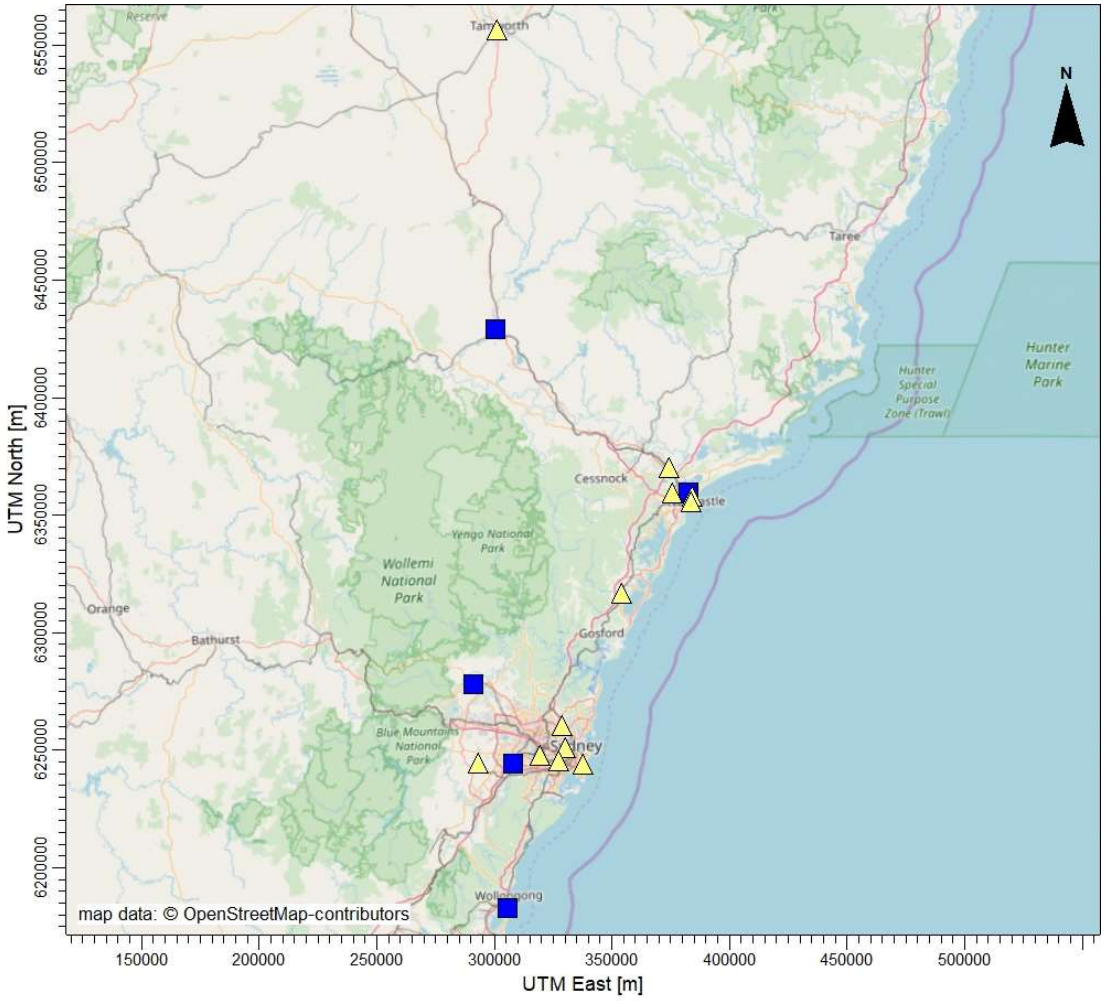

Figure 6-1: Locations of monitoring sites in the greater Sydney region (South East Australia), UTM Zone 56S, NSW OEH sites as yellow triangles, and joint OEH/ANSTO as blue squares.

6.3.1. NSW Office of Environment and Heritage

Meteorological and ambient air quality concentration data was downloaded from the New South Wales (NSW) government office of Environment and Heritage (OEH) website https://www.environment.nsw.gov.au/AQMS/search.htm for the three years, July 2015 to 2018. An air pollution index (API) was calculated as the sum over all pollutants of the hourly data divided by the daily criteria level specified by the National Environment Protection Measure for Ambient Air (NEPM) standard. The 97.5 percentile of the data was used to approximate the daily criteria for pollutants that did not have a daily standard. This approach

differed from OEH's Air Quality Index (AQI), which used inconsistent timescales for each pollutant (hours for SO_2, NO, and NO_2 but daily for particulate matter). Accordingly, we have renamed our index as Air Pollution Index (API) to highlight the difference.

6.3.2. ANSTO data

The Australian Nuclear Science and Technology Organization (ANSTO) has applied accelerator-based nuclear techniques to the characterization of fine $PM_{2.5}$ quantification of ambient air as part of the Sydney Fine Particle Study [16] and on-going monitoring. Fine particles were collected on filters over twenty-four hours twice a week. Each of these filters was analysed for 23 elemental and chemical species: hydrogen (H), sodium (Na), aluminium (Al), silicon (Si), phosphorus (P), sulfur (S), chlorine (Cl), potassium (K), calcium (Ca), titanium (Ti), vanadium (V), chromium (Cr), manganese (Mn), iron (Fe), cobalt (Co), nickel (Ni), copper (Cu), zinc (Zn), selenium (Se), bromium (Br), lead (Pb), black carbon (BC) and total nitrogen (Total N).

Positive matrix factorization (PMF) source apportionment techniques were applied to this data to identify different source components or fingerprints that make up the measured total $PM_{2.5}$ mass at each of these monitoring sites [281, 288]. Table 6-1 presents a summary of three years PMF data provided by ANSTO (July 2015 to 2018) for five sites (Liverpool, Mayfield, Musslebrook, Richmond, and Warrawong) across the greater Sydney region.

ANSTO determined seven or eight characteristic fingerprints for each of the five ANSTO sites using PMF analysis. These fingerprints included soil, sea-spray, secondary sulfates (coal-fired power stations, oil refineries, motor vehicles, and industry), smoke (biomass burning, domestic wood heaters, and motor vehicles) and Auto1 (primary automobile source) components. Industrial emission profiles (Ca, S, Fe, and metals) and Auto2 (secondary automobile source) were only supplied where those profiles contributed significantly to a site.

Table 6-1: Average $PM_{2.5}$ concentration and aerosol percentages (by mass) PMF categories for each ANSTO site.

Site	Liverpool	Mayfield	Musslebrook	Richmond	Warrawong
$PM_{2.5}$ ($\mu g/m^3$)[1]	8.37	6.98	5.84	6.89	9.47
Smoke	31.7%	26.2%	17.4%	35.1%	1.58%
Auto1	20.5%	23.8%	28.2%	11.2%	2.12%
Secondary Sulfate[3]	17.1%	18.6%	21.4%	18.1%	16.9%
Industrial Sulfur	13.2%	NS	12.9%	18.0%	18.4%
Sea-spray[3]	9.7%	17.0%	4.4%	5.6%	30.9%
Soil	3.22%	4.93%	6.55%	3.84%	12.42%
Industrial Ca	NS[2]	1.87%	NS	NS	7.43%
Industrial Fe	NS	1.98%	NS	3.37%	4.81%
Industrial Metals	NS	NS	5.36%	NS	NS
Auto2	1.39%	0.59%	NS	NS	NS

[1]: Average hourly $PM_{2.5}$ concentration ($\mu g/m^3$).
[2]: NS indicates that the PMF parameter was not supplied for that site.
[3]: Secondary Sulfate and sea-spray is abbreviated to SecS and sea respectively in subsequent discussions, and the Industrial metals are amalgamated into Industry (Ind).

6.3.3. Himawari-8

Raw data files of all ten infrared bands from the Himawari-8 satellite were obtained from the Australian Bureau of Meteorology (BOM) for the period from July 2015 to July 2018. These data files were cropped to the study domain and analysed using the "Climate Data Operators" (CDO) [216]. The raw brightness temperature data were averaged per hour (per pixel) and across the study domain (to obtain a temporal background absorbance which took into consideration diurnal temperature and atmospheric changes), and this hourly average was subtracted from the raw brightness temperature (per pixel) before calculating the BTD index value. Unlike the AOD methodology, the data was not spatially aggregated, nor was it screened based on cloud cover. The analysis considered five hourly BTD indices, which were matched in time to the hourly monitored OEH and interpolated hourly ANSTO data.

6.4. Methodology

6.4.1. Overview

It was assumed that concentration by event type was related to the five pre-selected BTD indices. However, to *quantitate* the concentrations, the composition, humidity, and particle size must be *qualified*, as these parameters influence the spectral response [74]. This study analysed the concentration distribution of different pollution events over the three-year data period. A pollution index was developed, from the BTD indices, which considered compositional, humidity, and particle size changes. Predictive pollutant equations for relative humidity and percentage fine particulate matter were quantified using regression from the pollution index and verified against the two datasets, and a Weibull function was determined and used to estimate compositional probability against the pollution index.

6.4.2. Variations in the measured OEH and ANSTO data

The variance of the data was investigated by classifying the measured concentration, according to percentiles. The daily guideline for $PM_{2.5}$, PM_{10}, and SO_2 coincided with the 97.5 percentile, and this statistic was used for pollutants that did not have a daily guideline. An Air Pollution Index (API) was defined as:

$$\boldsymbol{API = \sum_i Concentration_i / daily\ guideline_i} \qquad \boldsymbol{(1)}$$

An air quality event (or incident) was indicated when at least one of the measured pollutants exceeded the guideline. Carbon monoxide was subsequently removed from the list of pollutants as it had few events compounded by a limited number of monitoring sites. Competing spectral interferences from other pollutants were reduced by restricting the analysis to single pollutant events. Using an air pollution index allowed comparisons of severity between pollutants to be undertaken and enabled the temporal addition of combined impacts from all pollutants to be determined.

Primary (emitted from source) and secondary (chemical reactions) aerosols are expected from combustion by-products and photochemical reactions [29, 30] from both gaseous pollutants (NO, NO_2, SO_2, and O_3) and particulate matter ($PM_{2.5}$ and PM_{10}). The OEH data indicated that the measured PM_{10} included coarse particles with an aerodynamic diameter (i.e. particle size) of 2.5 µm to 10 µm as there were instances in the data where the concentration of PM_{10} was less than $PM_{2.5}$ – which could not occur if PM_{10} included $PM_{2.5}$. The percentage of fine particles (0-100%) in the measured OEH data was therefore defined as:

$$\boldsymbol{Fines = 100\frac{PM_{2.5}}{PM_{2.5}+PM_{10}}} \qquad \boldsymbol{(2)}$$

The data were screened to exclude background concentrations (i.e. where API < 1). Boxplots were generated to determine the impacts of the site location, relative humidity (moisture), and particle sizes on the concentration. These air quality events were classified according to Boolean logic, and this allowed event types to be categorized and ranked by occurrence. The bit significance was determined by the number of measurements above the detection limit for each pollutant. CO, which was monitored at the least number of sites was the least significant, while PM_{10} was the most significant.

$$\boldsymbol{Event\ type} = \sum_i \boldsymbol{2^i \chi(i)} \qquad \boldsymbol{(3)}$$

$$where\ \chi(i) = \begin{cases} 1 & if \quad Pollutant_i > daily\ guideline_i \\ 0 & otherwise \end{cases}$$

The ratio of the hourly to daily $PM_{2.5}$ OEH data was used to scale the ANSTO data (expressed as a mass basis) to hourly concentrations. The correlations between the two measured datasets were determined on both an hourly and daily basis.

6.4.3. Development of a pollution index

Preliminary regression analysis at calibrating concentration scale factors per event type from the five BTD index values resulted in low correlations (0.05 to 0.3). Investigating the analysis of variance (ANOVA) of the API showed that the within variance (of a narrow range (1/100th) of the BTD index) was significantly greater than the between variances. This variance was further noted in the boxplots that were produced (Figure 6-2) (API by event type, severity, humidity,

and particle size) that depicted both the relationship between the variables and the variance of the data. Removal of outliers and discrepancies between scale factors (slope, intercept, and median prediction) did not improve the predicted API/BTD regression correlations.

The failure of traditional regression methods necessitated an alternative approach. The OEH data analysis suggested that the API was related to changing event types, humidity, and particle size consequently, the variance within these categories was hindering quantification. A pollution index was therefore proposed that encompassed composition, humidity, particle size, and compositional changes.

The production of the boxplots (Figure 6-2) by humidity and percentage fines showed a consistent ordering of pollutants with three pollutants showing minimal differences, three moderate differences, and one major difference. These differences were used to determine a Bayesian "prior" pollution index with an initial index change of five, ten, and twenty for minimal, moderate, and large differences, respectively. A Bayesian approach was used to include prior information that cannot be easily included via classical methods and where the data set includes a significant number of outliers and non-normal distributions [289]. Bayesian regression was applied iteratively to determine the pollution index from the prior (dependent variable) against the five BTD indices as input (independent variables). Two BTD indices were subsequently discarded based on the lack of significance to the predicted coefficients from the final stepwise iteration.

6.4.4. Calculating concentration from the pollution index

The measured concentrations, relative humidity, and particle sizes were grouped and aggregated according to the integer of the pollution index. The aggregation minimized high concentrations from severe events, that may not represent the concentration across the entire Himawari pixel (4 km^2). Regression was used to determine coefficients for relative humidity, and particle size from the pollution

index and maximum likelihood probabilities were determined by fitting a Weibull function (eq 4) to the event (composition) probabilities across the pollution index.

$$\textbf{\textit{Event probability}} = a \cdot \left(\frac{\beta}{\alpha}\right) \cdot \left(\frac{PI}{\alpha}\right)^{\beta-1} \exp\left(-\left(\frac{PI}{\alpha}\right)^{\beta}\right) \qquad (4)$$

Where:

a is a scale parameter to convert the cumulative sum (=1) to a constant maximum of unity in the graph, and according to the 99.9 percentile.

α is the Weibull scale parameter that affects the curve width.

β is the Weibull shape parameter that changes the position of the maxima where one is asymptotic at low PI values, and five is asymptotic at high PI values; and

PI is the pollutant index.

6.5. Results

6.5.1. Variations in the measured OEH and ANSTO data

Percentiles

The data recovery rates in Table 6-2 reflected that not all pollutants were measured at each site. Table 6-2 shows that while the guidelines (97.5%) represented most of the measured data, they accounted for only seven percent of the measured OEH concentrations. The skewed data distribution is further reflected in the fivefold increase in concentrations between the 99.9 percentile and the maximum.

Table 6-2: Total data recovery rates (including parameters not monitored at sites) and concentration percentiles from a) the OEH dataset, and b) the ANSTO dataset. The number of valid measurements per element is provided with the values in brackets representing the percentage of valid data recovered from total data records for each element.

	a) OEH data							
N	**SO_2 pphm[1]**	**NO pphm**	**NO_2 pphm**	**CO ppm**	**O_3 pphm**	**PM10 µg/m3**	**PM2.5 µg/m3**	**API**
486014 (100%)	395504 (81%)	428122 (88%)	428530 (88%)	158650 (33%)	349422 (72%)	481059 (99%)	402973 (83%)	243973 (50%)
50%	0	0.1	0.6	0.2	1.8	16.5	6.5	1.6
95%	0.5	3.7	2.3	0.6	3.7	42.1	19.7	3.5
97.5%	0.7	5.7	2.7	0.7	4.3	51.6	24.5	4.2
99.0%	1.2	8.4	3	0.9	5.2	67.2	32.6	5.1
99.9%	3.4	15.6	4	1.5	7.7	138	66.7	8.6
100%	21	33.5	6.7	3.6	13.5	729	335	30.5
	b) ANSTO data							
N	**PM2.5 µg/m3**	**Smoke µg/m3**	**Sea µg/m³**	**Auto1 µg/m3**	**Soil µg/m3**	**S µg/m3**	**SecS µg/m3**	**Fe µg/m3**
33324	31293 (94%)	31317 (94%)	31317 (94%)	31297 (94%)	31325 (94%)	24583 (74%)	31373 (94%)	19461 (58%)
50%	5.8	0.5	0.3	0.8	0.2	0.7	0.8	0.1
95%	20.4	6.7	5.0	3.9	1.7	4.1	4.6	1.0
97.5%	25.9	10.0	7.3	5.2	2.8	5.5	5.9	1.6
99.0%	35.3	15.6	10.9	7.4	4.8	7.6	7.5	2.8
99.9%	61.2	35.7	20.9	14.1	11.9	14.1	12.5	6.5
100%	89.7	51.2	40.8	33.6	23.4	26.0	20.5	10.4

[1]: pphm = Parts per hundred million.

Quantifying impacts by site, relative humidity, and particle size

There were minimal differences in measured concentrations between locations despite urban, rural, coastal, and forested land-use differences. Most events had an API of three to five (Figure 6-2a-b) and were within the 95th percentile of event concentrations but PM_{10}, and to a lesser extent SO_2, had a considerable number of exceedances above the 95% percentile level.

NO events coincided with high relative humidity (Table 6-2 and Figure 6-2a), while NO, NO_2, SO_2, and PM_{10} all reflected an inverse concentration relationship with relative humidity. PM_{10} events were the only events that occurred significantly during low humidity (0 to 20%) potentially from enhanced windblown dust events over dry soil. Ozone and $PM_{2.5}$ showed a reversed trend with concentrations increasing with relative humidity and reached a maximum at about 80%

humidity, and this can be ascribed to moisture coagulating on fine particles (and increasing their mass) with wet deposition potentially occurring above 80% humidity.

Figure 6-2b shows that coarse particles dominated PM_{10} measurements (as expected by the definition of > 2.5 μm) and NO events, while $PM_{2.5}$ events were from fine particles with a concentration (API) that decreased according to particle size (arguably related to volume). Ozone concentrations also exhibit an inverse concentration relationship with particle size. Similar, but weaker, trends were noted in the ANSTO data (Figure 6-2c-d).

Event types

Table 6-3 lists the most frequent event types in descending order. From the table, it is apparent that air quality events in the OEH dataset were dominated (80%) by six single-pollutant incidents, five two-pollutant incidents (10%), and the remaining (10%) occurred from low-frequency, multi-component incidents. While there are significant differences in maximum API concentrations, each singular pollutant event type had an API concentration of approximately 3.0. While the lack of PMF categories across all sites precluded a similarly detailed analysis of the ANSTO dataset, seventy percent of the ANSTO events were related to a single PMF source category. Concentration maxima from smoke and sea-spray were double that of the other categories.

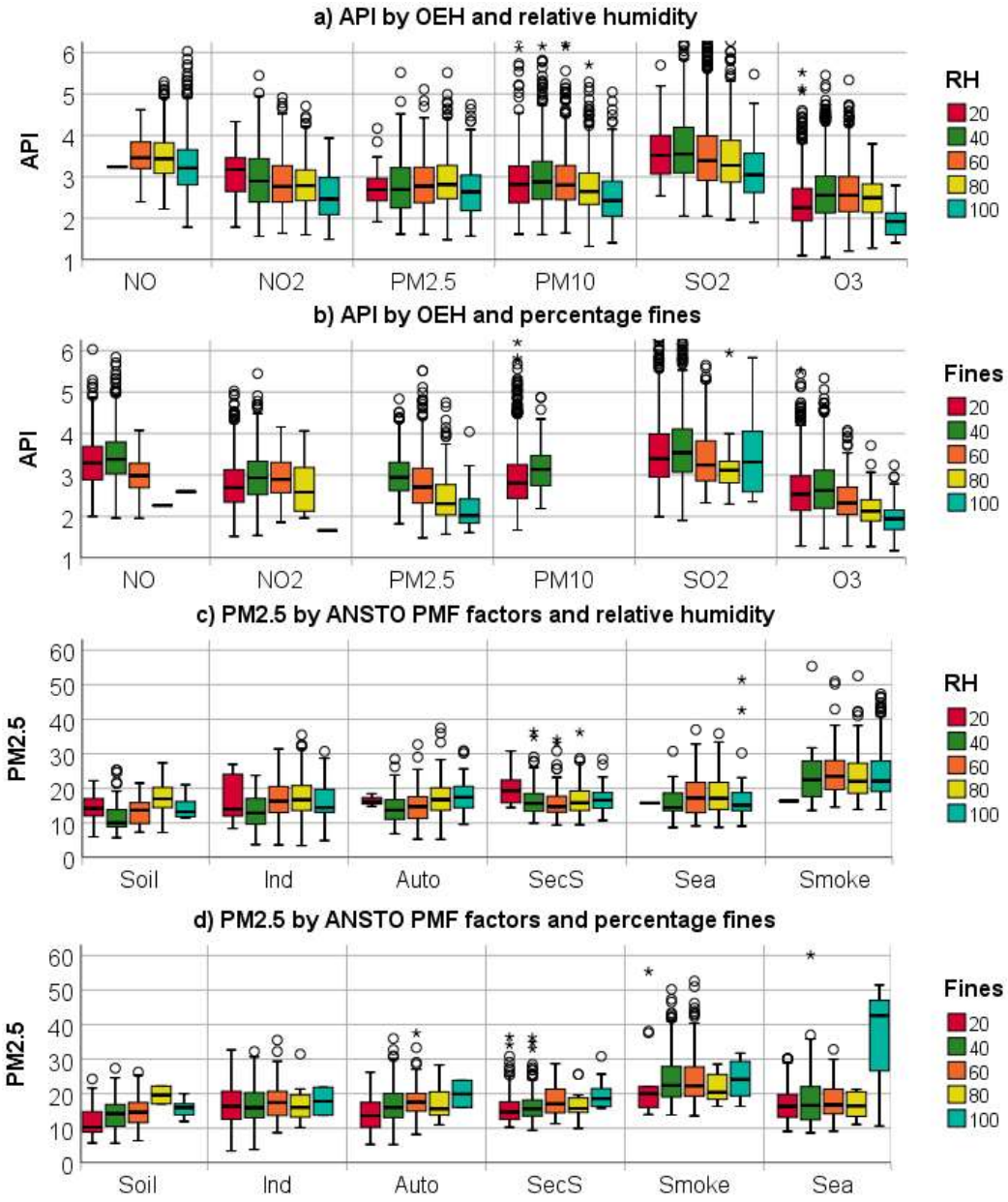

Figure 6-2: Box and whisker plots by: a) OEH relative humidity; b) OEH percentage fines; c) ANSTO relative humidity, d) ANSTO percentage fines depicting API per pollutant (where a singular pollutant exceeded an API of unity for each monitoring site.

Table 6-3: The most commonly occurring event types for a) the OEH API dataset and b) the ANSTO $PM_{2.5}$ dataset monitored over the three years (July 2015 to 2018) at the selected monitoring sites.

Event Type	No of events	Percent	Cumulative Percent	Std. Deviation	Mean	Maximum
	a) OEH data					
PM_{10}	8635	18.2	18.2	0.8	2.9	16.2
O_3	7033	14.8	33.1	0.6	2.5	5.5
SO_2	6665	14.1	47.1	1	3.6	13.2
NO	5605	11.8	59	0.6	3.4	6
$PM_{2.5}$	5324	11.2	70.2	0.6	2.8	5.5
NO_2	4789	10.1	80.3	0.6	2.8	5.4
TSP ($PM_{2.5}$+PM_{10})	1394	2.9	83.2	2.1	4.8	22.5
NO_x (NO+NO_2)	1100	2.3	85.6	0.7	4.1	7.3
O_3+PM_{10}	804	1.7	87.3	0.6	3.6	7
NO+CO	599	1.3	88.5	0.7	4.2	6.7
NO+$PM_{2.5}$	598	1.3	89.8	0.8	4.9	8.4
TSP+NO_x+CO	571	1.2	91	1.7	6.6	16.6
NO_x+CO	562	1.2	92.2	0.9	4.7	8
SO_2+PM_{10}	494	1	93.2	1.4	4.9	11.9
NO+PM_{10}	383	0.8	94	0.8	4.1	8.4
	b) ANSTO data					
SecS	411	13	13	4.6	16.8	36.4
Smoke	408	12.9	25.9	8.5	24.5	89.2
Sea	401	12.6	38.5	6.3	17.6	60.1
Auto1	325	10.3	48.8	4.3	17.9	37.5
Soil	196	6.2	55	4.6	13.3	27.4
S	194	6.1	61.1	4.8	18.8	35.5
Auto2	115	3.6	64.7	4.8	12.3	26.9
Fe	98	3.1	67.8	5.3	17.5	30.7
Metals	58	1.8	69.6	4.5	9.3	20.4
Smoke+Auto1	55	1.7	71.3	9.1	33.9	60.8
Ca	17	0.5	71.8	2.2	12.1	17.2

Comparing ANSTO and OEH data

The correlation between the ANSTO and OEH datasets was 0.760 for the hourly ANSTO interpolation and 0.625 for the daily OEH summation. This correlation is less than expected when comparing between two analytical methods and is more typical of comparisons between remote sensing AOD and ground-based AERONET correlations [61, 144, 287]. While the different timescales may contribute to the low correlation on the ANSTO interpolation, a higher correlation would be expected on the daily OEH summation if the timescales were the cause of the low correlation. The low correlation arises from location differences and indicates the

plume's spatial variability rather than compositional differences between the two datasets.

6.5.2. Development of a pollution index

API by BTD boxplots

Boxplots (Figure 6-3) were produced for each of the five BTD indices, per event type and severity (the integer of API), showed that half of the plots depict a lack of change in concentration against the BTD index value (e.g. NO and $BTD_{3.9\text{-}6.2\ \mu m}$). The lack of sensitivity in these plots accounts for the high-within, low-between ANOVA results. The index values were similar across three pollutant categories: [NO, NO_2, and $PM_{2.5}$]; [PM_{10}, and SO_2]; and O_3 with minimal changes within a group.

Low background concentrations covered a broader spectral response in the data than the events due to the larger dataset (97.5%) and the combined spectral result of other the pollutants. In contrast, some extreme events had a low frequency of observance, and the lack of data is evident in the narrow spectral range, which did not follow the trend of the other data (e.g. NO for $BTD_{11\text{-}12\ \mu m}$). These background and low-frequency events were excluded from subsequent analysis.

Nitric oxide (NO) has a low spectral sensitivity to the five BTD indices, with only $BTD_{6.9\text{-}7.3\ \mu m}$ showing a definitive relationship in the boxplots. Similarly, ozone is best qualified by the singular $BTD_{9.6\text{-}13\ \mu m}$ index, although both $BTD_{3.9\text{-}6.2\ \mu m} > 50°C$ and $BTD_{11\text{-}12\ \mu m} > 2°C$ are potentially useful as thresholds. Sulfur dioxide (SO_2) has the best spectral sensitivity across all five BTD indices, followed by nitrogen dioxide (NO_2) across three indices. Both $PM_{2.5}$ and PM_{10} exhibit a lack of spectral sensitivity to concentration.

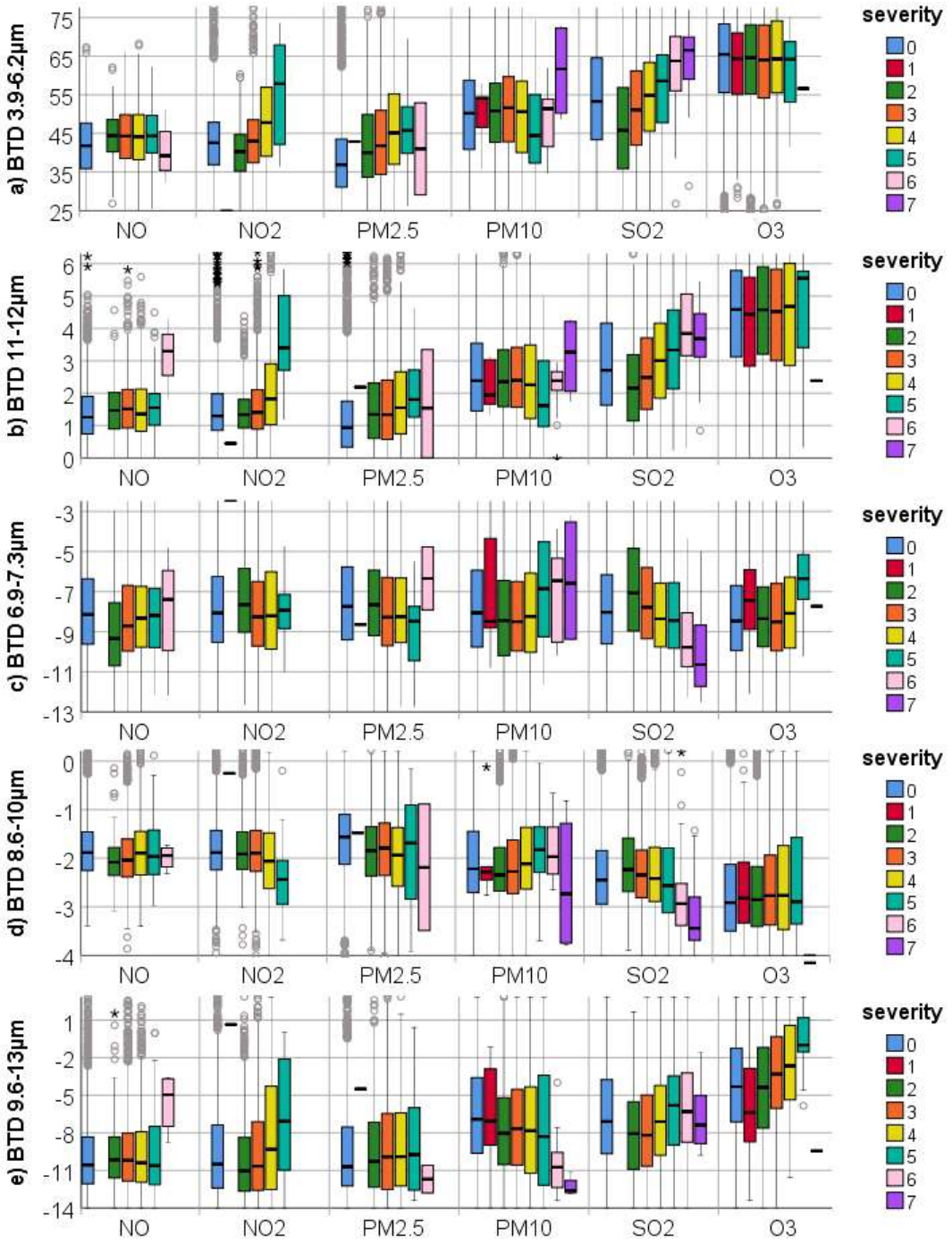

Figure 6-3: Boxplots depicting BTD by event and severity (concentration).

Determining the pollution index

Iterative regression analysis to predict the pollution index (PI) determined the following BTD coefficients.

$$\boldsymbol{Pollution\ index = 17.3 + 4.69BTD_{14-15} + 0.499BTD_{9-10} + 0.577BTD_{12-16}} \quad \textbf{(5)}$$

Figure 6-4 presents boxplots depicting the variation of the pollutant index across event types, fine fraction, and relative humidity. The pollutant type has the most significant impact on the pollution index with NO, NO_2, and $PM_{2.5}$ having low index values, PM_{10} and SO_2 having intermediate levels and O_3 the highest. There is an inverse relationship between humidity and pollutant index, while the particle size relationship is less well defined.

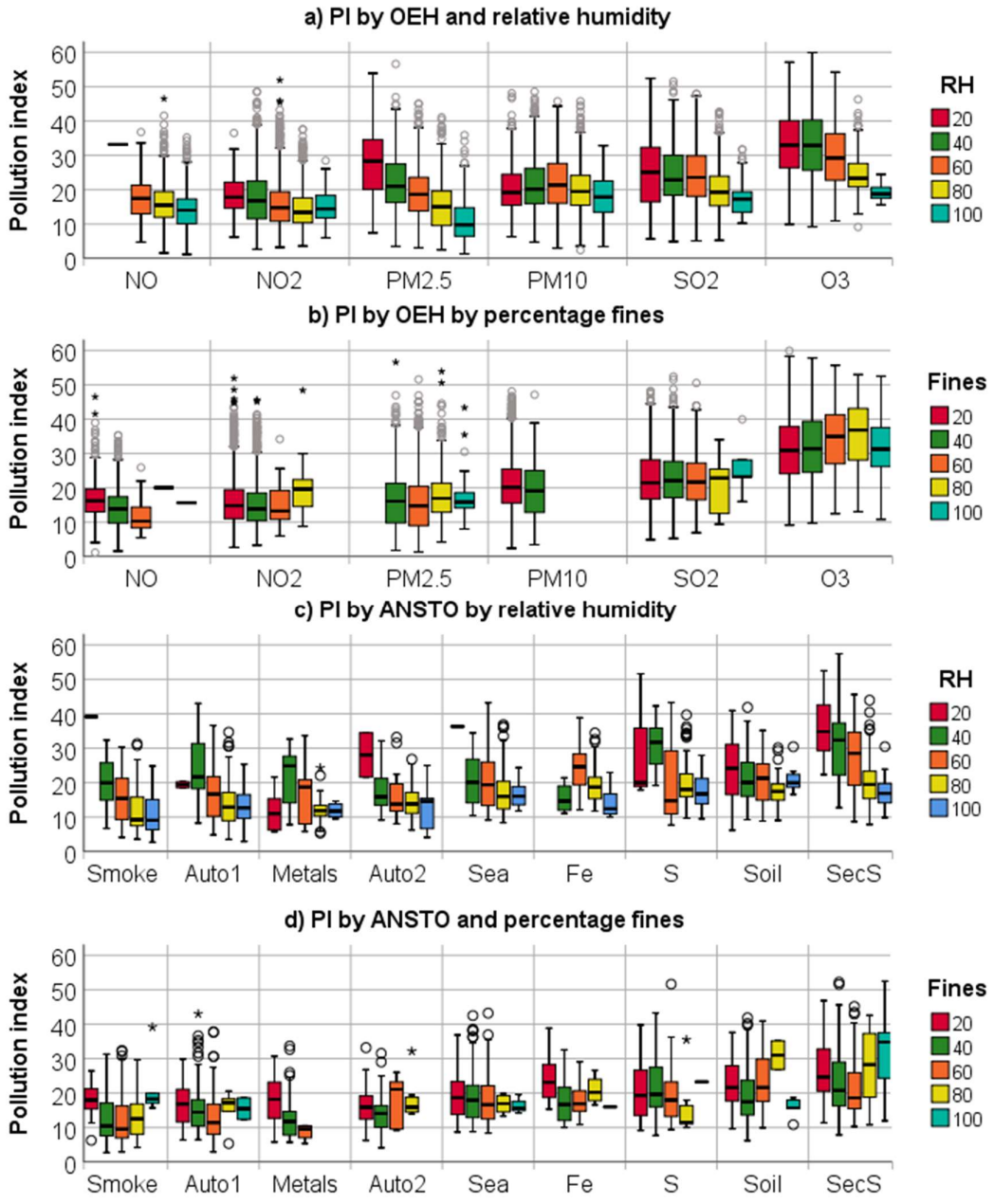

Figure 6-4: Pollution index (PI) as a function of a) OEH events by relative humidity, b) OEH events by percentage fine aerosol, c) ANSTO events by relative humidity, and d) ANSTO events by percentage fine aerosol.

6.5.3. Determining concentration from the pollution index

Figure 6-5 depicts the mean concentrations and probabilities aggregated across the integer of the spectral pollution indices. Figure 6-5a demonstrates high correlations between relative humidity and percentage fines with the pollution index (PI). The regression coefficients were scaled to span the data range and simplified to:

$$\boldsymbol{Relative\ humidity = 100 - 10\,PI/6} \qquad \textbf{(6)}$$

$$\boldsymbol{Fines = 100 - 6PI + PI^2/10} \qquad \textbf{(7)}$$

Figure 6-5b depicts the probability that the predicted concentration is below the mean (P50) or above the event threshold (97.5%) according to the pollution index. At a pollution index of 14, there is a 60% probability that an hourly measurement would be below the annual mean. With a pollution index in the range of 8 to 20 (blue shaded region) the probability that the measurement is below the mean is greater than the uncorrelated 50th percentile.

Similarly, with a pollution index in the range of 8 to 30 (red shading), there is less of a probability that it is an event. At lower or higher pollution index values, the probability decreases that the hourly concentration is below the annual mean and simultaneously increases the probability of an event. This relationship is more robust at higher pollution index values, and at a pollution index of 40, there is an eighty percent probability that the measurement is above the mean and the probability that it is an event doubles from 2.5% (100-97.5%) to 5%.

Figure 6-5 (c and d) shows that for most pollutants, the measured concentration is independent of the pollution index. SO_2 and O_3 show a slight positive correlation against index values, and the ANSTO data reflects a cut-off at an index value of about 25 in accordance with the $PM_{2.5}$ data in Figure 6-5c. The ANSTO data reflects a much smaller dataset (two days per week), which was interpolated to hourly estimates, and consequently, there are fewer exceedances and more "noise" in the data. Figure 6-5d has been simplified to include only three PMF components to minimize overlapping factors.

The probability of an event type is related to the pollutant index for the OEH data (Figure 6-5e), but less dependence was noted for the ANSTO data (Figure 6-5f). The probability of a $PM_{2.5}$ event increases hyperbolically with decreasing pollution index with a probability of 0.1 at an index value of 25 increasing to 0.5 at an index of 5. Ozone increases with increasing index values, in contrast to all other pollutants, such that at an index value of greater than thirty-five is most probably an ozone event. SO_2 and PM_{10} are similar, with both having a quadratic function with a maximum at an index value of about 25. Both NO_x components (NO and NO_2) have similar quadratic profiles with little probability differences between them and overlap the $PM_{2.5}$ probability profile except at low index values (<10) where $PM_{2.5}$ is asymptotic while NO_x decreases to zero. The derived Weibull parameters are supplied in Table 6-4.

Table 6-4: Weibull parameters per pollutant/aerosol factor sorted according to increasing shape parameter (β).

Factor	$PM_{2.5}$	Smoke	Auto	NO	NO_2	PM_{10}	S	SO_2	Soil	Sea	SecS	O_3
β	1.03	1.27	1.68	1.88	1.96	2.23	2.84	2.93	3.19	3.21	3.41	4.68
α	17.6	13.2	18.5	15.4	20.4	31.1	29.9	36.3	30.9	27.0	45.2	48.8
Scale	1483	637	336	291	96	4645	376	107	296	453	430	202

Similarities in the probability distributions were noted between the OEH and ANSTO data specifically for the O_3-Secondary Sulfates; $PM_{2.5}$-Smoke; and NO_x-Auto pairs. This similarity is also seen in the comparisons of event types with relative humidity and percentage fines as depicted in Figure 6-2.

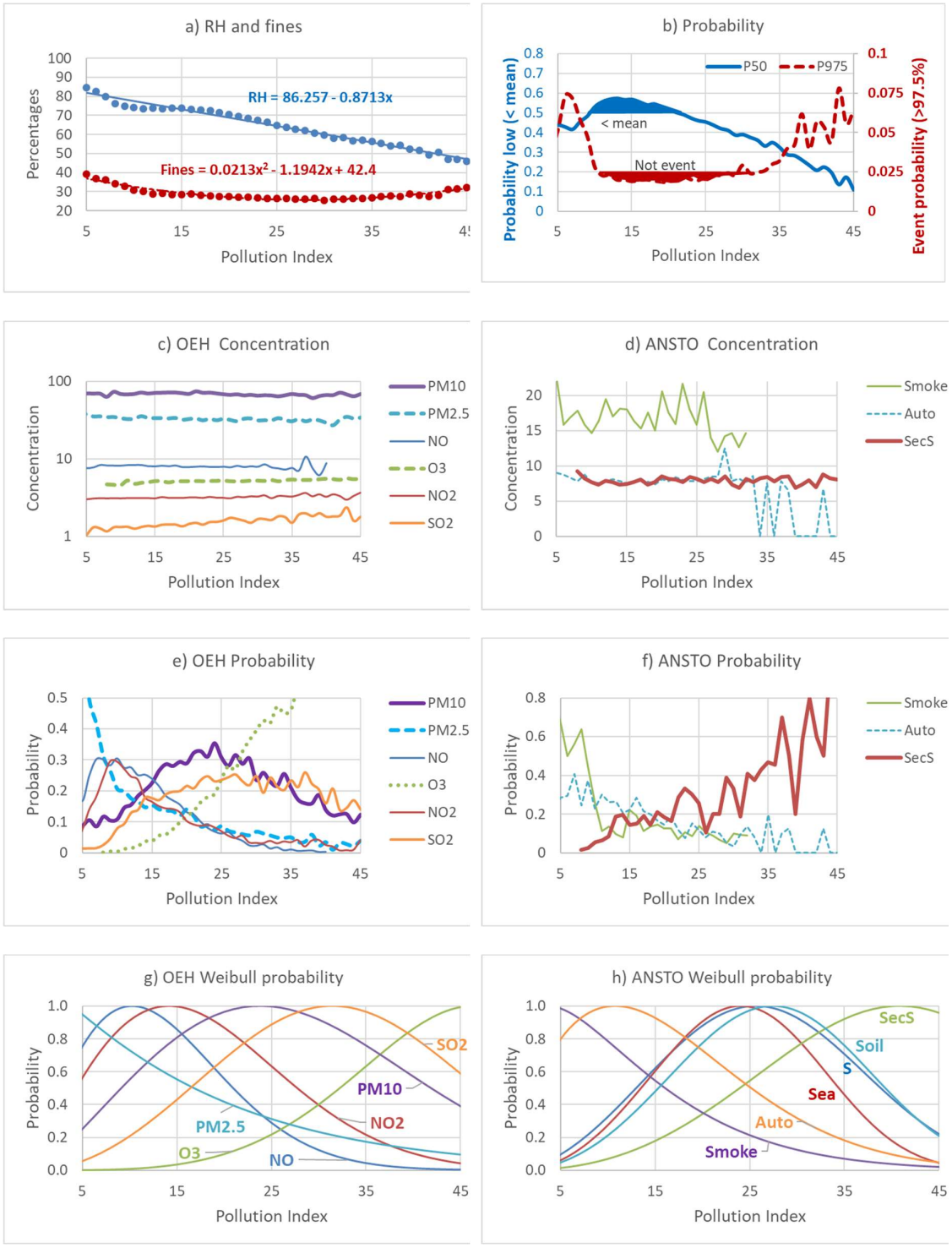

Figure 6-5: Average concentration and probability as a function of the pollution index. a) OEH relative humidity and particle size; b) probability below the mean or above the guideline (97.5%); c/d) OEH/ANSTO concentration; e/f) OEH/ANSTO probability; g/h) OEH/ANSTO probability as a Weibull function.

6.6. Discussion

6.6.1. Variations in the measured OEH and ANSTO data

Percentiles

The skewed concentration data indicates that air quality events reflect the log-normal nature of environmental data. Quantifying air quality events in standard statistical terms of means and population variances describes these sample populations poorly, as illustrated by comparing the measured maximum concentration of $PM_{2.5}$ of 335 $\mu g/m^3$ against the mean of 6.5 $\mu g/m^3$.

The concentrations reflect the cumulative probabilities of the wind blowing towards a sensor, the homogeneity of the plume over the monitoring area (4 km^2 for Himawari), the probability of an emission - which may be transient (such as smoke from a fire, wind-blown dust, passing vehicles), and the probability of favourable dispersion conditions (stability and wind speed). Average background concentrations are two to three orders of magnitude lower than the maximum concentrations, and it is this large skewed distribution between maxima, incident, and background concentrations that make it challenging to describe concentrations in terms of means and standard deviations.

Quantifying impacts by site, relative humidity, and particle size

Minor differences were noted between site locations despite differences in land type (sea/urban/forest/rural) between the sites. Both particle size and relative humidity demonstrated evidence of a causal relationship with concentration across all pollutant types. The weaker trends in the ANSTO data were ascribed to less data, the PMF categorization, and from interpolating daily data to hourly.

Event types

The data shows that a single pollutant per incident dominates air quality events. This indicates that the different event types seldom impact a receptor simultaneously, and this assists the quantification as multi-spectral contamination is reduced. However, it also indicates the dynamic nature of air pollution as one event type may be subsiding while another may be initiating (e.g.

vehicular activity may be diminishing at sunset, but simultaneously the land-sea temperature differentials may initiate a wind directional change bringing in salt or crustal material) and the resulting mix of pollutants may, therefore, have continually changing compositional and particle size attributes.

Comparing ANSTO and OEH data

The correlation coefficient between the OEH and ANSTO data is less than expected between two analytical methods. This lower correlation may be due to: a) narrow plumes which may partly miss the other site; b) different monitoring methods (electronic or filter) which may respond differently to changes in relative humidity (as filters would be indicative of the final relative humidity and/or dried prior to analysis in contrast to the instantaneous amount of moisture absorbed on the particles); and c) differences in the temporal resolution of the two sampling methods requires an interpolation from the daily ANSTO measurements equivalent to the hourly NSW EPA data. Nevertheless, the correlation coefficient between the two monitoring methods represents a "best-case" scenario that could be expected when comparing predictive methodologies with inherently higher uncertainty.

6.6.2. Pollution index

API by BTD boxplots

The BTD by event and severity boxplots (Figure 6-3) demonstrate that approximately half of the concentration relationships are insensitive to the BTD index. NO, NO_2, and $PM_{2.5}$ exhibit similar spectral responses to changing concentration, as does PM_{10} and SO_2. There is some justification in determining thresholds for ozone (e.g. $BTD_{3.9\text{-}6.2\ \mu m} > 50°C$ and $BTD_{11\text{-}12\ \mu m} > 2°C$ as only $BTD_{9.6\text{-}13\ \mu m}$ depicts a concentration index relationship. However, from the plots, there are no apparent thresholds for the other pollutants that would simplify qualification and would not be best served by setting upper and lower bounds as per the OEH data summary.

Based on the BTD by event and severity boxplots (Figure 6-3) ozone, sulfur dioxide, and nitrogen dioxide exhibit the best spectral sensitivity to changes in

concentration while particulate matter (both $PM_{2.5}$ and PM_{10}) are intermediate and nitric oxide has reduced spectral sensitivity to the BTD indices.

Determining the pollution index

Dispersion of an air pollution episode takes time to dissipate, and consequently, air pollution changes constantly in composition and magnitude. The advantage of using a pollution index rather than a classification by event type is that it allows for a gradual transitioning (i.e. a continual function rather than a binary true/false) between pollutants considering changes in event type, particle size, and humidity. Figure 6-4 depicts the gradual transition in the index as the dominance and emission intensity of sources change, or temperature and evaporation effects affect the aerosol composition. Aggregation of the pollutant index is possible, both spatially and temporally, due to the continual function, unlike categorical variables such as event types, which cannot be averaged between categories. Finally, the resultant equations are simpler to code than a series of nested if-statements per site-specific threshold.

The pollutant index is derived from six out of the ten infrared BT absorbances and utilizes three BTD components $BTD_{11\text{-}12\,\mu m}$, $BTD_{9\text{-}10\,\mu m}$, and $BTD_{9.6\text{-}13.3\,\mu m}$. Two BTD indices were rejected $BTD_{3.9\text{-}6.2\,\mu m}$ and $BTD_{8.6\text{-}10\,\mu m}$ because of low significance to the regression coefficients (for this study). Using six wavelengths enables most of the spectral variance to be described by these three indices and enables a more comprehensive pollutant index to be developed than using only three or four wavelengths. $BTD_{11\text{-}12\,\mu m}$ has traditionally been used to detect AOD. $BTD_{9\text{-}10\,\mu m}$ is a strong predictor of water vapor and indicates the difference between high and low cloud, which affects the vertical dispersion of the plume. Finally, $BTD_{8.6\text{-}10\,\mu m}$ gives a measure of the ozone column. Therefore, these three indices can be expected to contribute to the determination of particle size, relative humidity, column to ground level, and an indicator of photochemical precursor species. While the pollution index methodology could be extended to other regions, the coefficients are expected to be different because of the location-specific thresholds [95], moisture, and particle sizes.

6.6.3. Calculating concentration from the pollution index

The frequency distribution (Table 6-1) and boxplots (Figure 6-2) depict the full range of concentrations that occur in the measured datasets. However, the average concentration is insensitive to the pollution index, as depicted in Figure 6-5(c & d), and this explains why BTD has been used to detect but not quantify events. It has previously been suggested [74] that the subtraction of the two-wavelength channels accounts for the loss of sensitivity and that quantification should use the raw spectra instead (after correcting of atmospheric effects).

Fitting a Weibull function on the probability data enables an assessment of the resolving power of the pollution index (i.e. the ability of the pollution index to categorize the event type). Ozone and $PM_{2.5}$ are inversely correlated, and as one increases, the other decreases. Unfortunately, the other components are not well resolved, and for example, soil, sea-spray, and SO_2 are highly correlated and challenging to resolve. Additional external information, such as distance to coast or wind direction, may enable the resolution to be enhanced. Table 6-4 provides the Weibull parameters, which enable a coarse assessment of concentration to be determined, assuming that a probability of one equates to the 99.9 percentile.

The high correlation between the probability distributions of the OEH and ANSTO datasets were noted. It was rationalized that this was a causal relationship, and not merely auto-correlation based on the relative humidity and particle size because the ANSTO PMF factors do generate the OEH components. Smoke does generate $PM_{2.5}$; coal-fired power stations (the main contributor to secondary sulfates) are contributing factors in ozone formation; wind-blown soil and sea-spray does generate sulfates; and motor vehicles do generate NO_x. This is an interesting observation in that it shows that a) the PMF analysis of particulate matter on the filters can estimate the gaseous pollutant concentrations; b) it verifies the PMF analysis; and c) indicates that the gaseous surface concentrations can be detected using remote sensing infrared wavelengths.

6.7. Conclusion

Data relating to air quality events are best interpreted according to percentiles rather than means and population variances as the concentrations are dependent on the cumulative probabilities of wind direction, speed, and emissions factors. While air quality events are typically dominated by a single event type per incident, the dynamic nature of air pollution implies a constant change in composition, absorbed moisture, and particle sizes. Significant differences were noted between OEH and ANSTO's $PM_{2.5}$ concentrations, and this was attributed to narrow plumes, different monitoring methods, and temporal resolution between the two sampling techniques. These differences are expected to be amplified when comparing data across a coarse (4 km^2) satellite monitoring grid.

The pollution index allows for a gradual temporal transitioning between pollutants, particle size, and humidity, and the continuous index scale can be aggregated both spatially and temporally. While the five BTD indices are related to chemical composition, and this is independent of location, the pollution index is dependent on moisture and particle size, and it is therefore expected to be location-specific. Weibull parameterization of the probability distributions allows an estimate of the probability of particulate matter source factors (ANSTO PMF) and gaseous events (OEH) to be determined. While some compounds are well resolved (e.g. $PM_{2.5}$ and O_3), others (e.g. PM_{10} and SO_2) are poorly resolved. External information such as wind direction may assist in resolving the event type.

Unfortunately, BTD is unsuitable for quantification as the low regression correlations prevent a direct quantification of concentrations. However, the predicted probabilities can be scaled to the maxima (or average) concentration, and in so doing provide period statistics that are comparative to dispersion modelling in accuracy but with the benefit of no wind field errors (as the plume is where it is observed) and sporadic events are detected in contrast to dispersion modelling which cannot model unknown sources.

The pollution index is in the process of being validated both spatially and temporally (i.e. is a sea-spray plume coherent across space and does it develop and dissipate according to the prevailing meteorology) and verified for global

applicability to investigate if it is susceptible to underlying local land use (e.g. sea, sand, and vegetation) effects. Preliminary investigations indicate that prior screening, based on cloud cover and atmospheric stability, may improve quantification and that the plumes are coherent across space and time (see https://www.linkedin.com/posts/miles-sowden-6a1b704_duststorm-remotesensing-aerosol-activity-6586901543742726144-aglZ).

6.8. Appendix

6.8.1. SPSS OEH syntax code

```
* do some calculations.
USE ALL.
compute pSize=RND(100*PM25/(PM25+PM10)).
formats pSize (f3.0).
compute API = 0.00.
formats API (f5.1).
compute API = API + O3 / 4.3.
compute API = API + SO2 / 0.7.
compute API = API +NO / 5.8.
compute API = API  +NO2 / 2.7.
compute API = API  + PM25 / 25.
compute API = API + PM10 / 50.
EXECUTE.

*categorize on integers to display in graphs.
compute severity=0.
formats severity (f3.0).
if (API >1) severity=rnd( (API)).
if severity > 9 severity=9.

* do a boolean test on the daily criteria (or 97.5 if no daily), ordered by increasing N .
compute event=0.
formats event (f3.0).
if (CO > 0.7) event = 1.
if (O3 > 4.3) event = event + 2.
if (SO2 > 0.8) event = event + 4.
if (NO > 5.8) event = event + 8.
if (NO2 > 2.7) event = event + 16.
if (PM25 > 25) event = event + 32.
if (PM10 > 50) event = event + 64.

* Give a text label to the classification.
string etype(a10).
compute etype =STRING(event,N3).
compute etype="other".
* singular events.
if (event=0) etype = "low".
if (event=64) etype = "PM10".
if (event=8) etype = "NO".
if (event=4) etype = "SO2".
if (event=2) etype = "O3".
if (event=16) etype = "NO2".
if (event=32) etype = "PM2.5".
if (event=1) etype = "CO".
* severe events.
if (event=96) etype = "TSP".
if (event=121) etype = "TSP+NOx+CO".
if (event=89) etype = "TSP+NOx+CO".
if (event=97) etype = "TSP+CO".
if (event=113) etype = "TSP+NOx+CO".
if (event=105) etype = "TSP+NOx+CO".
if (event=112) etype = "TSP+NO".
if (event=98) etype = "TSP+O3".
if (event=57) etype = "TSP+NOx+CO".
```

```
* high events.
if (event=24) etype = "NOx".
if (event=25) etype = "NOx+CO".
if (event=9) etype = "NO+CO".
if (event=66) etype = "O3+PM10".
if (event=41) etype = "NO+PM2.5+CO".
if (event=80) etype = "NO+PM10".
* low events.
if (event=40) etype = "NO+PM2.5".
if (event=68) etype = "SO2+PM10".
if (event=80) etype = "NO+PM10".

* classify BTD into ~ 100 categories.
compute I7_8=rnd(B7_8).
compute I14_15=rnd(8*B14_15)/8.
compute I9_10=rnd(6*B9_10)/6.
compute I11_13 =rnd(8*B11_13)/8.
compute I12_16 =rnd(2*B12_16)/2.
compute RH =rnd(HUMID/20)*20.
compute Fines=rnd(pSize/20)*20.
formats RH (f3.0).
formats Fines (f3.0).
execute.
if RH gt 100 RH = 100.
*string s_events (a25).
*compute s_events = CONCAT(RTRIM(etype),' RH ',rtrim(STRING(RH,f3)),' Fines ',rtrim(STRING(Fines,f3))
).
execute.

* show probabilities and API percentiles for ALL, Incident, and pollutants.
USE ALL.
 * FREQUENCIES VARIABLES=etype RH Fines  /BARCHART PERCENT  /FORMAT=DFREQ
/ORDER=ANALYSIS.
* TABLE 1 ============================================================================.
FREQUENCIES VARIABLES=Hour SO2 to PM25 API HUMID pSize /FORMAT=NOTABLE
/PERCENTILES=50 95.0 97.5 98 99 99.99 100  /ORDER=ANALYSIS.
*============================================================================.

COMPUTE filter_$=event GT 1.
VARIABLE LABELS filter_$ 'event > 0 (FILTER)'.
VALUE LABELS filter_$ 0 'Not Selected' 1 'Selected'.
FORMATS filter_$ (f1.0).
FILTER BY filter_$.
EXECUTE.

* TABLE 2 ============================================================================.
FREQUENCIES VARIABLES=etype  /BARCHART PERCENT  /FORMAT=DFREQ  /ORDER=ANALYSIS.
MEANS TABLES=API by etype /CELLS= COUNT NPCT STDDEV MEAN MAX.
*
============================================================================.

 * FREQUENCIES VARIABLES=API  /FORMAT=NOTABLE  /PERCENTILES=50 95.0 97.5 100
/ORDER=ANALYSIS.
COMPUTE filter_$=(event GT 1  and ( etype EQ 'PM10' or  etype EQ 'PM2.5' or etype EQ 'NO' or etype EQ
'NO2' or etype EQ 'SO2' or etype EQ 'O3' or etype EQ 'CO'   )).
* or etype EQ 'NOx' or etype EQ 'TSP' or etype EQ 'TSP+NOx+CO'.
FILTER BY filter_$.
EXECUTE.
 * FREQUENCIES VARIABLES=etype /BARCHART PERCENT  /FORMAT=DFREQ
/ORDER=ANALYSIS.
```

```
* FIGURE 2 ==========================================================================.
EXAMINE VARIABLES=API BY etype BY SiteID  /PLOT=BOXPLOT  /STATISTICS=NONE  /NOTOTAL.
EXAMINE VARIABLES=API BY etype BY Fines  /PLOT=BOXPLOT  /STATISTICS=NONE  /NOTOTAL.
EXAMINE VARIABLES=API BY etype BY RH  /PLOT=BOXPLOT  /STATISTICS=NONE  /NOTOTAL.
* ============================================================================================.

* FIGURE 3
============================================================================================.
USE ALL.
COMPUTE filter_$=(etype EQ 'PM10' or  etype EQ 'PM2.5' or etype EQ 'NO' or etype EQ 'NO2' or etype EQ
'SO2' or etype EQ 'O3')
and (HUMID GT 1 and HUMID LT 99 and pSize GT 1 and pSize LT 99 and API GT 0 and API LT 15).
FILTER BY filter_$.
EXECUTE.
EXAMINE VARIABLES=B7_8 BY etype BY severity  /PLOT=BOXPLOT  /STATISTICS=DESCRIPTIVES
/NOTOTAL.
EXAMINE VARIABLES=B14_15 BY etype BY severity  /PLOT=BOXPLOT
/STATISTICS=DESCRIPTIVES  /NOTOTAL.
EXAMINE VARIABLES=B9_10 BY etype BY severity  /PLOT=BOXPLOT  /STATISTICS=DESCRIPTIVES
/NOTOTAL.
EXAMINE VARIABLES=B11_13 BY etype BY severity  /PLOT=BOXPLOT
/STATISTICS=DESCRIPTIVES  /NOTOTAL.
EXAMINE VARIABLES=B12_16 BY etype BY severity  /PLOT=BOXPLOT
/STATISTICS=DESCRIPTIVES  /NOTOTAL.
* ============================================================================================.

*Determine poll ID (priors).
compute poll=0.
formats poll (f3.0).
if (event=8) poll = 0.
if (event=16) poll = 5.
if (event=32) poll = 10.
if (event=64) poll = 20.
if (event=4) poll = 30.
if (event=2) poll = 50.
execute.

* Determine pollution index
============================================================================.
* manually looped this multiple times ~20 times.
DELETE VARIABLES pPoll.
execute.
REGRESSION  /MISSING LISTWISE  /STATISTICS COEFF OUTS R ANOVA CHANGE
/CRITERIA=PIN(.05) POUT(.10)
  /NOORIGIN   /DEPENDENT poll  /METHOD=ENTER B14_15 B9_10 B12_16  /save PRED (pPoll).
compute poll=pPoll.
execute.
EXAMINE VARIABLES=pPoll BY etype  /PLOT=BOXPLOT  /STATISTICS=DESCRIPTIVES
/NOTOTAL.

DELETE VARIABLES pPoll.
execute.
compute pPoll  = 17.258 +  4.687 * B14_15 +  0.499 * B9_10 +  0.577 * B12_16.
execute.
EXAMINE VARIABLES=pPoll BY etype by Fines  /PLOT=BOXPLOT  /STATISTICS=DESCRIPTIVES
/NOTOTAL.
EXAMINE VARIABLES=pPoll BY etype by RH  /PLOT=BOXPLOT  /STATISTICS=DESCRIPTIVES
/NOTOTAL.
```

```
* show what happens with all ==========================================================.
use all.
compute pPoll  = 17.258 +  4.687 * B14_15 +  0.499 * B9_10 +  0.577 * B12_16.
compute iPoll=1*RND(pPoll/1).
formats iPoll (f3.0).
COMPUTE filter_$=(iPoll GT 1) and (iPoll LT 53).
FILTER BY filter_$.
EXECUTE.

EXAMINE VARIABLES=API by iPoll  /PLOT=BOXPLOT  /STATISTICS=DESCRIPTIVES  /NOTOTAL.
EXAMINE VARIABLES=HUMID by iPoll  /PLOT=BOXPLOT  /STATISTICS=DESCRIPTIVES
/NOTOTAL.
EXAMINE VARIABLES=pSize by iPoll  /PLOT=BOXPLOT  /STATISTICS=DESCRIPTIVES  /NOTOTAL.
EXAMINE VARIABLES=NO by iPoll  /PLOT=BOXPLOT  /STATISTICS=DESCRIPTIVES  /NOTOTAL.
EXAMINE VARIABLES=NO2 by iPoll  /PLOT=BOXPLOT  /STATISTICS=DESCRIPTIVES  /NOTOTAL.
EXAMINE VARIABLES=PM25 by iPoll  /PLOT=BOXPLOT  /STATISTICS=DESCRIPTIVES  /NOTOTAL.
EXAMINE VARIABLES=PM10 by iPoll  /PLOT=BOXPLOT  /STATISTICS=DESCRIPTIVES  /NOTOTAL.
EXAMINE VARIABLES=SO2 by iPoll  /PLOT=BOXPLOT  /STATISTICS=DESCRIPTIVES  /NOTOTAL.
EXAMINE VARIABLES=O3 by iPoll  /PLOT=BOXPLOT  /STATISTICS=DESCRIPTIVES  /NOTOTAL.


* FIGURE 6 ============================================================================.
* summarize per pollutant.
Use All.
VARIABLE LABELS iPoll 'Pollutant Index' .
DATASET NAME TmpMain WINDOW=FRONT.
COMPUTE filter_$=etype EQ 'NO'.
FILTER BY filter_$.
EXECUTE.
DATASET DECLARE Aggr.
SORT CASES BY iPoll etype.
AGGREGATE  /OUTFILE='Aggr'  /PRESORTED  /BREAK=iPoll etype  /Concentration=MEAN(NO)
/Counts=N.
DATASET ACTIVATE TmpMain.

Use All.
COMPUTE filter_$=etype EQ 'NO2'.
FILTER BY filter_$.
EXECUTE.
DATASET DECLARE Tmp.
SORT CASES BY iPoll etype.
AGGREGATE  /OUTFILE='Tmp'  /PRESORTED  /BREAK=iPoll etype  /Concentration=MEAN(NO2)
/Counts=N.
DATASET ACTIVATE Aggr.
ADD FILES /FILE=*   /FILE='Tmp'.
EXECUTE.
DATASET ACTIVATE TmpMain.
DATASET CLOSE Tmp.

Use All.
COMPUTE filter_$=etype EQ 'PM2.5'.
FILTER BY filter_$.
EXECUTE.
DATASET DECLARE Tmp.
SORT CASES BY iPoll etype.
AGGREGATE  /OUTFILE='Tmp'  /PRESORTED  /BREAK=iPoll etype  /Concentration=MEAN(PM25)
/Counts=N.
DATASET ACTIVATE Aggr.
ADD FILES /FILE=*   /FILE='Tmp'.
EXECUTE.
```

```
DATASET ACTIVATE TmpMain.
DATASET CLOSE Tmp.

Use All.
COMPUTE filter_$=etype EQ 'PM10'.
FILTER BY filter_$.
EXECUTE.
DATASET DECLARE Tmp.
SORT CASES BY iPoll etype.
AGGREGATE  /OUTFILE='Tmp'  /PRESORTED  /BREAK=iPoll etype  /Concentration=MEAN(PM10)
/Counts=N.
DATASET ACTIVATE Aggr.
ADD FILES /FILE=*   /FILE='Tmp'.
EXECUTE.
DATASET ACTIVATE TmpMain.
DATASET CLOSE Tmp.

Use All.
COMPUTE filter_$=etype EQ 'SO2'.
FILTER BY filter_$.
EXECUTE.
DATASET DECLARE Tmp.
SORT CASES BY iPoll etype.
AGGREGATE  /OUTFILE='Tmp'  /PRESORTED  /BREAK=iPoll etype  /Concentration=MEAN(SO2)
/Counts=N.
DATASET ACTIVATE Aggr.
ADD FILES /FILE=*   /FILE='Tmp'.
EXECUTE.
DATASET ACTIVATE TmpMain.
DATASET CLOSE Tmp.

Use All.
COMPUTE filter_$=etype EQ 'O3'.
FILTER BY filter_$.
EXECUTE.
DATASET DECLARE Tmp.
SORT CASES BY iPoll etype.
AGGREGATE  /OUTFILE='Tmp'  /PRESORTED  /BREAK=iPoll etype  /Concentration=MEAN(O3)
/Counts=N.
DATASET ACTIVATE Aggr.
ADD FILES /FILE=*   /FILE='Tmp'.
EXECUTE.
DATASET ACTIVATE TmpMain.
DATASET CLOSE Tmp.

DATASET ACTIVATE Aggr.
SORT CASES BY iPoll.
AGGREGATE  /OUTFILE=* MODE=ADDVARIABLES  /PRESORTED  /BREAK=iPoll
/Counts_sum=SUM(Counts).
compute Probability=Counts/Counts_sum.
execute.

GRAPH  /SCATTERPLOT(BIVAR)=iPoll WITH Concentration BY etype  /MISSING=LISTWISE.
GRAPH  /SCATTERPLOT(BIVAR)=iPoll WITH Probability BY etype  /MISSING=LISTWISE.
DATASET ACTIVATE TmpMain.
DATASET CLOSE Aggr.

* now setup dummy events for RH, Fines, Low, Med, High
* Give a text label to the classification.
use all.
```

```
string Tag(a10).
compute Tag =STRING(event,N3).
compute Tag="RH".

COMPUTE filter_$=Tag EQ 'RH' and API > 0.
FILTER BY filter_$.
EXECUTE.
DATASET DECLARE Aggr.
SORT CASES BY iPoll Tag.
AGGREGATE  /OUTFILE='Aggr'  /PRESORTED  /BREAK=iPoll Tag  /Concentration=MEAN(RH)
/Counts=N.
DATASET ACTIVATE TmpMain.

compute Tag="Fines".
Use All.
COMPUTE filter_$=Tag EQ 'Fines' and API > 0.
FILTER BY filter_$.
EXECUTE.
DATASET DECLARE Tmp.
SORT CASES BY iPoll Tag.
AGGREGATE  /OUTFILE='Tmp'  /PRESORTED  /BREAK=iPoll Tag  /Concentration=MEAN(pSize)
/Counts=N.
DATASET ACTIVATE Aggr.
ADD FILES /FILE=*   /FILE='Tmp'.
EXECUTE.
DATASET ACTIVATE TmpMain.
DATASET CLOSE Tmp.

use all.
if (API > 0 and API < 1.416) TAG = 'Low'.
if (API > 1.416 and API < 3.78) TAG = 'Med'.
if (API > 3.78 ) TAG = 'High'.

Use All.
COMPUTE filter_$=Tag EQ 'Low'.
FILTER BY filter_$.
EXECUTE.
DATASET DECLARE Tmp.
SORT CASES BY iPoll Tag.
AGGREGATE  /OUTFILE='Tmp'  /PRESORTED  /BREAK=iPoll Tag  /Concentration=MEAN(API)
/Counts=N.
DATASET ACTIVATE Aggr.
ADD FILES /FILE=*   /FILE='Tmp'.
EXECUTE.
DATASET ACTIVATE TmpMain.
DATASET CLOSE Tmp.

Use All.
COMPUTE filter_$=Tag EQ 'Med'.
FILTER BY filter_$.
EXECUTE.
DATASET DECLARE Tmp.
SORT CASES BY iPoll Tag.
AGGREGATE  /OUTFILE='Tmp'  /PRESORTED  /BREAK=iPoll Tag  /Concentration=MEAN(API)
/Counts=N.
DATASET ACTIVATE Aggr.
ADD FILES /FILE=*   /FILE='Tmp'.
EXECUTE.
DATASET ACTIVATE TmpMain.
DATASET CLOSE Tmp.
```

```
Use All.
COMPUTE filter_$=Tag EQ 'High'.
FILTER BY filter_$.
EXECUTE.
DATASET DECLARE Tmp.
SORT CASES BY iPoll Tag.
AGGREGATE  /OUTFILE='Tmp'  /PRESORTED  /BREAK=iPoll Tag  /Concentration=MEAN(API)
/Counts=N.
DATASET ACTIVATE Aggr.
ADD FILES /FILE=*   /FILE='Tmp'.
EXECUTE.
DATASET ACTIVATE TmpMain.
DATASET CLOSE Tmp.

DATASET ACTIVATE Aggr.
SORT CASES BY iPoll.
AGGREGATE  /OUTFILE=* MODE=ADDVARIABLES  /PRESORTED  /BREAK=iPoll
/Counts_sum=SUM(Counts).
compute Probability=3*Counts/Counts_sum.
execute.
GRAPH  /SCATTERPLOT(BIVAR)=iPoll WITH Concentration BY Tag  /MISSING=LISTWISE.
GRAPH  /SCATTERPLOT(BIVAR)=iPoll WITH Probability BY Tag  /MISSING=LISTWISE.
DATASET CLOSE Aggr.
```

7. Future Directions

7.1. Abstract

A recent review on air quality remote sensing using geostationary spectrometers listed 81 authors [290], and this highlighted the ambitious nature of the thesis in presenting a unified IR methodology to replace two decades of AOD research. Several potential further topics were noted that are beyond the scope of this thesis but are presented here with limited (or no) evidential data as a prompt for further development and potential follow-up articles.

Additionally, the analytical methods were developed using limited surface monitoring in a predominantly urban environment. It is vital that the methodology and predicted concentrations are verified for global applicability, spatial consistency, plausibility (i.e. does sea-spray predominant along the coast), and long-term period statistics (annual averages, maximum daily and hourly) to confirm predictions against both monitored data and expert opinion. Full validation of the methodology is beyond the scope of this thesis, and limited spatial validation is presented here, using three case studies described in the OEH website, to demonstrate spatial consistency and plausibility.

7.2. New GLCs product

There is scope for the development of a new ground-level concentrations (GLCs) remote-sensing product. Given the widespread adoption of AOD methodologies, a new product rather than a replacement of AOD is suggested - as the AOD product infers spatial averaging, use of visible wavelengths, and the vertical AOD column [48]. The introduction detailed how AOD does not meet the needs of the air quality community which requires hourly (or faster) GLCs using IR to determine concentrations continually. In contrast chapter five (composition) and the validation results (later in this chapter) detail the improvements in using continuous infrared to obtain plausible spatial distributions that eliminates cloud masking, spatial aggregation and land-type issues.

7.3. Hybrid methods

Satellite methods to determine concentration are excellent at determining the spatial and temporal plume characteristics. However, determining absolute concentrations are subject to greater uncertainties. It is suggested that integrating geostationary infrared data with dispersion modelling or low-cost ground-level monitoring could increase the accuracy of the combined predictions.

7.4. Background subtraction

The spectral signal received by the satellite is derived from the cumulative response from the satellite to the surface, or cloud. For optically thin clouds and plumes this is then the total column whereas for heavy cloud the lower layers are invisible to the satellite. As this thesis was developing new techniques the background surface layer was not considered in detail and the average across the region was used as the background which ignores land-use changes but has some compensation for diurnal effects. While the region has a high degree of homogenisation, and this lends itself to the simplified method, a more rigorous background approach should be considered that included land-use classes, solar angle, and cloud opacity.

7.5. Rate of change

The review paper hypothesised that the differential equation provided by the rate of change could provide additional evidence to quantify plume changes. This concept was expanded in chapter three (time) but was removed during the journal review as it detracted from the main argument of the paper. This improvement by the change over the previous hour is depicted in Figure 7-1 showing band seven a) at the start of the Onslow dust storm and b) the hourly difference. The improved spatial resolution between the two images is evident as the fire is distinguishable from the smoke plume, and the cloud bank is beginning to develop.

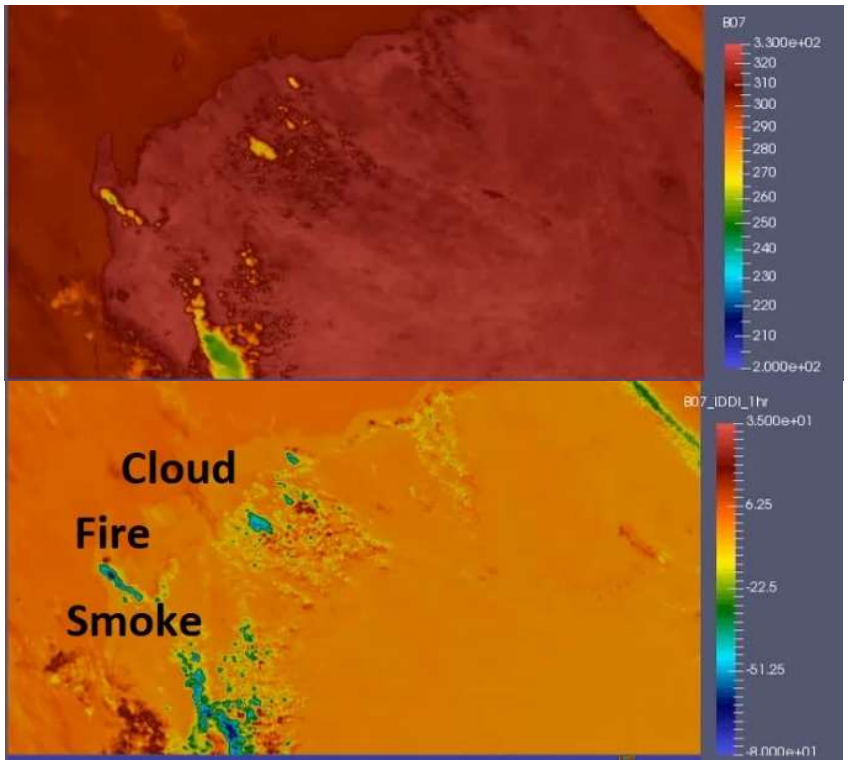

Figure 7-1: (a) Band 07, (b) Hourly change of band 07.

7.6. Atmospheric stability

Atmospheric stability is an essential parameter in dispersion modelling that needs to be considered in determining GLCs. Rapidly rising air is termed unstable while stagnate (inversion) conditions are termed stable. The $BTD_{6.9\text{-}7.3\mu m}$ index reflects the difference between mid and lower level moisture and therefore is a measure of stability, and if the index is positive (i.e. mid-level moisture is greater than lower level), this indicates rising unstable air as depicted in Figure 7-2.

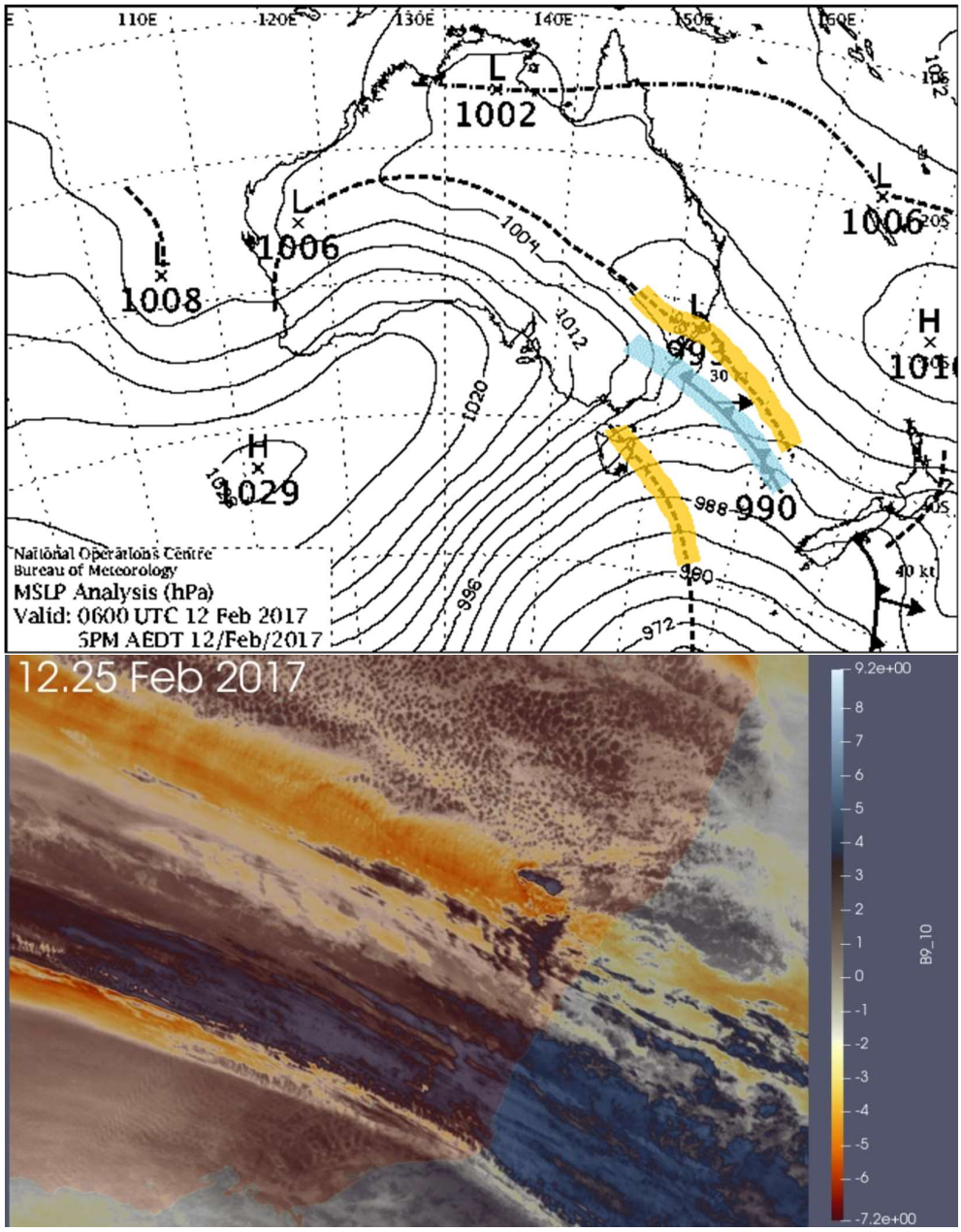

Figure 7-2: MSLP synoptic chart and atmospheric instability 5 PM AEDT 12 Feb 2017.

7.7. Cloud height

Cloud dynamics were noted in Figure 5-8 and are reproduced in Figure 7-3 with additional indication of water phases. The adiabatic lapse rate of 9.8°C/km allows an approximation of the cloud height to be determined as estimated in Figure 7-4.

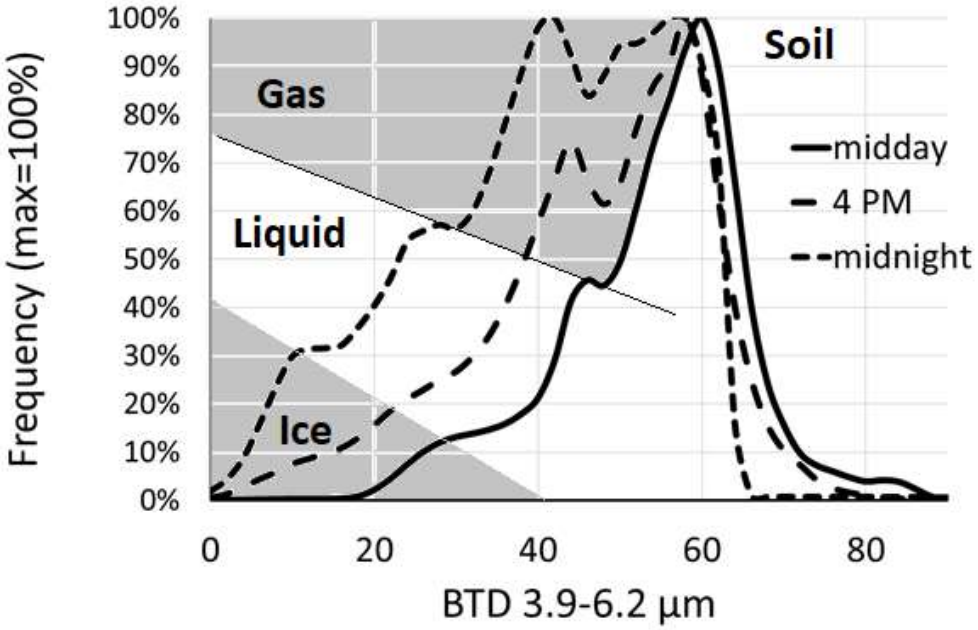

Figure 7-3: Cloud phase and temperature.

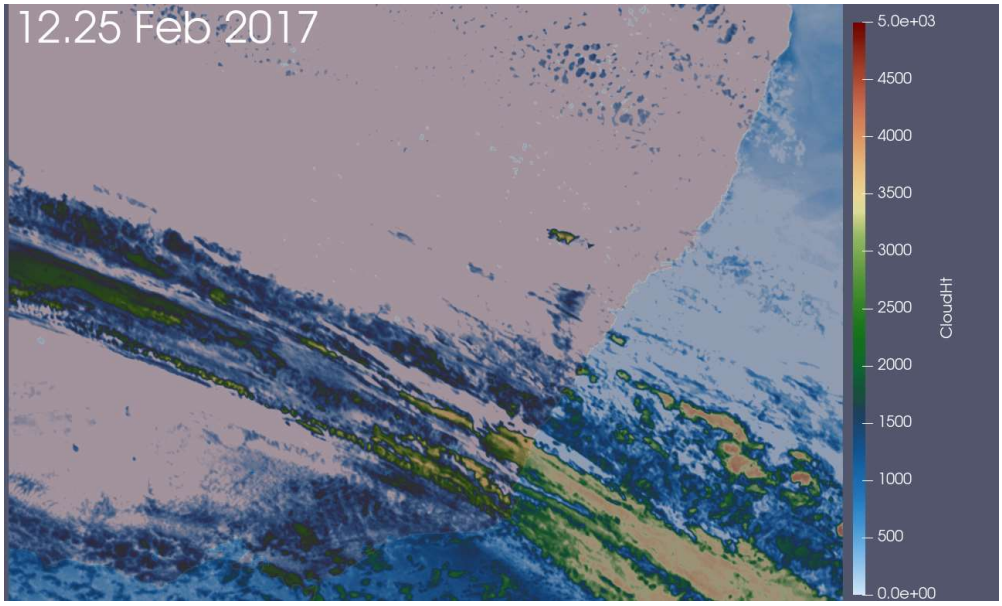

Figure 7-4: Estimate of cloud height 5 PM AEDT 12 Feb 2017.

7.8. Fires

While fire observation and burn scars are an excellent mature product that uses visible and near-infrared wavelengths, it needs to be augmented at night to use infrared wavelengths and, more importantly, determine smoke GLCs. Figure 7-1 depicts estimated $PM_{2.5}$ and PM_{10} concentrations emitted by a fire and shows that incomplete combustion and coarse PM predominates in the smoke near the fire while finer particles are transported greater distances.

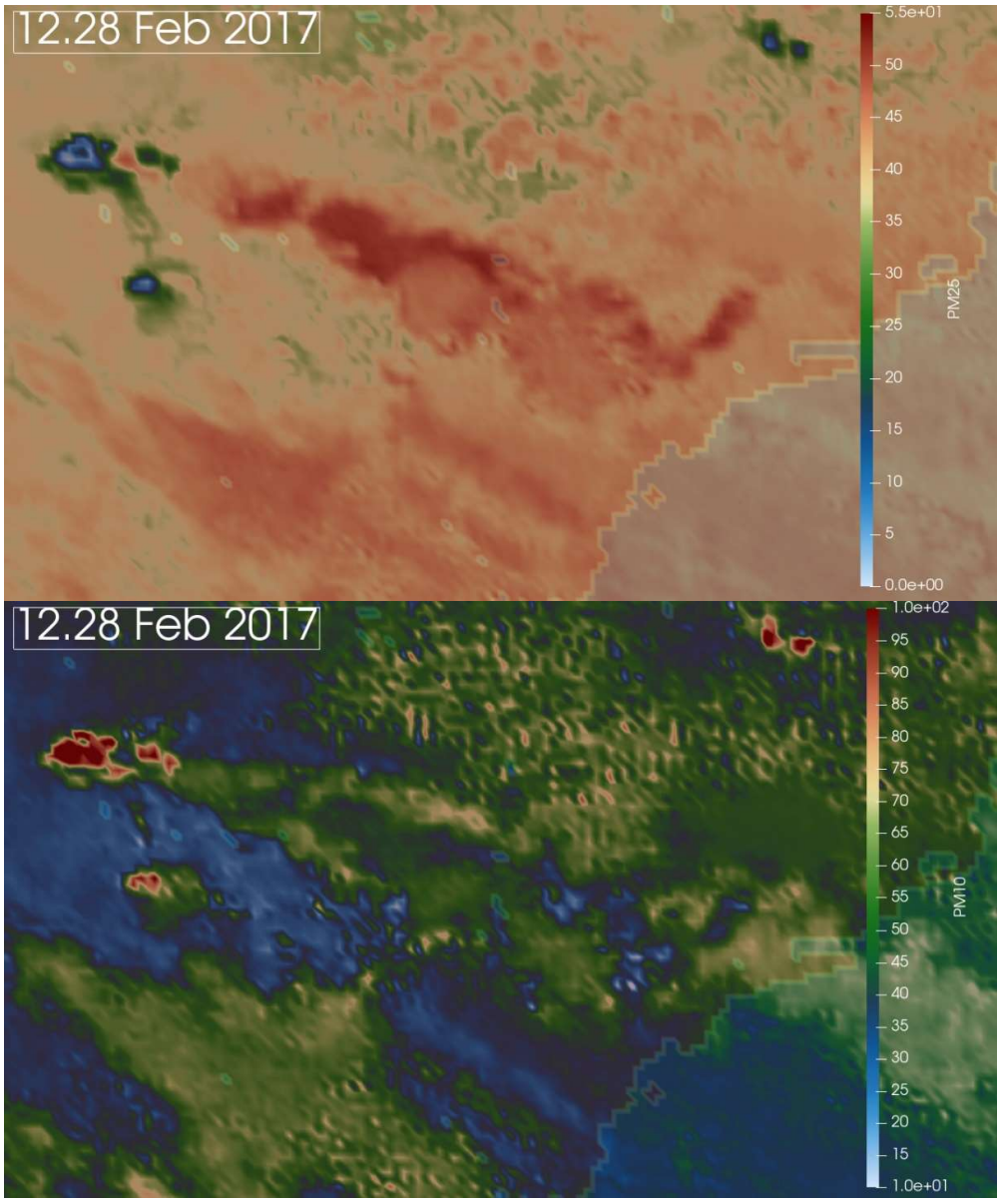

Figure 7-5: $PM_{2.5}$ and PM_{10} emitted from a fire depicting size discrimination with downwind distance.

7.9. Roll cloud dynamics

The roll cloud in the Onslow storm was investigated using the satellite imagery and estimation of cloud height to depict the cloud dynamics in Figure 7-6. This highlights the ability to determine how cloud dynamics impact GLCs.

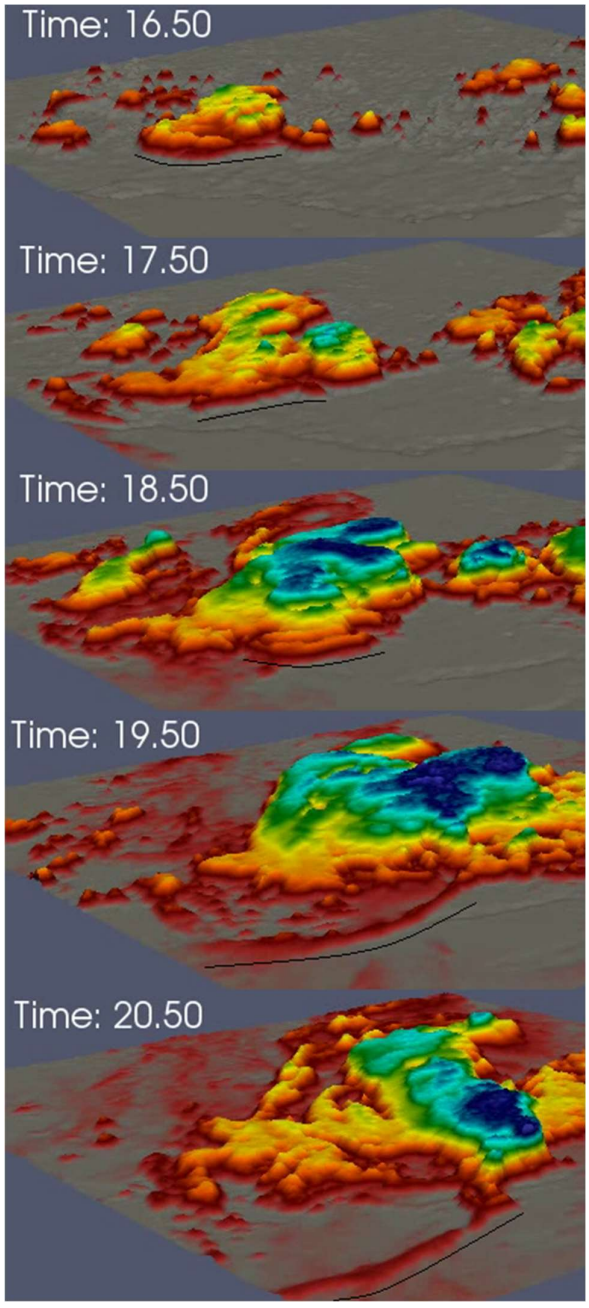

Figure 7-6: Hourly depiction of the roll cloud (demarcated) from the Onslow dust storm, depicted from the air towards the south-west using cooling of band seven to depict cloud height.

7.10. Validation

Five BTD indices were developed in chapter five (indices) that utilise all ten infrared wavelength bands. A pollution index was subsequently developed in chapter six to identify the composition, relative humidity and percentage fines from these five BTD indices. This chapter considered if the revised methodology improved the analysis by considering three significant events (ozone, smoke and dust) that typically impact the greater Sydney metropolitan region. These events were chosen by OEH and are described on their website.

7.10.1. Methodology

The three reports from the OEH website were reviewed and summarised. Corresponding ambient data, described in more detail in chapter six (composition), were downloaded from OEH and used to quantify meteorology and ambient concentrations during the three incidents. The NOAA HYSPLIT model was used to determine the backwards trajectory (i.e. determine potential source regions and highlight meteorological conditions). MODIS natural colour, AOD, and thermal abnormalities (from the worldview website) were used to visually identify regions of clouds, smoke and dust plumes during the three incidents. Himawari-8 data was processed on the NCI supercomputer using the methodology developed in chapter six to determine the pollution index, composition, relative humidity, percentage fines, and concentration.

7.10.2. Summer ozone episode (11 to 12 Feb 2017)

OEH description of the incident

An extensive ozone pollution episode from 10 to 11 February 2017 affected NSW coastal regions during a severe, four-day heatwave when a slow-moving high-pressure system over NSW provided hot and calm conditions. The hot and light north-westerly synoptic flows interacted with afternoon north-easterly sea breezes and determined the spatial extent, location and duration of elevated ozone [291].

Data analysis

The maximum daily ozone concentration and the temperature was analysed using the OEH dataset and is depicted in Figure 7-7. Both measurements had a minimum on the 8 February and reached a maximum on the 11th (similar maxima on the 10th) before rapidly decreasing over the following two days. The HYSPLIT back trajectory analysis Figure 7-8 confirmed the OEH analysis of the westerly synoptic flows interacted with the southerly sea breezes which trapped pollutants over the Sydney region. Slight differences in the wind direction between the HYSPLIT and OEH data are due to the differences between upper and surface wind directions in the two datasets, respectively.

Figure 7-9 depicts the Aqua natural colour product and shows fires to the north-west of Sydney and a sharp delineation of cloud east of Sydney. The absence of cloud could potentially be from a heat island effect over the metropolitan area, or it could indicate photochemical reactions with the water vapour.

Results

The stability product (Figure 7-2) and estimated cloud height (Figure 7-4) confirmed the passage of a cold front. The fire was observed by the emitted radiation (as per Figure 7-1) and differences between PM fractions (Figure 7-5) with coarse (PM_{10}) particles being observed near the fire and finer particles ($PM_{2.5}$) further downwind. Potential ozone sources are depicted in Figure 7-10 from volatile organic compounds (VOCs) from fires, and isoprene emissions from vegetation. The ozone plume moved northwards along the coast as described in

the OEH report. The passage of the cold front and associated clouds impacted the ability and confidence of the predict concentrations.

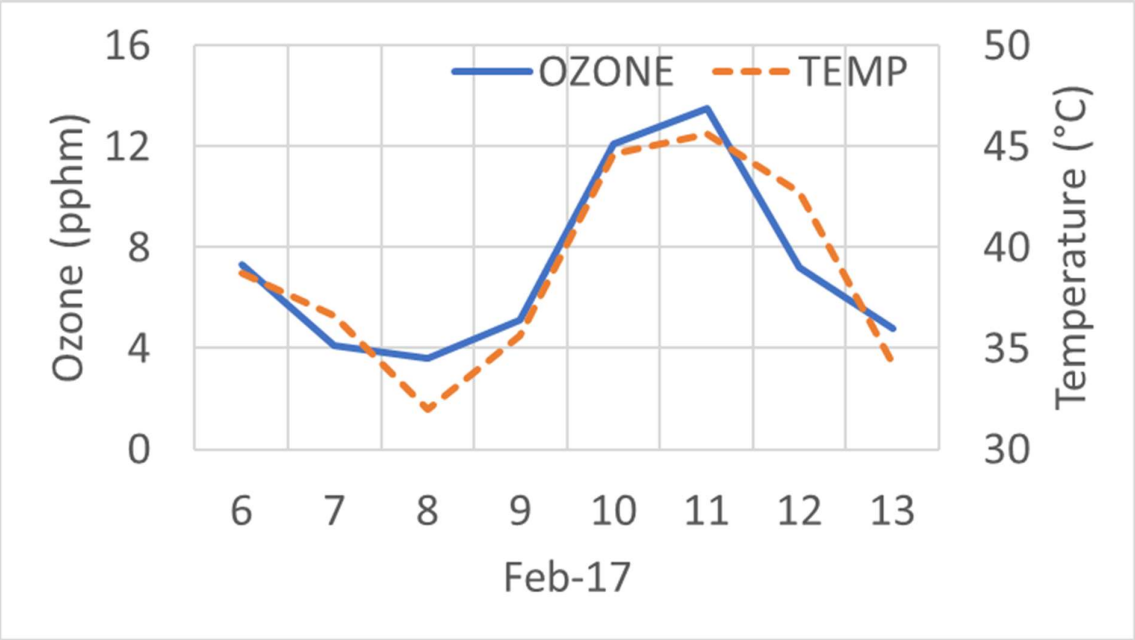

Figure 7-7: Maximum daily Ozone and temperature across all OEH monitoring sites for February 2017.

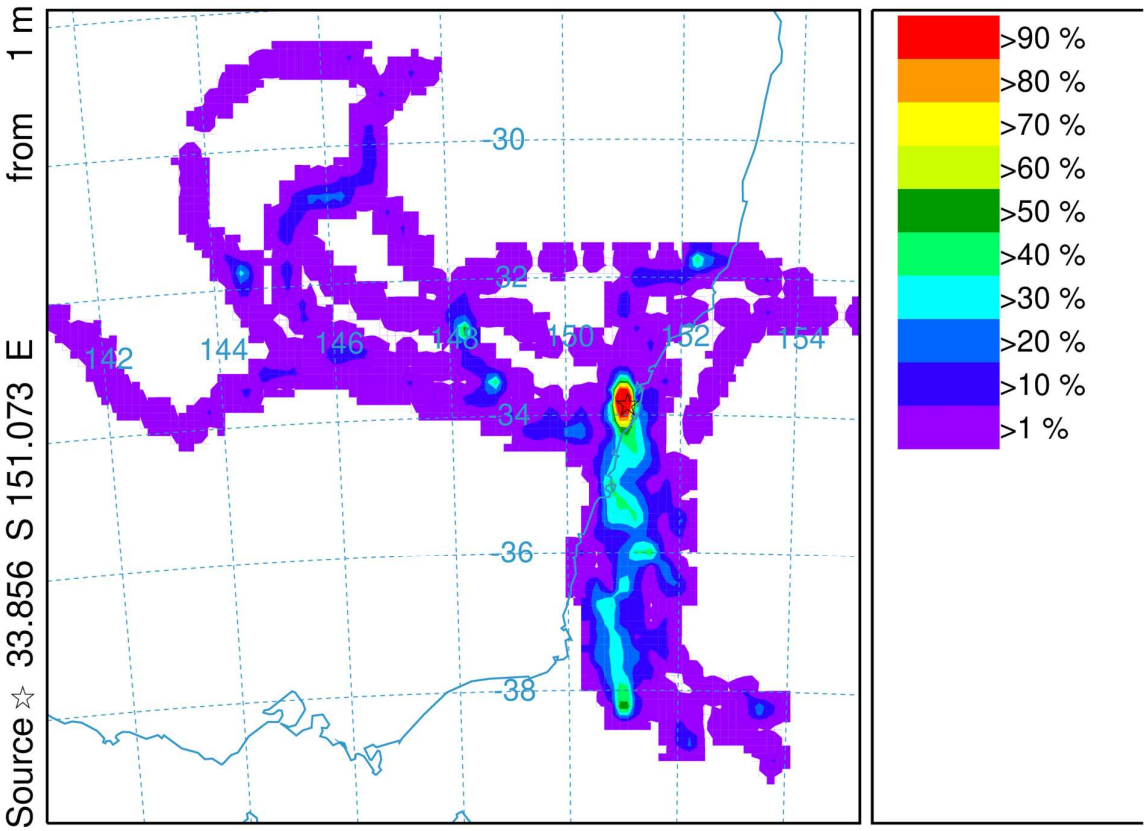

Figure 7-8: HYSPLIT backwards four-day trajectory analysis for the period 10 to 12 February 2017.

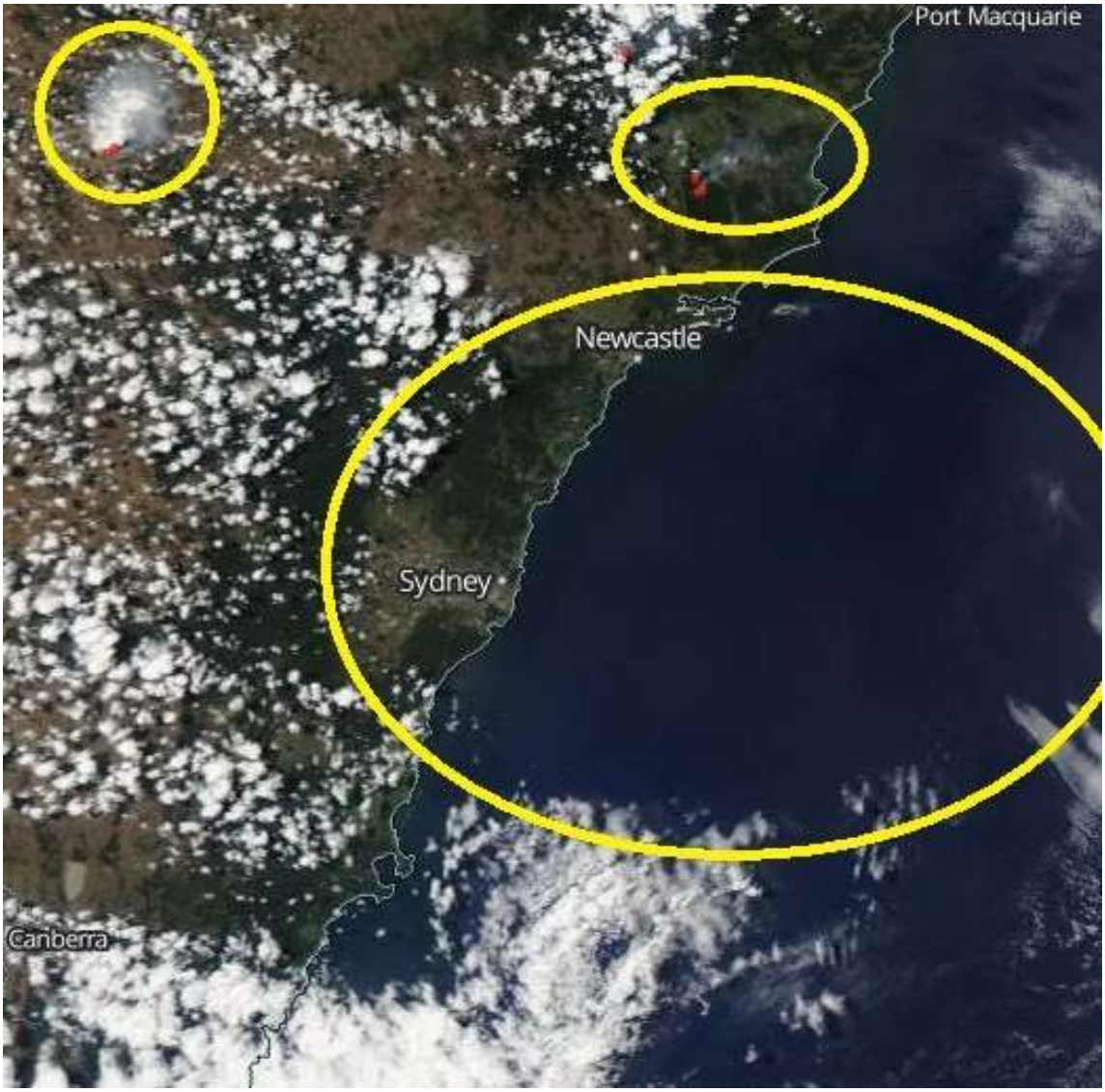

Figure 7-9: Terra Natural Colour 11 September 2017.

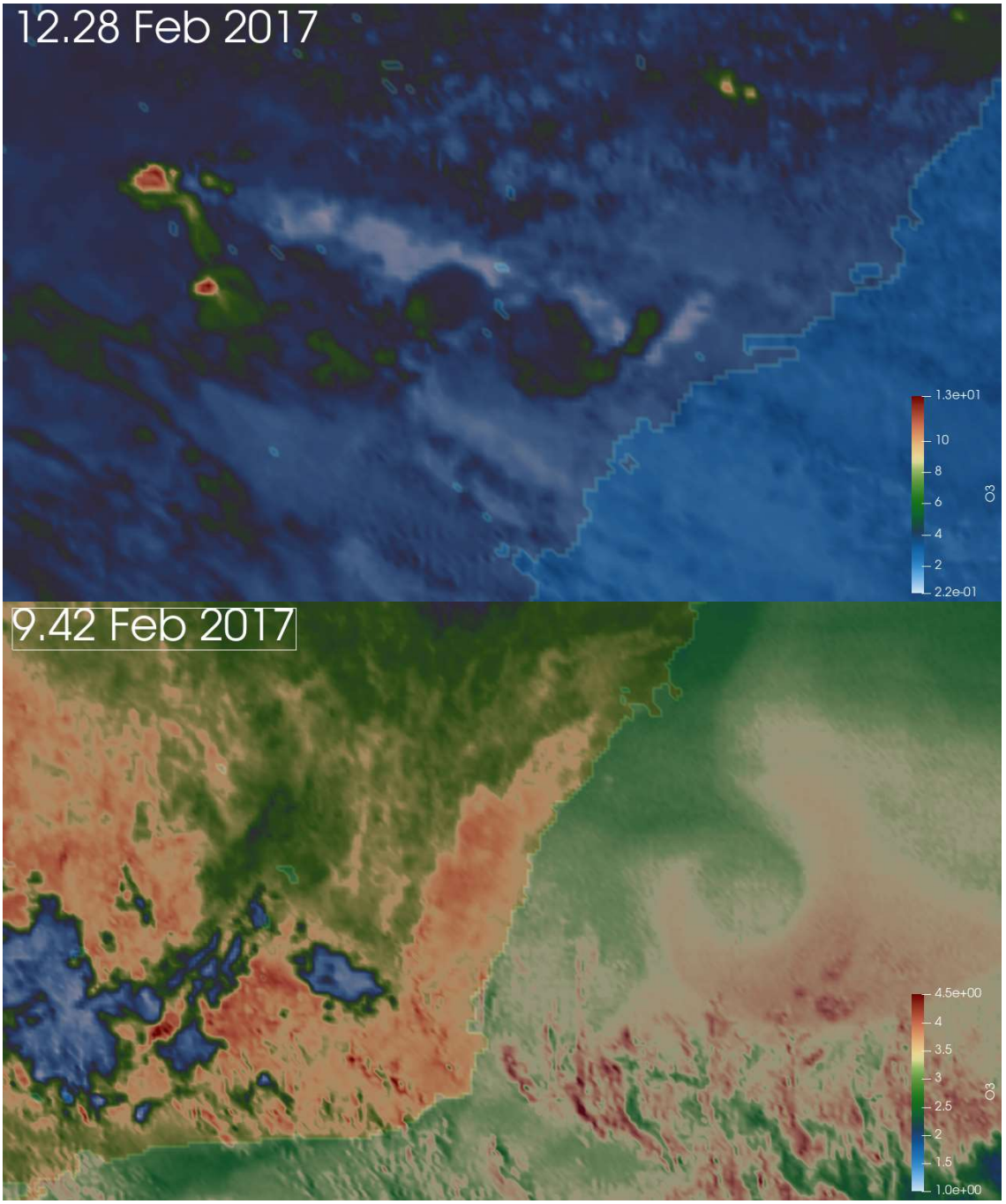

Figure 7-10: Potential ozone sources a) VOC's from fire and b) isoprene from vegetation.

Ten-minute time-series videos of the incident are at https://tinyurl.com/CloudHeight, ./AtmosStability, ./RelHumidity, ./FineParticles, ./CoarseParticles, ./GLC-NO2 and ./GLC-O3

7.10.3. Smoke from prescribed burns (2 to 3 Sept 2017)

OEH description of the incident

During 2nd and 3rd September 2017, the greater Sydney metropolitan region experienced reduced visibility and exceedances of the daily $PM_{2.5}$ national standard due to smoke from hazard reduction burns undertaken in the north and west of the Sydney basin. During this period, there was a high-pressure system over the east coast of Australia, which created a strong temperature inversion with calm atmospheric conditions and light north-westerly air flows into the region. The afternoon north-easterly sea breeze blocked the smoke dispersion, causing additional build-up and exceedances of the daily $PM_{2.5}$ national standard until the passage of a cold front with stronger south-westerlies dispersed the smoke [292].

Data analysis

The maximum daily PM_{10} and $PM_{2.5}$ concentrations from the OEH dataset are presented in Figure 7-11. Both PM measurements increased sharply on the 2 February although $PM_{2.5}$ increased slower and only reached a maximum on the 3rd but dispersed faster than PM_{10}. HYSPLIT back trajectory analysis Figure 7-12 confirmed the OEH analysis of stagnant inversion conditions with weak north-westerly winds and westerly long-range transport of air from Adelaide and Lake Eyre regions.

Results

While the fire was visible on the 1 September 2017 in the satellite data, it appears from Figure 7-13 that the principal cause of the high concentrations was recirculated air from the west. The stagnate conditions were apparent in the negative stability determination (B9_10) and few clouds (B7_8). The coarse particles preceded the fine particles, which is unusual as PM_{10} usually falls to the ground near the source, but supported by the measurements (Figure 7-11) and indicates that stagnate conditions caused local sources, potentially from freshly eroded material, to dominate concentrations.

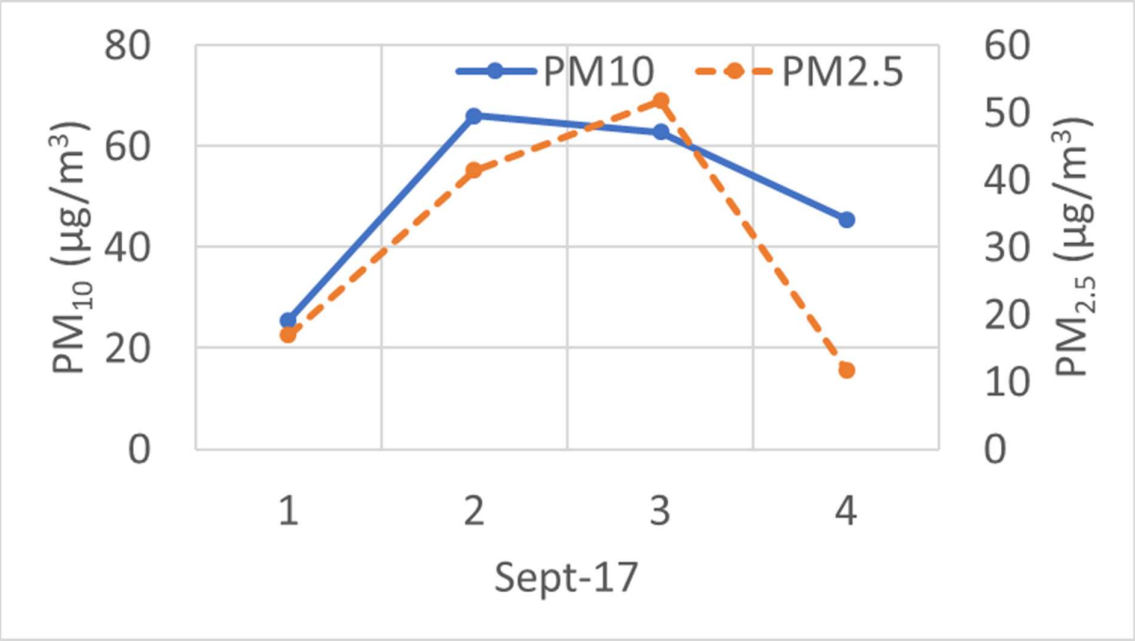

Figure 7-11: Maximum daily PM_{10} and $PM_{2.5}$ concentrations across all OEH monitoring sites for September 2017.

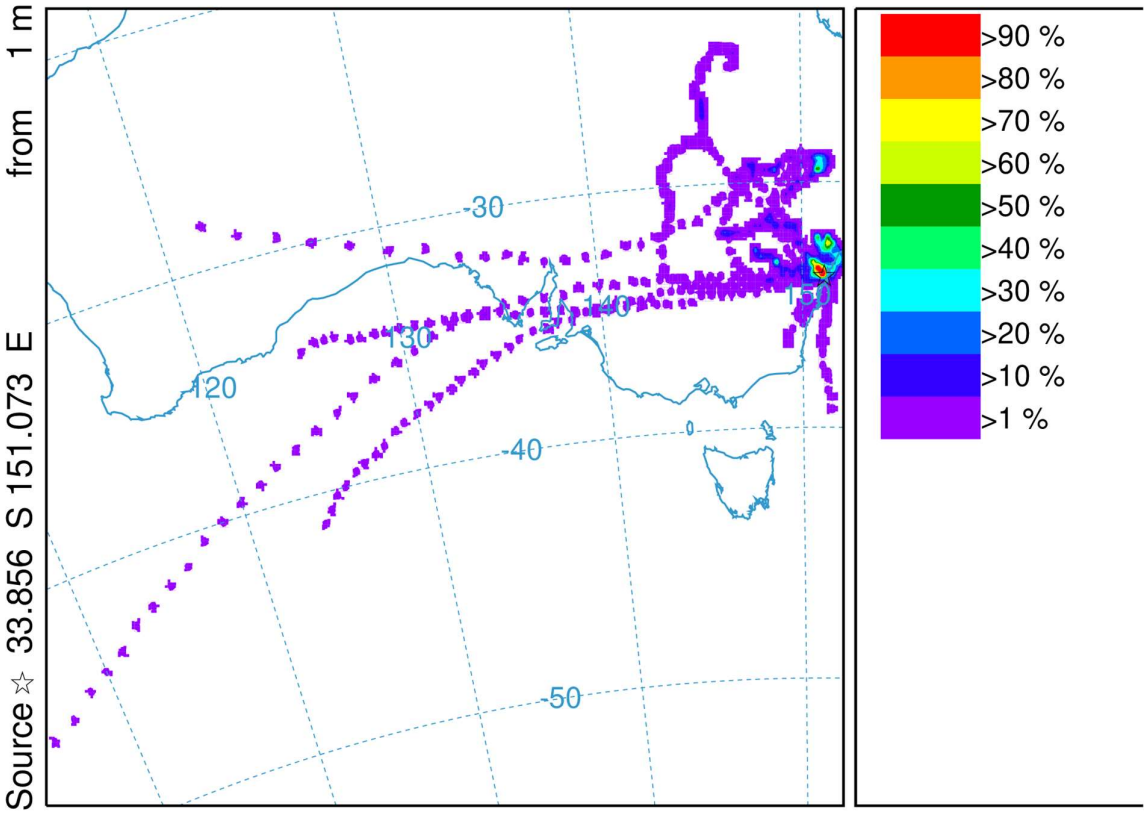

Figure 7-12: HYSPLIT backwards four-day trajectory analysis for the period 2 to 4 September 2017.

Video available at: https://tinyurl.com/SmokeEvent.

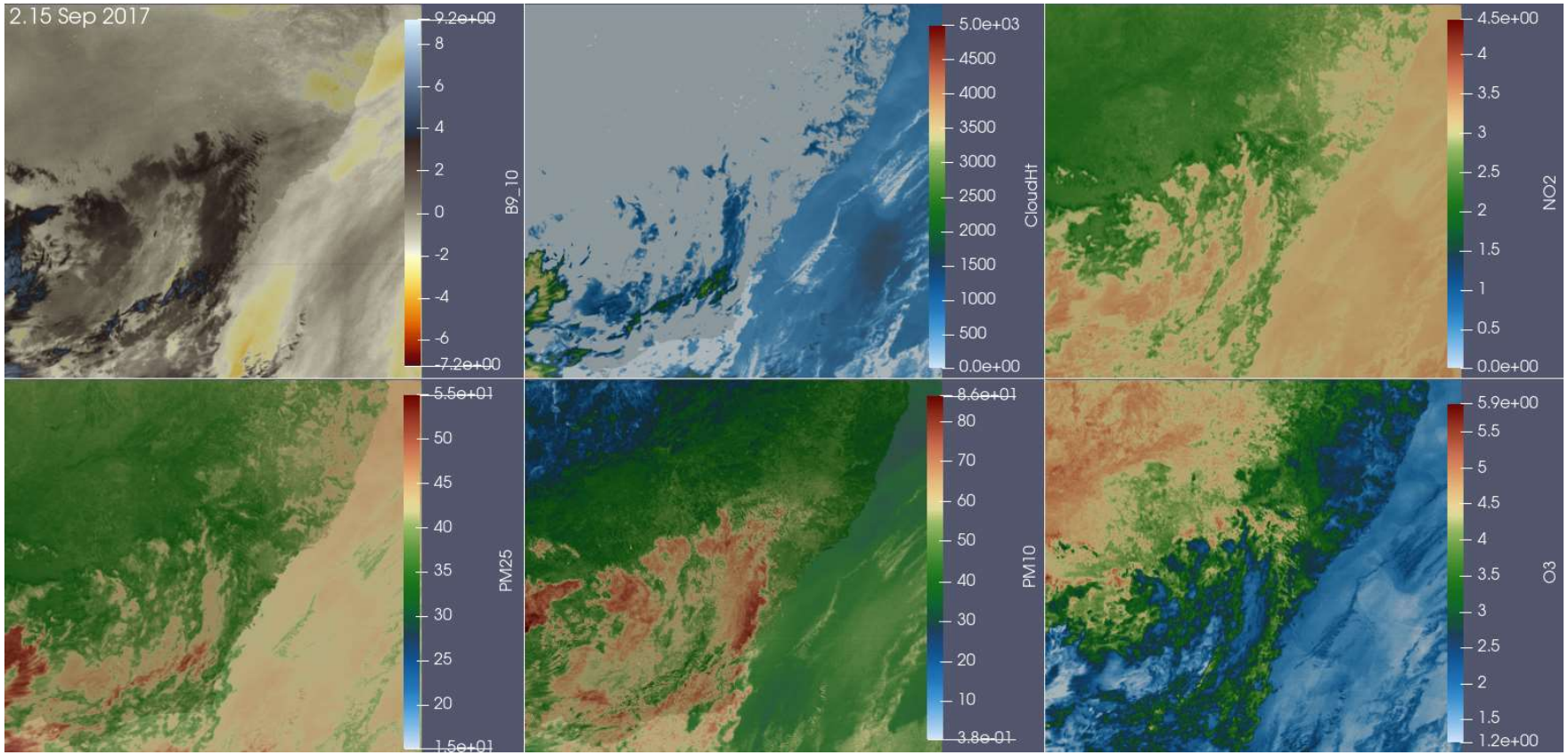

Figure 7-13: Analysis of smoke event on 2 Sept 2017 showing a) stability; b) cloud height; c) NO_2, d) $PM_{2.5}$, e) PM_{10}, and O_3.

7.10.4. Dust episode from 22 to 24 Sept 2017

OEH description of the incident

Air quality in New South Wales was affected on the 24 September 2017 by long-range transport of desert dust from the drought in north-west NSW, and potentially from smoke and dust activity in the Northern Territory and Western Australia. September 2017 had record spring temperatures and reached its warmest September day on the 23rd, caused by a sequence of troughs and very strong north-westerly winds during the passage of a cold front. The cold front resulted in a substantial dust event in western NSW, exacerbated by drought-induced below-average soil moisture and reduced groundcover, which caused the elevated PM_{10} concentrations [293].

Data analysis

The maximum daily PM_{10} and $PM_{2.5}$ concentrations from the OEH dataset are presented in Figure 7-14. PM_{10} concentrations increased systematically from the 19 September and reached a maximum on the 24th. $PM_{2.5}$ concentrations spiked on the 22nd but showed no definitive trend during this period. The HYSPLIT back trajectory analysis (Figure 7-15) indicated that long-range transport of dust and smoke was the primary source, and this was supplemented by freshly eroded material from the drought-stricken regions of north-west NSW and Southern Australia. A massive dust storm is visible over Lake Eyre on the 20th in Figure 7-16(a) and is discernible over Newcastle on the 23rd in NSW in Figure 7-16(c). Extensive cloud cover on the 24th restricted the AOD analysis during the peak of the Sydney concentrations.

Results

Figure 7-17 depicts the remnants of an extensive dust storm on the 24 September 2017. The dust storm was evident over both the centre of Australia and the Lake Eyre region and spanned hundreds of kilometres. Smoke from fires in the Pilbara region compounded the elevated concentrations and a persistent trough of low pressure resulted in poor dispersion of the dust. The coarse fraction (PM_{10} >> $PM_{2.5}$) depicted in Figure 7-17 indicates that freshly eroded material contributed to the elevated aerosol concentrations.

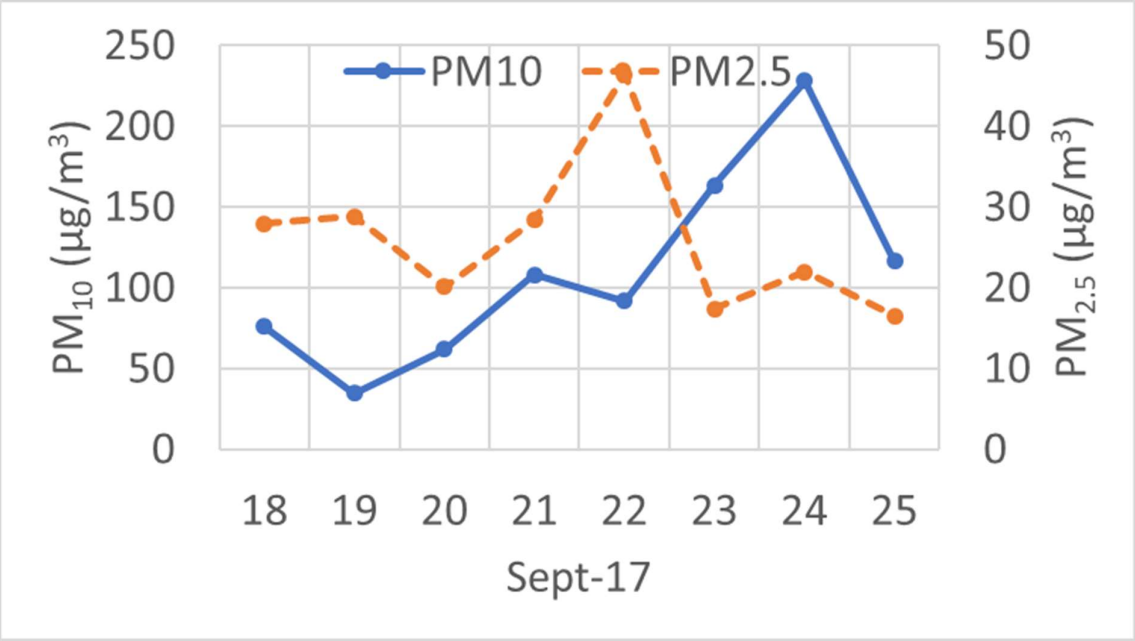

Figure 7-14: Maximum daily PM_{10} and $PM_{2.5}$ concentrations across all OEH monitoring sites for September 2017.

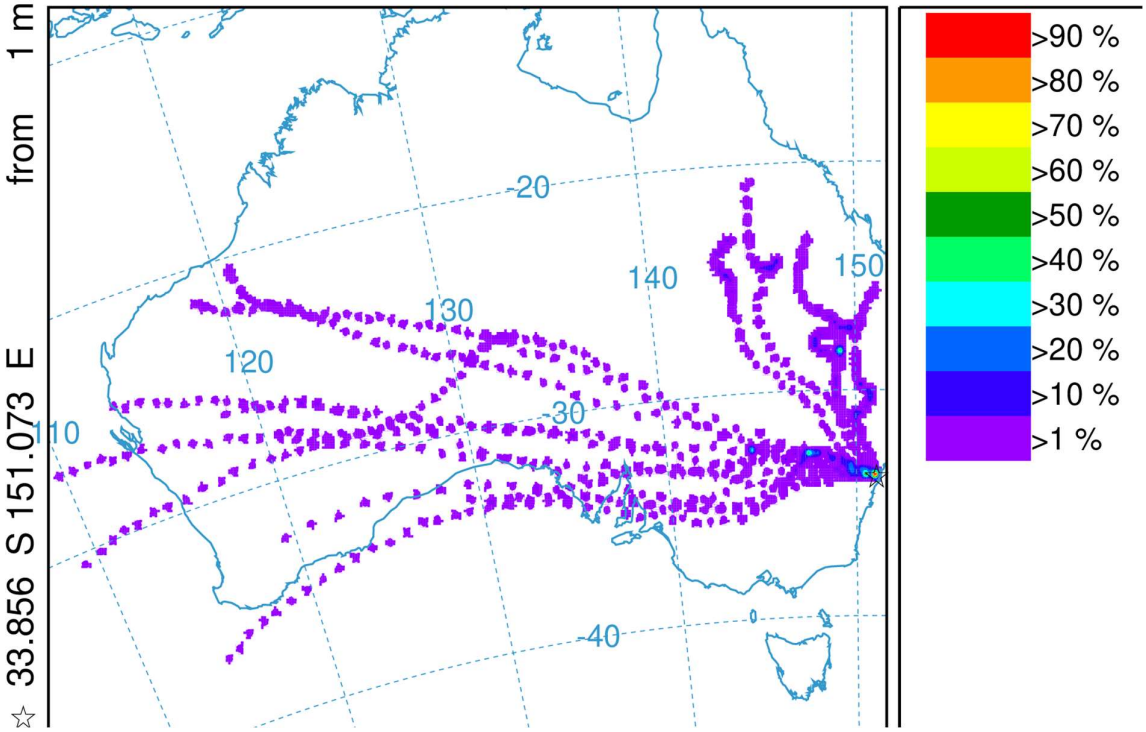

Figure 7-15: HYSPLIT backwards four-day trajectory analysis for the period 20 to 24 September 2017.

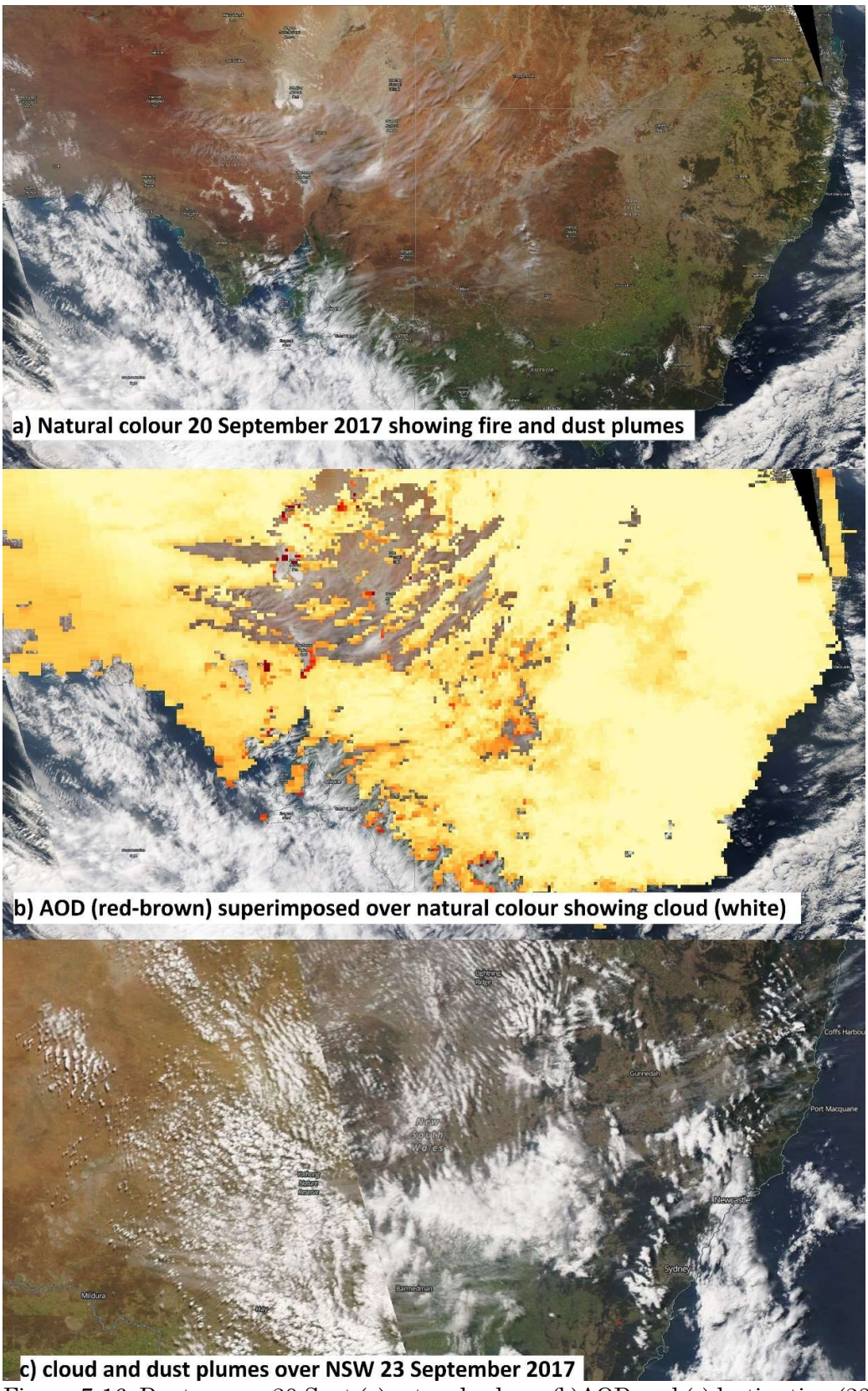

Figure 7-16: Dust source 20 Sept (a)natural colour, (b)AOD and (c)destination (23rdSept).

Video available at: https://tinyurl.com/DustEvent.

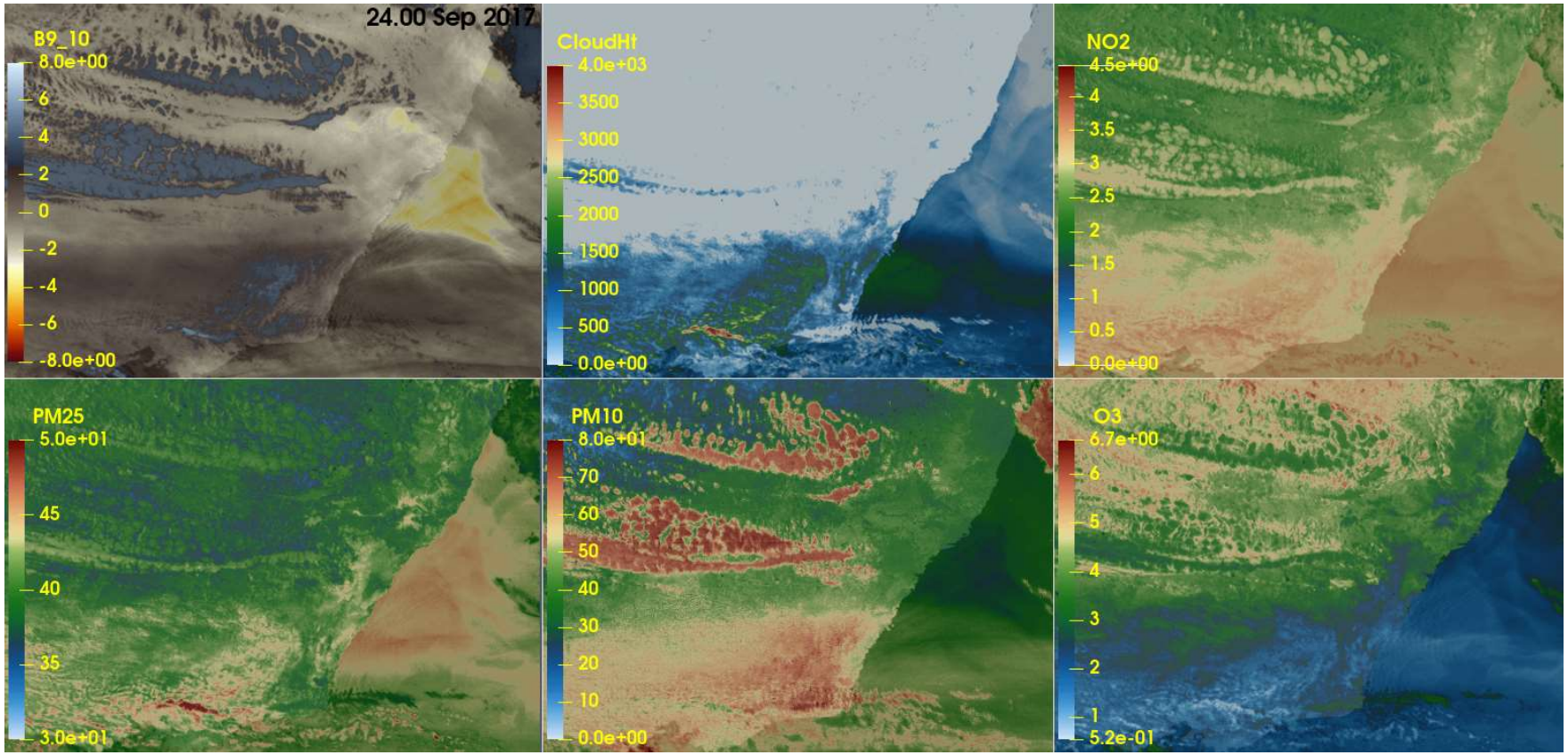

Figure 7-17: Analysis of dust event on 24 Sept 2017 showing a) stability; b) cloud height; c) NO_2, d) $PM_{2.5}$, e) PM_{10}, and O_3.

7.10.5. Discussion and conclusions

The pollutant isopleths in figures A-12, A-17, A-20, and A-24 depict plausible, coherent plumes consistent with the OEH analysis. Concentration maxima (y-axis) agree with the daily maxima in figures A-14, A-18, and A-21 indicating a correct order of magnitude estimate that is potentially within a factor of two accurate (i.e. equal or better than dispersion modelling in accuracy).

The predicted atmospheric stability correlates to the trough of low pressure and cold front on the synoptic chart in Figure 7-2. Cloud height and relative humidity track the movement of the stability indicator. The pollutant isopleths are strongly dependent on atmospheric stability, cloud height and relative humidity and potentially calibration factors could be refined by classifying according to these parameters. While the calibration coefficients do include a measure of atmospheric stability and cloud height, and therefore should represent ground-level concentrations rather than columnar amounts, it appears as though cloudy conditions are resulting in abnormally high estimations. Separating the calibration by cloud cover and stability should improve the accuracy of the estimated concentrations.

Analysing external data, it appears as though atmospherics stability, cloud height, relative humidity, $PM_{2.5}$, and PM_{10} are producing plausible and accurate results. NO, NO_2, and O_3 produce plausible plumes but have insufficient external data to comment on accuracy. Unfortunately, SO_2 and aerosol speciation (soil, sea-spray, fires, auto, and secondary sulphates) do not produce plausible plumes and require further development.

In contrast to AOD methodology, consistent calibration factors were used across all land-use types, and as a result plumes are not disjointed over sea, vegetation, desert or urban boundaries. Neither cloud masking nor spatial aggregation was implemented, and consequently there are no cloud gaps and the full temporal (ten-minutes) and spatial resolution (2 km) of the data is used.

8. Summary

Sowden, M., U. Mueller, and D. Blake.
Determining ground-level composition and concentration of particulate matter across regional areas using the Himawari-8 satellite.
Air Quality and Health. 2020, Special issue of the 15th International Conference on Atmospheric Sciences and Applications to Air Quality.

8.1. Abstract.

Speciated air quality data inform health studies and quantitates impacts. However, monitoring is concentrated around population centres, and large regions remain unmonitored despite severe risks of dust-storms and wild-fires. Monitoring of Aerosol Optical Depth (AOD) is restricted to visible spectra (daytime only) while newer quantification methods using geostationary infrared (IR) data have focussed on detecting the presence, or absence, of an event. The determination of aerosol composition (such as sulphates, black carbon, sea salt and mineral dust) or particle size using IR exclusively, has received little attention.

More appropriate IR methods have been developed using data from the Himawari-8 satellite that improve the understanding of source impacts. The research considered: (i) what temporal resolution is required for remote sensing to be able to detect sporadic aerosol incidents such as fires and dust storms; (ii) which IR wavelengths best represent changing aerosol composition; (iii) how to identify aerosol concentration, composition, and particle size amongst atmospheric changes (such as wind, humidity and clouds). Three severe air quality incidents, namely a dust storm, smoke from prescribed burns and an ozone smog incident near Sydney in eastern Australia, were studied to demonstrate the ability of the methodology to detect and quantify severe air quality incidents.

Keywords: Aerosol, Remote sensing, Himawari-8.

8.2. Introduction

Severe air pollution concentrations may have fatal consequences, and consequently, six commonly occurring criteria air pollutants (CO, O_3, SO_2, NO_2, Pb and particles) are routinely monitored to protect health and the environment. Particulate matter (PM) is of concern due to its ubiquitous nature as urbanization, coupled with increased affluence, leads to an increase in vehicles and industrial activities with concurrent increases in ambient particulate levels that, together with geogenic emissions from fires and wind-blown events, contribute to PM being present in most populated, arid, and forested regions. Health impacts of PM depend on particle size and composition [294], and it is vital that PM monitoring provides speciated concentrations in order to assess health risks.

Ambient monitoring using fixed locations provides reliable concentration data. However, monitoring sites may be sparse outside of metropolitan centres, because of cost and infrastructure, and sited according to population numbers rather than at areas of risk in arid or mining regions [15]. Methods to determine concentration must have sufficient spatial and temporal resolution to accurately represent an event, typically hourly at 1 km^2 resolution is required [279]. In regions without dedicated monitoring, it may be possible to estimate concentrations using dispersion modelling or remote sensing [4].

The use of remote sensing has been limited in the past because single daily snapshots from polar-orbiting satellites can miss high-intensity short-duration events, and may not be representative of daily average concentrations [222]. Second-generation geostationary earth orbiting (GEO) satellites such as Himawari-8 [144] and GOES-R [171] can detect these temporal changes, as these satellites supply sub-hourly data. Aerosol Optical Depth (AOD) [48] is a measure of the extinction of electromagnetic radiation by dust and haze, which absorbs and scatters light. AOD is dimensionless and is related to the total amount of aerosol in the vertical column of the atmosphere over a location.

In addressing the health impacts of PM, there is a need to extrapolate the total AOD column amount into respirable ground level concentrations (GLCs) using simple linear approximations or by including secondary effects such as humidity,

temperature inversions, and increased wind speeds [80]. While daily AOD measurements have been extrapolated to surface concentrations, short-term events such as fires and inversion weather conditions may be inactive during infrequent satellite observations, or clouds may obscure the scene, leading to the event being missed. Therefore, the rate of data acquisition should match the rate of compositional change in order to determine exposure levels [104, 161].

While traditional methods on quantifying aerosol use the daytime-only visible portion of the electromagnetic spectrum [48], more recent studies favour revising and utilizing older dust detection methodologies [74, 256] using infrared to provide continuous monitoring (i.e. 24 hours a day) [234]. These methods use brightness temperature differences (BTD) between two infrared wavelengths as a high-pass filter that enhances the differences (from trace constituents) between two similar wavelength bands while minimizing commonality (land, sea, and cloud). However, these dust detection methodologies provide a qualitative, not quantitative assessment of concentration, and there is a need to improve the methodology to provide speciated GLCs across unmonitored regions.

8.3. Material and methods

8.3.1. Data sources

Raw data files of all ten infrared bands from the Himawari-8 satellite were obtained from the Australian Bureau of Meteorology (BOM). These data files were cropped to the study domain and analysed using the "Climate Data Operators" (CDO) [216]. The satellite data were augmented with meteorological and ambient air quality data across the greater Sydney region in eastern Australia downloaded from the New South Wales (NSW) government office of Environment and Heritage (OEH) website https://www.environment.nsw.gov.au/AQMS/search.htm. The Australian Nuclear Science and Technology Organization (ANSTO) supplied fine $PM_{2.5}$ characterization, which was used to quantitate aerosol by source type [16].

8.3.2. Methodology

A literature review of surface particulate monitoring of dust events using geostationary satellite remote sensing was undertaken to understand the theory and limitations in the current methodology [6]. The review identified, amongst other findings, the reliance on visible reflectances and the lack of temporal resolution in polar-orbiting satellite data. As a result of this, a dust-storm was investigated to determine how rapidly the storm passed and what temporal data resolution is required to monitor these and other similar events [7]. Various dust indices were investigated to determine which are optimum in determining spectral change [8]. These indices were then used to qualify and quantitate dust events [9], and the methodology was validated against three severe air quality events described on the OEH website of: a dust storm; smoke from prescribed burns; and an ozone smog incident.

8.4. Results and discussions

8.4.1. Literature Review

The literature review found that the frequency of GEO satellite data exceeds the temporal resolution required for air quality studies. The requirement of near continual monitoring necessitates a change to the less sensitive infrared bands and converting from the vertical AOD profile to respirable GLCs is required. Surface parametrizations and the choice of aerosol inversion models present challenges in providing speciated aerosol concentrations.

8.4.2. Temporal resolution requirements

The probability of a polar-orbiting satellite overpass coinciding with a cloud-free aerosol event is low. Therefore, polar-orbiting satellites such as MODIS are unsuitable for detecting rapidly changing aerosol events, and geostationary satellites are required to provide suitable, temporally resolved data. Principal component analysis of BTD indices for a large dust storm in the Pilbara region of Western Australia identified that each aerosol phase of the dust storm lasted

between thirty minutes and two hours and that ten-minute data resolution is required to monitor these changes.

8.4.3. Selection of dual-band indices

Three index types were investigated: brightness temperature differences (BTD); normalized differences (NDDI); and division, for the forty-five dual-band IR indices from Himawari-8. BTD was marginally better than the other two index types at resolving aerosol and cloud plumes. Five optimum dual-band indices were selected ($BTD_{3.9\text{-}6.2\mu m}$, $BTD_{11\text{-}12\mu m}$, $BTD_{9.6\text{-}13\mu m}$, $BTD_{8.6\text{-}10\mu m}$, and $BTD_{6.9\text{-}7.3\mu m}$) that: resolved aerosol and cloud plumes; were least correlated; and utilized all ten infrared wavelengths, to optimize the aerosol quantification. Figure 5-10 depicts these dust indices across the full Himawari monitoring hemisphere on the morning of the Pilbara dust storm.

8.4.4. Calibrating aerosol change using the five BTD indices

Multilinear regression was used to determine a pollution index from the five BTD indices and quantitate composition of NO, NO_2, $PM_{2.5}$, PM_{10}, SO_2 and O_3 against measured OEH concentrations. The ANSTO data (soil, sea-spray, smoke, auto, secondary sulfates) correlated against the OEH data indicating that the method can detect both aerosol and gaseous components. Quantifying surface concentration remains challenging given the log-normal relationship of environmental data, low concentrations, reduced spectral sensitivity from the BTD filtering, and the transient nature of short-term plume movements. Quantification is best accomplished by scaling the predicted concentration by the probability of an event type predicted from the pollution index.

8.4.5. Severe event case studies

Three case studies of significant events (dust, smoke, and ozone) were analysed using the methodology and compared to the OEH's analysis. The spatial distribution (*where*) of aerosol species (*what*) and timing (*when*) of the events predicted from the satellite data agreed with the OEH data. The analysis was

hindered by severe cloud and concentrations (*how-much*) are limited to order of magnitude estimates.

8.5. Conclusions

GEO satellites have substantially improved the temporal data resolution from daily (e.g. MODIS) to ten-minutes (e.g. Himawari-8). This data frequency is comparable to real-time monitoring, and thus suitable for air quality studies. However, working with big-data presents challenges, and cloud gaps require down-scaling of the data to minimize cloud spectral contamination. Infrared wavelengths provide near-continuous data, but at the cost of lower spectral sensitivity to changes in composition, and the lack of spectral resolution between compounds makes determining concentration challenging.

The spectral sensitivity of IR to water enhances the qualitative determination of aerosol speciation as the speciation correlates with humidity and particle size. Correlations between aerosol species and gaseous components were noted. The reasons for the correlation are unknown and could be based on aerosol products or related to humidity. However, the correlations imply that both aerosol species and gaseous pollutants can be estimated from geostationary remote sensing data. Five indices were chosen that utilize all ten Himawari-8 IR bands ($BTD_{3.9\text{-}6.2\mu m}$, $BTD_{11\text{-}12\mu m}$, $BTD_{9.6\text{-}13\mu m}$, $BTD_{8.6\text{-}10\mu m}$, $BTD_{6.9\text{-}7.3\mu m}$). Using five indices increases the probability of detecting all aerosol types and is an improvement over current IR methods, which use fewer indices.

The pollution index that was developed correlates to aerosol species; relative humidity; particle size; ozone; and vertical stability and enables a qualitative assessment. Surface concentrations are subsequently quantified by scaling the predicted concentrations by the probability of the aerosol type. This produces an order of magnitude estimate and requires further studies to improve quantification. High pass filtering using BTD indices, from all IR bands, has improved the qualification of aerosol species but diminished quantification. Quantification might be improved by calibrating aerosol species against the raw spectra. Further verification beyond the limited New South Wales study region

and the three severe incident case studies are required to extend the applicability of the method to other regions.

This study has established a methodology to determine ground-level concentrations of particulate matter, speciated by particle size ($PM_{2.5}/PM_{10}$ ratio), source type (soil, sea-spray, smoke, auto, and secondary sulfates), and gaseous composition (NO, NO_2, SO_2, O_3, $PM_{2.5}$, PM_{10}). All ten infrared wavelength bands from the Himawari-8 geostationary satellite are used. The method provides speciated ground-level concentrations, at ten-minute intervals, in real-time, with a two-kilometer grid resolution, across a quarter of the globe, and addresses the lack of surface monitoring in remote and regional areas.

9. Synthesis

> "… air quality (AQ) managers are not taking full advantage of the data for these applications nor has the full potential of satellite data for air quality applications been realized. … Therefore, we strongly encourage [everyone] to express their needs to the scientists who develop the products so that they may be improved and tailored for the specific needs of the AQ community" Duncan et al. (2014).

It was these two sentences that inspired the choice of this thesis topic, and this thesis is, in essence, a response to those comments and a request for a new product (GLCs) to be developed that is tailored to the specific needs of the air quality community. The thesis introduction highlights both the need to have spatially and temporally resolved ground-level concentration data, but also the deficiencies in the current AOD determination, as depicted in Figure 1-11. These and other deficiencies were highlighted in the literature review paper [6], and it is not the "perceived difficulties" [1] that are restricting the broader adoption of AOD, but that the current AOD product does not meet the needs of the air quality community. The temporal resolution of polar-orbiting satellites is inadequate; the 3x3 km^2 spatial aggregation is too coarse; the predicted AOD over land (especially bright surfaces) is dubious and does not represent plumes (see Figure 1-11); ground-level concentrations, not a columnar number is needed for health studies; and the classification of aerosol into types such as "strongly absorbing" is not useful in determining health impacts. It is therefore unsurprising- that the air quality community has not adopted remote sensing practices in the past.

The most critical issue with current AOD products is the lack of temporal resolution in data from polar-orbiting satellites and the incorrect assumption that the instantaneous satellite overpass analysis equates to daily or hourly ground-based measurements. Numerous studies have demonstrated higher correlations between ground-based measurements and AOD than observed between our two surface measured datasets (OEH and ANSTO) of 0.65 (chapter six composition). The lower correlations are attributed to the differences in spatial plume distributions over the monitoring sites and it is argued that this represents a "best case" correlation that could be obtained when comparing AOD to GLCs.

Recent literature [295] using geostationary satellites report lower AOD to ground level correlations than earlier studies. These lower correlation studies are more plausible given the correlations we obtained between the surface datasets and suggests that earlier AOD studies either used longer time periods for surface monitoring or were conducted in regions where the pollution levels were high and did not have significant spatial or diurnal concentration fluctuations. Specifically, the paper on temporal resolution requirements [7], compares the instantaneous measurement during the Terra and Aqua overpasses to the probability of detecting a dust event (Figure 4-2) and concludes that MODIS has less than ten percent chance of the overpass coinciding with an aerosol event. This variability in short-term concentrations has been ascribed to the spatiotemporal variability of aerosols in urban [224, 225] and rural [227] environments and caused by changing meteorological conditions which affect all emission sources [228].

Chapter four (time) posed the question: if geostationary satellites are only limited in the temporary ability to capture and upload large data files, then what is an optimum sampling time? The temporal resolution paper [7] reiterated that turbulence drives air quality, and monitoring should, therefore, be conducted at the cusp of the turbulent zone (five to ten minutes) to maximise the detection of air quality events.

The review paper [6] also mentioned that the spatial requirements were related to the distance the air moved during the sampling time and that a 1 m/s wind-speed over ten minutes equates to a 600 m grid resolution requirement. Therefore, there is a need to increase the spatial resolution from the current two kilometres to 500 m (or even 250 m) to meet air quality requirements. However, this requires better optics (hardware), and a doubling in spatial resolution, quadruples data volumes - which are currently ~180 Gb/day for the full Himawari-disk. A potential trade-off is suggested to reduce the temporal resolution to hourly averages, and simultaneously increase the resolution to 1 km^2 which would decrease the data requirements to ~120 Gb/day.

The development of remote sensing AOD techniques using polar-orbiting satellites has favoured the more spectrally sensitive visible wavelengths to the detriment of

methods that use continuous infrared wavelengths. Air quality incidents at night and pre-dawn inversion conditions can generate high concentrations, and it is vital that these elevated concentration levels are measured. Current index methods are limited by localised thresholds and typically use two BTD dual-band wavelength combinations. In contrast, chapter five investigated which dual wavelength-band indices are best suited to determine compositional change and suggests using all ten infrared wavelength bands with five BTD indices to maximise the detection of compositional changes, from all potential source types. These five indices were applied to the entire Himawari-8 observational hemisphere (Figure 5-10) and differences were noted between the generally cloud-free indices over Australia in contrast to those over China. It is these compositional differences that are potentially related to the non-specificity of indices between various locations.

Converting these indices to a pollution index allowed relative humidity and the fraction of fine particles ($PM_{2.5}/(PM_{2.5} + PM_{10})$ to be determined. The pollution index allows for a gradual temporal transitioning between pollutants, particle size and humidity (as depicted in the monitoring data), and the continuous index scale can be aggregated both spatially and temporally. The maximum likelihood probability allowed both gaseous species NO, NO_2, SO_2, $PM_{2.5}$, PM_{10}, O_3 and aerosol categories of soil, sea-spray, smoke, auto and secondary sulfates to be determined across the greater Sydney region. While it is unlikely that these calibration factors are directly transferable to other regions, it indicates a potential methodology to determine composition. Chapter six (composition) [9] noted that each event is typically from a single pollutant (Table 6-3) due to meteorological changes upwind of source regions (Figure 1-8), and reduced probabilities of events from multiple sources. Therefore, the probability of an event is a reliable indicator of the magnitude (concentration) of the event or an indication of background levels.

Preliminary analysis using the three OEH case study data noted the plumes are plausibly represented and form coherent regions as expected of moving air masses. Cloud contamination represents an analysis problem as clouds need to be retained to depict the plume movement but should be calibrated separately to non-cloud

events and similarly, the background subtraction needs to take diurnal heating, clouds, and land-sea boundaries into consideration.

Within these constraints, this thesis has identified the requirements of atmospheric scientists for highly resolved spatiotemporal, speciated ground-level concentrations. It has considered the difficulties with the current determination of AOD, which are not fit for purpose, and argues for a new GLCs product that uses infrared geostationary data to provide continuous data. It has suggested using five BTD indices to detect the broadest range of pollutants and rejects spatial averaging and cloud masking in favour of a pollution index.

Preliminary validation suggests that the method can successfully determine atmospheric stability, cloud height, relative humidity, $PM_{2.5}$, and PM_{10} concentrations across regional areas using ten-minute infrared spectral data from the Himawari-8 satellite and in so doing address the requirement of the air quality community to understand the who, what, when, where, and why of aerosol events.

The major finding of this thesis is that all ten IR bands should be used with the five BTD indices to optimise the identification and quantification of aerosol speciation, particle size, and GLCs. The first $BTD_{3.9\text{-}6.2\mu m}$ is a moisture parameter, the second $BTD_{11\text{-}12\mu m}$ is related to particle size and the third $BTD_{6.9\text{-}7.3\mu m}$ is related to atmospheric stability. The remaining two are potentially related to the oxidation state of the atmosphere ($BTD_{9.6\text{-}13\mu m}$) and sulphates ($BTD_{8.6\text{-}10\mu m}$). The atmospheric stability parameter is vital in calibrating the columnar estimate (AOD equivalent) to GLCs while the absorbed moisture and particle size is indicative of source type (chapter 6). This study has shown that the availability and accuracy of regional GLCs of $PM_{2.5}$ and PM_{10} can be improved using ten-minute infrared spectral data from geostationary satellites.

10. References

1. Duncan, B.N., A.I. Prados, L.N. Lamsal, Y. Liu, D.G. Streets, P. Gupta, E. Hilsenrath, R.A. Kahn, J.E. Nielsen, A.J. Beyersdorf, S.P. Burton, A.M. Fiore, J. Fishman, D.K. Henze, C.A. Hostetler, N.A. Krotkov, P. Lee, M. Lin, S. Pawson, G. Pfister, K.E. Pickering, R.B. Pierce, Y. Yoshida, and L.D. Ziemba, *Satellite data of atmospheric pollution for U.S. air quality applications: Examples of applications, summary of data end-user resources, answers to FAQs, and common mistakes to avoid.* Atmospheric Environment, 2014. **94**: p. 647-662.
2. You, W., Z. Zang, L. Zhang, Y. Li, X. Pan, and W. Wang, *National-Scale Estimates of Ground-Level PM2.5 Concentration in China Using Geographically Weighted Regression Based on 3 km Resolution MODIS AOD.* Remote Sensing, 2016. **8**(3).
3. Muhammad, Z. and K.O. Nguyen Thi, *Relationship of MISR component AODs with black carbon and other ground monitored particulate matter composition.* Atmospheric Pollution Research, 2015. **6**(1): p. 62-69.
4. Li, J., B.E. Carlson, and A.A. Lacis, *How well do satellite AOD observations represent the spatial and temporal variability of PM2.5 concentration for the United States?* Atmospheric Environment, 2015. **102**: p. 260-273.
5. Xu, H., X. Ceamanos, J.L. Roujean, D. Carrer, and Y. Xue, *Can satellite-derived aerosol optical depth quantify the surface aerosol radiative forcing?* Atmospheric Research, 2014. **150**: p. 151-167.
6. Sowden, M., U. Mueller, and D. Blake, *Review of surface particulate monitoring of dust events using geostationary satellite remote sensing.* Atmospheric Environment, 2018. **183**: p. 154-164.
7. Sowden, M., U. Mueller, and D. Blake, *What temporal resolution is required for remote sensing of regional aerosol concentrations using the Himawari-8 geostationary satellite.* Atmospheric Environment, 2019. **216**: p. 116914.
8. Sowden, M. and D. Blake, *Which dual-band infrared indices are optimum for identifying aerosol compositional change using Himawari-8 data?* Atmospheric Environment, 2020: p. 117620.

9. Sowden, M., D. Blake, D. Cohen, A. Atanacio, and U. Mueller, *Development of an infrared pollution index to identify ground-level compositional, particle size, and humidity changes using Himawari-8.* Atmospheric Environment, 2020. **229**: p. 117435.
10. Sowden, M., U. Mueller, and D. Blake, *Determining ground-level composition and concentration of particulate matter across regional areas using the Himawari-8 satellite.* Air Quality and Health. Special issue of the 15th International Conference on Atmospheric Sciences and Applications to Air Quality, 2019.
11. Kloog, I., B. Ridgway, P. Koutrakis, B.A. Coull, and J.D. Schwartz, *Long- and Short-Term Exposure to PM2.5 and Mortality: Using Novel Exposure Models.* Epidemiology, 2013. **24**(4): p. 555-561.
12. Csavina, J., J. Field, M.P. Taylor, S. Gao, A. Landázuri, E.A. Betterton, and A.E. Sáez, *A review on the importance of metals and metalloids in atmospheric dust and aerosol from mining operations.* Science of The Total Environment, 2012. **433**: p. 58-73.
13. Melles, S.J., G.B.M. Heuvelink, C.J.W. Twenhöfel, A. van Dijk, P.H. Hiemstra, O. Baume, and U. Stöhlker, *Optimizing the spatial pattern of networks for monitoring radioactive releases.* Computers & Geosciences, 2011. **37**(3): p. 280-288.
14. Wang, J.-F., C.-S. Jiang, M.-G. Hu, Z.-D. Cao, Y.-S. Guo, L.-F. Li, T.-J. Liu, and B. Meng, *Design-based spatial sampling: Theory and implementation.* Environmental Modelling & Software, 2013. **40**: p. 280-288.
15. NSW, Office of Environment and Heritage, *Review of Air Quality Monitoring Network Design - Expert Working Group Project 2 for the National Environment Protection (Ambient Air Quality) Measure Review* 2019.
16. Cohen, D.D., A. Atanacio, E. Stelcer, and D. Garton, *Sydney Particle Characterisation Study. PM2.5 Source Apportionment in the Sydney Region between 2000 and 2014*. 2016, Australian Nuclear Science and Technology Organisation (ANSTO).
17. Van Vreeswyk, A., A. Payne, K. Leighton, and P. Hennig, *An inventory and condition survey of the Pilbara region, Western Australia*. 2004, DAFWA.

18. Physick, W.L. *Meteorology And Air Quality Of The Pilbara Region*. 2001; Available from: https://www.der.wa.gov.au/images/documents/your-environment/air/publications/meteorology-and-air-quality-of-the-pilbara-region.pdf.
19. DOE, *Pilbara Air Quality Study – Summary Report, Department of Environment, Technical Series No. 120, WA Dept. Of Environment*. 2004, WA. Dept Of Environment.
20. BOM. *Australian Bureau of Meteorology. Western Australian Observation Stations*. 2016; Available from: http://www.bom.gov.au/wa/observations/map.shtm.
21. PHPA, Port Hedland Port Authority. *Pilbara Ports Authority 2017/18 Highlights*. 2018; Available from: https://www.pilbaraports.com.au/PilbaraPortsAuthority/media/Documents/ABOUT%20THE%20PORT/Corporate%20Governance/Annual%20Reports/Pages-from-2312-PPA-AR-2018-ES.pdf.
22. PHIC, Port Hedland Industrial Council. *Air Quality Monitoring*. 2016; Available from: http://phicmonitoring.com.au/esys/rt/realtime.jsp?siteId=371.
23. Harper, J., *Ambient air quality monitoring report to the Port Hedland Dust Management Taskforce (2014-2015)*. 2015, Port Hedland Industries Council.
24. NSW, Office of Environment and Heritage, *NSW Annual Air Quality Statement 2018* 2019.
25. Taylor, G.I., *Diffusion by Continuous Movements*. Proceedings of the London Mathematical Society, 1922. **s2-20**(1): p. 196-212.
26. Wilson, R. and A. Venkatram, *Model evaluation results for AERMOD*. 1998.
27. US-EPA. *Preferred/Recommended Models*. Support Center for Regulatory Atmospheric Modeling. Available from https://www3.epa.gov/scram001/dispersion_prefrec.htm. 2016.
28. Holmes, N.S. and L. Morawska, *A review of dispersion modelling and its application to the dispersion of particles: An overview of different dispersion models available*. Atmospheric Environment, 2006. **40**(30): p. 5902-5928.

29. Carter, W., *A detailed mechanism for the gas-phase atmospheric reactions of organic compounds.* Atmospheric Environment, 2007. **41**: p. 80-117.
30. Yarwood, G., R.E. Morris, and G.M. Wilson, *Particulate Matter Source Apportionment Technology (PSAT) in the CAMx Photochemical Grid Model*, in *Air Pollution Modeling and Its Application XVII*, C. Borrego and A.-L. Norman, Editors. 2007, Springer US: Boston, MA. p. 478-492.
31. Hewson, E.W., *Meteorological Factors Affecting Causes and Controls of Air Pollution.* Journal of the Air Pollution Control Association, 1956. **5**(4): p. 235-241.
32. Stull, R.B., *Transilient turbulence theory.* Transport and Diffusion in Turbulent Fields: Modeling and Measurement Techniques, 1984. **62**: p. 21-96.
33. Dore, A.J., S. Hallsworth, A.G. McDonald, M. Werner, M. Kryza, J. Abbot, E. Nemitz, C.J. Dore, H. Malcolm, M. Vieno, S. Reis, and D. Fowler, *Quantifying missing annual emission sources of heavy metals in the United Kingdom with an atmospheric transport model.* Science of The Total Environment, 2014. **479–480**: p. 171-180.
34. Amato, F., F.R. Cassee, H.A.C. Denier van der Gon, R. Gehrig, M. Gustafsson, W. Hafner, R.M. Harrison, M. Jozwicka, F.J. Kelly, T. Moreno, A.S.H. Prevot, M. Schaap, J. Sunyer, and X. Querol, *Urban air quality: The challenge of traffic non-exhaust emissions.* Journal of Hazardous Materials, 2014. **275**: p. 31-36.
35. Chai, T., R. Draxler, and A. Stein, *Source term estimation using air concentration measurements and a Lagrangian dispersion model – Experiments with pseudo and real cesium-137 observations from the Fukushima nuclear accident.* Atmospheric Environment, 2015. **106**: p. 241-251.
36. de Foy, B., W. Lei, M. Zavala, R. Volkamer, J. Samuelsson, J. Mellqvist, B. Galle, A.P. Martínez, M. Grutter, A. Retama, and L.T. Molina, *Modelling constraints on the emission inventory and on vertical dispersion for CO and SO_2 in the Mexico City Metropolitan Area using Solar FTIR and zenith sky UV spectroscopy.* Atmospheric Chemistry and Physics, 2007. **7**(3): p. 781-801.

37. Van Leuken, J.P.G., A.N. Swart, A.H. Havelaar, A. Van Pul, W. Van der Hoek, and D. Heederik, *Atmospheric dispersion modelling of bioaerosols that are pathogenic to humans and livestock – A review to inform risk assessment studies*. Microbial Risk Analysis, 2016. **1**: p. 19-39.
38. Ashrafi, K. and G.A. Hoshyaripour, *A model to determine atmospheric stability and its correlation with CO concentration*. International Journal of Civil and Environmental Engineering, 2010. **2**(2).
39. Stein, A.F., R.R. Draxler, G.D. Rolph, B.J.B. Stunder, M.D. Cohen, and F. Ngan, *NOAA's HYSPLIT Atmospheric Transport and Dispersion Modeling System*. Bulletin of the American Meteorological Society, 2015. **96**(12): p. 2059-2077.
40. Eeftens, M., R. Beelen, K. de Hoogh, T. Bellander, G. Cesaroni, M. Cirach, C. Declercq, A. Dedele, E. Dons, A. de Nazelle, K. Dimakopoulou, K. Eriksen, G. Falq, P. Fischer, C. Galassi, R. Grazuleviciene, J. Heinrich, B. Hoffmann, M. Jerrett, D. Keidel, M. Korek, T. Lanki, S. Lindley, C. Madsen, A. Moelter, G. Nador, M. Nieuwenhuijsen, M. Nonnemacher, X. Pedeli, O. Raaschou-Nielsen, E. Patelarou, U. Quass, A. Ranzi, C. Schindler, M. Stempfelet, E. Stephanou, D. Sugiri, M.-Y. Tsai, T. Yli-Tuomi, M.J. Varro, D. Vienneau, S. von Klot, K. Wolf, B. Brunekreef, and G. Hoek, *Development of Land Use Regression Models for $PM_{2.5}$, $PM_{2.5}$ Absorbance, PM_{10} and PMcoarse in 20 European Study Areas; Results of the ESCAPE Project*. Environmental Science & Technology, 2012. **46**(20): p. 11195-11205.
41. Yoon, J., A. Pozzer, D.Y. Chang, J. Lelieveld, J. Kim, M. Kim, Y.G. Lee, J.H. Koo, J. Lee, and K.J. Moon, *Trend estimates of AERONET-observed and model-simulated AOTs between 1993 and 2013*. Atmospheric Environment, 2016. **125, Part A**: p. 33-47.
42. Guo, H.-D., L. Zhang, and L.-W. Zhu, *Earth observation big data for climate change research*. Advances in Climate Change Research, 2015. **6**(2): p. 108-117.
43. Hamm, N.A.S., R.J.S. Magalhaes, and A.C.A. Clements, *Earth Observation, Spatial Data Quality, and Neglected Tropical Diseases*. Plos Neglected Tropical Diseases, 2015. **9**(12).

44. Xie, Y., Z. Sha, and M. Yu, *Remote sensing imagery in vegetation mapping: a review.* Journal of Plant Ecology, 2008. **1**(1): p. 9-23.
45. Ruddick, K., G. Neukermans, Q. Vanhellemont, and D. Jolivet, *Challenges and opportunities for geostationary ocean colour remote sensing of regional seas: A review of recent results.* Remote Sensing of Environment, 2014. **146**: p. 63-76.
46. Mouillot, F., M.G. Schultz, C. Yue, P. Cadule, K. Tansey, P. Ciais, and E. Chuvieco, *Ten years of global burned area products from spaceborne remote sensing-A review: Analysis of user needs and recommendations for future developments.* International Journal of Applied Earth Observation and Geoinformation, 2014. **26**: p. 64-79.
47. Roy, D.P., M.A. Wulder, T.R. Loveland, W. C.E, R.G. Allen, M.C. Anderson, D. Helder, J.R. Irons, D.M. Johnson, R. Kennedy, T.A. Scambos, C.B. Schaaf, J.R. Schott, Y. Sheng, E.F. Vermote, A.S. Belward, R. Bindschadler, W.B. Cohen, F. Gao, J.D. Hipple, P. Hostert, J. Huntington, C.O. Justice, A. Kilic, V. Kovalskyy, Z.P. Lee, L. Lymburner, J.G. Masek, J. McCorkel, Y. Shuai, R. Trezza, J. Vogelmann, R.H. Wynne, and Z. Zhu, *Landsat-8: Science and product vision for terrestrial global change research.* Remote Sensing of Environment, 2014. **145**: p. 154-172.
48. Levy, R.C., S. Mattoo, L.A. Munchak, L.A. Remer, A.M. Sayer, F. Patadia, and N.C. Hsu, *The Collection 6 MODIS aerosol products over land and ocean.* Atmospheric Measurement Techniques, 2013. **6**(11): p. 2989-3034.
49. Uesawa, D., *Aerosol Optical Depth product derived from Himawari-8 data for Asian dust monitoring.* 2016.
50. Xiao, F., M.S. Wong, K.H. Lee, J.R. Campbell, and Y.-k. Shea, *Retrieval of dust storm aerosols using an integrated Neural Network model.* Computers & Geosciences, 2015. **85, Part B**: p. 104-114.
51. Lensky, I. and D. Rosenfeld, *Clouds-aerosols-precipitation satellite analysis tool (CAPSAT).* Atmospheric Chemistry and Physics, 2008. **8**(22): p. 6739-6753.
52. Han, K.M., R.S. Park, H.K. Kim, J.H. Woo, J. Kim, and C.H. Song, *Uncertainty in biogenic isoprene emissions and its impacts on tropospheric*

chemistry in East Asia. Science of The Total Environment, 2013. **463–464**: p. 754-771.

53. Fu, T.-M., D.J. Jacob, F. Wittrock, J.P. Burrows, M. Vrekoussis, and D.K. Henze, *Global budgets of atmospheric glyoxal and methylglyoxal, and implications for formation of secondary organic aerosols.* Journal of Geophysical Research-Atmospheres, 2008. **113**(D15).
54. Bioucas-Dias, J.M., A. Plaza, N. Dobigeon, M. Parente, Q. Du, P. Gader, and J. Chanussot, *Hyperspectral Unmixing Overview: Geometrical, Statistical, and Sparse Regression-Based Approaches.* Ieee Journal of Selected Topics in Applied Earth Observations and Remote Sensing, 2012. **5**(2): p. 354-379.
55. Verstraete, M.M., D.J. Diner, and J.-L. Bézy, *Planning for a spaceborne Earth Observation mission: From user expectations to measurement requirements.* Environmental Science & Policy, 2015. **54**: p. 419-427.
56. Bond, T.C. and R.W. Bergstrom, *Light absorption by carbonaceous particles: An investigative review*. Aerosol Science and Technology, 2006. **40**(1): p. 27-67.
57. EUMETSAT. *Dust Detection: The Dust RGB Product.* 2011; Available from: http://www.eumetsat.int/website/home/Data/Training/TrainingLibrary/DAT_2042669.html.
58. Schmit, T.J., S.S. Lindstrom, J.J. Gerth, and M.M. Gunshor, *Applications of the 16 spectral bands on the Advanced Baseline Imager (ABI).* Journal of Operational Meteorology, 2018. **06**(04): p. 33-46.
59. De Deckker, P., C.I. Munday, J. Brocks, T. O'Loingsigh, G.E. Allison, J. Hope, M. Norman, J.-B.W. Stuut, N.J. Tapper, and S. van der Kaars, *Characterisation of the major dust storm that traversed over eastern Australia in September 2009; a multidisciplinary approach.* Aeolian Research, 2014. **15**: p. 133-149.
60. Streets, D.G., T. Canty, G.R. Carmichael, B. de Foy, R.R. Dickerson, B.N. Duncan, D.P. Edwards, J.A. Haynes, D.K. Henze, M.R. Houyoux, D.J. Jacobi, N.A. Krotkov, L.N. Lamsal, Y. Liu, Z. Lu, R.V. Martini, G.G. Pfister, R.W. Pinder, R.J. Salawitch, and K.J. Wechti, *Emissions estimation from satellite*

retrievals: A review of current capability. Atmospheric Environment, 2013. **77**: p. 1011-1042.

61. Mhawish, A., M. Kumar, A.K. Mishra, P.K. Srivastava, and T. Banerjee, *Chapter 3 - Remote Sensing of Aerosols From Space: Retrieval of Properties and Applications A2 - Islam, Tanvir*, in *Remote Sensing of Aerosols, Clouds, and Precipitation*, Y. Hu, A. Kokhanovsky, and J. Wang, Editors. 2018, Elsevier. p. 45-83.
62. Benali, A., A. Russo, A.C.L. Sa, R.M.S. Pinto, O. Price, N. Koutsias, and J.M.C. Pereira, *Determining Fire Dates and Locating Ignition Points With Satellite Data*. Remote Sensing, 2016. **8**(4).
63. Levy, R.C., L.A. Remer, D. Tanre, S. Mattoo, and Y.J. Kaufman. *Algorithm for Remote Sensing of Tropospheric Aerosol from MODIS for Collection 005: Revision 2*. MODIS Atmosphere 2009; Available from: http://modis-atmos.gsfc.nasa.gov/_docs/ATBD_MOD04_C005_rev2.pdf.
64. Remer, L.A., Y.J. Kaufman, D. Tanre, S. Mattoo, D.A. Chu, J.V. Martins, R.R. Li, C. Ichoku, R.C. Levy, R.G. Kleidman, T.F. Eck, E. Vermote, and B.N. Holben, *The MODIS aerosol algorithm, products, and validation*. Journal of the Atmospheric Sciences, 2005. **62**(4): p. 947-973.
65. Hsu, N., M.J. Jeong, C. Bettenhausen, A. Sayer, R. Hansell, C. Seftor, J. Huang, and S.C. Tsay, *Enhanced Deep Blue aerosol retrieval algorithm: The second generation*. Journal of Geophysical Research: Atmospheres, 2013. **118**(16): p. 9296-9315.
66. Good, E.J., X. Kong, O. Embury, C.J. Merchant, and J.J. Remedios, *An infrared desert dust index for the Along-Track Scanning Radiometers*. Remote Sensing of Environment, 2012. **116**: p. 159-176.
67. Taylor, I., S. Mackie, and M. Watson, *Investigating the use of the Saharan dust index as a tool for the detection of volcanic ash in SEVIRI imagery*. Journal of Volcanology and Geothermal Research, 2015. **304**: p. 126-141.
68. BOM. *Effective training and use of RGB satellite products for Forecasters*. 2012; Available from: http://www5.bom.gov.au/files/7013/5580/7378/RGBWebinarforWebNoRefs.pdf.

69. Hu, X., N. Lu, T. Niu, and P. Zhang, *Operational retrieval of Asian sand and dust storm from FY-2C geostationary meteorological satellite and its application to real time forecast in Asia.* Atmospheric Chemistry and Physics, 2008. **8**(6): p. 1649-1659.
70. Prata, A. and F. Grant, *Retrieval of microphysical and morphological properties of volcanic ash plumes.* 2001.
71. Qu, J.J., X.J. Hao, M. Kafatos, and L.L. Wang, *Asian dust storm monitoring combining terra and aqua MODIS SRB measurements.* Ieee Geoscience and Remote Sensing Letters, 2006. **3**(4): p. 484-486.
72. Li, Z.-L., B.-H. Tang, H. Wu, H. Ren, G. Yan, Z. Wan, I.F. Trigo, and J.A. Sobrino, *Satellite-derived land surface temperature: Current status and perspectives.* Remote Sensing of Environment, 2013. **131**: p. 14-37.
73. Wen, S. and W.I. Rose, *Retrieval of sizes and total masses of particles in volcanic clouds using AVHRR bands 4 and 5.* Journal of Geophysical Research: Atmospheres, 1994. **99**(D3): p. 5421-5431.
74. Ackerman, S.A., *Remote sensing aerosols using satellite infrared observations.* Journal of Geophysical Research-Atmospheres, 1997. **102**(D14): p. 17069-17079.
75. Sofiev, M., T. Ermakova, and R. Vankevich, *Evaluation of the smoke-injection height from wild-land fires using remote-sensing data.* Atmospheric Chemistry and Physics, 2012. **12**(4): p. 1995-2006.
76. Lin, N.-H., S.-C. Tsay, H.B. Maring, M.-C. Yen, G.-R. Sheu, S.-H. Wang, K.H. Chi, M.-T. Chuang, C.-F. Ou-Yang, J.S. Fu, J.S. Reid, C.-T. Lee, L.-C. Wang, J.-L. Wang, C.N. Hsu, A.M. Sayer, B.N. Holben, Y.-C. Chu, X.A. Nguyen, K. Sopajaree, S.-J. Chen, M.-T. Cheng, B.-J. Tsuang, C.-J. Tsai, C.-M. Peng, R.C. Schnell, T. Conway, C.-T. Chang, K.-S. Lin, Y.I. Tsai, W.-J. Lee, S.-C. Chang, J.-J. Liu, W.-L. Chiang, S.-J. Huang, T.-H. Lin, and G.-R. Liu, *An overview of regional experiments on biomass burning aerosols and related pollutants in Southeast Asia: From BASE-ASIA and the Dongsha Experiment to 7-SEAS.* Atmospheric Environment, 2013. **78**: p. 1-19.

77. Ichoku, C., R. Kahn, and M. Chin, *Satellite contributions to the quantitative characterization of biomass burning for climate modeling.* Atmospheric Research, 2012. **111**: p. 1-28.
78. Kaiser, J.W., A. Heil, M.O. Andreae, A. Benedetti, N. Chubarova, L. Jones, J.J. Morcrette, M. Razinger, M.G. Schultz, M. Suttie, and G.R. van der Werf, *Biomass burning emissions estimated with a global fire assimilation system based on observed fire radiative power.* Biogeosciences, 2012. **9**(1): p. 527-554.
79. Li, S., E. Joseph, and Q. Min, *Remote sensing of ground-level PM2.5 combining AOD and backscattering profile.* Remote Sensing of Environment, 2016. **183**: p. 120-128.
80. Sotoudeheian, S. and M. Arhami, *Estimating ground-level PM10 using satellite remote sensing and ground-based meteorological measurements over Tehran.* Journal of Environmental Health Science and Engineering, 2014. **12**.
81. Kahn, R.A., D.L. Nelson, M.J. Garay, R.C. Levy, M.A. Bull, D.J. Diner, J.V. Martonchik, S.R. Paradise, E.G. Hansen, and L.A. Remer, *MISR Aerosol Product Attributes and Statistical Comparisons With MODIS.* Ieee Transactions on Geoscience and Remote Sensing, 2009. **47**(12): p. 4095-4114.
82. Kahn, R.A., B.J. Gaitley, M.J. Garay, D.J. Diner, T.F. Eck, A. Smirnov, and B.N. Holben, *Multiangle Imaging SpectroRadiometer global aerosol product assessment by comparison with the Aerosol Robotic Network.* Journal of Geophysical Research-Atmospheres, 2010. **115**(D23).
83. Bilal, M., J.E. Nichol, and M. Nazeer, *Validation of Aqua-MODIS C051 and C006 Operational Aerosol Products Using AERONET Measurements Over Pakistan.* Ieee Journal of Selected Topics in Applied Earth Observations and Remote Sensing, 2016. **9**(5): p. 2074-2080.
84. You, W., Z. Zang, L. Zhang, Y. Li, and W. Wang, *Estimating national-scale ground-level PM25 concentration in China using geographically weighted regression based on MODIS and MISR AOD.* Environmental Science and Pollution Research, 2016. **23**(9): p. 8327-8338.
85. Kumar, N., A. Chu, and A. Foster, *An empirical relationship between PM2.5 and aerosol optical depth in Delhi Metropolitan.* Atmospheric Environment, 2007. **41**(21): p. 4492-4503.

86. Achad, M., M.L. López, G.G. Palancar, and B.M. Toselli, *Retrieving the relative contribution of aerosol types from single particle analysis and radiation measurements and calculations: A comparison of two independent approaches.* Journal of Aerosol Science, 2013. **64**: p. 11-23.
87. Le, T.H., T.N. Thanh Nguyen, K. Lasko, S. Ilavajhala, K.P. Vadrevu, and C. Justice, *Vegetation fires and air pollution in Vietnam.* Environmental Pollution, 2014. **195**: p. 267-275.
88. Hyder, A., H.J. Lee, K. Ebisu, P. Koutrakis, K. Belanger, and M.L. Bell, *PM2.5 Exposure and Birth Outcomes Use of Satellite- and Monitor-Based Data.* Epidemiology, 2014. **25**(1): p. 58-67.
89. Zhang, X.Y., Y.Q. Wang, T. Niu, X.C. Zhang, S.L. Gong, Y.M. Zhang, and J.Y. Sun, *Atmospheric aerosol compositions in China: spatial/temporal variability, chemical signature, regional haze distribution and comparisons with global aerosols.* Atmospheric Chemistry and Physics, 2012. **12**(2): p. 779-799.
90. Kumar, N., A.D. Chu, A.D. Foster, T. Peters, and R. Willis, *Satellite Remote Sensing for Developing Time and Space Resolved Estimates of Ambient Particulate in Cleveland, OH.* Aerosol Science and Technology, 2011. **45**(9): p. 1090-1108.
91. Khoshsima, M., F. Ahmadi-Givi, A.A. Bidokhti, and S. Sabetghadam, *Impact of meteorological parameters on relation between aerosol optical indices and air pollution in a sub-urban area.* Journal of Aerosol Science, 2014. **68**: p. 46-57.
92. Tiwari, S., P.K. Hopke, A.S. Pipal, A.K. Srivastava, D.S. Bisht, S. Tiwari, A.K. Singh, V.K. Soni, and S.D. Attri, *Intra-urban variability of particulate matter (PM2.5 and PM10) and its relationship with optical properties of aerosols over Delhi, India.* Atmospheric Research, 2015. **166**: p. 223-232.
93. Wu, J., F. Yao, W. Li, and M. Si, *VIIRS-based remote sensing estimation of ground-level PM2.5 concentrations in Beijing–Tianjin–Hebei: A spatiotemporal statistical model.* Remote Sensing of Environment, 2016. **184**: p. 316-328.

94. Yu, T., W. Wang, P. Ciren, and Y. Zhu, *Assessment of human health impact from exposure to multiple air pollutants in China based on satellite observations.* International Journal of Applied Earth Observation and Geoinformation, 2016. **52**: p. 542-553.
95. Shang, H., H. Letu, X. Pan, Z. Wang, R. Ma, C. Liu, T. Dai, S. Li, L. Chen, C. Chen, and Q. Hu, *Diurnal haze variations over the North China plain using measurements from Himawari-8/AHI.* Atmospheric Environment, 2019. **210**: p. 100-109.
96. Leibensperger, E.M., L.J. Mickley, D.J. Jacob, W.T. Chen, J.H. Seinfeld, A. Nenes, P.J. Adams, D.G. Streets, N. Kumar, and D. Rind, *Climatic effects of 1950-2050 changes in US anthropogenic aerosols - Part 2: Climate response.* Atmospheric Chemistry and Physics, 2012. **12**(7): p. 3349-3362.
97. Weng, Q.H., B. Xu, X.F. Hu, and H. Liu, *Use of earth observation data for applications in public health.* Geocarto International, 2014. **29**(1): p. 3-16.
98. Li, Y., D.K. Henze, D. Jack, and P.L. Kinney, *The influence of air quality model resolution on health impact assessment for fine particulate matter and its components.* Air Quality Atmosphere and Health, 2016. **9**(1): p. 51-68.
99. Brunner, J., R.B. Pierce, and A. Lenzen, *Development and validation of satellite-based estimates of surface visibility.* Atmospheric Measurement Techniques, 2016. **9**(2): p. 409-422.
100. Lin, J.T. and J. Li, *Spatio-temporal variability of aerosols over East China inferred by merged visibility-GEOS-Chem aerosol optical depth.* Atmospheric Environment, 2016. **132**: p. 111-122.
101. Ge, C., J. Wang, S. Carn, K. Yang, P. Ginoux, and N. Krotkov, *Satellite-based global volcanic SO2 emissions and sulfate direct radiative forcing during 2005-2012.* Journal of Geophysical Research-Atmospheres, 2016. **121**(7): p. 3446-3464.
102. Ma, X.Y. and F.Q. Yu, *Seasonal and spatial variations of global aerosol optical depth: multi-year modelling with GEOS-Chem-APM and comparisons with multiple-platform observations.* Tellus Series B-Chemical and Physical Meteorology, 2015. **67**: p. 15.

103. Wainwright, C.D., J.R. Pierce, J. Liggio, K.B. Strawbridge, A.M. Macdonald, and R.W. Leaitch, *The effect of model spatial resolution on Secondary Organic Aerosol predictions: a case study at Whistler, BC, Canada.* Atmospheric Chemistry and Physics, 2012. **12**(22): p. 10911-10923.
104. Philip, S., R.V. Martin, and C.A. Keller, *Sensitivity of chemistry-transport model simulations to the duration of chemical and transport operators: a case study with GEOS-Chem v10-01.* Geoscientific Model Development, 2016. **9**(5): p. 1683-1695.
105. Athanasopoulou, E., A. Protonotariou, G. Papangelis, M. Tombrou, N. Mihalopoulos, and E. Gerasopoulos, *Long-range transport of Saharan dust and chemical transformations over the Eastern Mediterranean.* Atmospheric Environment, 2016. **140**: p. 592-604.
106. Solomos, S., V. Amiridis, P. Zanis, E. Gerasopoulos, F.I. Sofiou, T. Herekakis, J. Brioude, A. Stohl, R.A. Kahn, and C. Kontoes, *Smoke dispersion modeling over complex terrain using high resolution meteorological data and satellite observations - The Fire Hub platform.* Atmospheric Environment, 2015. **119**: p. 348-361.
107. Aquila, V., L.D. Oman, R.S. Stolarski, P.R. Colarco, and P.A. Newman, *Dispersion of the volcanic sulfate cloud from a Mount Pinatubo-like eruption.* Journal of Geophysical Research-Atmospheres, 2012. **117**: p. 14.
108. Tu, Q.G., Z.Z. Hao, and D.L. Pan, *Mass Deposition Fluxes of Asian Dust to the Bohai Sea and Yellow Sea from Geostationary Satellite MTSAT: A Case Study.* Atmosphere, 2015. **6**(11): p. 1771-1784.
109. Ridley, D.A., C.L. Heald, and B. Ford, *North African dust export and deposition: A satellite and model perspective.* Journal of Geophysical Research-Atmospheres, 2012. **117**: p. 21.
110. Kishcha, P., A.M. da Silva, B. Starobinets, and P. Alpert, *Air pollution over the Ganges basin and northwest Bay of Bengal in the early postmonsoon season based on NASA MERRAero data.* Journal of Geophysical Research-Atmospheres, 2014. **119**(3): p. 1555-1570.
111. D'Andrea, S.D., J.Y. Ng, J.K. Kodros, S.A. Atwood, M.J. Wheeler, A.M. Macdonald, W.R. Leaitch, and J.R. Pierce, *Source attribution of aerosol size*

distributions and model evaluation using Whistler Mountain measurements and GEOS-Chem-TOMAS simulations. Atmospheric Chemistry and Physics, 2016. **16**(1): p. 383-396.

112. Li, K., H. Liao, Y.H. Mao, and D.A. Ridley, *Source sector and region contributions to concentration and direct radiative forcing of black carbon in China.* Atmospheric Environment, 2016. **124**: p. 351-366.
113. Chan, K.L. and K.L. Chan, *Aerosol optical depths and their contributing sources in Taiwan.* Atmospheric Environment, 2017. **148**: p. 364-375.
114. Basha, G., D.V. Phanikumar, K.N. Kumar, T.B.M.J. Ouarda, and P.R. Marpu, *Investigation of aerosol optical, physical, and radiative characteristics of a severe dust storm observed over UAE.* Remote Sensing of Environment, 2015. **169**: p. 404-417.
115. El-Askary, H., S.K. Park, M.H. Ahn, A. Prasad, and M. Kafatos, *On the Detection and Monitoring of the Transport of an Asian Dust Storm Using Multi-Sensor Satellite Remote Sensing.* Journal of Environmental Informatics, 2015. **25**(2): p. 99-116.
116. Wong, M.S., F. Xiao, J. Nichol, J. Fung, J. Kim, J. Campbell, and P.W. Chan, *A multi-scale hybrid neural network retrieval model for dust storm detection, a study in Asia.* Atmospheric Research, 2015. **158**: p. 89-106.
117. Ortore, E., G. Laneve, and G. Bernini, *Detection of volcanic gases and particles by satellite.* Acta Astronautica, 2014. **93**: p. 304-316.
118. Lasslop, G. and S. Kloster, *Impact of fuel variability on wildfire emission estimates.* Atmospheric Environment, 2015. **121**: p. 93-102.
119. Tao, W., *Aeolian desertification and its control in Northern China.* International Soil and Water Conservation Research, 2014. **2**(4): p. 34-41.
120. Weber, S.A., T.Z. Insaf, E.S. Hall, T.O. Talbot, and A.K. Huff, *Assessing the impact of fine particulate matter (PM2.5) on respiratory cardiovascular chronic diseases in the New York City Metropolitan area using Hierarchical Bayesian Model estimates.* Environmental Research, 2016. **151**: p. 399-409.
121. Brindley, H.E. and A. Ignatov, *Retrieval of mineral aerosol optical depth and size information from Meteosat Second Generation SEVIRI solar reflectance bands.* Remote Sensing of Environment, 2006. **102**(3-4): p. 344-363.

122. Zhao, S., Y. Yu, D. Xia, D. Yin, J. He, N. Liu, and F. Li, *Urban particle size distributions during two contrasting dust events originating from Taklimakan and Gobi Deserts.* Environmental Pollution, 2015. **207**: p. 107-122.

123. Colarco, P.R., E.P. Nowottnick, C.A. Randles, B.Q. Yi, P. Yang, K.M. Kim, J.A. Smith, and C.G. Bardeen, *Impact of radiatively interactive dust aerosols in the NASA GEOS-5 climate model: Sensitivity to dust particle shape and refractive index.* Journal of Geophysical Research-Atmospheres, 2014. **119**(2): p. 753-786.

124. Trivitayanurak, W., P.I. Palmer, M.P. Barkley, N.H. Robinson, H. Coe, and D.E. Oram, *The composition and variability of atmospheric aerosol over Southeast Asia during 2008.* Atmospheric Chemistry and Physics, 2012. **12**(2): p. 1083-1100.

125. Philip, S., R.V. Martin, A. van Donkelaar, J.W.H. Lo, Y.X. Wang, D. Chen, L. Zhang, P.S. Kasibhatla, S.W. Wang, Q. Zhang, Z.F. Lu, D.G. Streets, S. Bittman, and D.J. Macdonald, *Global Chemical Composition of Ambient Fine Particulate Matter for Exposure Assessment.* Environmental Science & Technology, 2014. **48**(22): p. 13060-13068.

126. Poschl, U., *Atmospheric aerosols: Composition, transformation, climate and health effects.* Angewandte Chemie-International Edition, 2005. **44**(46): p. 7520-7540.

127. Čupr, P., Z. Flegrová, J. Franců, L. Landlová, and J. Klánová, *Mineralogical, chemical and toxicological characterization of urban air particles.* Environment International, 2013. **54**: p. 26-34.

128. Holben, B.N., T.F. Eck, I. Slutsker, D. Tanre, J.P. Buis, A. Setzer, E. Vermote, J.A. Reagan, Y.J. Kaufman, T. Nakajima, F. Lavenu, I. Jankowiak, and A. Smirnov, *AERONET - A federated instrument network and data archive for aerosol characterization.* Remote Sensing of Environment, 1998. **66**(1): p. 1-16.

129. Lin, C.Q., Y. Li, Z.B. Yuan, A.K.H. Lau, C.C. Li, and J.C.H. Fung, *Using satellite remote sensing data to estimate the high-resolution distribution of ground-level PM2.5.* Remote Sensing of Environment, 2015. **156**: p. 117-128.

130. Yasunari, T.J., P.R. Colarco, W.K.M. Lau, K. Osada, M. Kido, S.P.P. Mahanama, K.M. Kim, and A.M. da Silva, *Total dust deposition flux during precipitation in Toyama, Japan, in the spring of 2009: A sensitivity analysis with the NASA GEOS-5 Model.* Atmospheric Research, 2016. **167**: p. 298-313.
131. Li, S.S., L.F. Chen, M. Fan, J.H. Tao, Z.T. Wang, C. Yu, Y.D. Si, H. Letu, and Y. Liu, *Estimation of GEOS-Chem and GOCART Simulated Aerosol Profiles Using CALIPSO Observations over the Contiguous United States.* Aerosol and Air Quality Research, 2016. **16**(12): p. 3256-3265.
132. Taylor, M., P.G. Kosmopoulos, S. Kazadzis, I. Keramitsoglou, and C.T. Kiranoudis, *Neural network radiative transfer solvers for the generation of high resolution solar irradiance spectra parameterized by cloud and aerosol parameters.* Journal of Quantitative Spectroscopy & Radiative Transfer, 2016. **168**: p. 176-192.
133. Belis, C.A., F. Karagulian, B.R. Larsen, and P.K. Hopke, *Critical review and meta-analysis of ambient particulate matter source apportionment using receptor models in Europe.* Atmospheric Environment, 2013. **69**: p. 94-108.
134. van Donkelaar, A., R.V. Martin, M. Brauer, and B.L. Boys, *Use of Satellite Observations for Long-Term Exposure Assessment of Global Concentrations of Fine Particulate Matter.* Environmental Health Perspectives, 2015. **123**(2): p. 135-143.
135. Athanasopoulou, E., A.P. Protonotariou, E. Bossioli, A. Dandou, M. Tombrou, J.D. Allan, H. Coe, N. Mihalopoulos, J. Kalogiros, A. Bacak, J. Sciare, and G. Biskos, *Aerosol chemistry above an extended archipelago of the eastern Mediterranean basin during strong northern winds.* Atmospheric Chemistry and Physics, 2015. **15**(14): p. 8401-8421.
136. Tsay, S.C., H.B. Maring, N.H. Lin, S. Buntoung, S. Chantara, H.C. Chuang, P.M. Gabriel, C.S. Goodloe, B.N. Holben, T.C. Hsiao, N.C. Hsu, S. Janjai, W.K.M. Lau, C.T. Lee, J. Lee, A.M. Loftus, A.X. Nguyen, C.M. Nguyen, S.K. Pani, P. Pantina, A.M. Sayer, W.K. Tao, S.H. Wang, E.J. Welton, W. Wiriya, and M.C. Yen, *Satellite-Surface Perspectives of Air Quality and Aerosol-Cloud Effects on the Environment: An Overview of 7-SEAS/BASELInE.* Aerosol and Air Quality Research, 2016. **16**(11): p. 2581-2602.

137. Stafoggia, M., J. Schwartz, C. Badaloni, T. Bellander, E. Alessandrini, G. Cattani, F. de' Donato, A. Gaeta, G. Leone, A. Lyapustin, M. Sorek-Hamer, K. de Hoogh, Q. Di, F. Forastiere, and I. Kloog, *Estimation of daily PM10 concentrations in Italy (2006–2012) using finely resolved satellite data, land use variables and meteorology.* Environment International, 2017. **99**: p. 234-244.

138. Vanhellemont, Q., G. Neukermans, and K. Ruddick, *Synergy between polar-orbiting and geostationary sensors: Remote sensing of the ocean at high spatial and high temporal resolution.* Remote Sensing of Environment, 2014. **146**: p. 49-62.

139. Chance, K., X. Liu, R.M. Suleiman, D.E. Flittner, J. Al-Saadi, and S.J. Janz, *Tropospheric emissions: Monitoring of pollution (TEMPO)*, in *Earth Observing Systems Xviii*, J.J. Butler, X. Xiong, and X. Gu, Editors. 2013, Spie-Int Soc Optical Engineering: Bellingham.

140. Carn, S.A., L. Clarisse, and A.J. Prata, *Multi-decadal satellite measurements of global volcanic degassing.* Journal of Volcanology and Geothermal Research, 2016. **311**: p. 99-134.

141. Carrer, D., X. Ceamanos, B. Six, and J.L. Roujean, *AERUS-GEO: A newly available satellite-derived aerosol optical depth product over Europe and Africa.* Geophysical Research Letters, 2014. **41**(21): p. 7731-7738.

142. Romano, F., E. Ricciardelli, D. Cimini, F. Di Paola, and M. Viggiano, *Dust Detection and Optical Depth Retrieval Using MSG-SEVIRI Data.* Atmosphere, 2013. **4**(1): p. 35-47.

143. Naeger, A.R. and S.A. Christopher, *The identification and tracking of volcanic ash using the Meteosat Second Generation (MSG) Spinning Enhanced Visible and Infrared Imager (SEVIRI).* Atmospheric Measurement Techniques, 2014. **7**(2): p. 581-597.

144. Yumimoto, K., T.M. Nagao, M. Kikuchi, T.T. Sekiyama, H. Murakami, T.Y. Tanaka, A. Ogi, H. Irie, P. Khatri, H. Okumura, K. Arai, I. Morino, O. Uchino, and T. Maki, *Aerosol data assimilation using data from Himawari-8, a next-generation geostationary meteorological satellite.* Geophysical Research Letters, 2016. **43**(11): p. 5886-5894.

145. Wickramasinghe, C.H., S. Jones, K. Reinke, and L. Wallace, *Development of a Multi-Spatial Resolution Approach to the Surveillance of Active Fire Lines Using Himawari-8*. Remote Sensing, 2016. **8**(11): p. 13.
146. Sekiyama, T.T., K. Yumimoto, T.Y. Tanaka, T. Nagao, M. Kikuchi, and H. Murakami, *Data Assimilation of Himawari-8 Aerosol Observations: Asian Dust Forecast in June 2015*. Sola, 2016. **12**: p. 86-90.
147. Greenwald, T.J., R.B. Pierce, T. Schaack, J. Otkin, M. Rogal, K. Bah, A. Lenzen, J. Nelson, J. Li, and H.L. Huang, *Real-Time Simulation of the GOES-R ABI for User Readiness and Product Evaluation*. Bulletin of the American Meteorological Society, 2016. **97**(2): p. 18.
148. Reid, J.S., E.J. Hyer, R.S. Johnson, B.N. Holben, R.J. Yokelson, J.L. Zhang, J.R. Campbell, S.A. Christopher, L. Di Girolamo, L. Giglio, R.E. Holz, C. Kearney, J. Miettinen, E.A. Reid, F.J. Turk, J. Wang, P. Xian, G.Y. Zhao, R. Balasubramanian, B.N. Chew, S. Janjai, N. Lagrosas, P. Lestari, N.H. Lin, M. Mahmud, A.X. Nguyen, B. Norris, N.T.K. Oanh, M. Oo, S.V. Salinas, E.J. Welton, and S.C. Liew, *Observing and understanding the Southeast Asian aerosol system by remote sensing: An initial review and analysis for the Seven Southeast Asian Studies (7SEAS) program*. Atmospheric Research, 2013. **122**: p. 403-468.
149. Hoff, R.M. and S.A. Christopher, *Remote Sensing of Particulate Pollution from Space: Have We Reached the Promised Land?* Journal of the Air & Waste Management Association, 2009. **59**(6): p. 645-675.
150. Yang, Y., H. Liao, and S.J. Lou, *Decadal trend and interannual variation of outflow of aerosols from East Asia: Roles of variations in meteorological parameters and emissions*. Atmospheric Environment, 2015. **100**: p. 141-153.
151. Guehenneux, Y., M. Gouhier, and P. Labazuy, *Improved space borne detection of volcanic ash for real-time monitoring using 3-Band method*. Journal of Volcanology and Geothermal Research, 2015. **293**: p. 25-45.
152. Freeborn, P.H., M.J. Wooster, G. Roberts, and W. Xu, *Evaluating the SEVIRI Fire Thermal Anomaly Detection Algorithm across the Central African Republic Using the MODIS Active Fire Product*. Remote Sensing, 2014. **6**(3): p. 1890-1917.

153. Liu, Y., Z.F. Wang, J. Wang, R.A. Ferrare, R.K. Newsom, and E.J. Welton, *The effect of aerosol vertical profiles on satellite-estimated surface particle sulfate concentrations.* Remote Sensing of Environment, 2011. **115**(2): p. 508-513.
154. Lee, K.H., K.T. Lee, and S.R. Chung, *Time-resolved observation of volcanic ash using COMS/MI: A case study from the 2011 Shinmoedake eruption.* Remote Sensing of Environment, 2016. **173**: p. 122-132.
155. van Donkelaar, A., R.V. Martin, R.J.D. Spurr, E. Drury, L.A. Remer, R.C. Levy, and J. Wang, *Optimal estimation for global ground-level fine particulate matter concentrations.* Journal of Geophysical Research-Atmospheres, 2013. **118**(11): p. 5621-5636.
156. Tegen, I., K. Schepanski, and B. Heinold, *Comparing two years of Saharan dust source activation obtained by regional modelling and satellite observations.* Atmospheric Chemistry and Physics, 2013. **13**(5): p. 2381-2390.
157. Karlsson, K.G., E. Johansson, and A. Devasthale, *Advancing the uncertainty characterisation of cloud masking in passive satellite imagery: Probabilistic formulations for NOAA AVHRR data.* Remote Sensing of Environment, 2015. **158**: p. 126-139.
158. Lary, D.J., A.H. Alavi, A.H. Gandomi, and A.L. Walker, *Machine learning in geosciences and remote sensing.* Geoscience Frontiers, 2016. **7**(1): p. 3-10.
159. Xiao, F., G.Y.K. Shea, M.S. Wong, and J. Campbell, *An automated and integrated framework for dust storm detection based on OGC web processing services*, in *Isprs Technical Commission Ii Symposium*, S. Li and S. Dragicevic, Editors. 2014, Copernicus Gesellschaft Mbh: Gottingen. p. 151-156.
160. Mei, L.L., Y. Xue, A.A. Kokhanovsky, W. von Hoyningen-Huene, G. de Leeuw, and J.P. Burrows, *Retrieval of aerosol optical depth over land surfaces from AVHRR data.* Atmospheric Measurement Techniques, 2014. **7**(8): p. 2411-2420.
161. O'Loingsigh, T., R.M. Mitchell, S.K. Campbell, N.A. Drake, G.H. McTainsh, N.J. Tapper, and D.L. Dunkerley, *Correction of dust event frequency from MODIS Quick-Look imagery using in-situ aerosol measurements over the*

Lake Eyre Basin, Australia. Remote Sensing of Environment, 2015. **169**: p. 222-231.

162. Zhang, X.Y., S. Kondragunta, and B. Quayle, *Estimation of Biomass Burned Areas Using Multiple-Satellite-Observed Active Fires.* Ieee Transactions on Geoscience and Remote Sensing, 2011. **49**(11): p. 4469-4482.
163. Baldassarre, G., L. Pozzoli, C.C. Schmidt, A. Unal, T. Kindap, W.P. Menzel, S. Whitburn, P.F. Coheur, A. Kavgaci, and J.W. Kaiser, *Using SEVIRI fire observations to drive smoke plumes in the CMAQ air quality model: a case study over Antalya in 2008.* Atmospheric Chemistry and Physics, 2015. **15**(14): p. 8539-8558.
164. Brauer, M., M. Amann, R.T. Burnett, A. Cohen, F. Dentener, M. Ezzati, S.B. Henderson, M. Krzyzanowski, R.V. Martin, R. Van Dingenen, A. van Donkelaar, and G.D. Thurston, *Exposure Assessment for Estimation of the Global Burden of Disease Attributable to Outdoor Air Pollution.* Environmental Science & Technology, 2012. **46**(2): p. 652-660.
165. Hoven, I.V.d., *Power Spectrum of Horizontal Wind Speed in the Frequency Range from 0.0007 to 900 Cycles Per Hour*. Journal of Meteorology, 1957. **14**(2): p. 160-164.
166. Stull, R.B., *An introduction to boundary layer meteorology*. Vol. 13. 2012: Springer Science & Business Media.
167. Chow, J.C., *Measurement Methods to Determine Compliance with Ambient Air Quality Standards for Suspended Particles.* Journal of the Air & Waste Management Association, 1995. **45**(5): p. 320-382.
168. Chow, J.C. *Guideline on Speciated Particulate Monitoring.* 1998; Available from: http://www3.epa.gov/ttnamti1/files/ambient/pm25/spec/drispec.pdf.
169. Fernandes, A.P., M. Riffler, J. Ferreira, S. Wunderle, C. Borrego, and O. Tchepeld, *Comparisons of aerosol optical depth provided by SEVIRI satellite observations and CAMx air quality modelling*, in *36th International Symposium on Remote Sensing of Environment*, G. Schreier, P.E. Skrovseth, and H. Staudenrausch, Editors. 2015, Copernicus Gesellschaft Mbh: Gottingen. p. 187-193.

170. Choi, J.K., Y.J. Park, J.H. Ahn, H.S. Lim, J. Eom, and J.H. Ryu, *GOCI, the world's first geostationary ocean color observation satellite, for the monitoring of temporal variability in coastal water turbidity*. Journal of Geophysical Research-Oceans, 2012. **117**: p. 10.
171. Wang, J., X.G. Xu, S.G. Ding, J. Zeng, R. Spurr, X. Liu, K. Chance, and M. Mishchenko, *A numerical testbed for remote sensing of aerosols, and its demonstration for evaluating retrieval synergy from a geostationary satellite constellation of GEO-CAPE and GOES-R*. Journal of Quantitative Spectroscopy & Radiative Transfer, 2014. **146**: p. 510-528.
172. Fukuda, S., T. Nakajima, H. Takenaka, A. Higurashi, N. Kikuchi, T.Y. Nakajima, and H. Ishida, *New approaches to removing cloud shadows and evaluating the 380 nm surface reflectance for improved aerosol optical thickness retrievals from the GOSAT/TANSO-Cloud and Aerosol Imager*. Journal of Geophysical Research: Atmospheres, 2013. **118**(24): p. 13,520-13,531.
173. Mackie, D.S., P.W. Boyd, G.H. McTainsh, N.W. Tindale, T.K. Westberry, and K.A. Hunter, *Biogeochemistry of iron in Australian dust: From eolian uplift to marine uptake*. Geochemistry, Geophysics, Geosystems, 2008. **9**(3).
174. Al-Dousari, A.M., J. Al-Awadhi, and M. Ahmed, *Dust fallout characteristics within global dust storm major trajectories*. Arabian Journal of Geosciences, 2013. **6**(10): p. 3877-3884.
175. Tewkesbury, A.P., A.J. Comber, N.J. Tate, A. Lamb, and P.F. Fisher, *A critical synthesis of remotely sensed optical image change detection techniques*. Remote Sensing of Environment, 2015. **160**: p. 1-14.
176. Chang, I. and S.A. Christopher, *Identifying Absorbing Aerosols Above Clouds From the Spinning Enhanced Visible and Infrared Imager Coupled With NASA A-Train Multiple Sensors*. Ieee Transactions on Geoscience and Remote Sensing, 2016. **54**(6): p. 3163-3173.
177. Di, A.J., Y. Xue, X.H. Yang, J. Leys, J. Guang, L.L. Mei, J.L. Wang, L. She, Y.C. Hu, X.W. He, Y.H. Che, and C. Fan, *Dust Aerosol Optical Depth Retrieval and Dust Storm Detection for Xinjiang Region Using Indian National Satellite Observations*. Remote Sensing, 2016. **8**(9): p. 17.

178. Mishra, M.K., G. Rastogi, and P. Chauhan, *Operational retrieval of aerosol optical depth over Indian subcontinent and Indian ocean using INSAT-3D/imager and product validation*, in *Isprs Technical Commission Viii Symposium*, V.K. Dadhwal, et al., Editors. 2014, Copernicus Gesellschaft Mbh: Gottingen. p. 277-282.
179. Naeger, A.R., P. Gupta, B.T. Zavodsky, and K.M. McGrath, *Monitoring and tracking the trans-Pacific transport of aerosols using multi-satellite aerosol optical depth composites.* Atmospheric Measurement Techniques, 2016. **9**(6): p. 2463-2482.
180. Wooster, M.J., G. Roberts, P.H. Freeborn, W. Xu, Y. Govaerts, R. Beeby, J. He, A. Lattanzio, D. Fisher, and R. Mullen, *LSA SAF Meteosat FRP products - Part 1: Algorithms, product contents, and analysis.* Atmospheric Chemistry and Physics, 2015. **15**(22): p. 13217-13239.
181. Firas, A.J. and H.A. Fawzi, *Image Interpolation Using Kriging Technique for Spatial Data.* Canadian Journal on Image Processing and Computer Vision, 2013. **4**(2): p. 16-21.
182. CHEOS. *China space report*. China High-definition Earth Observation System. Available from https://chinaspacereport.com/spacecraft/gaofen/#gf4. 2018.
183. Tanré, D., Y.J. Kaufman, M. Herman, and S. Mattoo, *Remote sensing of aerosol properties over oceans using the MODIS/EOS spectral radiances.* Journal of Geophysical Research: Atmospheres, 1997. **102**(D14): p. 16971-16988.
184. Lyapustin, A. and Y. Wang, *MAIAC - Multi-Angle Implementation of Atmospheric Correction for MODIS.* American Geophysical Union, 2007(Spring Meeting): p. A51B-05.
185. Kim, P.S., D.J. Jacob, J.A. Fisher, K. Travis, K. Yu, L. Zhu, R.M. Yantosca, M.P. Sulprizio, J.L. Jimenez, P. Campuzano-Jost, K.D. Froyd, J. Liao, J.W. Hair, M.A. Fenn, C.F. Butler, N.L. Wagner, T.D. Gordon, A. Welti, P.O. Wennberg, J.D. Crounse, J.M. St Clair, A.P. Teng, D.B. Millet, J.P. Schwarz, M.Z. Markovic, and A.E. Perring, *Sources, seasonality, and trends of southeast US aerosol: an integrated analysis of surface, aircraft, and satellite*

observations with the GEOS-Chem chemical transport model. Atmospheric Chemistry and Physics, 2015. **15**(18): p. 10411-10433.

186. Xu, X.G., J. Wang, D.K. Henze, W.J. Qu, and M. Kopacz, *Constraints on aerosol sources using GEOS-Chem adjoint and MODIS radiances, and evaluation with multisensor (OMI, MISR) data.* Journal of Geophysical Research-Atmospheres, 2013. **118**(12): p. 6396-6413.
187. Jackson, J.M., H. Liu, I. Laszlo, S. Kondragunta, L.A. Remer, J. Huang, and H.-C. Huang, *Suomi-NPP VIIRS aerosol algorithms and data products.* Journal of Geophysical Research: Atmospheres, 2013. **118**(22): p. 12,673-12,689.
188. Matter, S. *GOES- R Advanced Baseline Imager (ABI) Algorithm Theoretical Basis Document For Suspended Matter/Aerosol Optical Depth and Aerosol Size Parameter.* 2010; Available from: https://www.goes-r.gov/products/ATBDs/baseline/AAA_AODASP_v2.0_no_color.pdf.
189. Zoogman, P., X. Liu, R.M. Suleiman, W.F. Pennington, D.E. Flittner, J.A. Al-Saadi, B.B. Hilton, D.K. Nicks, M.J. Newchurch, J.L. Carr, S.J. Janz, M.R. Andraschko, A. Arola, B.D. Baker, B.P. Canova, C.C. Miller, R.C. Cohen, J.E. Davis, M.E. Dussault, D.P. Edwards, J. Fishman, A. Ghulam, G.G. Abad, M. Grutter, J.R. Herman, J. Houck, D.J. Jacob, J. Joiner, B.J. Kerridge, J. Kim, N.A. Krotkov, L. Lamsal, C. Li, A. Lindfors, R.V. Martin, C.T. McElroy, C. McLinden, V. Natraj, D.O. Neil, C.R. Nowlan, E.J. O'Sullivan, P.I. Palmer, R.B. Pierce, M.R. Pippin, A. Saiz-Lopez, R.J.D. Spurr, J.J. Szykman, O. Torres, J.P. Veefkind, B. Veihelmann, H. Wang, J. Wang, and K. Chance, *Tropospheric emissions: Monitoring of pollution (TEMPO).* Journal of Quantitative Spectroscopy & Radiative Transfer, 2017. **186**: p. 17-39.
190. Hess, M., P. Koepke, and I. Schult, *Optical properties of aerosols and clouds: The software package OPAC.* Bulletin of the American Meteorological Society, 1998. **79**(5): p. 831-844.
191. Christopher, S.A., *Simulation of GOES-R ABI aerosol radiances using WRF-CMAQ: a case study approach.* Atmospheric Chemistry and Physics, 2014. **14**(7): p. 3183-3194.

192. Huang, G.H., M.G. Ma, S.L. Liang, S.M. Liu, and X. Li, *A LUT-based approach to estimate surface solar irradiance by combining MODIS and MTSAT data.* Journal of Geophysical Research-Atmospheres, 2011. **116**: p. 14.
193. Sessions, W.R., J.S. Reid, A. Benedetti, P.R. Colarco, A. da Silva, S. Lu, T. Sekiyama, T.Y. Tanaka, J.M. Baldasano, S. Basart, M.E. Brooks, T.F. Eck, M. Iredell, J.A. Hansen, O.C. Jorba, H.M.H. Juang, P. Lynch, J.J. Morcrette, S. Moorthi, J. Mulcahy, Y. Pradhan, M. Razinger, C.B. Sampson, J. Wang, and D.L. Westphal, *Development towards a global operational aerosol consensus: basic climatological characteristics of the International Cooperative for Aerosol Prediction Multi-Model Ensemble (ICAP-MME).* Atmospheric Chemistry and Physics, 2015. **15**(1): p. 335-362.
194. Huneeus, N., M. Schulz, Y. Balkanski, J. Griesfeller, J. Prospero, S. Kinne, S. Bauer, O. Boucher, M. Chin, F. Dentener, T. Diehl, R. Easter, D. Fillmore, S. Ghan, P. Ginoux, A. Grini, L. Horowitz, D. Koch, M.C. Krol, W. Landing, X. Liu, N. Mahowald, R. Miller, J.J. Morcrette, G. Myhre, J. Penner, J. Perlwitz, P. Stier, T. Takemura, and C.S. Zender, *Global dust model intercomparison in AeroCom phase I.* Atmospheric Chemistry and Physics, 2011. **11**(15): p. 7781-7816.
195. Safarpour, S., K. Abdullah, H. San Lim, M. Dadras, and Iop, *Accuracy assessment of Terra-MODIS aerosol optical depth retrievals*, in *7th Igrsm International Remote Sensing & Gis Conference and Exhibition*. 2014.
196. Mann, G.W., K.S. Carslaw, C.L. Reddington, K.J. Pringle, M. Schulz, A. Asmi, D.V. Spracklen, D.A. Ridley, M.T. Woodhouse, L.A. Lee, K. Zhang, S.J. Ghan, R.C. Easter, X. Liu, P. Stier, Y.H. Lee, P.J. Adams, H. Tost, J. Lelieveld, S.E. Bauer, K. Tsigaridis, T.P.C. van Noije, A. Strunk, E. Vignati, N. Bellouin, M. Dalvi, C.E. Johnson, T. Bergman, H. Kokkola, K. von Salzen, F. Yu, G. Luo, A. Petzold, J. Heintzenberg, A. Clarke, A. Ogren, J. Gras, U. Baltensperger, U. Kaminski, S.G. Jennings, C.D. O'Dowd, R.M. Harrison, D.C.S. Beddows, M. Kulmala, Y. Viisanen, V. Ulevicius, N. Mihalopoulos, V. Zdimal, M. Fiebig, H.C. Hansson, E. Swietlicki, and J.S. Henzing, *Intercomparison and evaluation of global aerosol microphysical properties*

among AeroCom models of a range of complexity. Atmospheric Chemistry and Physics, 2014. **14**(9): p. 4679-4713.

197. Buchard, V., A.M. da Silva, C.A. Randles, P. Colarco, R. Ferrare, J. Hair, C. Hostetler, J. Tackett, and D. Winker, *Evaluation of the surface PM2.5 in Version 1 of the NASA MERRA Aerosol Reanalysis over the United States.* Atmospheric Environment, 2016. **125**: p. 100-111.
198. Alvarado, M.J., C.R. Lonsdale, H.L. Macintyre, H.S. Bian, M. Chin, D.A. Ridley, C.L. Heald, K.L. Thornhill, B.E. Anderson, M.J. Cubison, J.L. Jimenez, Y. Kondo, L.K. Sahu, J.E. Dibb, and C. Wang, *Evaluating model parameterizations of submicron aerosol scattering and absorption with in situ data from ARCTAS 2008.* Atmospheric Chemistry and Physics, 2016. **16**(14): p. 9435-9455.
199. Brindley, H., S. Osipov, R. Bantges, A. Smirnov, J. Banks, R. Levy, P.J. Prakash, and G. Stenchikov, *An assessment of the quality of aerosol retrievals over the Red Sea and evaluation of the climatological cloud-free dust direct radiative effect in the region.* Journal of Geophysical Research-Atmospheres, 2015. **120**(20): p. 10862-10878.
200. Curci, G., C. Hogrefe, R. Bianconi, U. Im, A. Balzarini, R. Baro, D. Brunner, R. Forkel, L. Giordano, M. Hirtl, L. Honzak, P. Jimenez-Guerrero, C. Knote, M. Langer, P.A. Makar, G. Pirovano, J.L. Perez, R. San Jose, D. Syrakov, P. Tuccella, J. Werhahn, R. Wolke, R. Zabkar, J. Zhang, and S. Galmarini, *Uncertainties of simulated aerosol optical properties induced by assumptions on aerosol physical and chemical properties: An AQMEII-2 perspective.* Atmospheric Environment, 2015. **115**: p. 541-552.
201. Kim, M., J. Kim, U. Jeong, W. Kim, H. Hong, B. Holben, T.F. Eck, J.H. Lim, C.K. Song, S. Lee, and C.Y. Chung, *Aerosol optical properties derived from the DRAGON-NE Asia campaign, and implications for a single-channel algorithm to retrieve aerosol optical depth in spring from Meteorological Imager (MI) on-board the Communication, Ocean, and Meteorological Satellite (COMS).* Atmospheric Chemistry and Physics, 2016. **16**(3): p. 1789-1808.

202. Lee, K.H., M.S. Wong, S.R. Chung, and E. Sohn, *Improved volcanic ash detection based on a hybrid reverse absorption technique.* Atmospheric Research, 2014. **143**: p. 31-42.
203. Lee, K.H. and K.T. Lee, *Volcanic ash retrieval using a new geostationary satellite*, in *Iwidf 2015*, J. Zhang, Z. Lu, and Y. Zeng, Editors. 2015, Copernicus Gesellschaft Mbh: Gottingen. p. 67-74.
204. Puttaswamy, S.J., H.M. Nguyen, A. Braverman, X.F. Hu, and Y. Liu, *Statistical data fusion of multi-sensor AOD over the Continental United States.* Geocarto International, 2014. **29**(1): p. 48-64.
205. Roberts, G., M.J. Wooster, W. Xu, P.H. Freeborn, J.J. Morcrette, L. Jones, A. Benedetti, H. Jiangping, D. Fisher, and J.W. Kaiser, *LSA SAF Meteosat FRP products - Part 2: Evaluation and demonstration for use in the Copernicus Atmosphere Monitoring Service (CAMS).* Atmospheric Chemistry and Physics, 2015. **15**(22): p. 13241-13267.
206. Huang, Y., H. Shen, H. Chen, R. Wang, Y. Zhang, S. Su, Y. Chen, N. Lin, S. Zhuo, Q. Zhong, X. Wang, J. Liu, B. Li, W. Liu, and S. Tao, *Quantification of Global Primary Emissions of PM2.5, PM10, and TSP from Combustion and Industrial Process Sources.* Environmental Science & Technology, 2014. **48**(23): p. 13834-13843.
207. Zhang, H., B. Xie, S.-Y. Zhao, and Q. Chen, *PM2.5 and tropospheric O3 in China and an analysis of the impact of pollutant emission control.* Advances in Climate Change Research, 2014. **5**(3): p. 136-141.
208. Hu, J., L. Wu, B. Zheng, Q. Zhang, K. He, Q. Chang, X. Li, F. Yang, Q. Ying, and H. Zhang, *Source contributions and regional transport of primary particulate matter in China.* Environmental Pollution, 2015. **207**: p. 31-42.
209. Bukowiecki, N., E. Weingartner, M. Gysel, M.C. Coen, P. Zieger, E. Herrmann, M. Steinbacher, H.W. Gaggeler, and U. Baltensperger, *A Review of More than 20 Years of Aerosol Observation at the High Altitude Research Station Jungfraujoch, Switzerland (3580 m asl).* Aerosol and Air Quality Research, 2016. **16**(3): p. 764-788.
210. Hagemann, R., U. Corsmeier, C. Kottmeier, R. Rinke, A. Wieser, and B. Vogel, *Spatial variability of particle number concentrations and NO_x in the*

Karlsruhe (Germany) area obtained with the mobile laboratory 'AERO-TRAM'. Atmospheric Environment, 2014. **94**: p. 341-352.

211. Xu, J.W., R.V. Martin, A. van Donkelaar, J. Kim, M. Choi, Q. Zhang, G. Geng, Y. Liu, Z. Ma, L. Huang, Y. Wang, H. Chen, H. Che, P. Lin, and N. Lin, *Estimating ground-level PM2.5 in eastern China using aerosol optical depth determined from the GOCI satellite instrument*. Atmospheric Chemistry and Physics, 2015. **15**(22): p. 13133-13144.
212. Lin, J., A. van Donkelaar, J. Xin, H. Che, and Y. Wang, *Clear-sky aerosol optical depth over East China estimated from visibility measurements and chemical transport modeling*. Atmospheric Environment, 2014. **95**: p. 258-267.
213. Heald, C.L., D.A. Ridley, J.H. Kroll, S.R.H. Barrett, K.E. Cady-Pereira, M.J. Alvarado, and C.D. Holmes, *Contrasting the direct radiative effect and direct radiative forcing of aerosols*. Atmospheric Chemistry and Physics, 2014. **14**(11): p. 5513-5527.
214. Sorek-Hamer, M., D. Broday, R. Chatfield, R. Esswein, M. Stafoggia, J. Lepeule, A. Lyapustin, and I. Kloog, *Monthly Analysis of PM Ratio Characteristics and its Relation to AOD*. Journal of the Air & Waste Management Association, 2016. **67**(1): p. 27-38.
215. Wind, G., A.M. da Silva, P.M. Norris, S. Platnick, S. Mattoo, and R.C. Levy, *Multi-sensor cloud and aerosol retrieval simulator and remote sensing from model parameters - Part 2: Aerosols*. Geoscientific Model Development, 2016. **9**(7): p. 2377-2389.
216. CDO. *Climate Data Operators*. 2018; Available from: http://www.mpimet.mpg.de/cdo.
217. Ayachit, U., *The ParaView Guide: A Parallel Visualization Application*. 2015: Kitware, Inc. 276.
218. Zawadzka, O. and K. Markowicz, *Retrieval of Aerosol Optical Depth from Optimal Interpolation Approach Applied to SEVIRI Data*. Remote Sensing, 2014. **6**(8): p. 7182-7211.

219. Wang, W., F.Y. Mao, L. Du, Z.X. Pan, W. Gong, and S.H. Fang, *Deriving Hourly PM2.5 Concentrations from Himawari-8 AODs over Beijing-Tianjin-Hebei in China.* Remote Sensing, 2017. **9**(8).
220. Gonzalez, L. and X. Briottet, *North Africa and Saudi Arabia Day/Night Sandstorm Survey (NASCube).* Remote Sensing, 2017. **9**(9).
221. Adão, T., J. Hruška, L. Pádua, J. Bessa, E. Peres, R. Morais, and J. Sousa, *Hyperspectral Imaging: A Review on UAV-Based Sensors, Data Processing and Applications for Agriculture and Forestry.* Remote Sensing, 2017. **9**(11): p. 1110.
222. Guo, J.P., F. Xia, Y. Zhang, H. Liu, J. Li, M.Y. Lou, J. He, Y. Yan, F. Wang, M. Min, and P.M. Zhai, *Impact of diurnal variability and meteorological factors on the PM2.5 - AOD relationship: Implications for PM2.5 remote sensing.* Environmental Pollution, 2017. **221**: p. 94-104.
223. ESRL, Earth System Research Laboratory, Global Monitoring Division. *SURFRAD Aerosol Optical Depth.* 2018; Available from: https://www.esrl.noaa.gov/gmd/grad/surfrad/aod/algo2.html.
224. Gao, M., J. Cao, and E. Seto, *A distributed network of low-cost continuous reading sensors to measure spatiotemporal variations of PM2.5 in Xi'an, China.* Environmental Pollution, 2015. **199**: p. 56-65.
225. Saraswat, A., J.S. Apte, M. Kandlikar, M. Brauer, S.B. Henderson, and J.D. Marshall, *Spatiotemporal Land Use Regression Models of Fine, Ultrafine, and Black Carbon Particulate Matter in New Delhi, India.* Environmental Science & Technology, 2013. **47**(22): p. 12903-12911.
226. Wang, Y., Q. Ying, J. Hu, and H. Zhang, *Spatial and temporal variations of six criteria air pollutants in 31 provincial capital cities in China during 2013–2014.* Environment International, 2014. **73**: p. 413-422.
227. Kikuchi, M., H. Murakami, K. Suzuki, T.M. Nagao, and A. Higurashi, *Improved Hourly Estimates of Aerosol Optical Thickness Using Spatiotemporal Variability Derived From Himawari-8 Geostationary Satellite.* IEEE Transactions on Geoscience and Remote Sensing, 2018: p. 1-14.

228. Li, L., J. Qian, C.-Q. Ou, Y.-X. Zhou, C. Guo, and Y. Guo, *Spatial and temporal analysis of Air Pollution Index and its timescale-dependent relationship with meteorological factors in Guangzhou, China, 2001–2011.* Environmental Pollution, 2014. **190**: p. 75-81.
229. JMA. *Himawari-8: JMA's Next Generation Geostationary Meteorological Satellite.* 2015; Available from: http://www.icao.int/APAC/Meetings/2015%20METATMSeminar/SP11_JPN%20-%20Himawari-8_JMA's%20Next-Generation%20Geostationary%20Meteorological%20Satellite.pdf.
230. Luna, M.A.G., F.A.G. Luna, J.F.M. Espinosa, and L.C.B. Ceron, *Spatial and Temporal Assessment of Particulate Matter Using AOD Data from MODIS and Surface Measurements in the Ambient Air of Colombia.* Asian Journal of Atmospheric Environment, 2018. **12**(2): p. 165-177.
231. Goudie, A.S., *Desert dust and human health disorders.* Environ Int, 2014. **63**: p. 101-13.
232. Bell, T. and M. Adams, *Chapter 14 Smoke from Wildfires and Prescribed Burning in Australia: Effects on Human Health and Ecosystems*, in *Developments in Environmental Science*, A. Bytnerowicz, et al., Editors. 2008, Elsevier. p. 289-316.
233. Wuebbles, D.J., H. Lei, and J. Lin, *Intercontinental transport of aerosols and photochemical oxidants from Asia and its consequences.* Environmental Pollution, 2007. **150**(1): p. 65-84.
234. She, L., Y. Xue, X. Yang, J. Guang, Y. Li, Y. Che, C. Fan, and Y. Xie, *Dust Detection and Intensity Estimation Using Himawari-8/AHI Observation.* Remote Sensing, 2018. **10**(4): p. 490.
235. Sifakis, N.I. and C. Iossifidis, *CHRISTINE Code for High ResolutIon Satellite mapping of optical ThIckness and ÅNgstrom Exponent. Part I: Algorithm and code.* Computers & Geosciences, 2014. **62**: p. 136-141.
236. BOM. *Bureau of Meteorology, Himawari-8 and -9.* 2017; Available from: http://www.bom.gov.au/australia/satellite/himawari.shtml.

237. Mahowald, N., S. Albani, J.F. Kok, S. Engelstaeder, R. Scanza, D.S. Ward, and M.G. Flanner, *The size distribution of desert dust aerosols and its impact on the Earth system.* Aeolian Research, 2014. **15**: p. 53-71.

238. Han, H.J., B.J. Sohn, H.L. Huang, E. Weisz, R. Saunders, and T. Takamura, *An improved radiance simulation for hyperspectral infrared remote sensing of Asian dust.* Journal of Geophysical Research-Atmospheres, 2012. **117**.

239. Takemura, T., T. Nozawa, S. Emori, T.Y. Nakajima, and T. Nakajima, *Simulation of climate response to aerosol direct and indirect effects with aerosol transport-radiation model.* Journal of Geophysical Research-Atmospheres, 2005. **110**(D2).

240. Harper, J. and D. Tuxford, *Port Hedland Dust Management Taskforce - Cumulative Impact Study* 2007.

241. Miller, S.D., C.C. Schmidt, T.J. Schmit, and D.W. Hillger, *A case for natural colour imagery from geostationary satellites, and an approximation for the GOES-R ABI.* International Journal of Remote Sensing, 2012. **33**(13): p. 3999-4028.

242. Liu, Y., R. Liu, and X. Cheng, *Dust detection over desert surfaces with thermal infrared bands using dynamic reference brightness temperature differences.* Journal of Geophysical Research: Atmospheres, 2013. **118**(15): p. 8566-8584.

243. Koltunov, A., S.L. Ustin, and E.M. Prins, *On timeliness and accuracy of wildfire detection by the GOES WF-ABBA algorithm over California during the 2006 fire season.* Remote Sensing of Environment, 2012. **127**: p. 194-209.

244. Corradini, S., L. Merucci, A.J. Prata, and A. Piscini, *Volcanic ash and SO2 in the 2008 Kasatochi eruption: Retrievals comparison from different IR satellite sensors.* Journal of Geophysical Research: Atmospheres, 2010. **115**(D2): p. n/a-n/a.

245. Hache, E., J.L. Attie, C. Tourneur, P. Ricaud, L. Coret, W.A. Lahoz, L. El Amraoui, B. Josse, P. Hamer, J. Warner, X. Liu, K. Chance, M. Hopfner, R. Spurr, V. Natraj, S. Kulawik, A. Eldering, and J. Orphal, *The added value of a visible channel to a geostationary thermal infrared instrument to monitor ozone for air quality.* Atmospheric Measurement Techniques, 2014. **7**(7): p. 2185-2201.

246. VIC EPA, *Guidance Notes for using the Regulatory Air Pollution Model AERMOD in Victoria. EPA*

Victoria, 200 Victoria Street, Carlton. 2013.

247. Dourado, H., J. Santos, N.R. Junior, and A. Melo, *The effects of atmospheric turbulence on peak-to-mean concentration ratio and its consequence on the odour impact assessment using dispersion models.* Chem Eng Trans, 2012. **30**: p. 163-168.

248. The West Australian. *Pilbara dust cloud caught on camera by FIFO worker.* *https://thewest.com.au/news/pilbara/huge-dust-cloud-captured-rolling-over-pilbara-ng-b88410059z*. 2017; Available from: https://thewest.com.au/news/pilbara/huge-dust-cloud-captured-rolling-over-pilbara-ng-b88410059z.

249. Taylor, K.E., *Summarizing multiple aspects of model performance in a single diagram*. Journal of Geophysical Research: Atmospheres, 2001. **106**(D7): p. 7183-7192.

250. Letu, H., K. Yang, T.Y. Nakajima, H. Ishimoto, T.M. Nagao, J. Riedi, A.J. Baran, R. Ma, T. Wang, H. Shang, P. Khatri, L. Chen, C. Shi, and J. Shi, *High-resolution retrieval of cloud microphysical properties and surface solar radiation using Himawari-8/AHI next-generation geostationary satellite.* Remote Sensing of Environment, 2020. **239**: p. 111583.

251. Tran, H.N.Q. and N. Mölders, *Numerical investigations on the contribution of point source emissions to the PM2.5 concentrations in Fairbanks, Alaska.* Atmospheric Pollution Research, 2012. **3**(2): p. 199-210.

252. Kokaly, R.F., R.N. Clark, G.A. Swayze, K.E. Livo, T.M. Hoefen, N.C. Pearson, R.A. Wise, W.M. Benzel, H.A. Lowers, R.L. Driscoll, and A.J. Klein, *USGS Spectral Library Version 7*, in *Data Series*. 2017: Reston, VA. p. 68.

253. Bergstrom, R.W., P. Pilewskie, P.B. Russell, J. Redemann, T.C. Bond, P.K. Quinn, and B. Sierau, *Spectral absorption properties of atmospheric aerosols.* Atmospheric Chemistry and Physics, 2007. **7**(23): p. 5937-5943.

254. Taramelli, A., M. Pasqui, J. Barbour, D. Kirschbaum, L. Bottai, C. Busillo, F. Calastrini, F. Guarnieri, and C. Small, *Spatial and temporal dust source*

variability in northern China identified using advanced remote sensing analysis. Earth Surface Processes and Landforms, 2013. **38**(8): p. 793-809.

255. Shang, H., L. Chen, H. Letu, M. Zhao, S. Li, and S. Bao, *Development of a daytime cloud and haze detection algorithm for Himawari-8 satellite measurements over central and eastern China.* Journal of Geophysical Research: Atmospheres, 2017. **122**(6): p. 3528-3543.
256. Park, S.S., J. Kim, J. Lee, S. Lee, J.S. Kim, L.S. Chang, and S. Ou, *Combined dust detection algorithm by using MODIS infrared channels over East Asia.* Remote Sensing of Environment, 2014. **141**: p. 24-39.
257. Stagakis, S., N. Markos, O. Sykioti, and A. Kyparissis, *Monitoring canopy biophysical and biochemical parameters in ecosystem scale using satellite hyperspectral imagery: An application on a Phlomis fruticosa Mediterranean ecosystem using multiangular CHRIS/PROBA observations.* Remote Sensing of Environment, 2010. **114**(5): p. 977-994.
258. Samadi, M., A.D. Boloorani, S.K. Alavipanah, H. Mohamadi, and M.S. Najafi, *Global dust Detection Index (GDDI); a new remotely sensed methodology for dust storms detection.* Journal of Environmental Health Science and Engineering, 2014. **12**.
259. Xu, D., J.J. Qu, S.J. Niu, and X.J. Hao, *Sand and dust storm detection over desert regions in China with MODIS measurements.* International Journal of Remote Sensing, 2011. **32**(24): p. 9365-9373.
260. Alaibakhsh, M., I. Emelyanova, O. Barron, A. Mohyeddin, and M. Khiadani, *Multivariate detection and attribution of land-cover changes in the Central Pilbara, Western Australia.* International Journal of Remote Sensing, 2015. **36**(10): p. 2599-2621.
261. Viscarra Rossel, R.A., T. Behrens, E. Ben-Dor, D.J. Brown, J.A.M. Demattê, K.D. Shepherd, Z. Shi, B. Stenberg, A. Stevens, V. Adamchuk, H. Aïchi, B.G. Barthès, H.M. Bartholomeus, A.D. Bayer, M. Bernoux, K. Böttcher, L. Brodský, C.W. Du, A. Chappell, Y. Fouad, V. Genot, C. Gomez, S. Grunwald, A. Gubler, C. Guerrero, C.B. Hedley, M. Knadel, H.J.M. Morrás, M. Nocita, L. Ramirez-Lopez, P. Roudier, E.M.R. Campos, P. Sanborn, V.M. Sellitto, K.A. Sudduth, B.G. Rawlins, C. Walter, L.A. Winowiecki, S.Y. Hong, and W.

Ji, *A global spectral library to characterize the world's soil.* Earth-Science Reviews, 2016. **155**: p. 198-230.

262. Machiwal, D. and M.K. Jha, *Identifying sources of groundwater contamination in a hard-rock aquifer system using multivariate statistical analyses and GIS-based geostatistical modeling techniques.* Journal of Hydrology: Regional Studies, 2015. **4, Part A**: p. 80-110.
263. WHO, *Global report on urban health: equitable, healthier cities for sustainable development, World Health Organization*. 2016, World Health Organisation.
264. Prüss-Üstün, A. and C. Corvalán, *Preventing disease through healthy environments*. 2006: World Health Organization Geneva, Switzerland.
265. Australia Government, Dept Of Environment, *National Environment Protection (Ambient Air Quality) Measure Variation, 2015*. 2016.
266. Bennett, J.E., H. Tamura-Wicks, R.M. Parks, R.T. Burnett, C.A. Pope, III, M.J. Bechle, J.D. Marshall, G. Danaei, and M. Ezzati, *Particulate matter air pollution and national and county life expectancy loss in the USA: A spatiotemporal analysis.* PLOS Medicine, 2019. **16**(7): p. e1002856.
267. Watanabe, M., H. Noma, J. Kurai, K. Kato, H. Sano, T. Tatsukawa, H. Nakazaki, A. Yamasaki, and E. Shimizu, *Association between pulmonary function and daily levels of sand dust particles assessed by light detection and ranging in schoolchildren in western Japan: A panel study.* Allergology International, 2016. **65**(1): p. 56-61.
268. Tonne, C., J.I. Halonen, S.D. Beevers, D. Dajnak, J. Gulliver, F.J. Kelly, P. Wilkinson, and H.R. Anderson, *Long-term traffic air and noise pollution in relation to mortality and hospital readmission among myocardial infarction survivors.* International Journal of Hygiene and Environmental Health, 2016. **219**(1): p. 72-78.
269. Lin, H., J. Tao, Y. Du, T. Liu, Z. Qian, L. Tian, Q. Di, W. Zeng, J. Xiao, L. Guo, X. Li, Y. Xu, and W. Ma, *Differentiating the effects of characteristics of PM pollution on mortality from ischemic and hemorrhagic strokes.* International Journal of Hygiene and Environmental Health, 2016. **219**(2): p. 204-211.

270. Barnett, A.G., J.F. Fraser, and L. Munck, *The effects of the 2009 dust storm on emergency admissions to a hospital in Brisbane, Australia.* International Journal of Biometeorology, 2012. **56**(4): p. 719-726.
271. Simpson, R., G. Williams, A. Petroeschevsky, T. Best, G. Morgan, L. Denison, A. Hinwood, G. Neville, and A. Neller, *The short-term effects of air pollution on daily mortality in four Australian cities.* Aust N Z J Public Health, 2005. **29**(3): p. 205-12.
272. Pirani, M., N. Best, M. Blangiardo, S. Liverani, R.W. Atkinson, and G.W. Fuller, *Analysing the health effects of simultaneous exposure to physical and chemical properties of airborne particles.* Environment International, 2015. **79**: p. 56-64.
273. Bell, M.L., K. Ebisu, R.D. Peng, J.M. Samet, and F. Dominici, *Hospital Admissions and Chemical Composition of Fine Particle Air Pollution.* American Journal of Respiratory and Critical Care Medicine, 2009. **179**(12): p. 1115-1120.
274. Kumar, P., L. Morawska, W. Birmili, P. Paasonen, M. Hu, M. Kulmala, R.M. Harrison, L. Norford, and R. Britter, *Ultrafine particles in cities.* Environment International, 2014. **66**: p. 1-10.
275. Font, A., T. Baker, I.S. Mudway, E. Purdie, C. Dunster, and G.W. Fuller, *Degradation in urban air quality from construction activity and increased traffic arising from a road widening scheme.* Science of The Total Environment, 2014. **497–498**: p. 123-132.
276. Zielinski, T., T. Petelski, A. Strzalkowska, P. Pakszys, and P. Makuch, *Impact of wild forest fires in Eastern Europe on aerosol composition and particle optical properties.* Oceanologia, 2016. **58**(1): p. 13-24.
277. Acosta-Martínez, V., S. Van Pelt, J. Moore-Kucera, M.C. Baddock, and T.M. Zobeck, *Microbiology of wind-eroded sediments: Current knowledge and future research directions.* Aeolian Research, 2015. **18**: p. 99-113.
278. Marshall, J.D., E. Nethery, and M. Brauer, *Within-urban variability in ambient air pollution: Comparison of estimation methods.* Atmospheric Environment, 2008. **42**(6): p. 1359-1369.

279. Zhao, S., Y. Yu, D. Yin, J. He, N. Liu, J. Qu, and J. Xiao, *Annual and diurnal variations of gaseous and particulate pollutants in 31 provincial capital cities based on in situ air quality monitoring data from China National Environmental Monitoring Center.* Environment International, 2016. **86**: p. 92-106.

280. Bencs, L., K. Ravindra, J. de Hoog, Z. Spolnik, N. Bleux, P. Berghmans, F. Deutsch, E. Roekens, and R. Van Grieken, *Appraisal of measurement methods, chemical composition and sources of fine atmospheric particles over six different areas of Northern Belgium.* Environmental Pollution, 2010. **158**(11): p. 3421-3430.

281. Cohen, D.D., E. Stelcer, A. Atanacio, and J. Crawford, *The application of IBA techniques to air pollution source fingerprinting and source apportionment.* Nuclear Instruments and Methods in Physics Research Section B: Beam Interactions with Materials and Atoms, 2014. **318**: p. 113-118.

282. Ancona, C., C. Badaloni, F. Mataloni, A. Bolignano, S. Bucci, G. Cesaroni, R. Sozzi, M. Davoli, and F. Forastiere, *Mortality and morbidity in a population exposed to multiple sources of air pollution: A retrospective cohort study using air dispersion models.* Environmental Research, 2015. **137**: p. 467-474.

283. Hopke, P.K., *Review of receptor modeling methods for source apportionment.* Journal of the Air & Waste Management Association, 2016. **66**(3): p. 237-259.

284. Hurley, P.J., W.L. Physick, and A.K. Luhar, *TAPM: a practical approach to prognostic meteorological and air pollution modelling.* Environmental Modelling & Software, 2005. **20**(6): p. 737-752.

285. Sowden, M., E. Cairncross, G. Wilson, M. Zunckel, E. Kirillova, V. Reddy, and S. Hietkamp, *Developing a spatially and temporally resolved emission inventory for photochemical modeling in the City of Cape Town and assessing its uncertainty.* Atmospheric Environment, 2008. **42**(30): p. 7155-7164.

286. Draxler, R., D. Arnold, M. Chino, S. Galmarini, M. Hort, A. Jones, S. Leadbetter, A. Malo, C. Maurer, G. Rolph, K. Saito, R. Servranckx, T. Shimbori, E. Solazzo, and G. Wotawa, *World Meteorological Organization's model simulations of the radionuclide dispersion and deposition from the*

Fukushima Daiichi nuclear power plant accident. Journal of Environmental Radioactivity, 2015. **139**: p. 172-184.

287. Bennouna, Y.S., V.E. Cachorro, D. Mateos, M.A. Burgos, C. Toledano, B. Torres, and A.M. de Frutos, *Long-term comparative study of columnar and surface mass concentration aerosol properties in a background environment.* Atmospheric Environment, 2016. **140**: p. 261-272.
288. Cohen, D.D., J. Crawford, E. Stelcer, and A.J. Atanacio, *Application of positive matrix factorization, multi-linear engine and back trajectory techniques to the quantification of coal-fired power station pollution in metropolitan Sydney.* Atmospheric Environment, 2012. **61**: p. 204-211.
289. Lee, M. and E. Wagenmakers, *Bayesian data analysis for cognitive science: A practical course*. 2013, New York, NY: Cambridge University Press.
290. Kim, J., U. Jeong, M.-H. Ahn, J.H. Kim, R.J. Park, H. Lee, C.H. Song, Y.-S. Choi, K.-H. Lee, J.-M. Yoo, M.-J. Jeong, S.K. Park, K.-M. Lee, C.-K. Song, S.-W. Kim, Y. Kim, S.-W. Kim, M. Kim, S. Go, X. Liu, K. Chance, C. Chan Miller, J. Al-Saadi, B. Veihelmann, P.K. Bhartia, O. Torres, G.G. Abad, D.P. Haffner, D.H. Ko, S.H. Lee, J.-H. Woo, H. Chong, S.S. Park, D. Nicks, W.J. Choi, K.-J. Moon, A. Cho, J. Yoon, S.-k. Kim, H. Hong, K. Lee, H. Lee, S. Lee, M. Choi, P. Veefkind, P. Levelt, D.P. Edwards, M. Kang, M. Eo, J. Bak, K. Baek, H.-A. Kwon, J. Yang, J. Park, K.M. Han, B.-R. Kim, H.-W. Shin, H. Choi, E. Lee, J. Chong, Y. Cha, J.-H. Koo, H. Irie, S. Hayashida, Y. Kasai, Y. Kanaya, C. Liu, J. Lin, J.H. Crawford, G.R. Carmichael, M.J. Newchurch, B.L. Lefer, J.R. Herman, R.J. Swap, A.K.H. Lau, T.P. Kurosu, G. Jaross, B. Ahlers, M. Dobber, C.T. McElroy, and Y. Choi, *New Era of Air Quality Monitoring from Space: Geostationary Environment Monitoring Spectrometer (GEMS).* Bulletin of the American Meteorological Society, 2019: p. 00.
291. NSW, Office of Environment and Heritage, *Summer ozone episode from 11 to 12 February 2017*. 2019.
292. NSW, Office of Environment and Heritage, *Smoke from hazard reduction burning from 2 to 3 September 2017*. 2019.
293. NSW, Office of Environment and Heritage, *Dust episode from 22 to 24 September 2017*. 2019.

294. DSD, *Western Australian Department of Health - Impact of Dust on Port Hedland*. 2010, WA. Dept of Health.

295. Wei, J., Z. Li, L. Sun, Y. Peng, Z. Zhang, Z. Li, T. Su, L. Feng, Z. Cai, and H. Wu, *Evaluation and uncertainty estimate of next-generation geostationary meteorological Himawari-8/AHI aerosol products.* Science of The Total Environment, 2019. **692**: p. 879-891.

Annexure A:
Co-authorship statements for thesis with publication

With reference to ECU thesis with publication policy, statements from co-author attesting to the PhD candidate's contribution to the joint publications must be included in the appendix.

- -

Elsevier Publishing Agreement - Author Rights for Scholarly Purposes

I understand that I retain or am hereby granted (without the need to obtain further permission) the Author Rights (see description below), and that no rights in patents, trademarks or other intellectual property rights are transferred to Elsevier Ltd.

The Author Rights include the right to use the Preprint , Accepted Manuscript and the Published Journal Article for Personal Use and Internal Institutional Use . They also include the right to use these different versions of the Article for Scholarly Sharing purposes, which include sharing:

the Preprint on any website or repository at any time;

the Accepted Manuscript on certain websites and usually after an embargo period;

the Published Journal Article only privately on certain websites, unless otherwise agreed by Elsevier Ltd.

In the case of the Accepted Manuscript and the Published Journal Article the Author Rights exclude Commercial Use (unless expressly agreed in writing by Elsevier Ltd), other than use by the author in a subsequent compilation of the author's works or to extend the Article to book length form or re-use by the author of portions or excerpts in other works (with full acknowledgment of the original publication of the Article).

Paper title: Review of surface particulate monitoring of dust events using geostationary satellite remote sensing.

Journal:. *Atmospheric Environment*, 2018 **183**, 154-164.

List of authors: Sowden, M., U. Mueller, and D. Blake

PhD candidate: Miles Sowden

Scientific contributions to the paper: The PhD candidate contributed to the article with regards to development of the idea, numerical analysis, and manuscript writing constituting 80% of the work.

Ute Mueller contributed to the checking of the results, and critical revision of the manuscript (10%).

David Blake contributed to the interpretation of the results, and critical revision of the manuscript (10%).

Signature, PhD student

I, as a co-author, endorse that this level of contribution by the candidate indicated above is appropriate.

Signatures, co-authors

Associate Professor Ute Mueller  Date: **25/06/2020**

Dr David Blake:  Date: **25/06/2020**

Paper title: What temporal resolution is required for remote sensing of regional aerosol concentrations using the Himawari-8 geostationary satellite?

Journal:. *Atmospheric Environment*, 2019, **216**, 116914.

List of authors: **Sowden, M., U. Mueller, and D. Blake**

PhD candidate: Miles Sowden

Scientific contributions to the paper: The PhD candidate contributed to the article with regards to development of the idea, numerical analysis, and manuscript writing constituting 80% of the work.

Ute Mueller contributed to the checking of the results, and critical revision of the manuscript (10%).

David Blake contributed to the interpretation of the results, and critical revision of the manuscript (10%).

Signature, PhD student

I, as a co-author, endorse that this level of contribution by the candidate indicated above is appropriate.

Signatures, co-authors

Associate Professor Ute Mueller  Date: **25/06/2020**

Dr David Blake:  Date: **25/06/2020**

Paper title: Which dual-band infrared indices are optimum in identifying aerosol compositional change using Himawari-8 data?

Journal:. *Atmospheric Environment*, 2020: 117620.

List of authors: **Sowden, M., and D. Blake**

PhD candidate: Miles Sowden

Scientific contributions to the paper: The PhD candidate contributed to the article with regards to development of the idea, numerical analysis, and manuscript writing constituting 90% of the work.

David Blake contributed to the interpretation of the results, and critical revision of the manuscript (10%).

Signature, PhD student

[redacted]

I, as a co-author, endorse that this level of contribution by the candidate indicated above is appropriate.

Signature, co-author

Dr David Blake: [redacted] Date: **25/06/2020**

Paper title: Development of an infrared pollution index to identify ground-level compositional, particle size, and humidity changes using Himawari-8.

Journal:. *Atmospheric Environment*, 2020, **229**, 117435.

List of authors: **Sowden, M., D. Blake, D.D. Cohen, A. Atanacio, and U. Mueller**

PhD candidate: Miles Sowden

Scientific contributions to the paper: The PhD candidate contributed to the article with regards to development of the idea, numerical analysis, and manuscript writing constituting 80% of the work.

David Blake (5%) contributed to the interpretation of the results, and critical revision of the manuscript.

D.D. Cohen (5%) contributed to the $PM_{2.5}$ collection, elemental analysis, positive matrix factorisation analysis of the original study, verified the paraphrased descriptions of the positive matrix factorisation results and reviewed the manuscript.

A. Atanacio (5%) contributed to the $PM_{2.5}$ collection, elemental analysis, positive matrix factorisation analysis of the original study, verified the paraphrased descriptions of the positive matrix factorisation results and reviewed the manuscript.

U. Mueller (5%) contributed to the checking of the results, and critical revision of the manuscript.

[redacted]
Signature, PhD student

I, as a co-author, endorse that this level of contribution by the candidate indicated above is appropriate.

Signatures, co-authors

Associate Professor Ute Mueller: [redacted] Date: **25/06/2020**

Dr David Blake:: [redacted] Date: **25/06/2020**

Dr David D Cohen: [redacted] Date: **25 June 2020**

Dr A Atanacio: [redacted] Date: 25-Jun-

Paper title: Determining ground-level composition and concentration of particulate matter across regional areas using the Himawari-8 satellite

Journal:. ASAAQ15 *Special Issue, Air Quality, Atmosphere and Health*

List of authors: Sowden, M., U. Mueller, and D. Blake

PhD candidate: Miles Sowden

Scientific contributions to the paper: The PhD candidate contributed to the article with regards to development of the idea, numerical analysis, and manuscript writing constituting 80% of the work.

Ute Mueller contributed to the checking of the results, and critical revision of the manuscript (10%).

David Blake contributed to the interpretation of the results, and critical revision of the manuscript (10%).

[redacted]
Signature, PhD student

I, as a co-author, endorse that this level of contribution by the candidate indicated above is appropriate.

Signatures, co-authors

Associate Professor Ute Mueller [redacted] Date: **25/06/2020**

Dr David Blake: [redacted] Date: **25/06/2020**